A TEST OF THE CHARGE DENSITY WAVE MODEL OF POTASSIUM USING THE INDUCED TORQUE METHOD

By

PHILIP GEORGE COULTER, B.Sc. (Eng.)

A Thesis

Submitted to the School of Graduate Studies

in Partial Fulfilment of the Requirements

for the Degree

Doctor of Philosophy

McMaster University

1983

INDUCED TORQUE IN POTASSIUM

DOCTOR OF PHILOSOPHY (1983)
(Physics)

McMASTER UNIVERSITY
Hamilton, Ontario

TITLE: Test of the Charge Density Wave Model of Potassium Using the Induced Torque Method

AUTHOR: Philip George Coulter, B.Sc. (Eng.) Queen's University

SUPERVISOR: Professor W.R. Datars

NUMBER OF PAGES: xxii,207

SCOPE AND CONTENTS:

The theory of the charge density wave model of potassium was examined. The theory of the induced torque technique was examined and extended to predict the phase of the induced torque. The response of two induced torque magnetometers was calculated. The induced torque was measured in fields up to 8.5 T and over the temperature range 1.1 to 2.1 K. The charge density wave model and other possible explanations were examined.

ABSTRACT

The conductivity tensor of potassium was studied using the induced torque technique in two magnetometers. The response of the two magnetometers was calculated and tested with standard materials. The phase of the induced torque was calculated.

The induced torque in potassium showed different behaviour in magnetic fields, below 0.2 T, between 0.2 and 4 T and above 4 T. A two-fold torque anisotropy with peaks separated by 180° was observed at low fields and a four-fold pattern with peaks separated by 90° is dominant up to fields of 4 T. At high fields there are peaks in the induced torque rotation pattern which are characteristic of open orbits in a metal. The amplitude and magnetic field direction of some of the peaks changes non-monotonically with temperature over the temperature range 1.1 to 2.1 K. The high field peaks are independent of the presence of the four-fold torque which depends on sample preparation.

The amplitude and phase of the induced torque were calculated for two models, an ellipsoidal sample with free electron conductivity and a sample with a charge density wave ground state. The four-fold induced torque was quantitatively explained by an ellipsoidal sample. Reasons why a model of an ellipsoidal sample is valid were presented.

Qualitative agreement between the high field peaks

and the charge density wave model which predicts open orbits was obtained. A quantitative explanation of the temperature dependence could not be obtained. Other possible explanations of the high field peaks were considered and found to be unsuitable.

ACKNOWLEDGEMENTS

I should like to thank my supervisor, Dr. W.R. Datars for suggesting the problem and his interest and enthusiasm through all phases of the work. Thanks also to Dr. Overhauser for discussions on the charge density wave model and his communication of results prior to publication.

I would also like to thank the other members of the group, Zaven Altounian, Erwin Batalla, Ray Dinser, Fereidon Razavi, Afaf Rahman, Steve Shier, and Henryk Zaleski for useful discussions and assistance with experimental work. Special thanks to Clarence Verge for constructing and maintaining his magnetometer.

Thanks also to Elizabeth Mistele for general support and help with computing and proof-reading. Mrs. Kennelly's rapid and accurate typing of this thesis is appreciated, as is Mr. George Wilton's excellent drawing.

Financial support from the Natural Sciences and Engineering Research Council of Canada is gratefully acknowledged.

TABLE OF CONTENTS

LIST OF TABLES

LIST OF FIGURES

LIST OF SYMBOLS

$\vec{A}$	displacement of ions due to a CDW
A	induced torque amplitude due to an open orbit
$\vec{a}$	arbitrary vector
a	lattice constant
$a_{\pm}$	amplitude of electron displacement due to a CDW
$\vec{B}$	magnetic field
$\vec{B}_{ac}$	changing magnetic field
B_1	amplitude of B_{ac}
B_0	magnetic field required for magnetic breakdown
b	distortion of ellipsoid, in Lass model, from spherical
C	compliance of magnetometer support
c	constant
D	domain size
d	constant
$\vec{E}$	electric field
E_g	energy gap
E_F	Fermi energy
e	charge on electron
F	torque anisotropy
f	constant
f_n	volume fraction of CDW domain n
$\vec{G}$	reciprocal lattice vector
G	amplitude of CDW potential

g	acceleration due to gravity
H	hamiltonian
$\hbar$	Planck's constant
I	moment of inertia
J	Bessel function
$\vec{j}$	current density
$\overleftrightarrow{K}$	matrix describing the orientation of an ellipsoid
$\vec{K}$	magnetic susceptibility of a sphere
K	constant
$\vec{k},\vec{k}'$	arbitrary wave vector
k,k'	constant
k_F	Fermi wave vector
k_{FE}	Fermi wave vector for free electron sphere
L	magnetometer amplitude
ℓ	length of quartz rod in rotating sample magnetometer
$\vec{M}$	total induced moment
$\vec{M}$	first induced moment
$\vec{M}'$	second induced moment
m	mass of electron
$\vec{N}$	induced torque
$\vec{n}$	normal to surface of sample
n	electron density
δ	skin depth
P	charge density for CDW
P_0	average charge density for CDW

p	amplitude of electrons distortion in a CDW.
$\vec{Q}$	arbitrary tensor
$\vec{Q}$	CDW wave vector
$\vec{Q}'$	reduced CDW wave vector $\vec{G}_{110}-\vec{Q}$
$\vec{q}$	arbitrary small wave vector
q, q_1	resistivity tensor elements
$\vec{R}$	vector to ion positions
R	radius of states altered by CDW
R	sample radius
R	Hall coefficient
r	arbitrary position
S	structure factor
$\overleftrightarrow{s}$	transformation tensor to change sphere into ellipsoid
s	Kohler slope
$\overleftrightarrow{T}$	transformation tensor to convert from xyz to x'y'z' coordinates
T	kinetic energy
T	temperature
T'	temperature sensitivity of open orbits
T_0	phason Debye temperature
t	time
$\overleftrightarrow{U}$	equivalent conductivity tensor for an ellipsoid
$\vec{U}$	ion displacement from equilibrium
U	potential energy

$\vec{V}$	electron velocity
V	ionic potential
V	twice the ratio of sample radius to skin depth
W	sample volume
α	phase shift in rotating sample magnetometer due to first moment
$\hat{\beta}$	effectiveness of a particular domain in changing the conductivity
β	phase shift in rotating sample magnetometer due to second moment
Γ	restoring torque due to springs of magnetometer
$\overleftrightarrow{\gamma}$	effective conductivity of an ellipsoid
γ	angle between open orbit and current axis
Δ	small change
δ	small angle
$\overleftrightarrow{\varepsilon}$	$\overleftrightarrow{s}^{\dagger}\overleftrightarrow{s}$
ε	angle between axis of current loop and rotation plane
η	anisotropy of ellipsoid in rotation plane
Θ	angle between CDW wavevector and [110] direction
θ	angular position of sample
κ	misalignment of axis in induced torque experiment
Λ	sensitivity of rotating sample magnetometer
λ	the angle between axis of current loops and rotation axis
μ	anisotropy of conductivity tensor caused by a CDW
ν	amplitude of static phason
Ξ	exchange integral

ξ	angle between M and M'
Π	angular width of open orbit peak
$\overleftrightarrow{\rho}$	resistivity tensor
ρ_0	resistivity of potassium at 300°K
ρ_t	resistivity of potassium of arbitrary temperature
$\overleftrightarrow{\sigma}$	conductivity tensor
τ	electron scattering time
Υ	exchange interaction
υ	power law exponent
Φ	wave function
ϕ	angle between symmetry axis of ellipsoid and rotation plane
Ψ	angle between open orbit and rotation plane
χ	magnetic susceptibility
Ψ	phase of magnetometer
ψ	phase of CDW
ω	angular frequency of rotation in induced torque experiment
ω_c	cyclotron frequency
ω_q	phason frequency
$\S$	angle between Q vector and (100) plane for a CDW state in potassium
η	open orbit fraction
∇	small change in induced torque

Co-ordinate systems

$\hat{x}\hat{y}\hat{z}$ - The z axis is along the magnetic field and torque measured about y.

$\hat{x}'\hat{y}'\hat{z}$ The magnetic field is along z and x' is along the axis of the current loops

$\hat{x}''\hat{y}''\hat{z}$ The magnetic field is along the z-axis and x" along the open orbit direction

$\hat{r}\hat{\theta}\hat{\zeta}$ The axis $\hat{\zeta}$ is along the axis of the current loops $\hat{r}$ and $\hat{\theta}$ form a polar co-ordinate system peprendicular to $\hat{\zeta}$.

Abbreviations

CDW	charge density wave
dHvA	de Haas van Alphen
ED	Elliott and Datars (1983)
LAK	Lifshitz, Azbel and Kaganov theory of magnetoresistance
NMR	nuclear magnetic resonance
RRR	residual resistivity ratio
SDW	spin density wave

CHAPTER 1

INTRODUCTION

Many theories of solid state physics have considered the electronic properties of the alkali metals to be described by particularly simple models (Ziman 1972). The Fermi surface of potassium for example, has been calculated (Ham 1962) using a single-orthogonalized-plane wave, to be spherical to one part in 4000. This result is supported by de Haas van Alphen (dHvA) experiments which showed the expected anisotropy of the Fermi surface although the measured radius of the Fermi surface is 0.7% less than that expected (Shoenberg and Stiles 1964).

The simplicity is tempting since it provides a convenient test metal in which to evaluate theories of electron properties and interactions. There are, however, a series of experiments which contradict this simple view. The results of experiments on magnetoresistance, both electrical [Taub, Schmidt, Maxfield and Bowers 1971] and thermal [Tausch, and Newrock 1977], induced torque [Holroyd and Datars 1975], electron spin resonance [Walsh, Rupp and Schmidt 1966], optical absorption [Mayer and El Naby 1963] and low temperature resistivity [Rowlands, Duvvury, and Woods 1978], for example, are inconsistent with simple theory.

There are two suggestions to explain this data. The first is that the anomalies are due to extrinsic causes, that

dislocations, strains, voids or inhomogeneities of shape give rise to all the observed anomalies. The second is that the ground state of potassium is a charge density wave (CDW) state. Although charge density waves are well established in low dimensional materials [Di Salvo and Rice 1979] and anisotropic materials [Sawoda and Satoh 1978] there is considerable debate among theorists about whether a CDW ground state is possible in an isotropic metal [Overhauser 1978 and Sanders, Rose and Shore 1978].

For a variety of reasons, both theoretical and experimental, potassium is chosen as the most suitable element in which to search for CDW's. Low electron density and weak ion-ion interactions, both of which are found in the alkali metals, favour CDW formation. The alkali metals have a nearly spherical Fermi surface in the absence of a CDW. The electrical properties are thus easy to calculate so the often subtle effects of a CDW would make the most spectacular changes in the alkali metals. Among the alkali metals both lithium and sodium undergo partial martensitic transformation at 80 and 40K, respectively (Barrett 1956). It would be difficult to separate effects due to a phase transformation from those due to a CDW state. Among the remaining alkali metals, potassium is the least reactive and thus can be made to the highest degree of purity. Fletcher (1977) found residual resistance ratios of 6000 for potassium and 500 for rubidium could be attained for samples prepared under the same conditions. Recent evidence

(Templeton 1982) indicates as well that rubidium undergoes a phase transformation at low temperature.

Overhauser [1971b] predicted that potassium with a CDW ground state will have open orbits. The present work uses the induced torque technique which is an ideal open orbit detector. Previous induced torque measurements [Lass and Pippard 1970, Schaefer and Marcus 1971 and Holroyd and Datars 1975] showed anomalies but not open orbits. Some of these results were used to support the CDW model [Overhauser 1971b, Bishop and Overhauser 1977]. The present work was undertaken to search for open orbits and test the predictions of the CDW model.

During the course of this work the induced torque was measured over the magnetic field range 0.005 to 8.5 T and the temperature 1.1 to 2.1 K. New techniques for measuring the induced torque were developed. The performance of the induced torque magnetometers was modeled and tested.

The organization of this thesis is as follows. In Chapter 2 the charge density wave model in potassium is described and its application to some of the experimental results in potassium outlined. In Chapter 3 the induced torque technique is described. The phase of the induced torque signal is calculated. The various approximations required in the solution are outlined and their validity discussed. The operation and performance of the two induced torque magnetometers that were used is described. Sample preparation and handling are described

in Chapter 4. The results of the induced torque experiments in potassium are given in Chapter 5 as well as tests on a variety of materials and experimental conditions which were used to characterize and calibrate the magnetometer. The low field results for amplitude and phase are presented and discussed in Chapter 6. The high field structure is then analyzed in terms of the charge density wave model in Chapter 7. Other possible explanations are advanced and discussed in this chapter as well. Conclusions about this work are presented in Chapter 8.

CHAPTER 2

CHARGE-DENSITY WAVES

i) Introduction

Overhauser (1960) introduced the concept of a spin density wave (SDW) as a Hartree-Fock ground state and applied it to the case of chromium (Overhauser 1962). He used the same theory in 1964 to explain the Mayer El Naby (1963) optical absorption in potassium. Overhauser (1968) extended the theory by considering the possibility of charge density waves. In this paper he proved the exchange interaction lowers the exchange energy in both cases, but the correlation energy increases the energy of the SDW state and decreases the energy of the CDW state. Further work on the properties of a metal with a CDW ground state has followed. In 1971a, Overhauser introduced the concept of phasons. They were found to be dynamic distortions of the phase of the CDW. They were also found to be linear combinations of the phonon modes which go linearly to zero in energy at a wave vector equal to the CDW wave vector (Overhauser 1978). The dispersion curves of the phasons was calculated (Guiliani and Overhauser 1980a). The effect of phasons on electron scattering (Boriak and Overhauser 1978a), specific heat (Boriak and Overhauser 1978b) and the effective mass (Boriak 1980b) were also determined.

The direction of the CDW wavevectors (Guiliani and Overhauser 1979) was calculated and then the magnitude of the charge distortion and the lattice distortion were estimated. This in turn was used to estimate the CDW satellite intensity (Guiliani and Overhauser 1980b). The magnetic susceptibility of an electron gas with a CDW was estimated by Boriak (1980a).

A static distortion of the phase was recently postulated and found to lower the overall energy for specific values of the phase distortion (Guiliani and Overhauser 1982). These additional periodicities give rise to energy gaps (Huberman and Overhauser 1982) which truncate the Fermi surface.

Concurrently with its development, the CDW model was applied to a series of experimental results or suggested experiments. The most recent references which are listed give earlier references. The Mayer El Naby optical absorption (Overhauser and Butler 1976), the splitting of conduction electron spin resonance (Overhauser and de Graff 1968), helicon propagation (Overhauser and Rodrigues 1966), magnetoflicker noise (Overhauser 1974), four-fold anisotropy of induced torque (Overhauser 1971b) and anisotropy extrapolated to zero field (Bishop and Overhauser 1978), low temperature specific heat (Guiliani and Overhauser 1980c), low temperature resistivity (Bishop and Overhauser 1981), neutron scattering (Guiliani and Overhauser 1980b), photoemission (Boriak and Overhauser 1978c) and high

field open orbit magnetoresistance (Huberman and Overhauser 1982) were investigated.

ii) Theory

The charge density wave model will now be outlined with particular emphasis on those aspects which affect the conductivity tensor in general and the induced torque in particular.

The theory is derived for the case of jellium and then the effects of the positive ion lattice are included as a perturbation. Jellium is the simplest metal to consider because it has a gas of free electrons with the positive ion background necessary for electrical neutrality smeared out into a uniform positive charge.

The Hamiltonian for this system can be expressed compactly by the following Hamiltonian.

$$H = T + U_{ion} + U_{el-ion} + U_{el} - U_{ex} - U_{cor} \quad . \qquad (2\text{-}1)$$

where T is the kinetic energy of the electrons.

U_{ion} is the electronic energy due to the positive background.

U_{el-ion} is the attraction of the electron gas by the ion background.

U_{el} is the self energy of a gas of distinguishable particles.

U_{ex} is the exchange energy due to the fact that particles of the same spin are indistinguishable and thus can be interchanged.

U_{cor} is the correlation energy due to all other factors not already considered.

The exchange and correlation terms lower the overall energy and thus, by definition must be positive. The ground state energy of a metal in the case where terms U_{ex} and U_{cor} are zero has been solved in some detail (Ziman 1972). The ground state is just the occupation of the n lowest energy, plane-wave states which is the free electron sphere. It would seem reasonable that the lowest energy state would always have uniform electron density. Overhauser (1962,1968) has shown, however, that this assumption is not valid if interactions are included. They lead to an electron density P, as will be shown,below, of the form

$$P = P_0(1 + p \cos(Q.r \pm \psi)) \qquad (2\text{-}2)$$

where P_0 is the average charge density and p the amplitude of a modulation of wave vector Q. ψ is a phase factor and the + and - signs refer to spin up and spin down electrons respectively. For $\psi = 0$, there is a Charge Density Wave.

```
        ↑↑
       ↑↑↑↑
↑   ↑↑↑↑↑↑   ↑        spin up
↑↑↑↑↑↑↑↑↑↑↑↑↑

        ↓↓
       ↓↓↓↓
↓   ↓↓↓↓↓↓   ↓        spin down
↓↓↓↓↓↓↓↓↓↓↓↓↓
```

The net magnetic moment at any point is constant while the total electronic charge density varies with position in the crystal.

For $\psi = \pi/2$ there is a Spin Density Wave

```
        ↑↑
       ↑↑↑↑
↑    ↑↑↑↑↑↑↑    ↑          spin up
↑↑↑↑↑↑↑↑↑↑↑↑↑↑

 ↓↓        ↓↓
↓↓↓↓      ↓↓↓↓
↓↓↓↓↓    ↓↓↓↓↓              spin down
↓↓↓↓↓↓↓↓↓↓↓↓↓↓
```

The total electronic charge density is constant but there is a net magnetic moment at all points.

A simple plausibility argument shows that states of the form of Equation (2-2) have lower energy (Overhauser 1962). Consider truncating the Fermi surface by a cap of radius R. Obviously $k_F > k_{FE}$ where k_{FE} is the Fermi wavevector of the free electron sphere and k_F is the Fermi wavevector of the distorted Fermi surface. This must increase the average kinetic energy. The kinetic energy increase ΔT, will be proportional to the number of states displaced times their average kinetic energy which gives

$$\Delta T = \left(\frac{\hbar^2}{96\pi^2 m k_F}\right) R^6 \quad . \tag{2-3}$$

where m and $\hbar$ have their usual meaning.

The exchange interaction $T(\vec{k})$ for a normal ground state is given by

$$T(\vec{k}) = -\frac{e^2 k_F}{\pi}\left\{1 + \frac{k_F^2 - k^2}{2k_F k} \ln\left|\frac{k_F + k}{k_F - k}\right|\right\} . \tag{2-4}$$

Increasing k_F slightly by truncating the Fermi surface by a vector of length Q increases $T(\vec{k})$ by

$$\Delta T(\vec{k}) = \frac{e^2 k^2}{\pi k_F} \ln \frac{2k_F}{R} . \tag{2-5}$$

Counting over all the electrons displaced gives

$$\Delta U_{ex} \simeq [-\frac{7}{12} + \ln \frac{2k_F}{R}] \frac{e^2 R^6}{96\pi^3 k_F^2} \tag{2-6}$$

and, since $\ln R$ is weakly varying for finite R, gives a value for the energy increase which is proportional to R^6.

However, electrons which take part in the charge density wave are physically closer together and thus have a stronger exchange interaction. Consider that only the states in a cylinder of radius R and arbitrary length participate in the charge density wave. The exchange integral Ξ where

$$\Xi = \langle \frac{4\pi e^2}{k'-k} \rangle_{av} \tag{2-7a}$$

gives

$$\Xi = \frac{4\pi e^2}{R^2} f \tag{2-7b}$$

where f is a constant. Integrating over the number of states involved gives $\Delta U_{ex} \propto R^4$. Since R is arbitrary in this derivation it can always be chosen to reduce the energy relative to the free electron value. Further calculation of the correlation energy shows it enhances the CDW instability and inhibits the SDW.

For the charge density wave, there is an additional energy increase due to the increased electrostatic interaction of the non uniform charge distribution. If the ionic distribution were perfectly rigid the size of this term would immediately

prohibit the CDW. By contrast, if the ions were in the form of an infinitely deformable jellium they could move to cancel this energy at no cost. Obviously for any real metal the truth lies at some intermediate point that cannot be readily calculated.

To find the form of the charge density wave, consider an ionic potential in the Hamiltonian of the form $V = V_0 + G \cos\vec{Q}.\vec{r}$ (Overhauser 1978). For simplicity a simple extension of the free electron model with $V_0 = 0$ and G a constant is chosen. The wave function $\Phi(\vec{k})$ has the form

$$\Phi(\vec{k}) = e^{i\vec{k}\cdot\vec{r}} + a_+ e^{i(\vec{k}+\vec{Q})\cdot\vec{r}} + a_- e^{i(\vec{k}-\vec{Q})\cdot\vec{r}} \qquad (2\text{-}8)$$

where the usual plane wave solution $e^{i\vec{k}\cdot\vec{r}}$ has added to it terms which mix in states of wave vector $\vec{Q}$ greater and less than $\vec{k}$. The factors a are small for a weak potential so terms in a^2 can be ignored. The probability density for an electron in state $\vec{k}$, $\Phi^*\Phi$ becomes

$$\Phi^*\Phi = 1 + 2(a_+ + a_-) \cos\vec{Q}\cdot\vec{r} \qquad (2\text{-}9)$$

when again terms in a^2 are dropped.

Thus, there is a non-uniform electron density of wave-vector $\vec{Q}$. An ionic potential of wave vector $\vec{Q}$ results, to cancel the electrostatic energy. This is the potential originally assumed in the Schrodinger equation creating a bootstrap phenomena in which the presence of non-uniform charge stabilizes

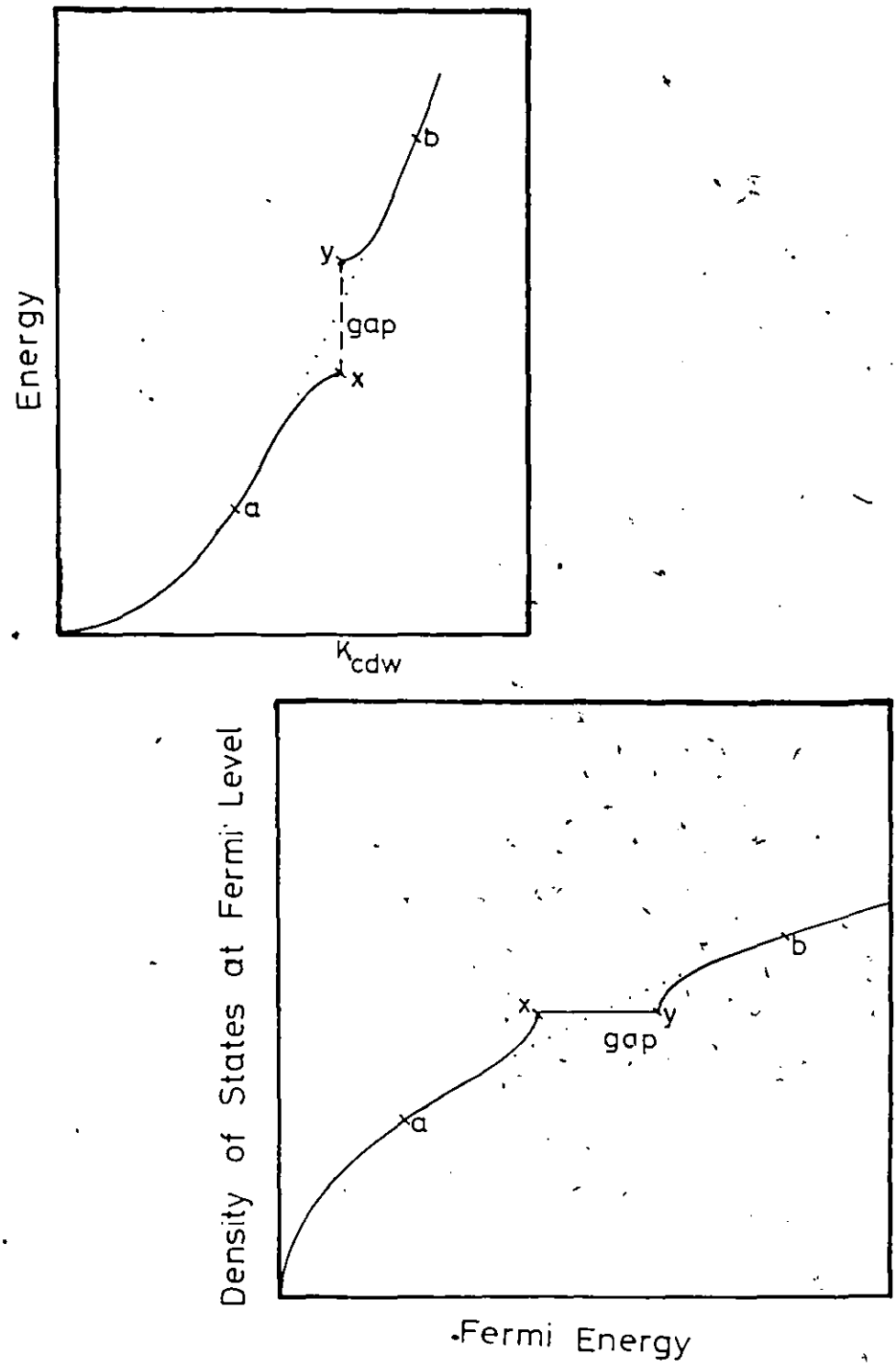

Fig. 2-1 The energy bands (a) and density of states at the Fermi surface (b) for a metal with a charge density wave ground state.

the non uniform charge.

It is now necessary to examine what value of Q is required to give the largest support to the CDW instability (Overhauser 1968). The presence of an additional periodicity of wave vector Q leads to an energy gap in one direction as shown in figure 2-1. This gap is analogous to those found in the nearly free electron theory. The gap causes the density of states at the Fermi surface to be enhanced for Fermi energy E_F in region x below the gap. The density of states is constant for E_F in the gap region as new states are added only in two dimensions until E_F is above the gap at y.

If the value of Q were such that E_F was at point a or b the spectrum would be essentially free-electron-like so no reason would exist for CDW formation. Varying Q so that the Fermi energy lies near the gap, increases the number of states at E_F which in turn increases the correlation energy and thus the stability of the charge density wave. The density of states is increased most above the free electron value for E_F at x. Thus, the CDW is strongest for $Q \approx 2k_F$ which will distort the Fermi surface from a sphere into the lemon shape shown in figure 2-2.

The wave vector Q could be oriented in any direction for the metal jellium. The effect of the lattice is to produce a preferred direction in a real metal such as potassium. Since the Fermi surface is distorted slightly from a sphere by the presence of the lattice there are directions in which

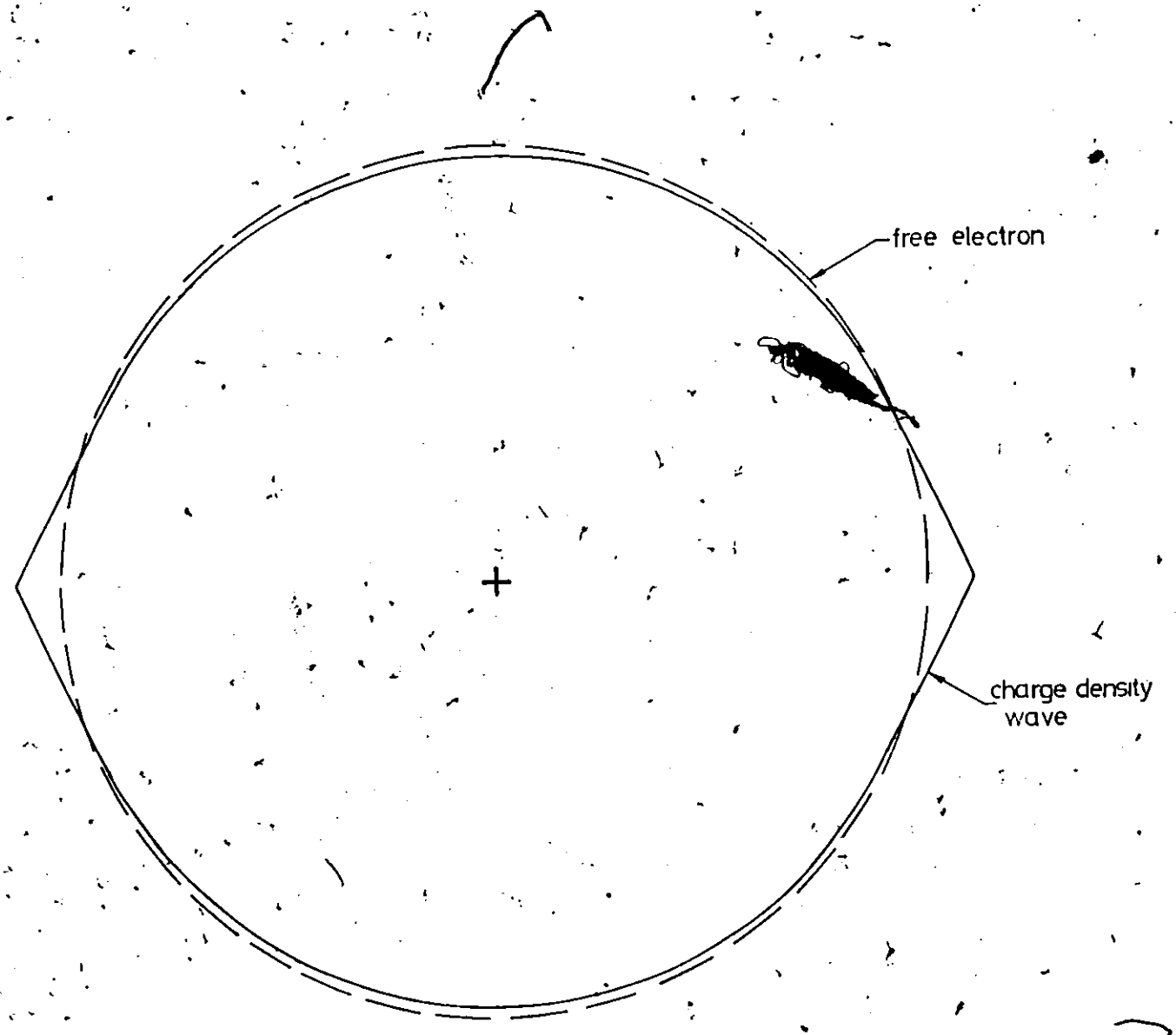

Fig. 2-2 The free electron sphere distorted into a lemon shape by the presence of a CDW.

the Fermi surface nesting is more effective. However a more significant effect is the requirement that the ions be displaced from equilibrium in order to cancel the large electrostatic energy resulting from the CDW. The wave vector of the static displaced ions has associated with it an energy of the corresponding dynamic phonon. The energy of this mode is a measure of the energy penalty extracted by the CDW formation. Thus, this wavevector should be as small as possible. Clearly since Q lies outside the Brillouin zone the wave vector required to screen the electrostatic energy must be of the form $\vec{Q}' = \vec{G} - \vec{Q}$ where $\vec{G}$ is a reciprocal lattice vector. Translation in the [110] direction allows a $\vec{Q}'$ vector of order $0.1(\frac{2\pi}{a})$ while the next direction [200] has a $\vec{Q}'$ associated with it of at least $0.7(\frac{2\pi}{a})$. All other reciprocal lattice points give $\vec{Q}'$ which lie outside the Brillouin zone. Examining the dispersion curves shows that there will be lowest energy with $\vec{Q}$ nominally along a [110] direction.

However, to get a precise determination of the $\vec{Q}'$ direction note that rotating $\vec{Q}$ away from [110] by several degrees does not increase the magnitude of $\vec{Q}'$ significantly. For $\vec{Q}$ precisely along the [110] direction, only longitudinal phonons can contribute. In potassium, these are of a much higher frequency than transverse phonons. It is therefore possible to take advantage of the lower energy of transverse phonons by changing the angle slightly. Guiliani and Overhauser (1979) minimized the total energy made up of the electrostatic energy and the energy due to the static phonons. Since these are long

wavelength phonons it was permissible to use only the best experimental determinations of the elastic constants. The resulting contours of the total energy due to the formation of the CDW as a function of the angle between the CDW $\vec{Q}$ vector and the [110] direction are shown in fig. 2-3. The minimum occurs for an angle θ of 4.1° between the $\vec{Q}$ vector and the [110] direction and an angle ϕ of 65.4° between the plane defined by $\vec{Q}$ and the [110] direction, and the (100) plane. Since $\vec{Q}$ is not in a symmetry direction or plane a total of 24 possible directions for $\vec{Q}$ are expected from the 4 equivalent directions associated with each of the 6 possible [110] directions. Thus in any given crystal there are 24 equivalent directions for $\vec{Q}$. The crystal is therefore expected to divide into a number of domains. The number and orientation of domains is expected to be determined by the previous metallurgical history of the sample. However without a detailed calculation of the interaction of the CDW lattice distortion with dislocations, strain fields, impurities, sample surfaces and each other, which is not presently available, a detailed theory of CDW domains on which to base predictions is not forthcoming. It is however necessary to remember that any experiment which measures a bulk property is of necessity going to involve a sum or average over many domains and is likely to show the cubic symmetry of the sample.

Several points of the above calculation require special mention. The calculation was done for $|\vec{Q}| = 1.33(\frac{2\pi}{a})$. While the angle θ is sensitive to varying the length of $\vec{Q}$, the vector

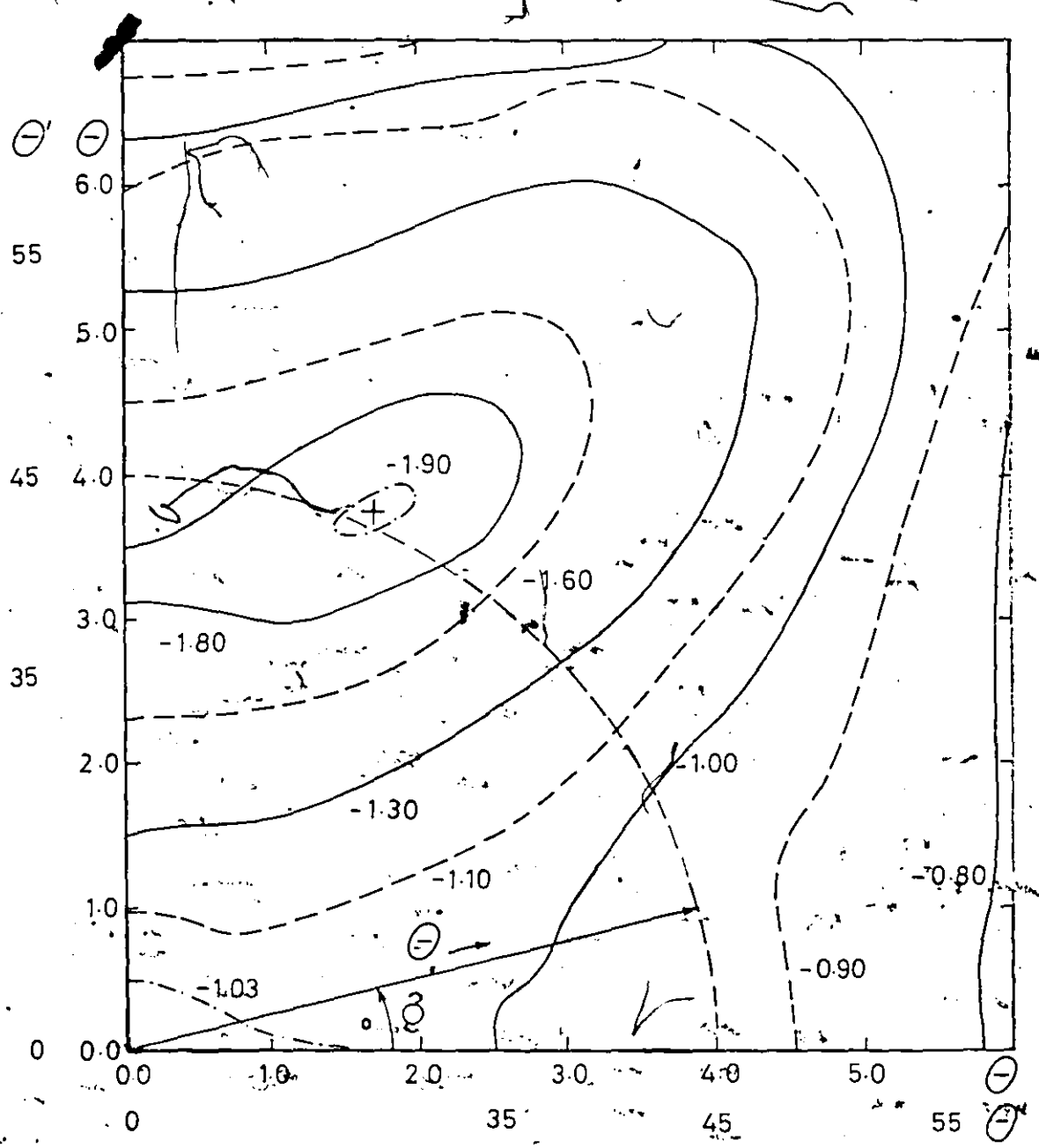

Fig. 2-3 The contours of the energy of potassium with a CDW relative to the free electron energy. The contours are drawn as a function of $\vec{Q}$ direction for $|\vec{Q}| = 1.33(2\pi/a)$. The optimum direction of $\vec{Q}$ is indicated by $\pm$.

$\vec{Q}'$ and the angle § = §' does not change by more than one percent over the reasonable range of $|\vec{Q}|$ from $1.30(\frac{2\pi}{a})$ to $1.36(\frac{2\pi}{a})$. Equally important is the fact that the minimum is very broad and thus can be modified easily by crystal strains or dislocations. The presence of a magnetic field is also expected to reorient the direction of $\vec{Q}$ slightly (Boriak 1980a). In addition the elastic constants used in the calculation were measured on bulk samples which were almost certainly multidomain. A more precise calculation would have to be self-consistent taking into account the effect of the CDW on the elastic constants. Thus, the above calculation should be used to indicate that a $\vec{Q}$ vector does not lie in any symmetry direction and not as a precise prediction of the direction of the $\vec{Q}$ vector. The presence of the $\vec{Q}$ vector produces an additional lattice periodicity. This additional periodicity in turn gives rise to several energy gaps and open orbits (Overhauser 1982). The charge density wave produces gaps of periodicity $\vec{Q}$. The lattice displacement by $\vec{Q}'$ will also contribute energy gaps.

In the above work it has been assumed that the ions and electronic charge density are static in their distorted position. However the charge density of conduction electrons can have the form

$$P_{\pm} = P_0(1+p\cos(\vec{Q}\cdot\vec{r}+\psi_{\pm})) \qquad (2\text{-}10)$$

where + and - refer to the values for spin up and spin down

respectively. In jellium the energy will be independent of the value of ψ for $\psi_+ = \psi_-$. In a real metal there are collective excitations called phasons of the charge density wave corresponding to the phase varying slowly in time and space. It can be noted that $\psi_\pm$ is expected to be of the form

$$\psi_\pm = \psi_0 \pm \delta\psi. \tag{2-11}$$

A $\delta\psi \neq 0$ mixes in some spin density wave and gives rise to a collective excitation analogous to the spin wave excitation in a ferromagnet. The phase of $\psi_\pm$ of equation (2) can have the form

$$\psi_0 = \psi_q \sin(\vec{q}\cdot\vec{r} - \omega_q t) \tag{2-12a}$$

and

$$\delta\psi_\pm = \pm\delta\psi_q \sin(\vec{q}\cdot\vec{r} - \omega_q t) . \tag{2-12b}$$

In either case new collective excitations of the electron gas arise. The ionic charge is displaced from equilibrium according to

$$\vec{U}(\vec{R}) = \vec{A}\sin(\vec{Q}\cdot\vec{R} + \psi) . \tag{2-13}$$

If the ψ given in (2-12a) is substituted into equation (2-13) for $\vec{q} << \vec{Q}$ the lattice displacement is

$$\vec{U}(\vec{R},t) = \vec{A}\sin\vec{Q}\cdot\vec{R} + \frac{1}{2}\vec{A}\psi_q \sin[(\vec{Q}+\vec{q})\cdot\vec{R} - \omega t]$$

$$+ \frac{1}{2}\vec{A}\psi_q \sin[(\vec{Q}-\vec{q})\cdot\vec{R} + \omega t] . \tag{2-14}$$

The last two terms due to the phasons are just a combination of phonons with wavevectors $\vec{Q}+\vec{q}$ and $\vec{Q}-\vec{q}$. They produce a dip in the phonon spectrum at wave vector $\vec{Q}$ as phonons are used to produce phasons. The resultant phonon dispersion curve and ionic displacements are shown in Figure 2-4.

It should be noted that for $\vec{q}$ much smaller than $\vec{Q}$ the period of the ionic displacement is determined by $\vec{Q}$ and so long wavelength disturbances do not require any gross movement of charge and thus no large electric field in the crystal.

The $\vec{Q}$ vector just spans the Fermi surface at its optimum position. Support for the charge density wave decreases rapidly as $\vec{Q}$ moves away from the Fermi surface. Rotating the $\vec{Q}$ vector with a phason leaves $\vec{Q}$ very nearly on the Fermi surface while lengthening $\vec{Q}$ does not. This will lead to a highly anisotropic distribution of phason frequencies with higher frequencies for $\vec{q}$ parallel to $\vec{Q}$ and lower frequencies for $\vec{q}$ perpendicular to $\vec{Q}$. These phasons have associated with them a Debye temperature different than that of the phonons, which gives rise to experimental effects.

The interaction of the CDW with the lattice selects particular static values of the phase to minimize total energy. ψ of the form

$$\psi = u\sin(\vec{q}\cdot\vec{R}) \tag{2-15}$$

reduces the total energy for specific values of $\vec{q}$.

Figure 2-4 a) The phonon spectrum (solid line) for a metal with a charge density wave along the [110] direction. The phonon spectrum and the phonon spectrum translated by the CDW wavevector $\vec{Q}$ (dotted line) combine to give phasons of reduced energy and amplitude modes of increased energy (dashed line).

b) The ion positions for a metal with a static charge density wave as given by equation (2-13). The CDW has wave vector along [110] and amplitudes A of 0.2 with a phase distortion ν of amplitude $\pi/4$ and wave vector $\vec{Q}-2\vec{Q}'$.

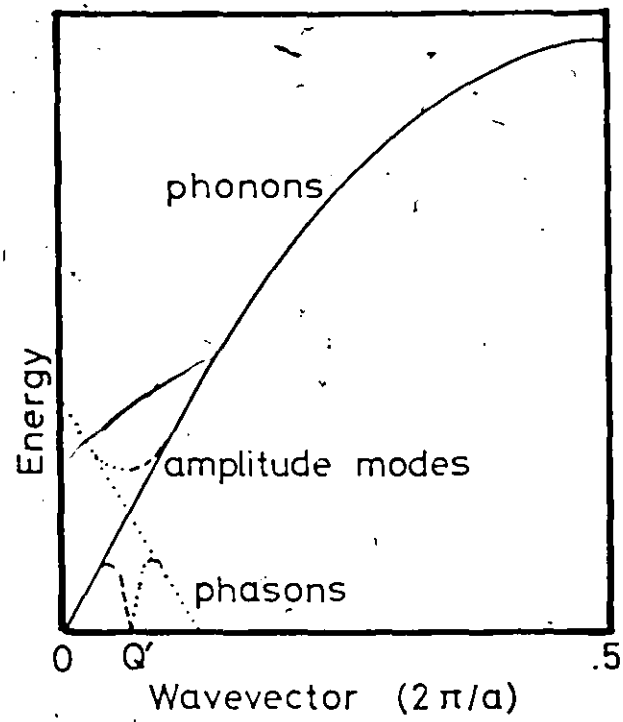
phonons
Energy
amplitude modes
phasons
0
Q'
.5
Wavevector (2π/a)

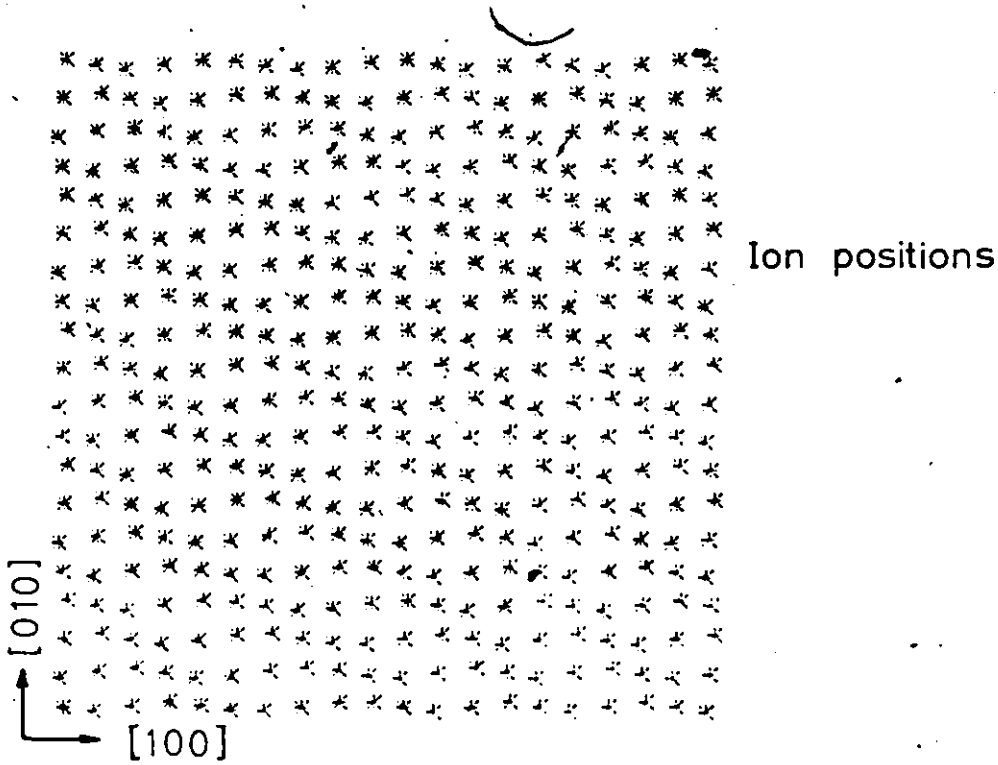
Ion positions
[010]
[100]

To find the appropriate value of q examine the structure factor for the lattice

$$S(\vec{q}) = \sum_i e^{-i\vec{q}\cdot\vec{R}_i} \tag{2-16}$$

where

$$\vec{R}_i = \vec{R}_{oi} + \vec{U}(\vec{r}) \ . \tag{2-17}$$

The structure factor reduces to

$$S = \sum_{\vec{G},n} (-1)^n J_n(\vec{q}\cdot\vec{A}_0) e^{in\phi} \delta(\vec{q} - (\vec{G}+n\vec{Q})) \tag{2-18}$$

where J_n is a Bessel function. The delta function allows components in the periodicity of form $\vec{q} = \vec{G}+n\vec{Q}$ while the Bessel function expanded for small $\vec{A}$ goes as

$$\frac{(\vec{q}\cdot\vec{A})^n}{n!} \tag{2-19}$$

which rapidly reduces the strength of periodicities for $n > 1$. If the phase is assumed to vary with position in equation (2-15) where both ν and $\vec{q}$ are small, the structure factor becomes

$$S = \sum_{\vec{G},n} (-1)^{n+m} J_n(\vec{q}\cdot\vec{A}_o) J_m(n\nu) \delta(\vec{q} - (\vec{G}+n\vec{Q}+m\vec{q}) \ . \tag{2-20}$$

An examination of the energy of the crystal shows that when $\vec{G}+n\vec{Q} = m\vec{q}$, which occurs when the periodicity due to phase modulation is equal to an existing periodicity, the energy is reduced, anomalously reinforcing those periodicities. Detailed

calculation shows the peak $\vec{q} = 2(\vec{G}\pm\vec{Q})$ gives rise to the largest energy reduction. In addition to the charge density wave periodicity Q and the static ion displacement $Q' = G_{110} - Q$, the periodicity of a phase modulation of the ionic displacement $\vec{Q} - 2\vec{Q}' = 3\vec{Q} - 2\vec{G}_{110}$ results. These gaps are indicated in fig. 2-5 which also lists the five possible open orbit directions.

Open orbits exist if the energy gaps are not broken down by the magnetic field. The probability of breakdown is given approximately by

$$P = e^{-\frac{KE_g^{\,2}}{B|V_x V_y|}} \qquad (2\text{-}21)$$

where K is a constant, E_g is the energy gap, B is the magnetic field and $V_x V_y$ are respectively the component of electron velocity parallel and perpendicular to the gap. For the gaps at C and G it can be seen that the velocities V_x and V_y go progressively to zero as you move from C to G. The probability of breakdown decreases as well. There always exists a region of the Fermi surface GO for which breakdown has not occured even if magnetic breakdown has occured at C. A similar analysis at the planes B and E is also valid. The number of orbits for which breakdown has not occured however drops rapidly as the magnetic field is increased.

It is important to note that this theory has given what are expected to be the 3 largest energy gaps and 5 strongest open orbits. However the actual magnitude of the gaps is not estimated. Thus in a real metal these gaps could

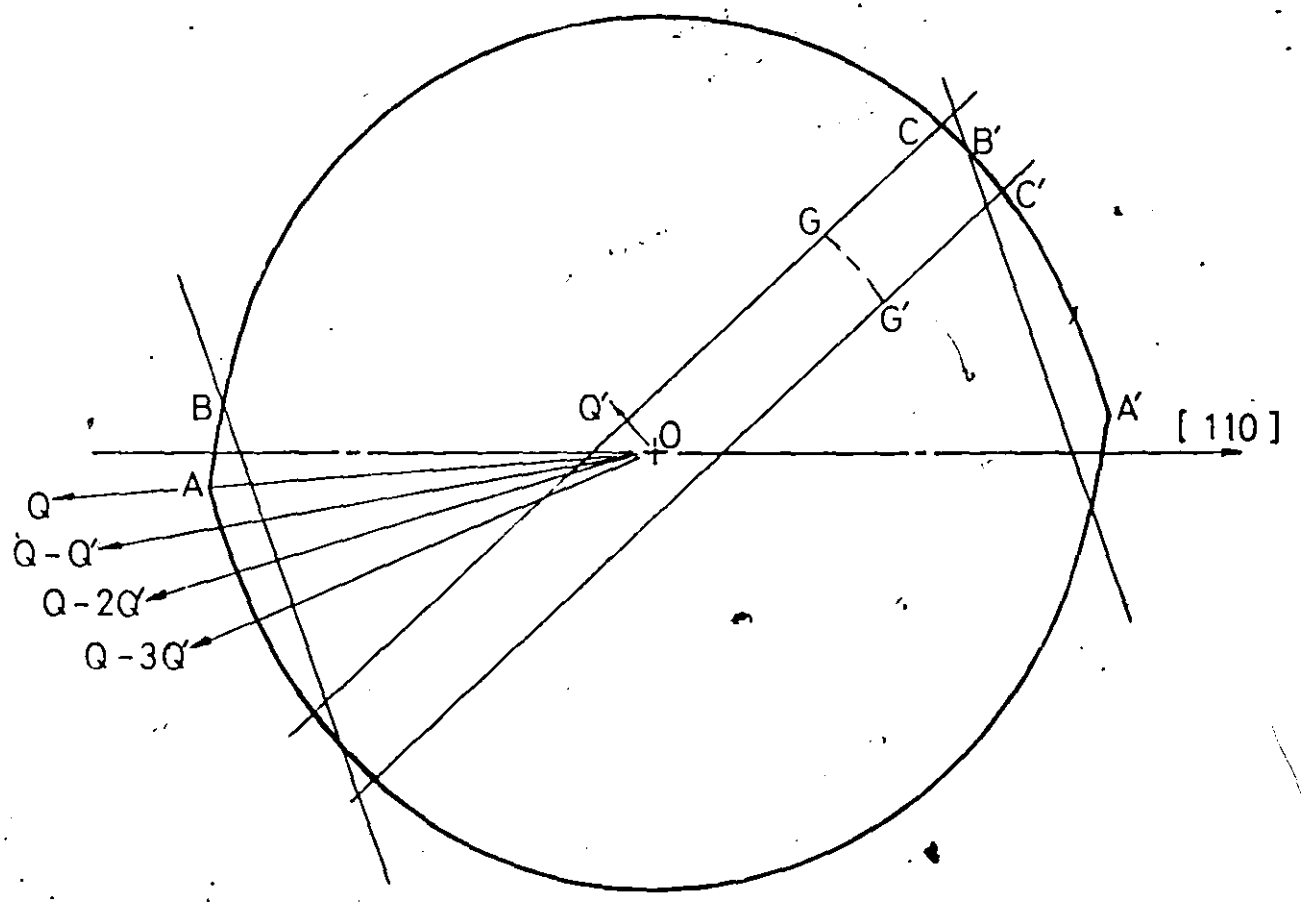

Figure 2-5 The predicted energy gaps and open orbit directions of a CDW state in potassium.

be entirely broken down or lower order gaps could be significant. As could be inferred from chromium results (Riefenberger, Holroyd and Fawcett 1980) attempts to estimate the magnitude of the gaps are subject to considerable error and appeals to experiment are necessary in order to find the open orbits which exist.

The problem of finding the conductivity is now a major one. There are 24 possible domains, each with 5 different open orbits. Clearly gross simplifications are required. Huberman and Overhauser (1981, 1982) made an attempt to solve the problem. Their first assumption was to take a Fermi surface made up of a sphere and 5 cylinders which could support open orbits. Each of the cylinders is then assumed to be of equal strength, with a fraction η of the total number of carriers. The conductivity of the mixture is

$$\overleftrightarrow{\sigma} = (1-5\eta)\overleftrightarrow{\sigma}_s + \eta \sum_{i=1}^{n} \overleftrightarrow{\sigma}_{ci} \qquad (2\text{-}22)$$

where $\overleftrightarrow{\sigma}_s$ is the conductivity of the spherical Fermi surface and $\overleftrightarrow{\sigma}_{ci}$ is the conductivity of a cylinder appropriately oriented.

The effective conductivity of the material is then for twenty-four types of domains

$$\overleftrightarrow{\sigma}_{eff} = \overleftrightarrow{\sigma}_{ext} + \sum_{n=1}^{24} f_n (\overleftrightarrow{\sigma}_m - \overleftrightarrow{\sigma}_{ext}) \cdot \overleftrightarrow{\beta}_n \qquad (2\text{-}23)$$

where $\overleftrightarrow{\sigma}_{eff}$ is an effective conductivity tensor, $\overleftrightarrow{\sigma}_{ext}$ is the

conductivity excluding the domain n, f_n is the volume fraction of domain n and $\overleftrightarrow{\beta}_n$ is a matrix describing the effectiveness of a change in conductivity of a domain in changing the overall conductivity. $\overleftrightarrow{\beta}_n$ was evaluated for a spherical inclusion in an isotropic host medium. Equation (2-23) was then iterated until the conductivity $\overleftrightarrow{\sigma}_{eff}$ converged to $\overleftrightarrow{\sigma}_{ext}$. These solutions lead to the reasonable result that open orbits still contribute peaks to the torque in the same magnetic field direction but the peaks are broadened and reduced in intensity compared to the results for a homogeneous sample.

The size of the domains enters only as an additional scattering term. If all electrons scatter on leaving the domains this gives a scattering length of order D/2 where D is the domain size or an extra contribution to scattering time of size 2/D. The scattering time becomes

$$\frac{1}{\tau} = \frac{1}{\tau_{bulk}} + \frac{2}{D} \qquad (2\text{-}24)$$

where τ_{bulk} is the intrinsic scattering time.

iii) <u>Experimental Anomalies</u>

Experiments on magnetoresistance, optical absorption, low temperature resistivity, induced torque, specific heat, point contact spectroscopy, phonon dispersion, nuclear magnetic resonance, de Haas van Alphen and neutron scattering are examined for anomalies in light of the preceding theory.

Kapitza in 1929 measured the magnetoresistance of polycrystalline wires. He found that the resistivity increased linearly with magnetic field. The theory by Lifshitz, Azbel and Kaganov (LAK) (1957) however predicts that for a simply connected Fermi surface the magnetoresistance for current flow perpendicular to the magnetic field (transverse geometry) saturates at high fields and the magnetoresistance for current flow parallel to the magnetic field (longitudinal geometry) is independent of field. Subsequent experiments (Taub et al 1971) have continued to find linear magnetoresistance with Kohler slope from 10^{-2} to 10^{-4}. The Kohler slope s is defined to be $\frac{1}{\omega_c \tau} \frac{\Delta\rho}{\rho_0}$ where ω_c is the cyclotron frequency, τ is the scattering time, $\Delta\rho$ is the change in restivity and ρ_0 is the resistivity at zero field. The effect is general, occurring in longitudinal and transverse geometry, for polycrystalline and single crystal samples in four probe and contactless experiments. In addition a variation of Kohler slope in the same sample has been found (Simpson 1973). The effect is not however specific to potassium or other alkali metals. Aluminum, lead and indium, materials with a simply connected Fermi surface which on the basis of the LAK theory would show saturation behaviour, also show linear magnetoresistance with comparable Kohler slopes (Kapitza 1929, Fletcher 1982).

The vast range of Kohler slope between different experiments and even from run to run with the same sample is unique to potassium. This indicates a variable over which the

experimentalists have no control.

Mayer and El Naby (1963) found when measuring the optical absorption of potassium in the form of bulk metal samples that there was absorption which began at 0.6 eV and peaked at 0.8 eV. This peak had the shape appropriate to an energy gap just touching the Fermi surface. Subsequent work on thin films did not show any evidence of this gap. Harms (1972) further discovered that the state of surface oxidation affected the absorption. An unoxidized sample did not show any absorption. The absorption grew steadily as trace amounts of H_2O were introduced to form a layer of KOH on the bulk metal. However, the absorption could not be attributed to energy gaps in the expected oxidation products. The absorption, explained in the CDW model as transitions across the energy gap, defines the main CDW energy gap to be 0.62 eV.

The resistivity of potassium has been measured at temperatures below 1.5K to sufficient accuracy to determine the temperature dependent component with accuracies of several percent. The resistivity is expected to vary as T^2 due to the presence of electron-electron scattering. Several groups have found a temperature dependence best fit by a $T^{1.5}$ power law (Rowlands et al 1978), while others have fit their data with T^2 power laws (van Kempen et al 1981, Pratt 1982). A recalibration of the temperature scale at University of Michigan (Pratt 1982) changed the best fit line from $T^{1.5}$ to T^2

showing the sensitivity of conclusions drawn from these experiments to small experimental inaccuracies. The accepted contributions to the resistivity in pure metals are phonon umklapp scattering giving an exponential term, normal phonon scattering giving a T^5 term and electron-electron scattering giving a T^2 term. Another mechanism is required to explain a $T^{1.5}$ term.

The induced torque is expected to be isotropic to less than one percent for a spherical fermi surface. That this is not so for potassium provides one of the strongest questions about the simple theory of the Fermi surface. This question shall provide the basis for the remainder of this thesis and will not be further discussed here.

In addition to the above phenomena which disagree with the nearly free electron theory there are a series of experiments for which the results are inconclusive. The Hall coefficient is expected to be 1/ne and constant above $\omega_c \tau \gg 1$. Experimental results show the expected value or a value (Penz 1968) several percent higher which changes by up to 4% in going from low field to 10 T. The thermal magnetoresistance as well shows variations among experimenters (Fletcher 1980, Tausch et al. 1979).

The above points out a feature of potassium which has plagued researchers for many years. The results obtained by different groups or the same group on different samples vary by much more than experimental error on samples nominally the same.

Were the above results the only data on potassium, the nearly free electron model would have been condemned. However the theory provides an accurate calculation of the phonon properties of the lattice. Phonon dispersion curves, phonon specific heat and the phonon contribution to the transport above 2K are well explained.

The de Haas-van Alphen effect is most commonly used to measure the extremal area of the Fermi surface. The measured Fermi surface (Shoenberg and Stiles 1964) is nearly spherical with an anisotropy accurately predicted by theory (Lee and Falicov 1968). By contrast the CDW model predicts a lemon-shaped Fermi surface with a 7% variation in extremal area. The existence of CDW domains reduces the anisotropy. The domains can be identified by beats in the dHvA frequency if the domains are small. A study of the dHvA amplitude (Springford 1981) found that all electrons contribute to a single dHvA frequency. There was no evidence of beats.

To explain the measured dHvA data remains one of the major unsolved problems for the CDW model.

The other commonly used experiment to directly calipher the Fermi surface, positron annihilation, also shows the radius of the Fermi surface expected from the normal ground state as well as the intensity distribution for a spherical Fermi surface (Kubica and Stewart 1975). No evidence of domains is found.

The Nuclear Magnetic Resonance (NMR) experimental results for potassium are consistent with a normal ground state (Follstaedt and Schlicter 1976). The presence of a static charge density gives rise to a Knight shift which would be easily measurable as a change in line shape. The presence of the electric field gradient in the conduction electrons and the corresponding gradient in the ion cores gives rise to a quadrupole shift. The presence of thermal fluctuations averages these shifts to zero, but the shifts could still be expected to be seen as increases in linewidth. Only if the fluctuations were very rapid would the CDW not make its presence known. The NMR results above put an upper limit on the average time between fluctuations of the CDW state of 1.3×10^{-7} sec.

The displacement of the ions due to the CDW interaction observed using neutron X-ray or electron diffraction would be the most unambiguous evidence for CDW's. A careful neutron diffraction experiment by Werner, Eckert and Shirane (1980) did not show any satellites in the directions calculated to the limit of sensitivity of the detection system, one part in 10^5 of the [110] Bragg reflection.

Any theory must be able to explain the anomalies found in some of the transport properties without affecting the results successfully obtained from using the normal ground state, particularly the lattice dynamics.

iv) Properties of a CDW

It is worthwhile at this point to summarize the assumptions inherent in the present CDW calculations and the properties inferred from experiment. Within the Hartree-Fock model in jellium a charge density wave instability is always possible. Correlation effects increase the strength of the instability. In a stress free sample, the CDW wavevector is along one of 24 directions equivalent by symmetry. The direction picked would be that most closely aligned with a strong magnetic field (Boriak 1980a). There are collective excitations of the phase of the charge density wave. These phasons go to zero energy linearly at the wavevector of the charge density wave. There are a series of energy gaps truncating the Fermi surface of which the five periodicities $\vec{Q}$, $\vec{G}_{110}-\vec{Q}$, $\vec{G}_{110}-2\vec{Q}$, $2\vec{G}_{110}-3\vec{Q}$, $3\vec{G}_{110}-4\vec{Q}$ are expected to be the most significant and in roughly decreasing magnitude. All others are assumed to give negligible gaps. It was then assumed that the conductivity of a sample with many domains could be calculated in the effective medium approximation. No assumption has been made about the nature of domains or domain boundaries. No assumptions have been made about the pinning of CDW's by stress or dislocations.

The optical experiment implies an energy gap of 0.62 eV which just touches the Fermi surface at a point. The CDW $\vec{Q}$ vector is perpendicular to the surface. The dHvA (and other) experiments require a domain structure. The domains are quite

tenuous and easily changed from experiment to experiment. The lattice distortion cannot be fixed but must vary rapidly in time and space due to the presence of phasons as shown by the NMR and resistivity experiments. The absence of magnetoflicker noise (Hockett and Lazarus, 1979) implies that in bulk samples the Q vector can not be freely aligned by a magnetic field but must be pinned.

The reader is referred to the work by Overhauser (1982) and co-workers for more detail about the CDW model and its use in explaining the measured anomalies.

Using the preceding theory as a background the induced torque experiments conducted in this work are presented and examined.

CHAPTER 3

INDUCED TORQUE TECHNIQUE

i) Introduction

The induced torque technique has proven to be an excellent technique for the detection of open orbits in metals. In its simplest form, a spherical metal sample is rotated slowly in a uniform magnetic field and the torque on the sample is measured (Datars and Cook 1969, Douglas and Datars 1973).

The results can be described physically for the sample geometry shown in figure 3-1. The magnet rotates about the y axis of a co-ordinate system fixed in the sample. If the strong magnetic field is instantaneously along the z axis the change in magnetic field direction is along the x-axis. Currents are induced in the sample in order to oppose the change in magnetic field.

The current is constrained by symmetry to flow in circles. The current loops have a magnetic moment which, in the limit of slow rotation and low field, lies in the x direction. This moment interacts with the uniform magnetic field to produce a torque on the sample about the y axis, the axis of rotation. The Hall effect causes electrons to be deflected out of the yz plane as the magnetic field is increased. The current will continue to flow in loops which create a moment lying

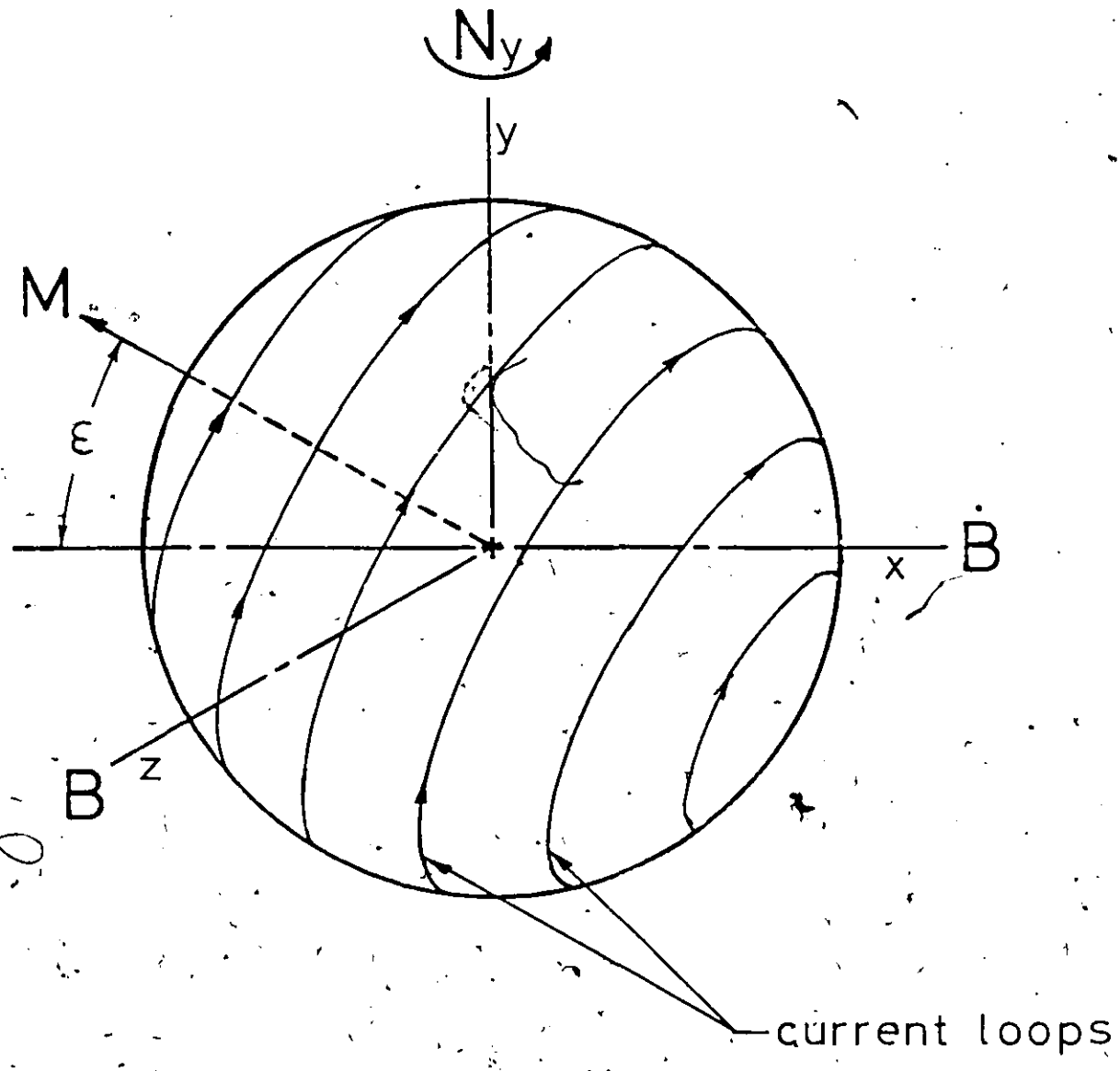

Fig. 3-1 Geometry of the induced torque experiment. The induced moment is rotated in the xy plane through an angle ε.

somewhere in the xy plane and torque which is not totally about the rotation axis. The component of the total torque along the y axis is measured.

ii) Induced Torque on a Sphere

The induced torque on a sphere can be calculated quantitatively (Visscher and Falicov 1970, Lass and Pippard 1970). The following derivation parallels that of Visscher and Falicov. However the current distribution and magnetic moment are calculated explicitly to provide additional physical insights into the problem. The following pair of Maxwell's equations

$$\nabla \times \vec{E} = -\frac{\partial \vec{B}}{\partial t} \tag{3-1}$$

$$\nabla \cdot \vec{j} = \frac{\partial P_c}{\partial t} \tag{3-2}$$

are used subject to the boundary condition at the surface of the sphere

$$\vec{j} \cdot \vec{n} = 0 \tag{3-3}$$

$\vec{E}$ is the total electric field, $\vec{B}$ the total magnetic field, $\vec{j}$ the current density, related to $\vec{E}$ by

$$\vec{j} = \overleftrightarrow{\sigma} \cdot \vec{E} \tag{3-4}$$

where $\overleftrightarrow{\sigma}$ is the conductivity tensor, the inverse of the resistivity tensor $\overleftrightarrow{\rho}$. $\vec{n}$ is a vector normal to the surface and P_c the bulk charge density in the sample.

The following assumptions are made. The charge distribution is assumed to be quasistatic so that its rate of change

$\partial P_c/\partial t$ can be set equal to zero. This assumption, equivalent to ignoring displacement currents, is valid to microwave frequencies in a metal. The mean free path of the electrons is assumed to be small compared to the sample radius so that non-local effects can be ignored. The induced currents are assumed to flow in circles. This current pattern is the simplest which allows equations (3-2) and (3-3) to be satisfied directly. This assumption is related to the assumption that the skin depth is much greater than the sample radius and is examined in more detail in section 3 (iv). The samples are assumed to be spherical and the resistivity tensor translationally invariant. The solution is generalized to an ellipsoidal sample or sample with resistivity that varies quadratically with position in section 3 (iii).

A polar co-ordinate system with the cylindrical axis along the axis of the current loops is chosen to simplify the solution.

The induced currents are first found in the polar co-ordinates and then the angle ϵ between the current axis and $\vec{B}$ is derived. The transformation between the co-ordinate systems x' y' z' and r θ ζ shown in figure 3-2a is given by

$$\vec{a}_{r\theta\zeta} = \overleftrightarrow{T}\vec{a}_{x'y'z'} \tag{3-5}$$

where

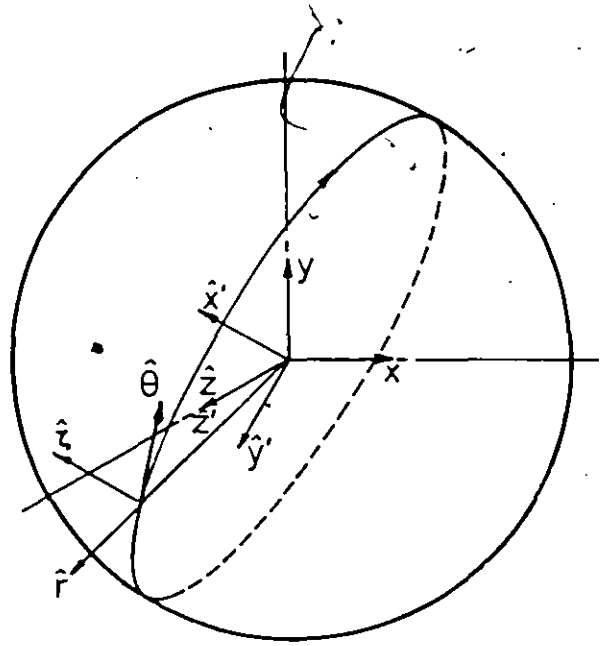

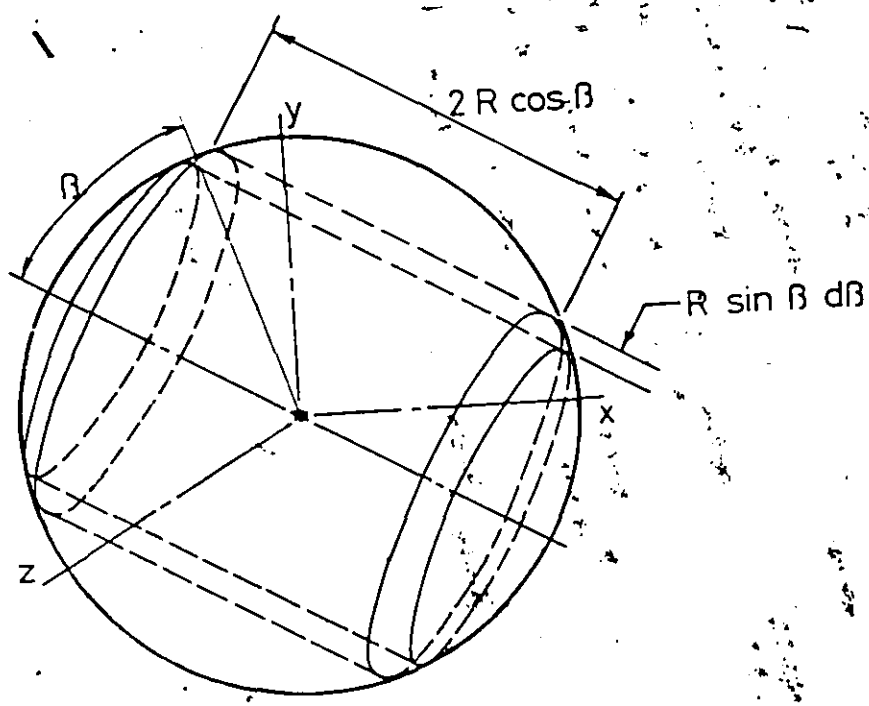

$$|\vec{M}| = 2 \int_0^{\pi/2} d\beta \, \frac{2\pi\mu\dot{B}\sin\varepsilon}{\rho_{xy}} R^5 \cos^3\beta \sin^2\beta$$

Figure 3-2 The co-ordinate systems used to calculate the magnitude of the induced currents and induced torque.

$$\overleftrightarrow{T} = \begin{vmatrix} 0 & \cos\theta & \sin\theta \\ 0 & -\sin\theta & \cos\theta \\ 1 & 0 & 0 \end{vmatrix} \tag{3-6}$$

for any vector $\vec{a}$.

The resistivity tensor of the metal in x'y'z' co-ordinate system is

$$\overleftrightarrow{\rho} = \begin{vmatrix} \rho_{xx} & \rho_{xy} & 0 \\ -\rho_{xy} & \rho_{yy} & 0 \\ 0 & 0 & \rho_{zz} \end{vmatrix} \tag{3-7}$$

The terms ρ_{xz} and ρ_{yz} are small in most metals and have been set to zero.

The change in magnetic field $\dot{B}\hat{x}$ when transformed into the r θ ζ co-ordinate system becomes

$$\dot{B}_r = -\dot{B}\sin\varepsilon\cos\theta\,\hat{r} \tag{3-8a}$$

$$\dot{B}_\theta = \dot{B}\sin\varepsilon\sin\theta\,\hat{\theta} \tag{3-8b}$$

$$\dot{B}_\zeta = \dot{B}\cos\varepsilon\,\hat{\zeta}' \tag{3-8c}$$

where ε is the angle between ζ' and x. The resistivity tensor in the same co-ordinate system is $\overleftrightarrow{T}\overleftrightarrow{\rho}\overleftrightarrow{T}^{-1}$ or

$$\overleftrightarrow{\rho}_c = \begin{vmatrix} \rho_{yy}\cos^2\theta+\rho_{zz}\sin^2\theta & (-\rho_{yy}+\rho_{zz})\cos\theta\sin\theta & -\rho_{xy}\cos\theta \\ (-\rho_{yy}+\rho_{zz})\cos\theta\sin\theta & \rho_{yy}\sin^2\theta+\rho_{zz}\cos^2\theta & \rho_{xy}\sin\theta \\ \rho_{xy}\cos\theta & -\rho_{xy}\sin\theta & \rho_{xx} \end{vmatrix} \tag{3-9}$$

The requirement of circular current loops implies that only J_θ is non zero and requires J_θ to be a function only of r. Equation (3-1) is then solved with $\vec{E}$ given by $\overleftrightarrow{\rho}_c\vec{J}$ and $(d\vec{B}/dt)$ given by equation (3-8).

The radial component is written as

$$\frac{1}{r}\frac{\partial}{\partial\theta}(J\,\rho_{xy}\sin\theta) = \dot{B}\cos\theta\sin\varepsilon \tag{3-10}$$

which when solved gives

$$J = -\,r\,\frac{\vec{B}\sin\varepsilon}{\rho_{xy}}\,. \tag{3-11}$$

The θ component adds no new information. The ζ component is

$$\frac{1}{r}\left(\frac{\partial}{\partial r}\left(rJ[\rho_{yy}\sin^2\theta+\rho_{zz}\cos^2\theta]\right)\right) - \frac{\partial}{\partial\theta}\quad(\rho_{zz}-\rho_{yy})\sin\theta\cos\theta$$

$$= -\,\dot{B}\cos\varepsilon\quad. \tag{3-12}$$

When the value of J found in equation (3-11) is substituted in equation (3-12) the angle ε is given by

$$\tan\varepsilon = \frac{\rho_{xy}}{\rho_{yy}+\rho_{zz}}\quad. \tag{3-13}$$

Next the current density is expressed in terms of diagonal elements of the resistivity tensor as:

$$J_\theta = r\dot{B}\,\frac{\cos\varepsilon}{\rho_{yy}+\rho_{zz}}\,. \tag{3-14}$$

The torque $\vec{N}$ on the sample is obtained from the relation

$$\vec{N} = \vec{M} \times \vec{B} \tag{3-15}$$

where $\vec{M}$ is the magnetic moment and $\vec{B}$ the magnetic induction.

The magnetic moment is found from the relation

$$\vec{M} = \int_{\tau} \vec{r} \times \vec{J} d\tau \tag{3-16}$$

where the integral is over the volume of the sample. Only the ζ component of the magnetic moment is non zero as can be seen from symmetry. Integrating over the contour shown in figure 3-2b gives

$$M_{\zeta} = \frac{4\pi \dot{B} R^5}{15} \frac{\cos\varepsilon}{\rho_{yy} + \rho_{zz}} . \tag{3-17}$$

The total torque on the sample is given by equation (3-15) and the component along the y axis by

$$N_y = M_{\zeta} B \cos\varepsilon . \tag{3-18}$$

Substituting the value of M_{ζ} found in equation (3-17) into equation (3-18) gives

$$N_y = \frac{4\pi \dot{B} B R^5}{15} \frac{\cos^2\varepsilon}{\rho_{yy} + \rho_{zz}} . \tag{3-19}$$

Equation (3-13) must be solved self consistently for the angle ε since ρ_{xy} and ρ_{yy} are in general functions of ε. However simple solutions are possible and physically enlightening in several common situations.

The tensor $\overleftrightarrow{\rho}_c$ is independent of the choice of axis ζ for a material which is symmetric about the magnetic field direction. For a free electron metal $\overleftrightarrow{\rho}_c$ further simplifies to $\rho_{xy} = -\rho_{yx} = \rho_t\omega_c\tau$ and $\rho_{xx} = \rho_{yy} = \rho_{zz} = \rho_t$.

The current density given by equation (3-11) and (3-13) becomes

$$J_\theta = \frac{r\dot{B}}{\rho_t(4+(\omega_c\tau)^2)^{\frac{1}{2}}} \tag{3-20}$$

and the measured induced torque

$$N_y = \frac{4\pi R^5\dot{B}B}{15\rho_t(4+(\omega_c\tau)^2)} . \tag{3-21}$$

For a sample rotating in a magnetic field $\dot{B}$ is given by ωB where ω is the angular frequency of rotation. Thus both the current and the measured induced torque saturate at high magnetic fields.

In the limit of high magnetic field equation (3-21) can be rearranged to give

$$N_y = \frac{8\pi n^2 e^2 \rho_0 \omega R^5}{15RRR} = K\,\frac{\omega R^5}{RRR} \tag{3-22}$$

where n is the free electron density, e the electron charge, ρ_0 the resistivity at 300°K,

R the sample radius and RRR the residual resistance ratio. The induced torque has thus been separated into two quantities $\omega R^5/RRR$ which depends on sample preparation and experimental parameters and

$$K = \frac{8\pi n^3 e^2 \rho_0}{15} \tag{3-23}$$

which is an intrinsic property of a metal. K, thus provides a quantity which can be used to compare different samples. For any metal with only closed orbits a value of K can be calculated but it no longer bears the simple relationship to sample parameters given in equation (3-23).

For potassium K equals 1.76×10^{-2} Nm when R and ω are converted to the dimensionless quantities of the sample radius divided by 1 cm and the angular frequency divided by one degree per minute.

A second common situation is a metal with an open orbit. There is a plane of high conductivity perpendicular to the open orbit when the open orbit direction is normal to the magnetic field. The current is expected to circulate in the plane of high conductivity at high magnetic fields. The angle ε is then given approximately by the angle between the open orbit and the x axis as shown in figure 3-3.

The resistivity tensor calculated in a co-ordinate system x"y"z' which has the x" axis along the open orbit direction has the form

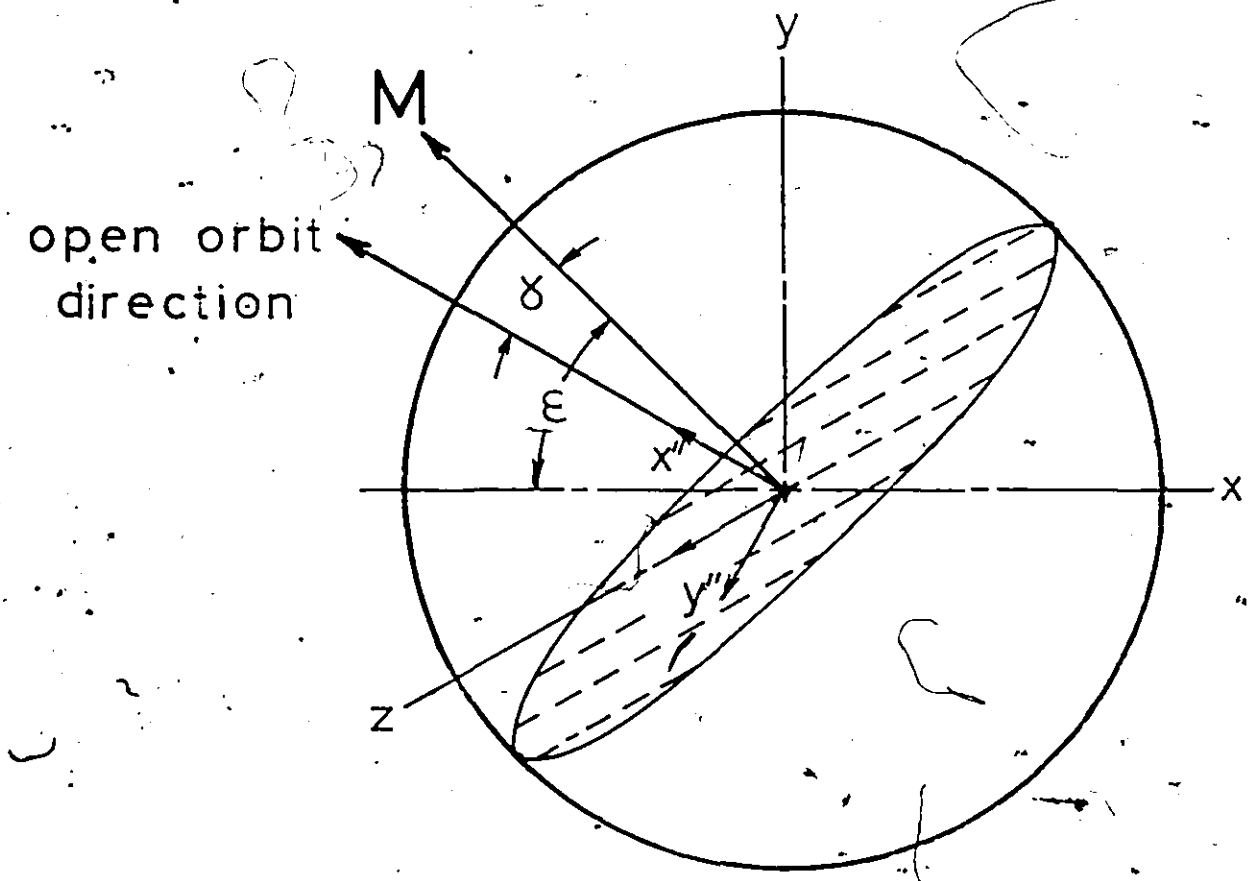

Figure 3-3 The induced moment M and the co-ordinate system x" y" z [illegible] a metal with an open orbit at an ang[illegible] to the x axis.

$$\overleftrightarrow{\rho}'' = \begin{vmatrix} f(\omega_c\tau)^2 & \omega_c\tau & 0 \\ -\omega_c\tau & c & 0 \\ 0 & 0 & d \end{vmatrix} . \qquad (3\text{-}24)$$

The axes x" y" z' are expected to be rotated from the x'y'z' axes only by a small angle γ.

The necessary resistivity tensor elements as defined in equation (3-7) become.

$$\rho_{yy} = f(\omega_c\tau)^2\sin^2\gamma + c\cos^2\gamma \qquad (3\text{-}25a)$$

$$\rho_{zz} = d \qquad (3\text{-}25b)$$

$$\rho_{xy} = \omega_c\tau + f(\omega_c\tau)^2 - c)\cos\gamma\sin\gamma \qquad (3\text{-}25c)$$

with f, c and d constants. Using the values of $\overleftrightarrow{\rho}$ from equation (3-25) in equation (3-13) gives

$$\tan\varepsilon = \frac{\omega_c\tau + f(\omega_c\tau)^2 - c)\cos\gamma\sin\gamma}{d + f(\omega_c\tau)^2\sin^2\gamma + c\cos^2\gamma} . \qquad (3\text{-}26)$$

Equation (3-26) can be easily solved for γ if $\gamma \ll 1$ to give

$$\gamma = -\frac{1}{f\omega_c\tau} . \qquad (3\text{-}27)$$

γ goes asymptotically to zero at high magnetic field as expected.

The current density given by equation (3-14) is, in the limit of high magnetic field

$$J_\theta = \frac{r\dot{B}\cos\varepsilon}{c+d^2 + \frac{1}{f}} \tag{3-28}$$

and equation (3-19) for the induced torque is

$$N_y = \frac{4\pi}{15}\,\dot{B}BR^5\,\frac{\cos^2\varepsilon}{c+d + \frac{1}{f}} \tag{3-29}$$

Several features of the induced torque can be identified from the preceding. An open orbit is excited when the open orbit direction is perpendicular to the magnetic field. For direct rotation of the sample, $\dot{B}$ is given by ωB so the induced torque increases quadratically with magnetic field. The induced torque varies quadratically with $\cos\varepsilon$ where ε is the angle between the open orbit and the rotation plane. In magnetic field directions in which the open orbit carriers are not excited the induced torque saturates. The result is sharp peaks in the induced torque as a function of magnetic field direction. The width of these peaks varies as $\frac{1}{B}$. The locus of magnetic field directions in which an induced torque peak lies, for rotation in a series of planes, forms a great circle on a stereographic projection. The pole of the great circle is the open orbit direction.

The calculation by Visscher and Falicov (1970) gives results which are more generally applicable but do not provide the physical insights of the preceding derivation. Their

result for the induced torque is

$$N_y = \frac{2\pi R^5}{15} \dot{B}B \, \overline{\sigma_{xx}} \tag{3-30}$$

with

$$\overline{\sigma_{xx}} = [\tfrac{1}{2} [\mathrm{Tr}\rho - \rho^{t}]]^{-1}_{xx} \tag{3-31}$$

If ρ_{xz} and ρ_{yz} are set equal to zero equation (3-31) becomes

$$\overline{\sigma_{xx}} = \frac{2[\rho_{xx}+\rho_{zz}]}{[\rho_{xx}+\rho_{zz}][\rho_{yy}+\rho_{zz}]-\rho_{xy}\rho_{yx}} \tag{3-32}$$

for a resistivity tensor defined in the xyz co-ordinates.

iii) <u>Induced Torque on an Ellipsoid</u>

Lass (1976) extended the theory of Visscher and Falicov to the case of an ellipsoid of revolution by using a straightforward though complicated transformation. He introduced a tensor $\overleftrightarrow{s}$ that transformed the ellipse into a sphere as

$$\vec{r}_s = \overleftrightarrow{s}\vec{r}_e \tag{3-33}$$

where $\vec{r}_s$ is a radius vector of the sphere and $\vec{r}_e$ a radius vector of the ellipse.

This derivation closely parallels that of Lass and his notation is used wherever possible. In this work Lass's results are generalized and the results necessary for the following

analysis are written out explicitly.

The Visscher and Falicov result can be applied directly to the sphere defined by equation (3-33) with the conductivity $\overleftrightarrow{\sigma}$ replaced by

$$\overleftrightarrow{U} = \overleftrightarrow{\varepsilon}\overleftrightarrow{\gamma}\overleftrightarrow{\varepsilon}/[\det\overleftrightarrow{s}]^3 \tag{3-34}$$

where the terms are defined later. The magnetic moment becomes

$$M_x = U_{11}\dot{B}_x + U_{12}\dot{B}_y + U_{13}\dot{B}_z \tag{3-35a}$$

$$M_y = U_{21}\dot{B}_x + U_{22}\dot{B}_y + U_{23}\dot{B}_z \tag{3-35b}$$

$$M_z = U_{31}\dot{B}_x + U_{32}\dot{B}_y + U_{33}\dot{B}_z \tag{3-35c}$$

where $\dot{B}_x$, $\dot{B}_y$ and $\dot{B}_z$ and M_x, M_y, M_z are the components of the changing magnetic field and magnetic moment respectively. The induced torque about the y axis N_y, with the magnetic field and change nominally along the z and x axes respectively is given by

$$N_y = B_z U_{11}\dot{B}_x + \dot{B}_z U_{12}\dot{B}_y + \dot{B}_z U_{13}\dot{B}_z$$
$$- B_x U_{31}\dot{B}_x - \dot{B}_x U_{32}\dot{B}_y - \dot{B}_x U_{33}\dot{B}_z \tag{3-36}$$

Thus magnetic fields along the torque axis do not enter the problem at all. For magnetic field, change in magnetic field and rotation axis precisely at right angles only the first term contributes.

It is always possible to choose a co-ordinate system in which B_x is zero so the last three terms become zero. However the terms involving $\dot{B}_y$ and $\dot{B}_z$ are not zero if the field and its rate of change are not at right angles and in some cases these terms become significant.

The tensor $\overleftrightarrow{U}$ can now be defined for a specific model consisting of an ellipsoid formed by compressing (or expanding) a sphere by a factor b along the y axis, then rotating it through an angle ϕ about the z axis and finally rotating about the y axis by an angle θ. The total transformation s is given by

$$\overleftrightarrow{s}^{-1} = \begin{vmatrix} \cos\theta & 0 & \sin\theta \\ 0 & 1 & 0 \\ -\sin\theta & 0 & \cos\theta \end{vmatrix} \begin{vmatrix} \cos\phi & \sin\phi & 0 \\ -\sin\phi & \cos\phi & 0 \\ 0 & 0 & 1 \end{vmatrix} \begin{vmatrix} 1 & 0 & 0 \\ 0 & b & 0 \\ 0 & 0 & 1 \end{vmatrix} . \qquad (3\text{-}37)$$

The following functions

$$\overleftrightarrow{\varepsilon} = \overleftrightarrow{s}^{\dagger}\overleftrightarrow{s} \qquad (3\text{-}38)$$

and

$$\overleftrightarrow{\gamma} = \{\frac{1}{2}\,(\mathrm{Tr}\,(\overleftrightarrow{\rho}\overleftrightarrow{\varepsilon}^{-1})\overleftrightarrow{\varepsilon}-\overleftrightarrow{\rho}^{\dagger})\}^{-1} \qquad (3\text{-}39)$$

define the terms introduced arbitrarily in equation (3-34) Extensive use is made of the relations

$$\overleftrightarrow{\varepsilon} = \overleftrightarrow{1}-\eta\overleftrightarrow{K} \qquad (3\text{-}40a)$$

where

$$\eta = (1-b^2)\sin^2\phi \tag{3-40b}$$

and

$$K_{ij} = \ell_i \ell_j \quad \text{with } \vec{\ell} = (\cos\theta, \cot\phi, -\sin\theta) \tag{3-40c}$$

$$\det \overleftrightarrow{s} = b^{-1} \tag{3-40d}$$

$$\det \overleftrightarrow{A}\overleftrightarrow{B} = \det \overleftrightarrow{A} \det \overleftrightarrow{B} \tag{3-40e}$$

$$(\mathrm{Tr}\overleftrightarrow{Q}-\overleftrightarrow{Q})(\overleftrightarrow{Q}^{-1}+\overleftrightarrow{Q}\mathrm{Tr}\overleftrightarrow{Q}\det\overleftrightarrow{Q}^{-1}) = \mathrm{Tr}\overleftrightarrow{Q}\mathrm{Tr}\overleftrightarrow{Q}^{-1}-\overleftrightarrow{1} \tag{3-40f}$$

Use of the above relations leads to the result that

$$\overleftrightarrow{U} = \frac{2b^3\{\overleftrightarrow{\varepsilon}\overleftrightarrow{\rho}^{-1}\overleftrightarrow{\varepsilon}+\overleftrightarrow{\rho}^{\dagger}\mathrm{Tr}[\overleftrightarrow{\varepsilon}^{-1}\overleftrightarrow{\rho}^{\dagger}]\det[\overleftrightarrow{\rho}^{\dagger^{-1}}\overleftrightarrow{\varepsilon}]\}}{\mathrm{Tr}[\overleftrightarrow{\varepsilon}^{-1}\overleftrightarrow{\rho}^{\dagger}]\mathrm{Tr}[\overleftrightarrow{\rho}^{\dagger^{-1}}\overleftrightarrow{\varepsilon}]-\overleftrightarrow{1}} \tag{3-41}$$

Substitution of the resistivity tensor elements into equation (3-41) allows an exact solution for the induced torque. Such an effort however is not very physically enlightening. Therefore the value of the components of $\overleftrightarrow{U}$ for the simplified resistivity tensor

$$\overleftrightarrow{\rho} = \rho_0 \begin{vmatrix} q & \omega_c\tau & 0 \\ -\omega_c\tau & q_1 & 0 \\ 0 & 0 & q \end{vmatrix} \tag{3-42}$$

are given. This model, which assumes ρ_{xz} and ρ_{yz} are zero

allows us to examine three cases

i)	$q = q_1$	a free electron metal	(3-43a)
ii)	$q = q_1 = 1+s\omega_c\tau$	a metal with linear magnetoresistance	(3-43b)
iii)	$q = 1 \quad q_1 = f(\omega_c\tau)^2$	a metal with an open orbit in the y direction.	(3-43c)

The complete expressions for U are given in Table 3-1. The result is expressed in terms of three parameters, b, η and $\eta\cot\phi$. The factor b is a constant multiplying factor arising because the transformation given by equation (3-37) does not preserve the volume of the ellipse. The factor η is a measure of the departure of the cross-section of the sample in the xz plane from a circle. The factor $\eta\cot\phi$ is a measure of the departure of the cross section of the sample in the yz plane from a circle and is of little significance in most cases.

The tensor U given in table 3-1 can be further simplified by keeping only the largest order terms.

$$U_{11} = \frac{\{(\frac{q+q_1}{q})^2 + \eta(q_1-3q)\cos^2\theta + \eta^2 (\frac{\omega_c\tau}{q})^2 \cos^2\theta\sin^2\theta\}}{2(q+q_1)^2 + (\frac{q+q_1}{q})(\omega_c\tau)^2} \tag{3-44a}$$

$$U_{12} = \frac{\{-(\frac{q+q_1}{q})\omega_c\tau - \eta(q+q_1)\cos\theta\cot\phi + \eta^2 (\frac{\cos\theta\sin^2\theta\cot}{q} (\omega_c\tau)^2)\}}{2(q+q_1)^2 + (\frac{q+q_1}{q})(\omega_c\tau)^2} \tag{3-44b}$$

Table 3-1

Elements of the tensor U for a general resistivity tensor

$$U_{11} = \frac{b}{\rho_0} \{\frac{(q+q_1)^2}{q} + \eta[q\cot^2\phi + (q_1-3q)\cos^2\theta - q_1 - q]$$

$$+ \eta^2[q\cos^2\theta(1+\cot^2\phi) + q_1\cos^2\theta\sin^2\theta + \frac{(\omega_c\tau)^2}{q}\cos^2\theta\sin^2\theta]\}$$

$$\times \{2(q+q_1)^2 + \frac{(q+q_1)}{q}(\omega_c\tau)^2$$

$$+\eta[\langle q+\cot^2\phi+(q_1-q)\cos^2\theta\rangle\langle q+2q_1+\frac{(\omega_c\tau)^2}{q}\rangle - (q+q_1)\cot^2\phi+(q_1-q)\sin^2\theta - \frac{(2q+q_1)}{q}\sin^2\theta(\omega_c\tau)^2]$$

$$+ \eta^2[q+q_1\cot^2\phi+(q_1-q)\cos^2\theta][-q_1\cot^2\phi-(q-q_1)\sin^2\theta]\}^{-1}$$

$$U_{12} = \frac{b}{\rho_0} \{-\frac{(q+q_1)}{q}\omega_c\tau$$

$$+ \eta[-(q+q_1)\cos\theta\cot\phi - 2\cos^2\theta\cot^2\phi\omega_c\tau - \cot^2\phi\omega_c\tau - \frac{(q_1-q)}{q}\cos^2\theta + \frac{(q+q_1)}{q}\omega_c\tau]$$

$$+ \eta^2[q\cos^3\theta\cot\phi + q_1\cos\theta\cot^3\phi + q_1\cos\theta\sin^2\theta\cot\phi + 2\cos^2\theta\cot^2\phi\omega_c\tau + \cos\theta\sin^2\theta\cot\phi\frac{(\omega_c\tau)^2}{q}]\}$$

$$\times \{2(q+q_1)^2 + \frac{(q+q_1)}{q}(\omega_c\tau)^2$$

$$+ \eta[\langle q+\cot^2\phi+(q_1-q)\cos^2\theta\rangle\langle q+2q_1+\frac{\omega_c\tau)^2}{q}\rangle - (q+q_1)\cot^2\phi+(q_1-q)\sin^2\theta - \frac{(2q+q_1)}{q}\sin^2\theta(\omega_c\tau)^2]$$

$$+ \eta^2[q+q_1\cot^2\phi+(q_1-q)\cos^2\theta][-q_1\cot^2\phi-(q-q_1)\sin^2\theta]\}^{-1}$$

$$U_{13} = \frac{b}{\rho_0} \{\eta[(q+q_1)\cos\theta\sin\theta + \cot\phi\sin\theta\omega_c\tau + \cos\theta\sin\theta\frac{(\omega_c\tau)^2}{q}]$$

$$+ \eta^2[-q\cos^3\theta\sin\theta - q_1\cos\theta\sin\theta\cot^2\phi - q_1\sin^3\theta\cos\theta - \sin^3\theta\cos\theta\frac{(\omega_c\tau)^2}{q}]\}$$

$$\times \{2(q+q_1)^2 + \frac{(q+q_1)}{q}(\omega_c\tau)^2$$

$$\eta[\langle q+\cot^2\phi+(q_1-q)\cos^2\theta\rangle\langle q+2q_1+\frac{(\omega_c\tau)^2}{q}\rangle - (q+q_1)\cot^2\phi+(q_1-q)\sin^2\theta - \frac{2q+q_1)}{q}\sin^2\theta(\omega_c\tau)^2]$$

$$+ \eta^2[q+q_1\cot^2\phi+(q_1-q)\cos^2\theta][-q_1\cot^2\phi-(q-q_1)\sin^2\theta]\}^{-1}$$

$$U_{13} = \frac{b}{\rho_0} \frac{\{\eta(q+q_1)\cos\theta\sin\theta+\eta\cot\phi\,\omega_c\tau\sin\theta+\eta\,\frac{\omega_c\tau^2}{q}\cos\theta\sin\theta\}}{2(q+q_1)^2+\frac{(q+q_1)}{q}(\omega_c\tau)^2} \quad (3\text{-}44c)$$

In the case of an open orbit, $q_1 = (\omega_c\tau)^2$ the denominator increases as $(\omega_c\tau)^4$. Only the term $(q+q_1)^2$ in the numerator of U_{11} increases as quickly with magnetic field. Thus U_{11} is constant at high field while U_{12} and U_{13} decrease as $1/(\omega_c\tau)^2$. The torque is dominated by the open orbit at high magnetic field so boundary conditions and small errors in alignment become much less significant.

The effects of a change in shape are more subtle in the case of a free electron-like metal. The complete simplified tensor U is given in table 3-2. The induced torque due to U_{11} has the following features. At low magnetic fields the term $\eta\cos^2\theta$ gives rise to a two-fold torque. The term in $\eta^2\omega_c\tau^2$ will become most significant at large magnetic fields and give rise to a four-fold torque. The four-fold torque becomes equal in magnitude to the two-fold torque when

$$\eta(\omega_c\tau)^2 = 12 \quad (3\text{-}45)$$

The effect of small misalignment of the changing magnetic field to give $\dot{B}_y$, $\dot{B}_z$ much less than $\dot{B}_x$ can be seen from the elements of tensor $\overleftrightarrow{U}$. The largest terms in U_{12} at high magnetic field are of order $\eta^2(\omega_c\tau)^2$, of the same order as the term U_{11}. Since $\dot{B}_y$ is much smaller than $\dot{B}_x$ small misalignments in the y direction

Table 3-2

Simplified elements of the tensor U for a free electron metal

$$U_{11} = \frac{b}{\rho_0} \frac{2-\eta\cos^2\theta + \frac{\eta^2}{2}(\omega_c\tau)^2\cos^2\theta\sin^2\theta}{(4+(\omega_c\tau)^2(1-\frac{\eta}{2}(1-3\sin^2\theta)))}$$

$$U_{12} = \frac{b}{\rho_0} \frac{(-\omega_c\tau-\eta\cot\phi\cos\theta + \frac{\eta^2}{2}(\omega_c\tau)^2\cot\phi\cos\theta\sin^2\theta)}{(4+(\omega_c\tau)^2(1-\frac{\eta}{2}(1-3\sin^2\theta)))}$$

$$U_{13} = \frac{b}{\rho_0} \frac{(\eta\cos\theta\sin\theta + \frac{\eta}{2}(\omega_c\tau)^2\cos\theta\sin\theta + \omega_c\tau\cot\phi\sin\theta) - \frac{\eta^2}{2}(\omega_c\tau)^2\cos\theta\sin^3\theta)}{(4+(\omega_c\tau)^2(1-\frac{\eta}{2}(1-3\sin^2\theta)))}$$

$$U_{22} = \frac{b}{\rho_0} \frac{(2-\eta\cot^2\phi + \frac{\eta^2}{2}(\omega_c\tau)^2\cot^2\phi\sin^2\theta)}{(4+(\omega_c\tau)^2(1-\frac{\eta}{2}(1-3\sin^2\theta)))}$$

$$U_{23} = \frac{b}{\rho_0} \frac{(\frac{\eta}{2}\cos\theta\sin\theta+\frac{\eta}{2}((\omega_c\tau)^2\cot\phi\sin\theta+\cot\phi\sin\theta) - \frac{\eta^2}{2}(\omega_c\tau)^2\cos\theta\sin^3\theta)}{(4+(\omega_c\tau)^2(1-\frac{\eta}{2}(1-3\sin^2\theta)))}$$

$$U_{33} = \frac{b}{\rho_0} \frac{(1+\frac{(\omega_c\tau)^2}{2} - \eta\sin^2\phi - \eta\omega_c\tau^2\sin^2\theta + \frac{\eta^2}{2}\sin^2\theta\cos^2\theta + \eta^2\sin^4\theta(\omega_c\tau)^2}{(4+(\omega_c\tau)^2(1-\frac{\eta}{2}(1-3\sin^2\theta)))}$$

The terms U_{21}, U_{31} and U_{32} are formed by replacing $\omega_c\tau$ by $-\omega_c\tau$ in U_{12}, U_{13} and U_{23} respectively.

have little effect. The largest term in U_{13} at high field will be $\eta(\omega_c\tau)^2\sin\theta\cos\theta$ giving a two-fold torque pattern. For $\dot{B}_z = \kappa\dot{B}_x$ the two-fold and four-fold torques are equal in magnitude when

$$\kappa = \frac{3\eta}{2} . \tag{3-46}$$

U_{13} contains only terms proportional to powers of η. Thus for a spherical sample U_{13} equals zero. Therefore the amount of induced torque measured about the y axis when the changing magnetic field is along the z axis gives a direct measure of the departure of the sample boundary conditions from spherical.

An interesting effect will arise in a free-electron metal with linear magnetoresistance of form $q = 1+s\omega_c\tau$. Experimentally it is found that $s << 1$. In that case the torque will go as found previously in the free-electron case up to $\omega_c\tau \sim 1/s$. At higher fields the terms of the form $(\omega_c\tau)^2/q$ reduce to $\omega_c\tau/s$. Thus at very high fields the torque in all directions increases linearly with magnetic field. The variation of torque with magnetic field direction continues to be four-fold.

The preceding calculation determines the induced torque on an ellipsoid. These results can be extended to a metal in which the conductivity tensor varies as a function of position in the sphere. A spherical sample in which impurities diffuse

in from the surface or impurities precipitate out near the surface upon solidification are examples of such a metal. If the resistivity varies quadratically with position in the sample the problem can be solved in three steps. The sphere with spatially varying resistivity is transformed into an ellipsoid with translationally invariant resistivity tensor where the parameter b is given by the ratio of surface resistivity to centre resistivity. The induced torque on the ellipsoid is then solved by the methods of the previous section. The same conclusions apply; the induced torque shows the four-fold induced torque characteristic of an ellipsoid.

For samples less regular than an ellipsoid an exact analytic solution becomes impossible and a complete numerical or series solution must be sought. Such a solution has not yet been attempted. However the insights gathered for an ellipsoid can be applied. In the case of an open orbit peak the induced torque will depend largely on the conductivity tensor and be insensitive to boundary conditions. By contrast the induced torque in a metal without open orbits is expected to vary strongly with sample shape. These qualitative conclusions are shown to be the case for copper and indium in chapter 5.

iv) Phase of Induced Torque

In early work on the induced torque (Datars 1970) the magnet was continuously rotated about the sample at angular frequencies of order 10^{-2} Hz. The moment of the induced currents was a negligible fraction of the change in magnetic field and could be ignored. At higher rotation rates the magnetic field of the induced moment $\vec{M}$ is large so its change induces an appreciable second moment $\vec{M}'$. The direction of the second moment is different in the two cases used experimentally; the changing magnetic field is created by continuous rotation of the magnet about a fixed sample or modulation of the magnetic field direction about an equilibrium position.

In the case of direct rotation of the magnet about a free electron metal there is an induced moment $\vec{M}$ created by the change in magnetic field, normal to the magnetic field. This moment is tilted at an angle to the rotation plane as described in chapter 3(i). The component of $\vec{M}$ along the axis of rotation is independent of time and does not enter the problem. The component of the moment in the rotation plane is always normal to $\vec{B}$ and produces the induced torque on the sample. In a co-ordinate system fixed in the sample there is a change in $\vec{M}$ along the z direction. This change acts to create a second moment in the direction opposite to the main magnetic field. This second moment does not contribute to the induced torque. The change in the second moment does however create a higher order moment which reduces $\vec{M}$. The measured induced

torque which increases linearly with rotation rate at low rotation rate, reaches a maximum and decreases at high rotation rates. This effect is apparent experimentally only in large samples with high conductivity.

The situation for direct rotation of an open orbit is different and can be described qualitatively by the following model. The direction of the magnetic moment changes in the xy plane from along the y axis to along the x axis and back as the sample is rotated through the magnetic field direction in which open orbits are excited. This change in moment induces a second moment along the x direction. The second moment changes sign as the sample passes the open orbit direction.

The induced torque due to the sum of the moments in the x direction will no longer be symmetric for either rotation direction and can go negative for sufficiently large rotation rates. Non linearities are more severe and occur at lower rotation rates in the induced torque at an open orbit. If the induced torque at an open orbit peak is shown to be linear with rotation rate the effects of second moments can be ignored.

The magnetometers used in this work employ modulation techniques and so differ from the direct rotation case in two important respects. The large magnetic field is in a fixed direction. The torque induced due to small excursions of the magnetic field or equivalently sample position from equilibrium are then measured.

The magnetometers described in chapters 3 v) and 3 vi) operate at frequencies from 2 to 20 Hz in order to increase sensitivity. In this case the induced second moment $\vec{M}'$ is an appreciable fraction of the induced moment $\vec{M}$ and must be considered. The induced moments however all lie in a plane perpendicular to the large magnetic field. The major effect of higher order moments is to alter the phase of the induced torque relative to the changing magnetic field.

Ford and Werner (1973) developed a solution to this problem, exact to second order in frequency, as a low frequency limiting case of the helicon problem in a sphere with free electron conductivity. This solution is applied to find the phase of the induced torque in a sphere for both closed and open orbits and extended to the case of an ellipsoid, with free electron conductivity, which does not depart significantly in shape from a sphere.

The change in external magnetic field

$$\vec{B}_{ac} = B_1 e^{i\omega t} \tag{3-47}$$

along the x axis induces currents which create a magnetic moment $\vec{M}$ to oppose the change in external field. $\vec{M}$ is given by

$$\vec{M} \propto i\omega B_1 e^{i\omega t} \tag{3-48}$$

and is 90° out ~~of phase with~~ $\vec{B}_{ac}$. The direction of moment $\vec{M}$ is at an angle ε given by

$$\tan\varepsilon = \omega_c \tau/2 \tag{3-49}$$

to the $\vec{B}_{ac}$ direction.

The magnetic moment $\vec{M}$ can now be considered as a changing magnetic field which drives further current loops. This second magnetic moment $\vec{M}'$ is given by

$$\vec{M}' \propto - i\omega\dot{\vec{M}} \propto - \omega^2 B_1 e^{i\omega t} . \qquad (3\text{-}50)$$

The moment $\vec{M}'$ is at an angle ε from $\vec{M}$ in the xy plane. It is therefore 180° out of phase with $\vec{B}_{ac}$ and at an angle 2ε from $\vec{B}_{ac}$.

The phase relationships of the induced moments are shown in figure 3-4a. These phase relationships do not change with magnetic field.

The directions of the induced moments change with magnetic field as shown in figure 3-4b. $\vec{M}$ is along the -x direction at low fields and rotates to nearly along the y direction at high field. $\vec{M}'$ rotates from along the x direction at low field to along the -x direction at high field. At $\omega_c\tau = 2$, $\vec{M}'$ lies along the -y direction. The total induced moment $\vec{M}$ is a vector sum of $\vec{M}$ and $\vec{M}'$ if higher order moments are ignored. The induced torque is proportional to the x component of $\vec{M}$.

At high magnetic fields the moment $\vec{M}'$ is in the opposite direction and opposite phase to $\vec{B}_{ac}$ and so acts to enhance $\vec{B}_{ac}$. $\vec{M}$ increases linearly and $\vec{M}'$ quadratically with the frequency of $\vec{B}_{ac}$. Thus at sufficiently high frequencies $\vec{M}'$ becomes equal to $\vec{B}_{ac}$ and the induced moment can be maintained with no external ac field giving a helicon resonance.

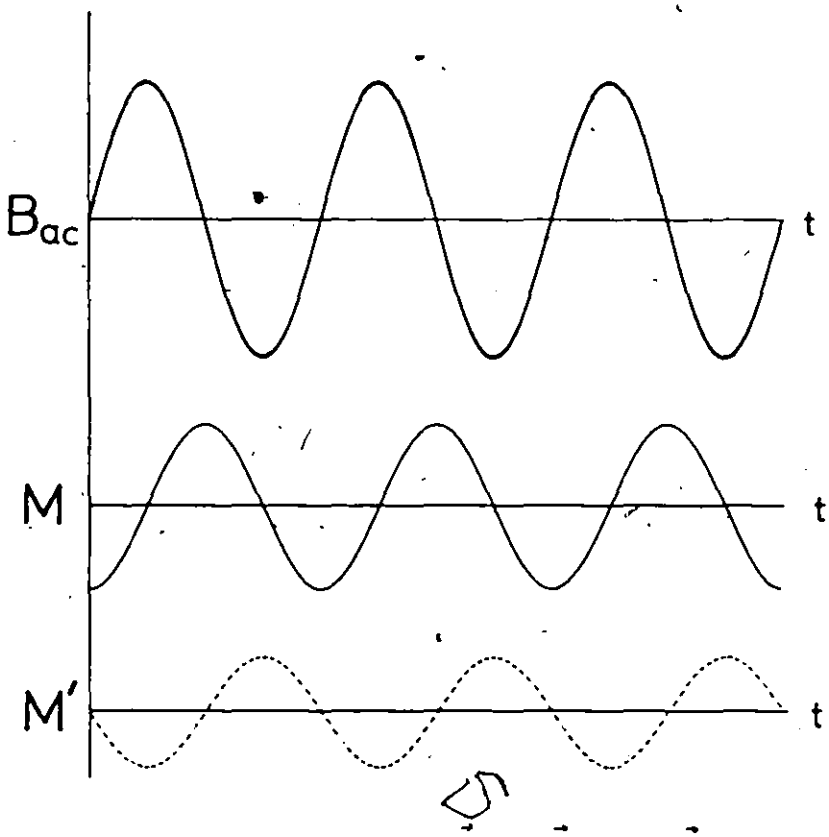

Figure 3-4 a) The phase of $\vec{B}_{ac}$, $\vec{M}$ and $\vec{M}'$ in a metal.

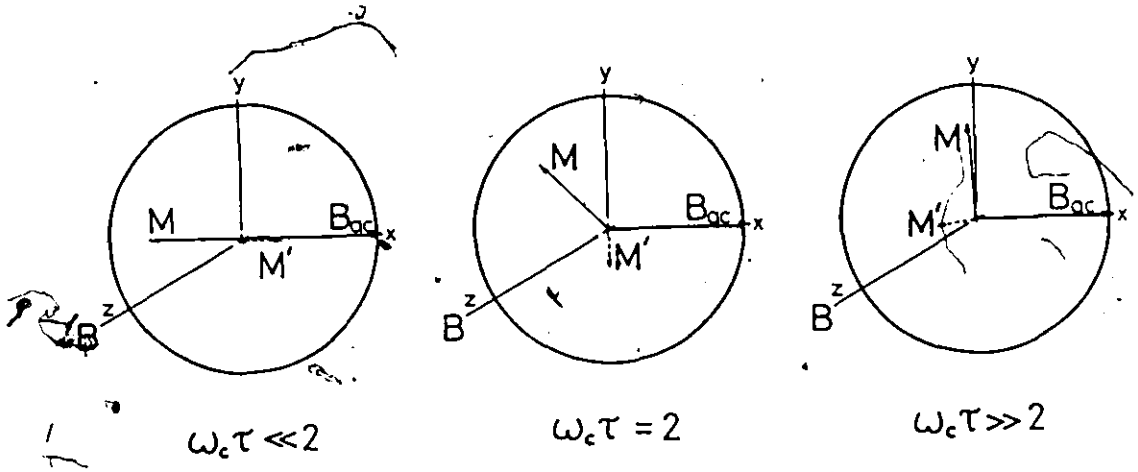

Figure 3-4 b) The direction of $\vec{B}_{ac}$, $\vec{M}$ and $\vec{M}'$ for a free electron metal at $\omega_c\tau \ll 2$ (i), $\omega_c\tau = 2$ (ii) and $\omega_c\tau \gg 2$ (iii).

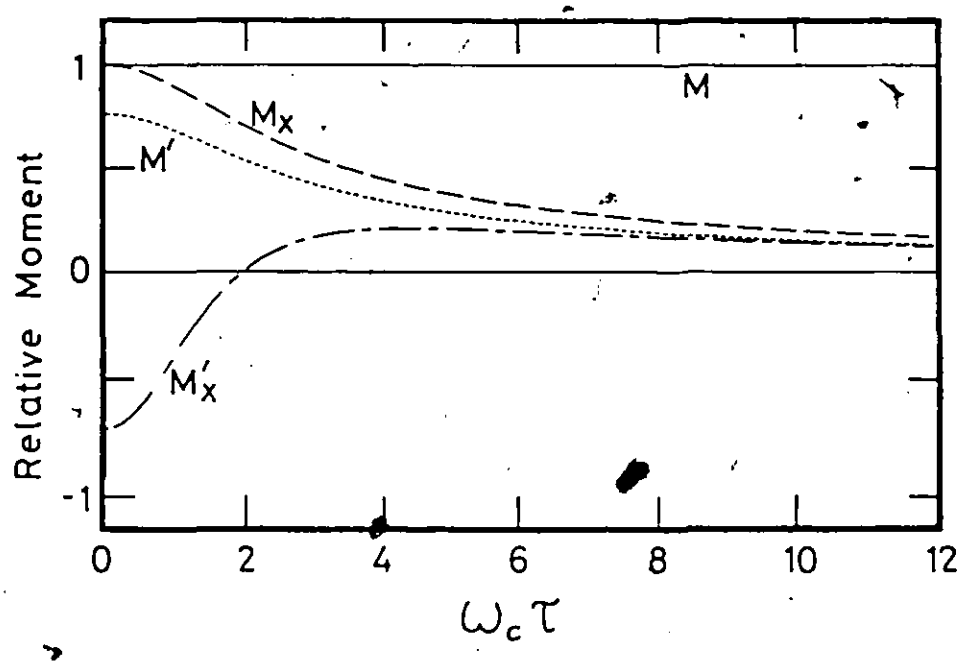

Figure 3-4 c) The amplitude of the induced moments relative to $\vec{M}$ for $V = 8$. The moments shown are $\vec{M}$—, M_x - - - -, $\vec{M}'$ ..... and M_x' —·—·— as a function of magnetic field.

The magnitude of the induced second moment is given by (Ford and Werner 1973)

$$|\vec{M}'| = -\frac{2V}{21}|\vec{M}|\cos\xi \tag{3-51}$$

where ξ is the angle between $\vec{M}$ and $\vec{M}'$. This gives the total moment in the x and y directions, for $\vec{B}_{ac}$ in the x-direction

$$M_x = \frac{V}{4+(\omega_c\tau)^2}\left(\frac{2B_1R^3}{15}\right)\left(-\frac{2}{21}\frac{(4-(\omega_c\tau)^2V}{(4+(\omega_c\tau)^2)} + i\right) \tag{3-52a}$$

$$M_y = \frac{V}{4+(\omega_c\tau)^2}\left(\frac{2B_1R^3}{15}\right)\left(\frac{8}{21}\frac{\omega_c\tau V}{(4+(\omega_c\tau)^2)} - \frac{\omega_c\tau i}{2}\right) \tag{3-52b}$$

where the real and imaginary elements are in and out of phase, respectively, with the external varying field of amplitude B_1. V equals $2(R/\delta)^2$ where R is the sample radius and δ the skin depth of the sample.

The magnitude of the induced moments $\vec{M}$ and $\vec{M}'$ and their x components M_x and M_x' relative to $\vec{M}$ are shown in figure 3-4c for $V = 8$. M_x is proportional to $\cos\varepsilon$ where ε is given by equation (3-49) and so M_x is proportional to 1/B at high field. M_x' is proportional to $\cos\xi$ where ξ equals ε for a free electron metal. Since M_x' equals M_x at high field M_x' is proportional to 1/B at high field. Thus M_x and M_x' are related by a scale factor which depends on V, at high field.

The phase of the induced torque relative to $\vec{B}_{ac}$ is given by

$$\frac{\pi}{2} + \tan^{-1}(M_x'/M_x) \quad . \tag{3-53}$$

The torque is 90° out of phase with the external changing magnetic field at zero frequency. At finite frequencies the phase of the induced torque varies with magnetic field. It varies between limits symmetrically placed about 90°. The phase increases from a minimum at low $\omega_c\tau$, passes through 90° at $\omega_c\tau = 2$ and asymptotically approaches a maximum at high field as shown in figure 3-5. $\omega_c\tau$ can thus be estimated from the field at which the phase of the induced torque is 90°. The phase does not vary as a function of magnetic field direction.

The physical arguments which have just lead to the phase shift for a sphere with closed orbits can be extended to a metal with open orbits. The phase shift will be like that of a free electron metal in directions at which no open orbits are excited. Thus the phase shift will vary as shown in figure 3-5 as the induced second moment tilts to lie in the opposite direction to the change in magnetic field. However in directions in which there are open orbits the induced moment $\vec{M}$ is forced to lie along the open orbit direction due to a high conductivity plane. The same high conductivity plane forces the second moment $\vec{M}'$ to lie in the same direction

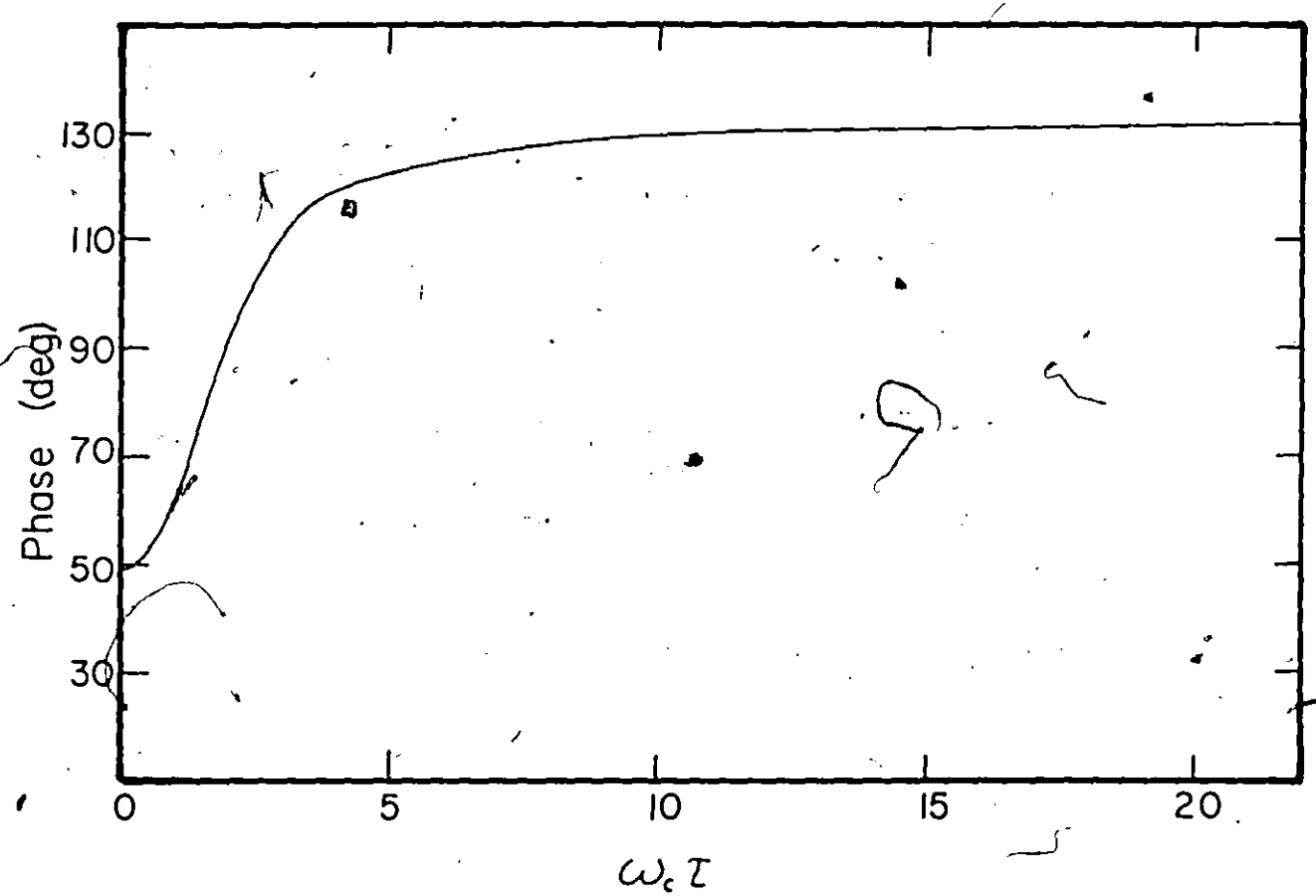

Figure 3-5 The variation with magnetic field ($\omega_c \tau$) of phase in a sphere for V = 9.7.

as $\vec{M}$. Since $\vec{M}$ and $\vec{M}'$ now lie in the same direction it is similar to the low field condition. Therefore there will be a phase dip accompanying an open orbit as indicated in figure 3-6. The magnitude of the phase dip depends on magnetic field and the angle between the open orbit and rotation axis.

The phase shift for an ellipsoid is complicated by a large induced moment in the magnetic field direction which varies in magnitude with magnetic field direction. A solution can be obtained for a nearly spherical sample however. The components of the induced moment $\vec{M}$ in the x, y and z directions are calculated separately. Each component of $\vec{M}$ is then used to generate a second induced moment $\vec{M}'$. The magnitude of the moments $\vec{M}'$ is calculated for a sphere. Corrections are second order in the parameter η, the departure of the ellipse from spherical. The directions of $\vec{M}'$ are those for the ellipsoid as found in chapter 3 iii).

The components of $\vec{M}'$ induced by each component of $\vec{M}$ are then added together to give a total imaginary moment. The x components of $\vec{M}$ and $\vec{M}'$ are compared using equation (3-53) to give a resultant phase shift.

The components which are needed are M_x and M'_{xx}, M'_{yx}, M'_{zx} where the last three terms are defined to be the component of $\vec{M}'$ in the direction of the second subscript induced by the moment in the direction of the first subscript. The direction and magnitude of $\vec{M}'$ are given by equation (3-51) where ξ is

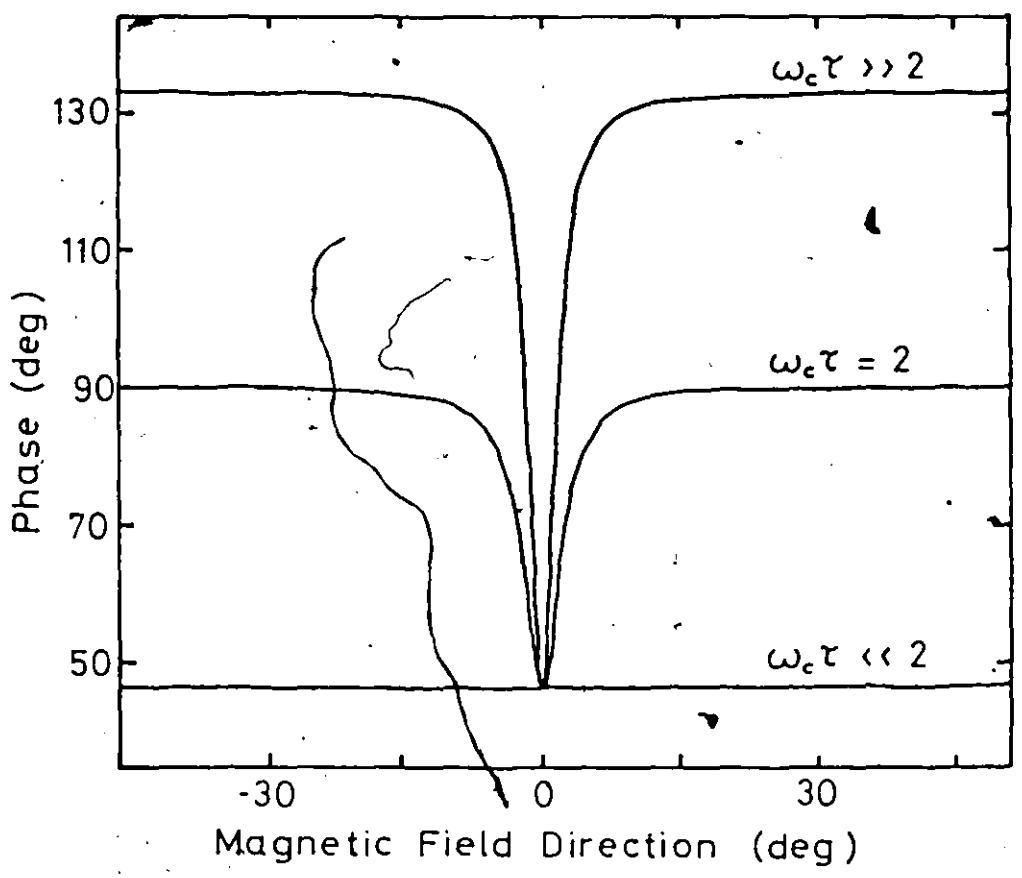

Figure 3-6 The phase of the induced torque in a metal with an open orbit along the x axis.

the angle between $\vec{M}$ and $\vec{M}'$. The angle ξ is in general a function of the direction of the second subscript. The component in the direction of the first subscript is then found.

The required components of $\vec{M}$ can be written directly from equation (3-35) as:

$$M_x = U_{11}\dot{B}_x \tag{3-54a}$$

$$M_y = U_{21}\dot{B}_x \tag{3-54b}$$

$$M_z = U_{31}\dot{B}_x \tag{3-54c}$$

The second moments then are written

$$M'_{xx} = -\frac{2V}{2I} M_x \cos^2\xi_1 \tag{3-55a}$$

$$M'_{yx} = -\frac{2V}{2I} M_y \cos\xi_2 \sin\xi_2 \tag{3-55b}$$

$$M'_{zx} = -\frac{2V}{3I} M_z \cos\xi_3 \sin\xi_3 = \frac{2V}{2I} M_z \frac{U_{31}}{U_{33}} . \tag{3-55c}$$

The angle ξ_1 is given by $\tan^{-1}(U_{12}/U_{11})$ and the angle ξ_2 by $\tan^{-1}(U_{21}/U_{22})$. The simplification for M'_{zx} results because M_{zx} is only a small component of the induced moment M_{zz} so that the angle ξ_3 is given by U_{31}/U_{33}.

At low magnetic fields the phase of the induced torque is dominated by the terms due to a spherical sample.

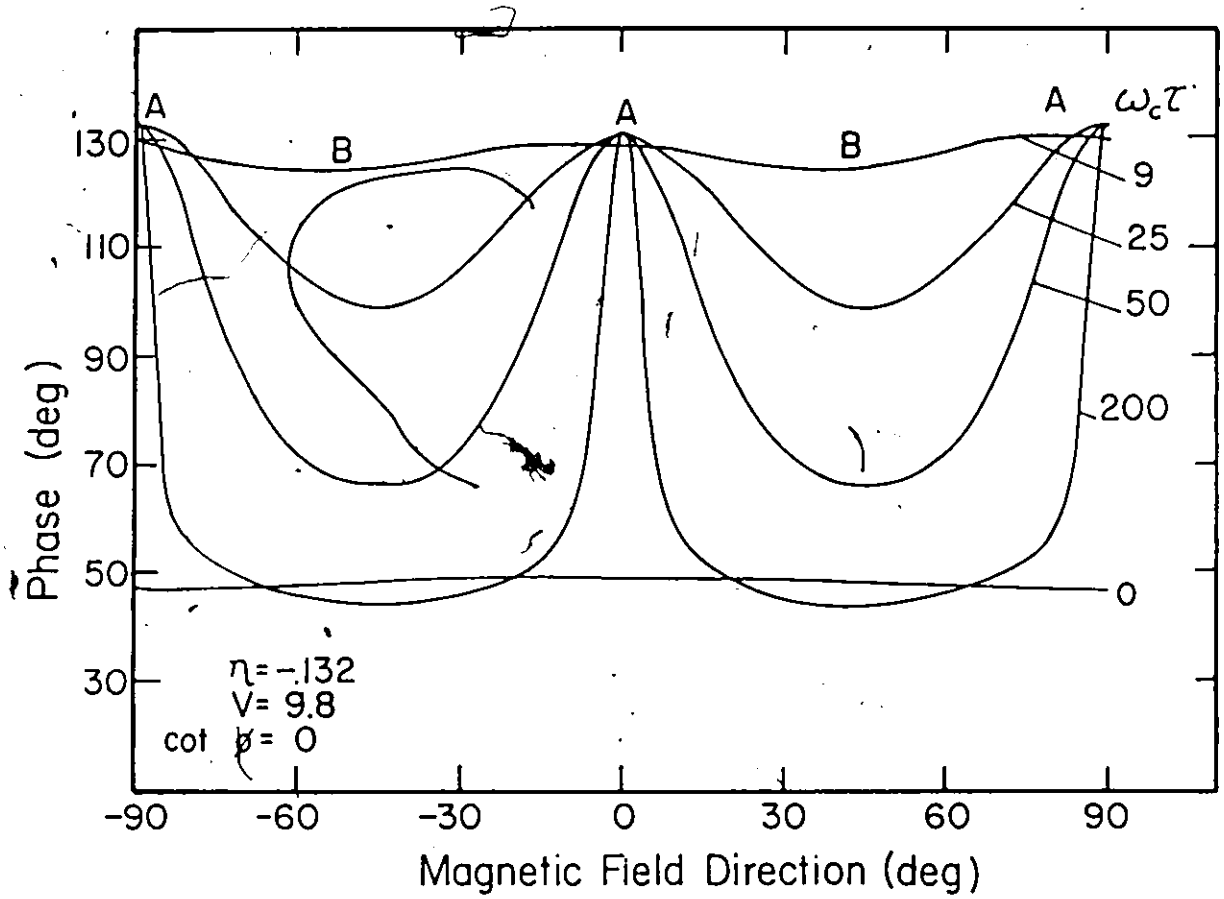

Figure 3-7 The variation of the phase in an ellipsoidal sample as a function of magnetic field direction for $\omega_c\tau$ = 0, 9, 25, 50, 200. The ellipse has η = -0.132 and cotϕ = 0.

However at higher magnetic fields terms due to ellipsoidal samples of the form $\eta^2(\omega_c\tau)^2\sin^2\theta\cos^2\theta$ in U_{11} and U_{13}^2 begin to dominate and the phase shows a four-fold pattern as shown in figure 3-7. In magnetic field directions at which $\sin\theta$ or $\cos\theta$ equal zero corresponding to the minima in the amplitude of the four-fold induced torque pattern the phase continues as predicted for a sphere. In all other directions the terms due to a non spherical sample will eventually dominate at sufficiently large magnetic field. This gives rise to phase spikes as shown for $\omega_c\tau$ equal to 200 in figure 3-7. There are 4 phase spikes per 360° rotation of an ellipsoid.

The terms due to $\cot\phi$, the angle between the symmetry axis and the rotation plane did not enter the calculation of the amplitude of the induced torque and were largely ignored. They do however have an appreciable effect on the phase. This is shown schematically in figure 3-8 for the two cases $\cot\phi = 0$ and $\cot\phi = 1$. For $\cot\phi = 0$ the phase change due to shape is antisymmetric about $\theta = 0$. However when $\cot\phi = 1$ the term M_y due to shape contributes an extra term to the phase of the induced torque through M'_{yx} which does not have the same symmetry. The effect of all shifts due to non-zero ϕ is shown in figure 3-9 at $\omega_c\tau$ equal to 25 and 50.

Several general conclusions can be drawn about the phase of the induced torque. An ellipsoidal sample will show phase spikes at high field. The phase increases at a phase spike.

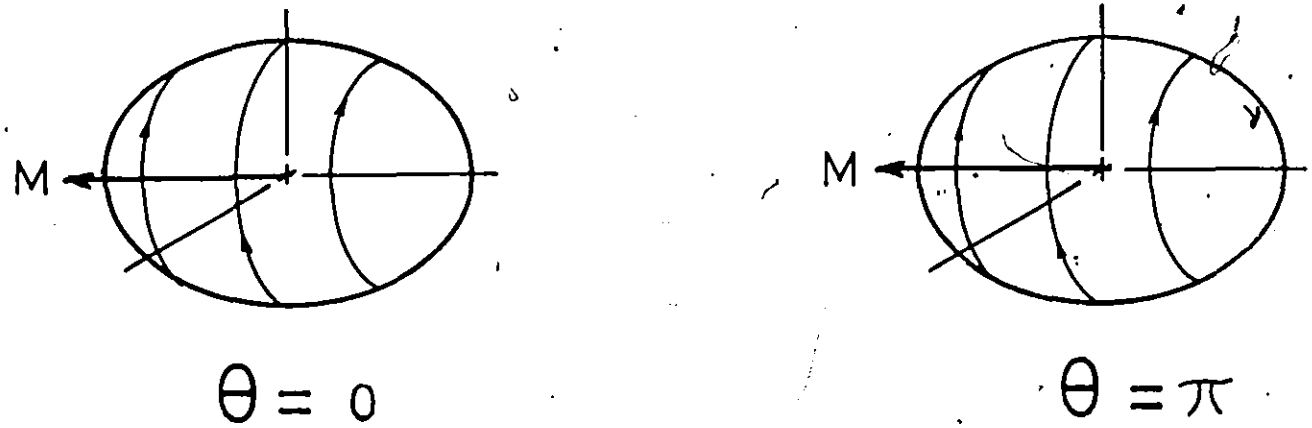

Figure 3-8 a) Schematic plot of the current flow and magnetic moment in an ellipsoidal sample for $\cot\phi = 0$.

Figure 3-8 b) The current flow and magnetic moment for $\cot\phi = 1$

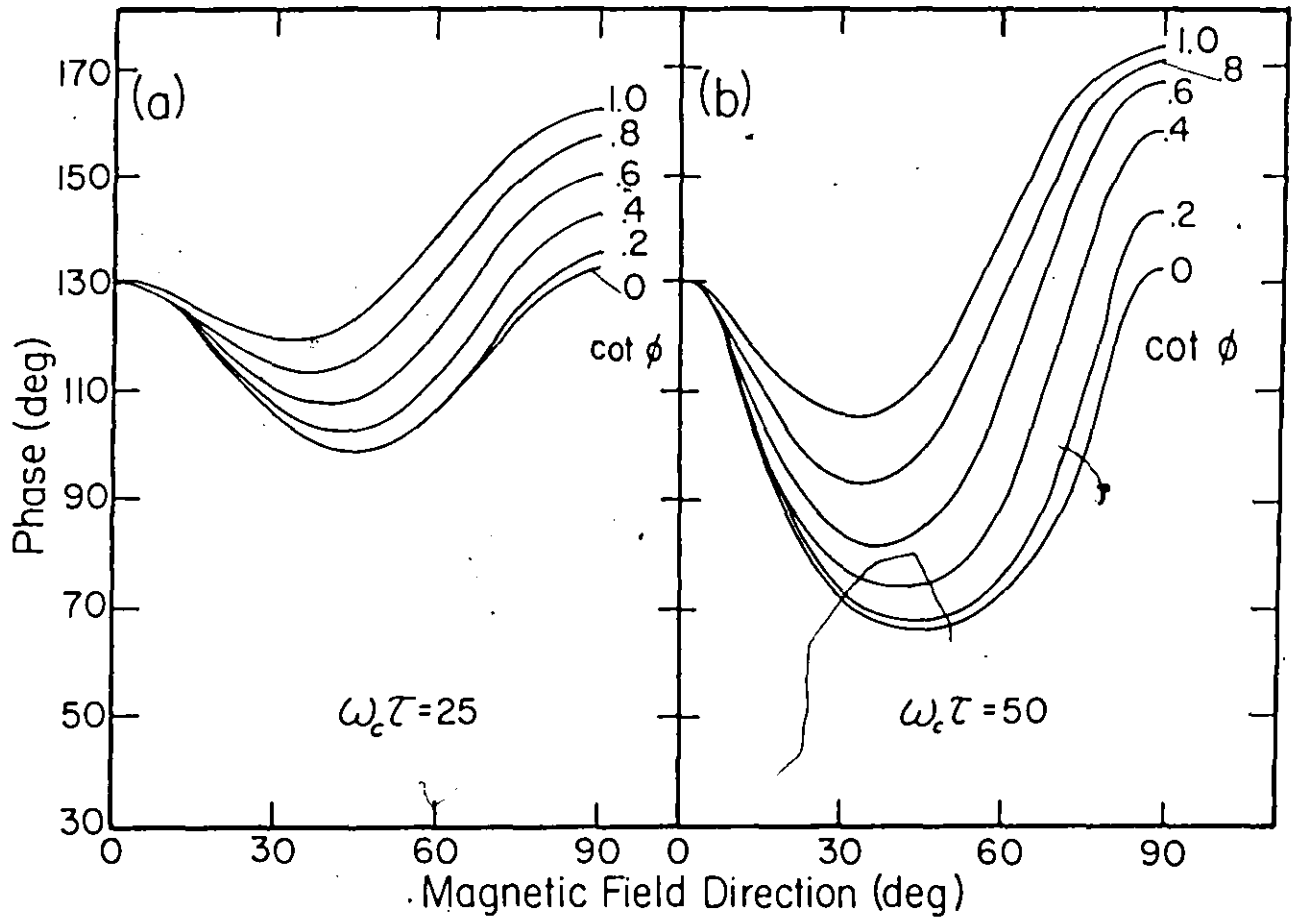

Figure 3-9 The variation of induced torque phase with cotϕ at $\omega_c\tau = 25$ (a) and $\omega_c\tau = 50$ (b).

Since this is such a spectacular effect it is unclear how to generalize the result to samples which are less regular than ellipsoids. It would be expected however that there are significant differences in the phase of the induced torque between high symmetry directions and directions of low symmetry. These changes take the form of phase spikes at high symmetry direction.

By examining the elements of the tensor $\overleftrightarrow{U}$ for an ellipsoid with an open orbit it is possible to qualitatively describe the phase shift. The direction of the induced moments $\vec{M}$ and $\vec{M}'$ and their relative magnitudes are fixed by the open orbit in the low field condition independent of boundary conditions. The phase at an induced torque peak is independent of magnetic field. This phase in general will be less than that for nearby magnetic field directions with only closed orbits. An induced torque peak due to an open orbit will be accompanied by a sharp decrease in phase over the same angular range that the induced torque amplitude varies. This effect does not alter the possibility of detecting open orbits experimentally.

v) Magnetometers Rotating Sample

Experimentally the torque is measured by rotating either the sample or the magnetic field and measuring the resultant induced torque. Since torques due to the dHvA effect and various static torques are added to the desired

induced torque, it is necessary to rotate the sample in both directions and subtract. Those torques which are independent of rotation direction cancel while the induced torque which changes sign upon a change in sense of rotation is left.

Two different magnetometers were used in these experiments. The magnetometer of Verge et al (1977) called the rotating sample magnetometer incorporates the subtraction feature directly. The second has a fixed sample while the magnet is rotated.

The sample is mounted in the centre of crossed coils which rotate on stainless steel pins in jewel bearing as shown in figures 3-10 and 3-11. The sample is positioned by weak springs L. A block diagram of the electrical circuit is shown in figure 3-12.

A direct current through the rotating coils, sets up a magnetic field which creates a torque to overcome the spring torque and to position the sample.

An alternating driving current is passed through the coils M_1 and M_2 to create an alternating magnetic field. This field causes the sample to oscillate about its equilibrium position inducing a torque on it. The sample moves out of phase with the driving signal due to this torque.

The two phase oscillator produces a sine and cosine signal at 100 KHz which are also applied to modulation coils M_1 and M_2 respectively. The phase of the resultant 100 KHz

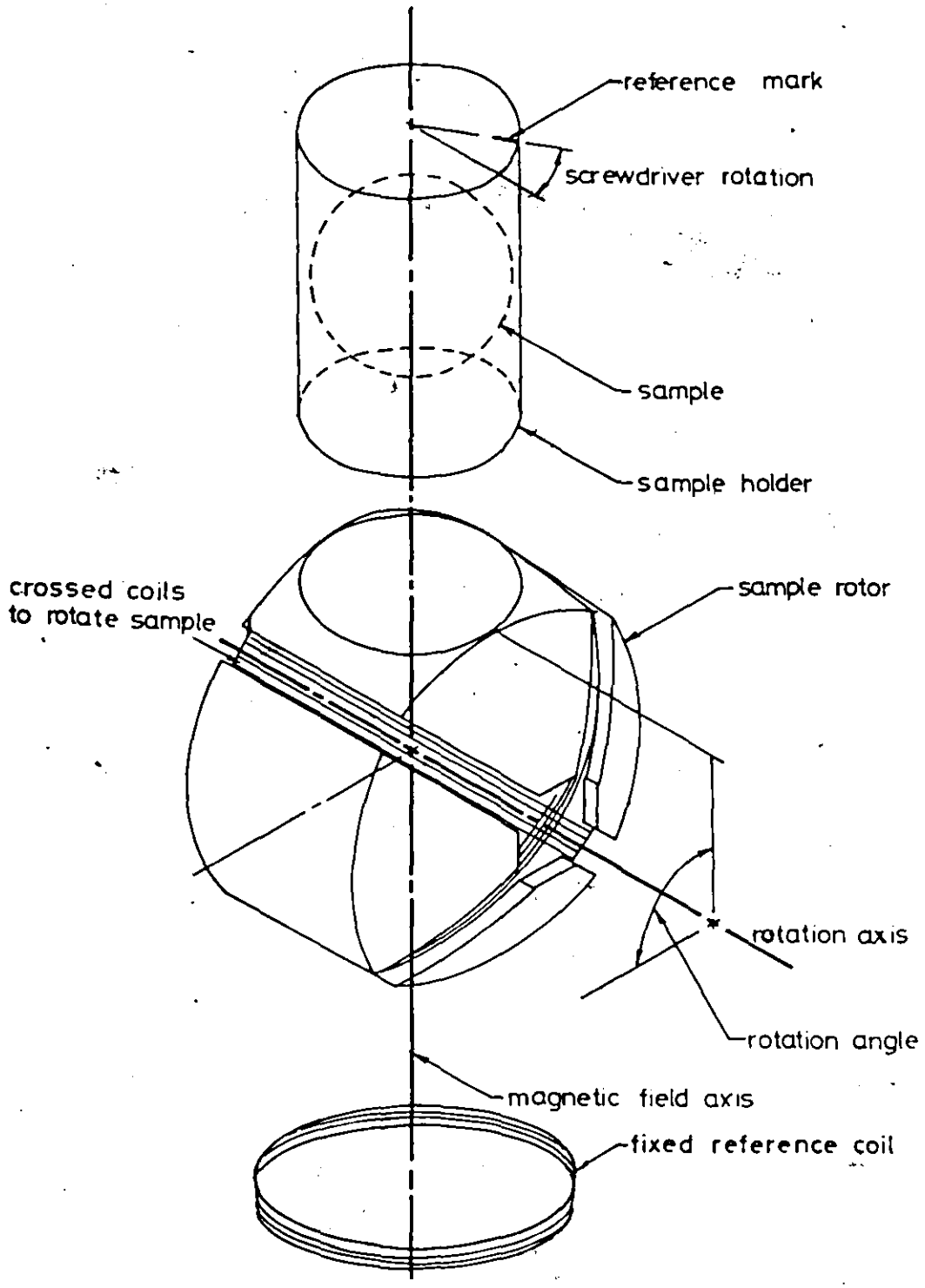

Figure 3-10 Construction of the rotating sample magnetometer.

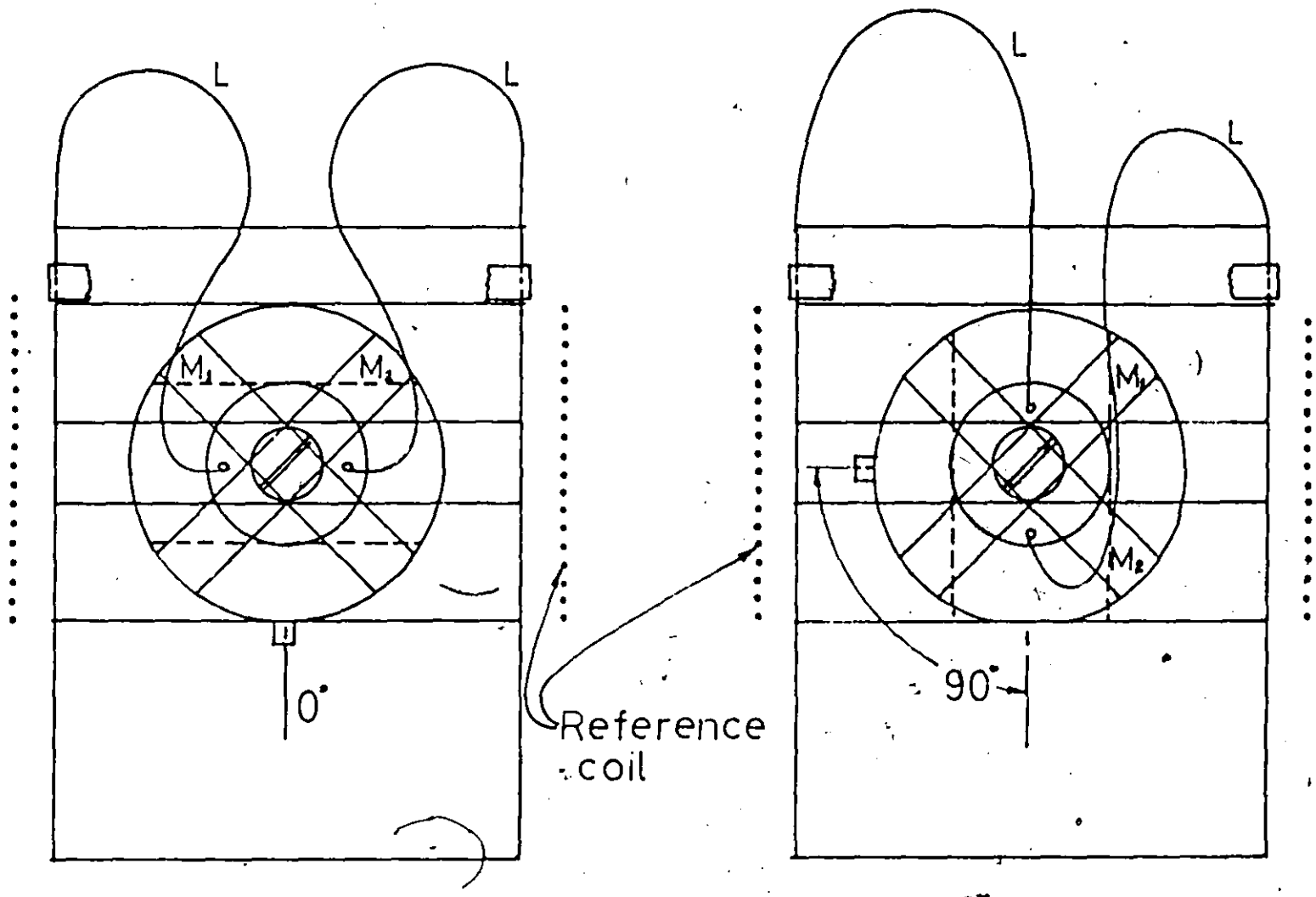

Figure 3-11 Electrical connection to the rotating sample magnetometer.

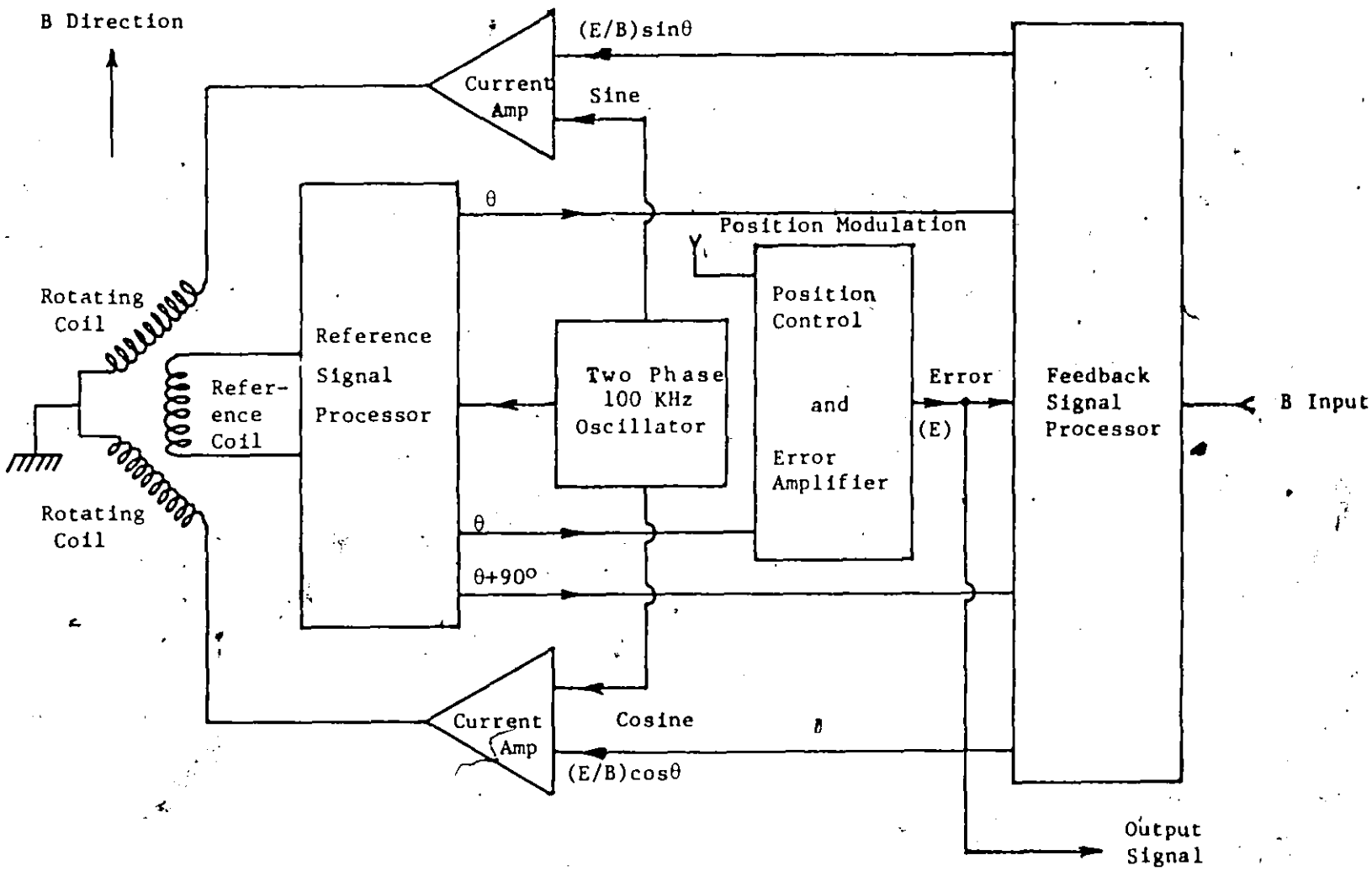

Figure 3-12 Block diagram of the rotating sample magnetometer electronics

signal in the reference coil is proportional to the angular position of the sample. An error output proportional to the torque is then obtained by subtracting a voltage proportional to the position from a voltage proportional to the driving force.

The error signal divided by field and multiplied by $\sin\theta$ is fed back to the modulation coil M_1 and the error signal divided by field and multiplied by $\cos\theta$ is fed back to the modulation coil M_2 to make the compliance of the magnetometer independent of angle and field. The induced torque is derived from the driving voltage and the error signal as shown in figure 3-13.

This magnetometer has several advantages which make it ideal for induced torque measurements. The torque can be measured at a fixed orientation. This allows the field dependence or temperature dependence of the induced torque to be measured directly. Modulating the position of the sample gives a larger effective rotation speed. The increased rotation speed and the ac variation of the torque signal which allows the use of phase sensitive detection greatly increases the sensitivity of the magnetometer.

Since the torque is being measured by small excursions about an equilibrium position a larger effective rotation speed can be used. For a primary orbit in copper at 7.5 T the measured induced torque at an open orbit begins to saturate

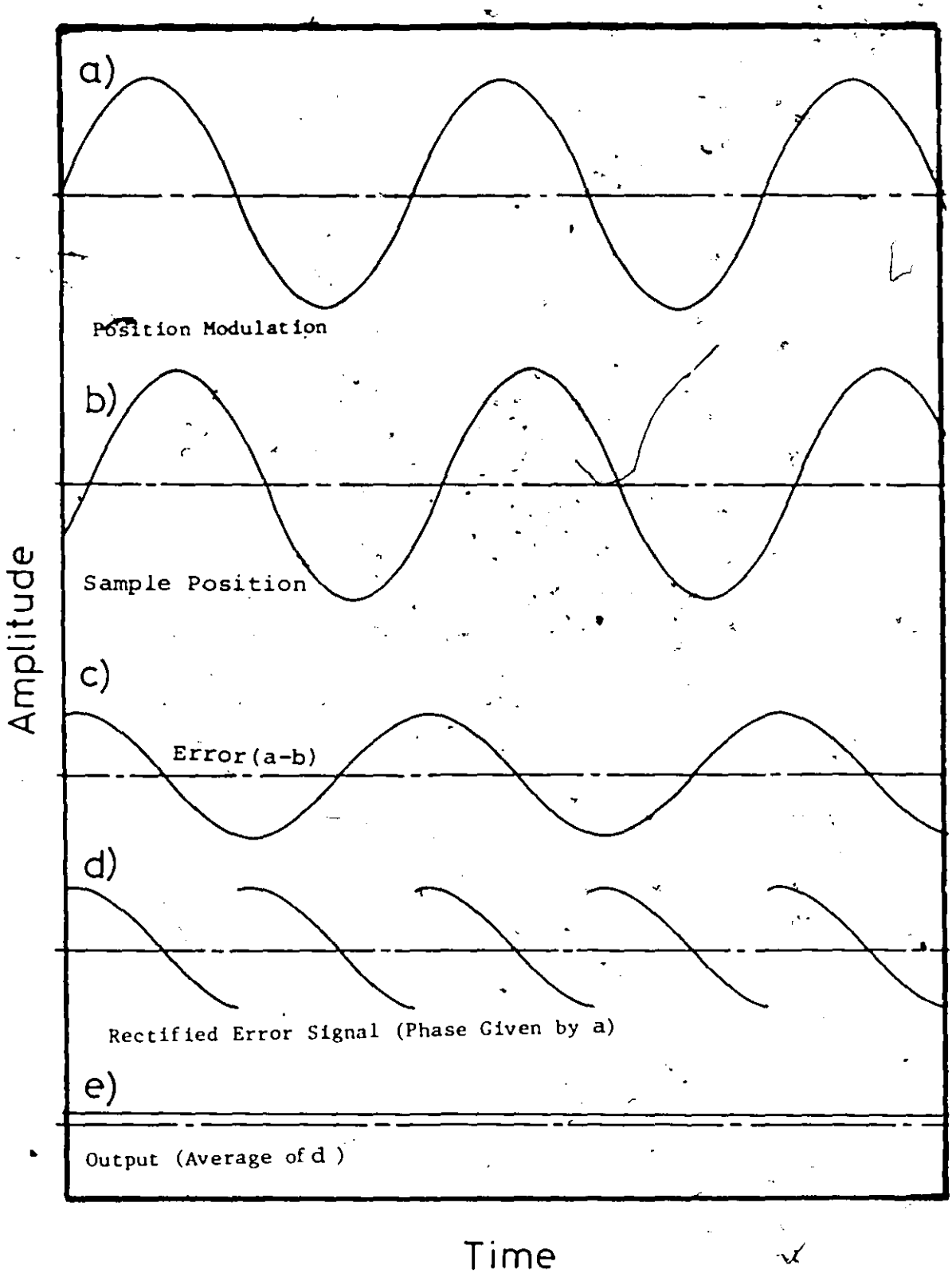

Figure 3-13 Signal processing to obtain the induced torque.

at a rotation rate of 10°/min while using the modulation method, the amplitude of the measured torque was directly proportional to the rotation rate at the highest effective rotation rate used as shown in figure 3-14.

It is also possible to operate the magnetometer by rotating the sample without position modulation and measuring the torque. The induced torque can then be derived from the torque measured with rotations in opposite directions. This is important since the measured output signal found while modulating the sample position includes both the induced torque and a constant offset due to the rotor inertia and signal processing. The direct rotation, therefore, provides an absolute calibration of this magnetometer.

A disadvantage of the method is that it requires a magnetic field to operate. There is thus a minimum field at which the magnetometer can operate, established by the maximum available feedback current. In practice this limit is about 0.1 T.

A second disadvantage of this technique is the phase shift in the induced torque signal which occurs at the frequencies used in these experiments, as described in Chapter 3 iv). If the induced torque is measured by direct sample rotation the effect of increased rotation rates causes the output to vary non linearly with rotation rate as shown in figure 3-14. At the frequencies used with the rotating sample magnetometer

Figure 3-14 Linearity of rotating sample magnetometer response to sample rotation rate. The data (x) were taken using modulation techniques and the data (o) were taken using direct rotation. The inset shows the low rotation rates in greater detail.

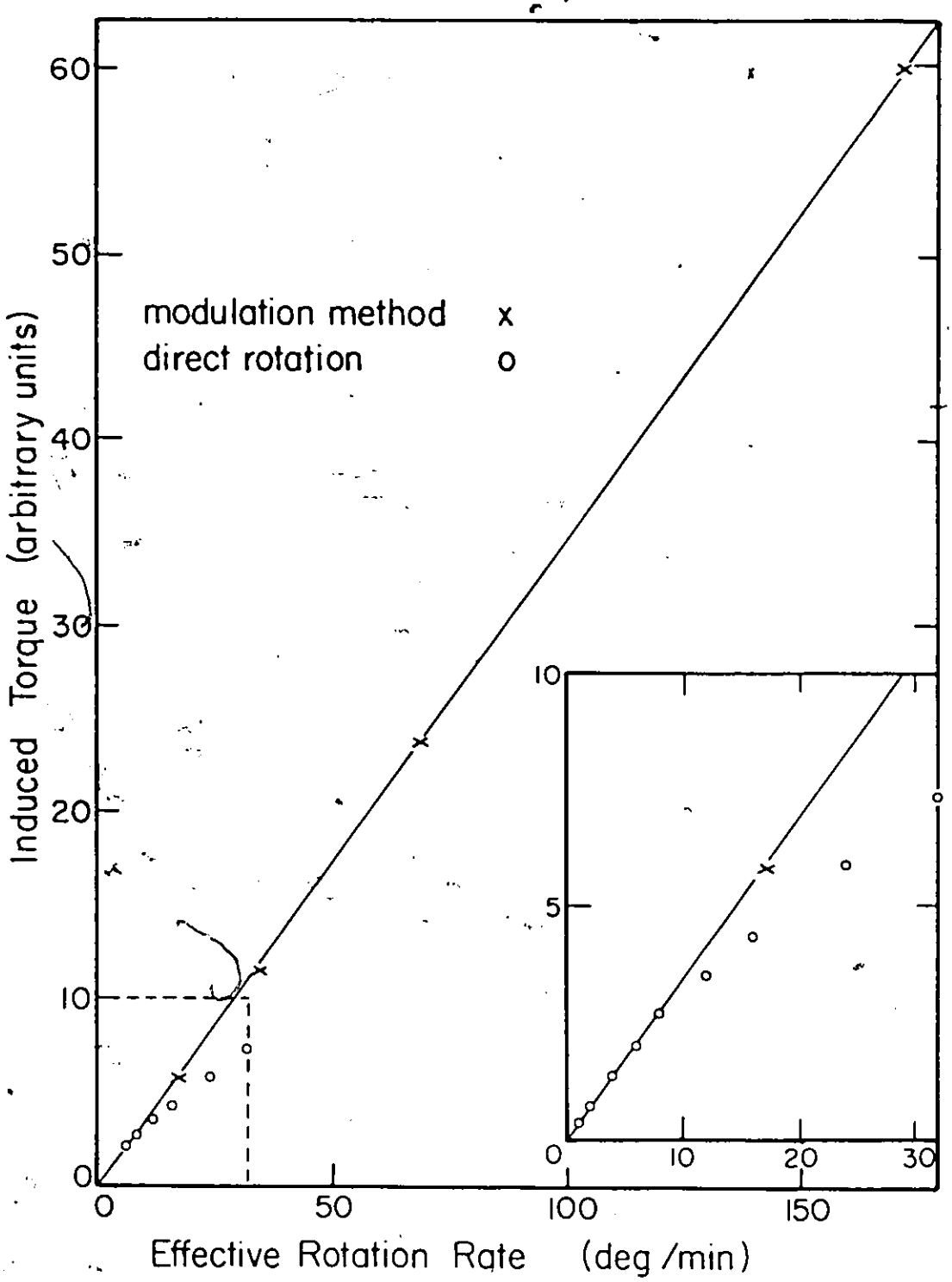
modulation method x
direct rotation o
Induced Torque (arbitrary units)
Effective Rotation Rate (deg /min)
0
10
20
30
40
50
60
0
50
100
150
0
5
10
0
10
20
30

however, 90° shifts in the phase of the induced torque with respect to sample position can occur.

To see the effect of phase shifts on the magnetometer output the following model of the induced torque magnetometer is employed. It is considered as a driven oscillator in which the driving force is provided by currents through the coils M_1 and M_2. The phase shift between sample position and driving current Ψ is given by

$$\sin\Psi = \frac{N\omega}{((\Gamma - I\omega^2)^2 + N^2\omega^2)^{\frac{1}{2}}} \tag{3-56}$$

and the amplitude L of the magnetometer angular excursion in suitable units by

$$L = (\Gamma - I\omega^2)^2 + N^2\omega^2)^{\frac{1}{2}} \tag{3-57}$$

for operation at angular frequency ω. N is the damping coefficient and includes both induced torque and electronic damping, Γ is the restoring torque due to the springs and I the moment of inertia of the sample and rotor.

At usual frequencies of operation, the induced torque is only a small component of the total torque. The phase of the induced torque due to the first moment is 90° from that of the sample position. The induced torque due to the second moment is in phase with the sample position and acts like an inertia torque. The sensitivity of the magnetometer to both first and

second moments is given by

$$\Lambda_M = \frac{\partial \sin\Psi}{\partial N} \tag{3-58a}$$

$$\Lambda_{M'} = \frac{\partial \sin\Psi}{\partial I} \tag{3-58b}$$

the derivative of $\sin\Psi$ with respect to N and I respectively.

The result is demonstrated qualitatively in figure 3-15. the phase relations are shown as angles in the plane. The equilibrium condition is shown by the solid line. A small change ∇ in the induced torque due to the first moment adds to $N\omega$ and causes a phase shift α. The same small change ∇ in the induced torque due to the second moment adds to $I\omega^2$ and causes phase shift β. The output which is proportional to the phase shift is smaller for a torque due to the second moment than the first moment.

This induced torque magnetometer thus has reduced sensitivity to phase changes and so can discriminate against them to some extent. However a phase spike as described in section iv) will give rise to a change in measured torque. The existence of a significant phase change at frequencies 2 to 20 Hz gives rise to the suggestion that phase shifts in the 100 KHz signal need be considered. To do this the values $\omega_c\tau = 400$ and $V = 2\times10^5$ are taken as upper limits for the samples used in these experiments at highest magnetic fields.

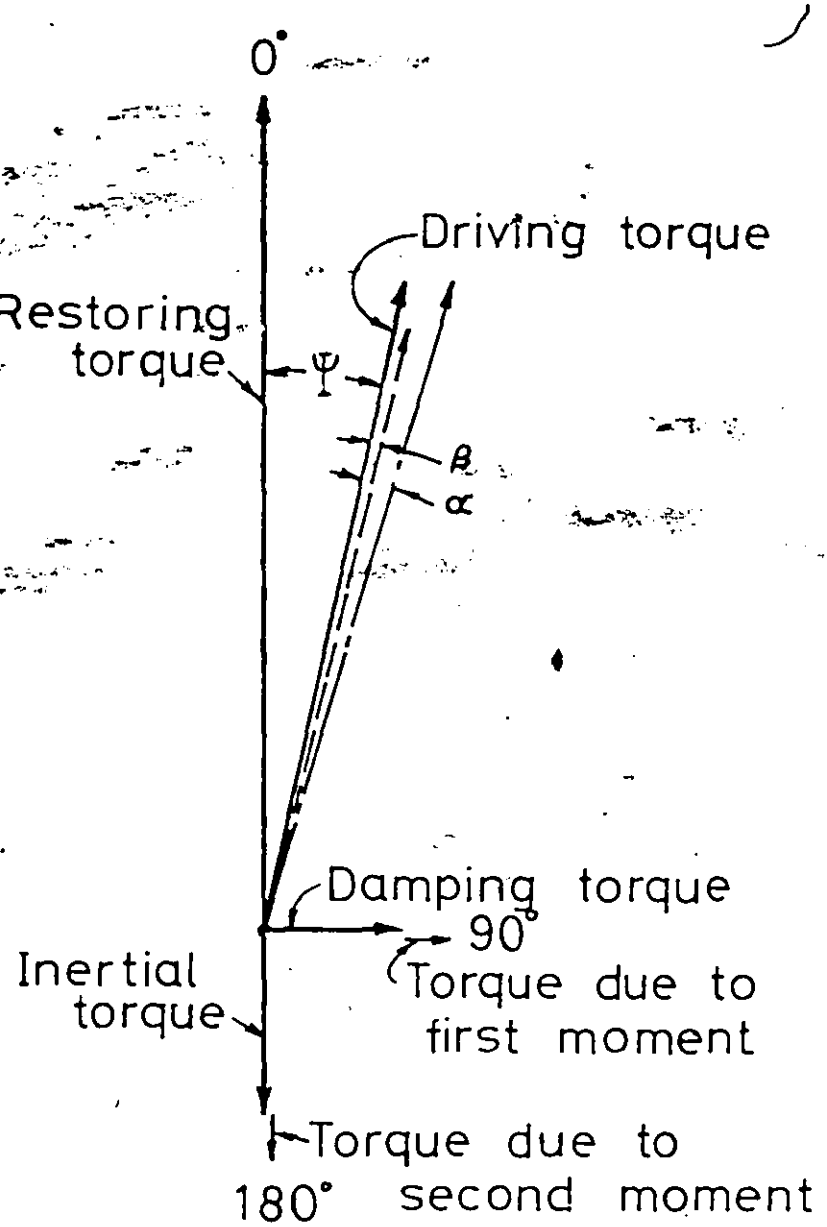

Figure 3-15 Phase relationship of torques on rotating sample magnetometer.

Examination of the results of Ford and Werner shown in figure 3-16 shows that this is clearly in the high field limit. Any helicon resonances at this frequency will be of negligible amplitude. The resultant magnetic moment is therefore $-\frac{1}{2} B_1 R^3$ for a sphere. This moment is in phase with and in the opposite direction to the inducing field. The properties of the moment do not depend on the conductivity of the sample or the constant magnetic field. To extend this result to a non spherical sample it is therefore appropriate to use the high frequency result of Landau and Lifshitz for zero constant field. In that case the magnitude and direction of the moment are determined by the size and shape of the sample. Thus for a non-spherical sample it will not necessarily be in the same direction as the inducing field. To see the effect of this moment on the measured output it is necessary to examine the position sensing system in detail. The sample is held in a fixed position relative to the modulation coils M_1 and M_2 as shown in figure 3-10.

100 kHz sine and cosine waves are applied to coils M_1 and M_2 respectively. The phase of the signal induced in the reference coil relative to cosine wave gives the rotation angle θ. The presence of the sample adds additional moments due to currents induced by both M_1 and M_2. The amplitude of these extra moments is equal to $\frac{1}{2}$ the filling factor of the sample and they are in a direction defined by sample shape. The direction does not vary relative to the modulation coils as the sample is rotated. The moments due to the sample therefore con-

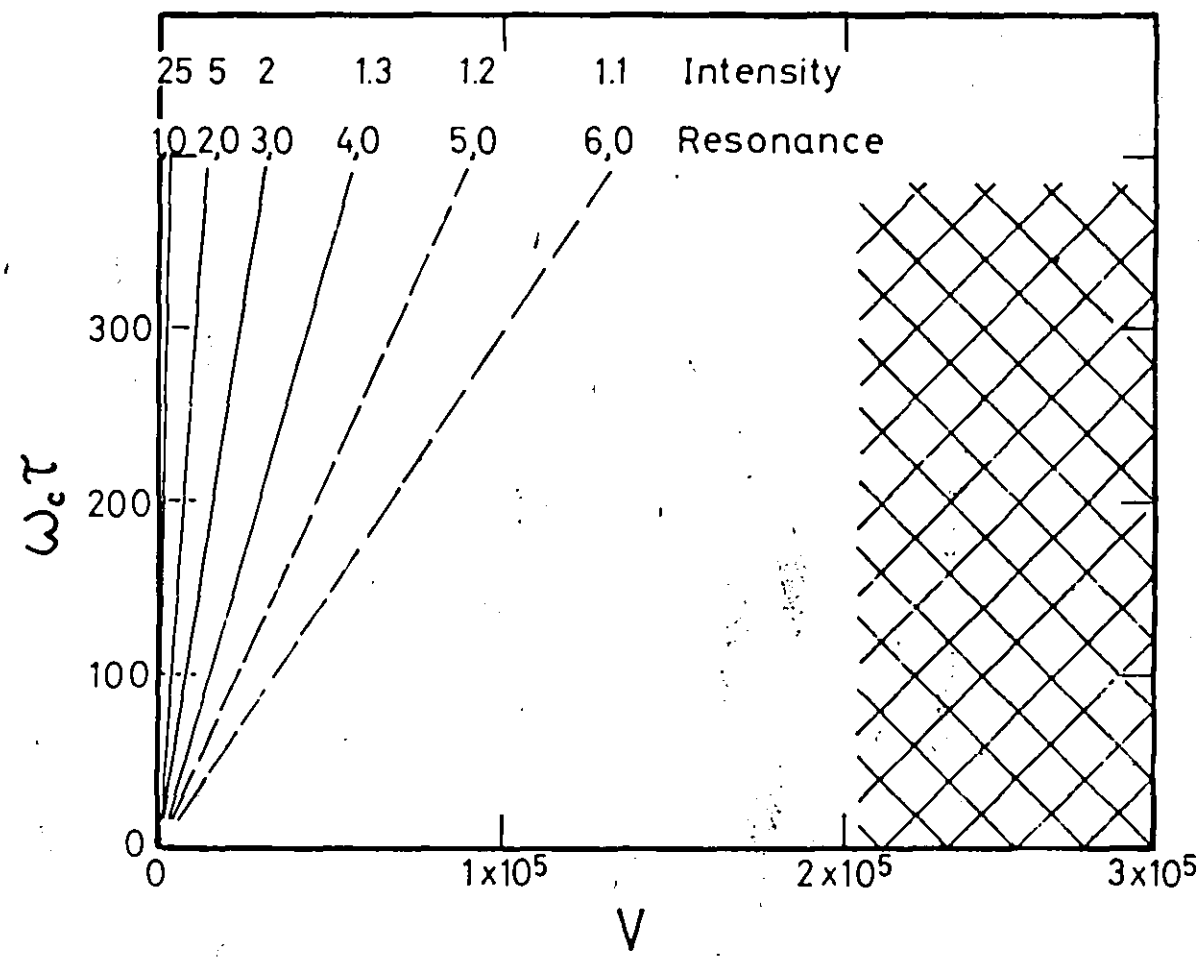

Figure 3-16 Helicon resonant frequencies and amplitude as a function of frequency (V) and magnetic field ($\omega_c\tau$).

tribute a small constant phase shift to the voltage in the reference coil. This small offset is seen by the magnetometer as an extra restoring torque which does not affect its operation.

vi) Magnetometer Rotating Magnet

The induced torque was also measured using a quartz rod magnetometer as sketched in figure 3-17. This is called the rotating magnet magnetometer. The rotation of the coil is detected and a feedback current applied to return the coil to its zero position. The magnitude of the required feedback current gives a measure of the torque on the sample. The details of the electronics are provided by Vanderkooy (1967).

A magnetic field was supplied by a 5.5 T split coil magnet with a transverse magnetic field which could be rotated about a vertical axis. The torque induced was measured as the magnet rotated through 180°. The versatility of the instrument was however increased by the addition of modulation coils perpendicular to the magnetic field. The coils were wound on accurately machined formers and mounted along an axis perpendicular to the magnetic field and rotation axis with error of less than 0.5°. A modulation current with frequency between 2 and 20 Hz was passed through the coils to provide a small modulation field perpendicular to the main magnetic field. This modulation field induced currents in the sample and so gave rise to a torque, which is measured by phase sensitive detection. The induced torque is proportional to $\dot{B}$, the rate of change of

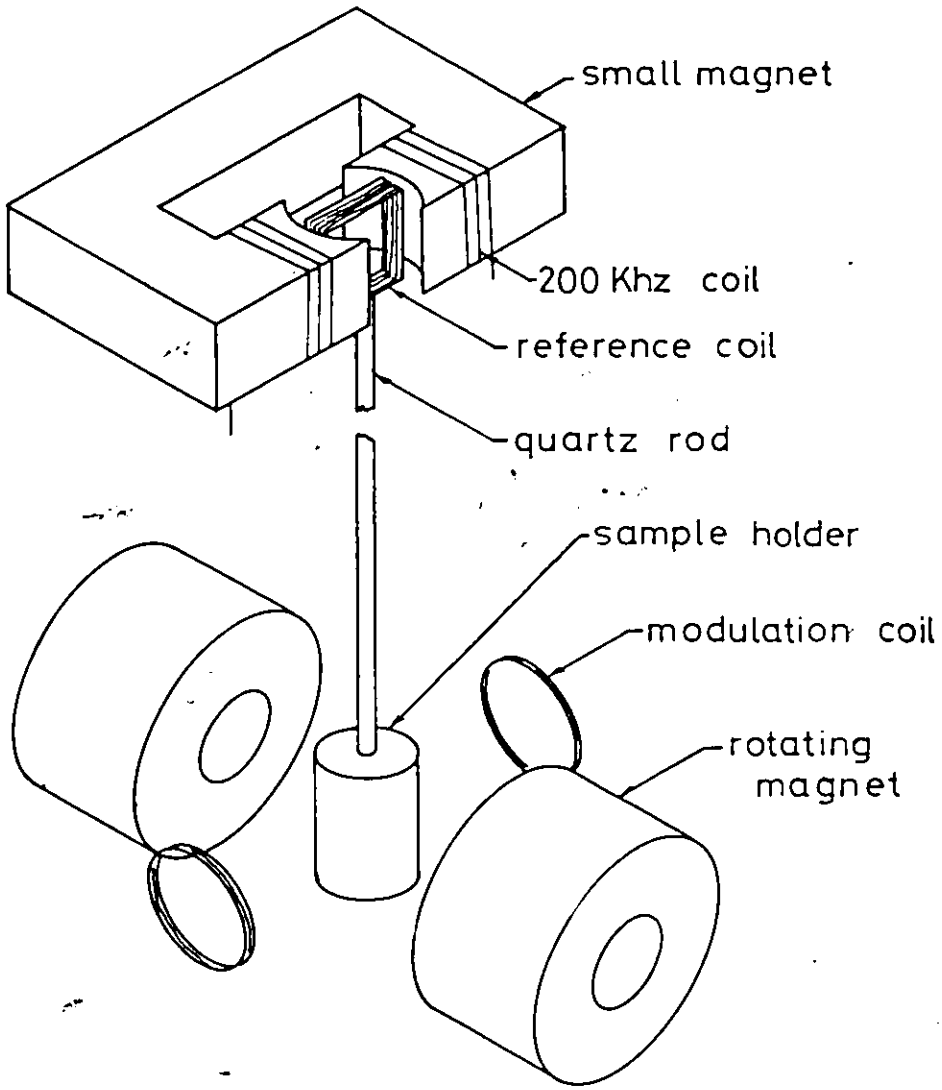

Figure 3-17 Construction of the rotating magnet magnetometer.

magnetic field B. $\dot{B}$ is given by ωB where ω is the angular frequency of rotation for rotating the magnet. For the change in field provided by coils with constant current however, $\dot{B}$ is a constant independent of magnetic field. The torque measured by this technique will be reduced by a factor of B compared to the torque measured by rotating the magnet directly. The induced torque for a free electron metal given by equation (3-21) is proportional to

$$\omega_c\tau/(4+(\omega_c\tau)^2) \quad . \qquad (3\text{-}58)$$

The torque will increase linearly at low magnetic field, reach a maximum at $\omega_c\tau = 2$ and vary inversely with magnetic field at high magnetic fields. The behaviour for other commonly observed resistivity tensors is listed in table 3-3 along with the results for the rotating sample magnetometer.

The sample and holder act as a driven oscillator in which the driving force is supplied by the induced torque. This rotates the sample against the restoring force supplied by the feedback current. Since damping is very small the sample motion is in phase with the induced torque and feedback current. The measured signal is thus linear with induced torque at low frequency. The phase of the sample position varies directly with the phase of the induced torque. Small phase changes with frequency will result since the damping constant is not precisely zero.

Table 3-3

Field Dependence of Magnetoresistance

Metal	Magnetic Field $\omega_c\tau$	ρ_{yy}	Induced Torque: Rotating sample magnetometer	Induced Torque: Rotating magnet magnetometer
free electron	<1	const.	B^2	B
	>>1	const.	const.	1/B
closed orbits non-compensated	<1	B^2	B^2	B
	>>1	const.	const.	1/B
closed orbits compensated	<1	B^2	B^2	B
	>>1	B^2	const.	1/B
linear magneto-resistance	<1	B^2	B^2	B
	>>1	B	B	const.
open orbits	<1	B^2	B^2	B
	>>1	B^2	B^2	B

This method has some advantages. The modulation field is supplied by an alternating current and so allows the use of phase sensitive detection methods for reduction of noise. The magnetic field can be held in a fixed direction and the induced torque measured as the magnetic field or temperature was varied. The method is suitable at low magnetic fields since the modulation field does not vary.

The magnetic field is limited only by the requirement that the modulation field not be a significant fraction of the static field. In the system used this set the lowest useful magnetic field to be 0.008 T.

The rotating magnet magnetometer is not well suited to high field measurements. The torque on the sample for an open orbit will go as B while the torque for only closed orbits will go as 1/B. There is however a large component of torque proportional to $\omega_c\tau$ about the x axis. Since the quartz rod is freely suspended, gravity and the compliance of the rod provides the restoring force against such torques. The quartz rod swings about its support point through an angle δ. This provides a restoring torque $mg\,\delta\ell$ where m is the mass of the sample and holder, g is the acceleration due to gravity and ℓ is the length of the quartz rod as shown in figure 3-18. The angle between the axis of the current loops and the quartz rod, λ', is now given by $\cos\lambda' = \cos\delta\,\cos\lambda$ where λ is the angle between a rigid support and the axis of the current loops. Since δ increases as $\omega_c\tau$ while λ decreases as $1/\omega_c\tau$ the angle λ' will reach a

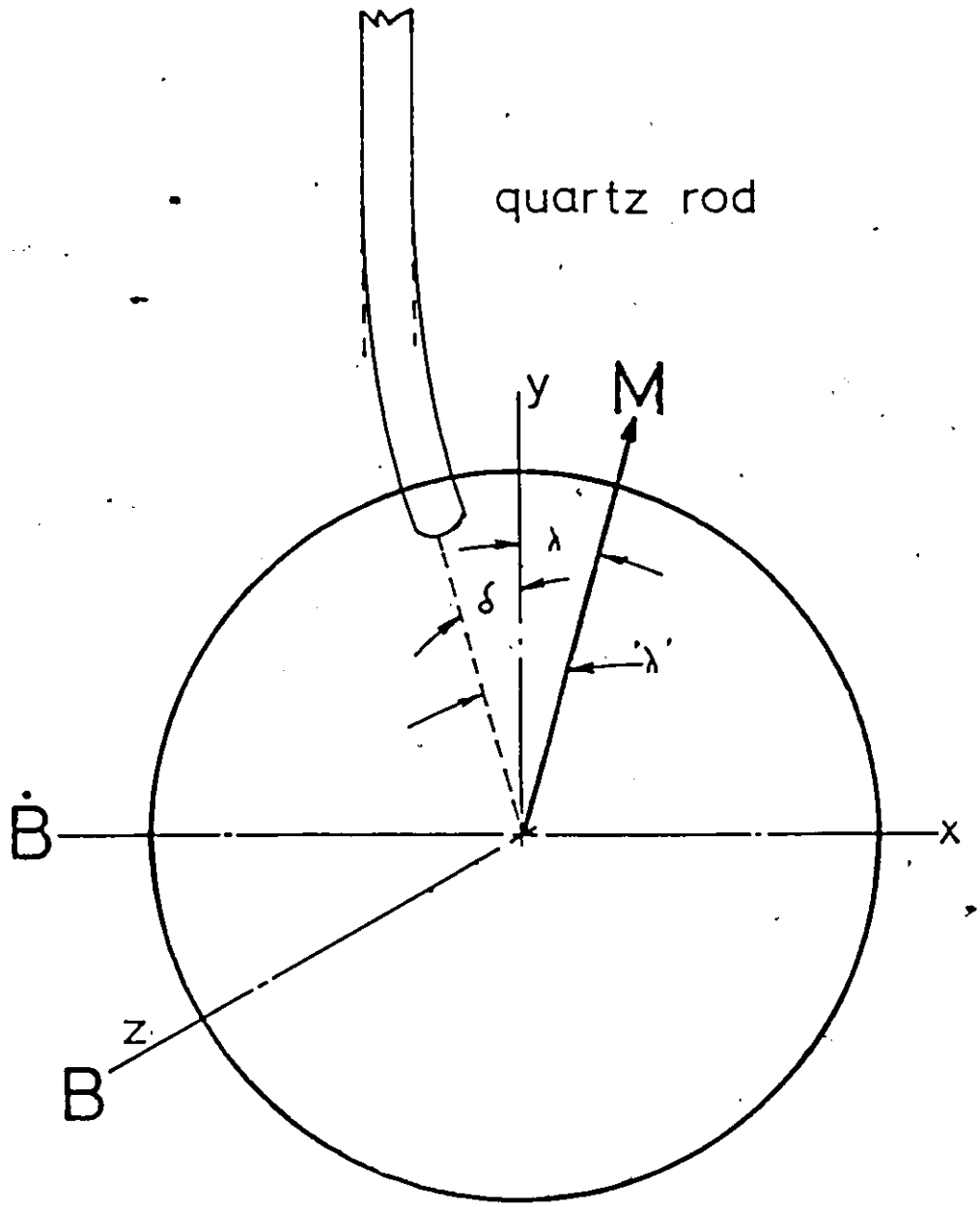

Figure 3-18 Schematic sketch of the support rod twist due to the total torque on the sample.

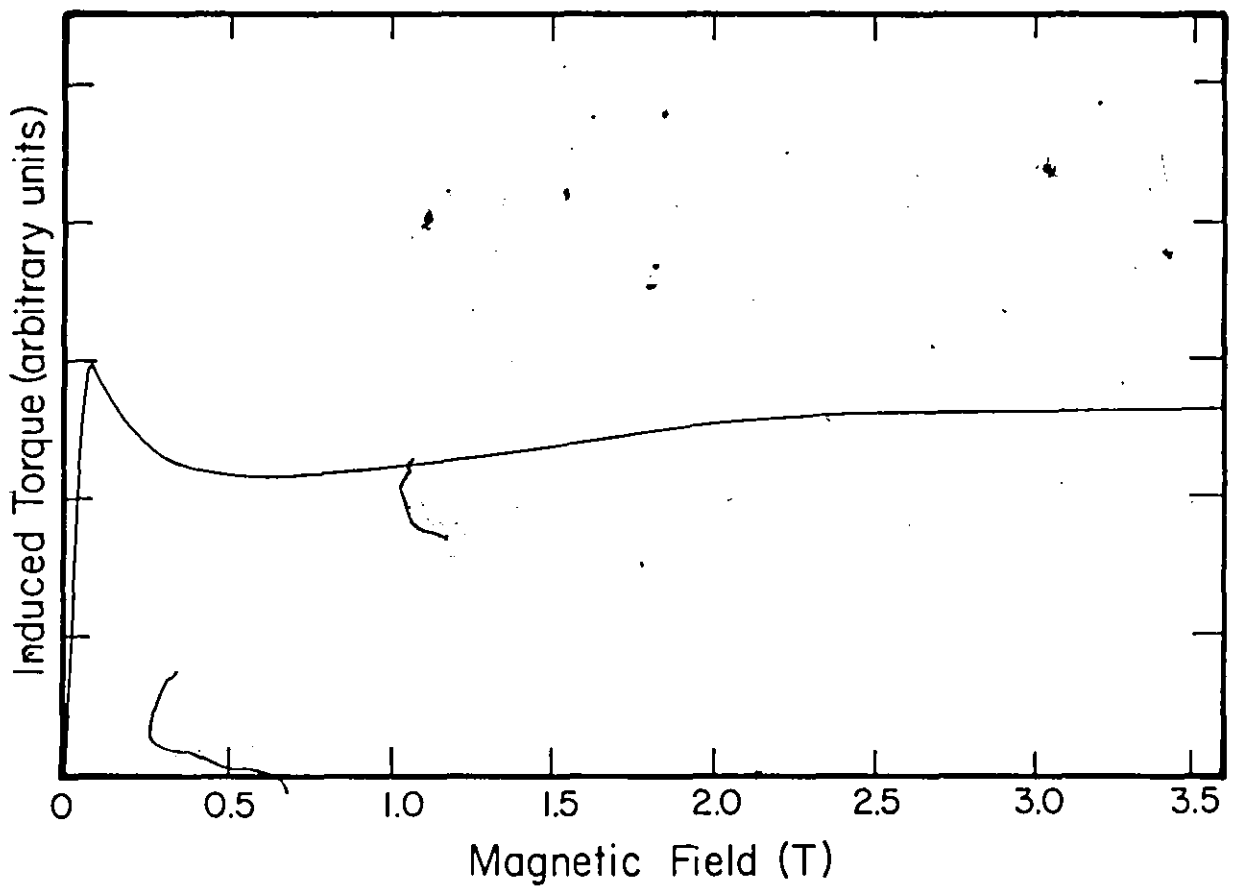

Figure 3-19 Induced torque as a function of magnetic field for the rotating magnet magnetometer.

minimum and begin to increase again. Thus the measured torque will reach a minimum at some field and begin again to increase as B. The increase in torque at high magnetic fields is shown in figure 3-19. The torque due to high conductivity directions by contrast will be largely unaffected since the angle δ would be smaller and λ' is insensitive to δ for large values of λ. The net effect of these processes is that the background torque will increase at the same rate as the torque due to high conductivity directions. This makes the method weak at high fields since the measured difference between torque peaks and the background becomes a small fraction of the total measured torque. In the present experiments in which the noise increased at high field as well, the sensitivity was sharply reduced at high fields.

The two techniques thus prove complementary and allow the induced torque to be measured accurately over the magnetic field range from 0.008 to 8.5 T.

vi) Magnetometer Response

The analysis in the preceding sections shows the induced torque to be proportional to both the frequency of modulation and the modulation amplitude. The magnetometer responses however are those of driven oscillators and thus not directly proportional to the induced torque. The dependence of the measured signal on modulation amplitude is shown in figure 3-20. For both magnetometers the measured output increases linearly with

modulation amplitude and therefore increases linearly with induced torque until it reaches a saturation value. The saturation value is established largely by the feedback electronics.

The sensitivity of the rotating sample magnetometer is shown in figure 3-21a. The dots give the measured frequency response. The solid line is the sensitivity of a damped driven oscillator calculated from equation (3-58a) using estimates of the spring torque, moment of inertia and electronic damping. The output increases linearly up to 5 Hz, reaches a maximum at 6 Hz the resonant frequency of the oscillator and decreases at higher frequencies. The sensitivity of the magnetometer to second moments as calculated from equation (3-58b) is indicated by the chain line. This sensitivity falls to zero at 6 Hz. Operation was typically chosen to be in the linear region at 5 Hz. This gave a large sensitivity to induced torques due to the first moment with a reduced sensitivity to induced torque from the second moment.

The frequency dependence of the induced torque for the rotating magnet magnetometer is shown in figure 3-21b. The variation is linear at low frequencies and reaches a broad maximum at 9 Hz. Superimposed on this are two peaks at 4.8 and 16 Hz due to mechanical resonances of parts of the system. The induced torque which supplies the driving force varies linearly with frequency and since the magnetometer's mechanical response, far below its resonant frequency is almost constant, the output

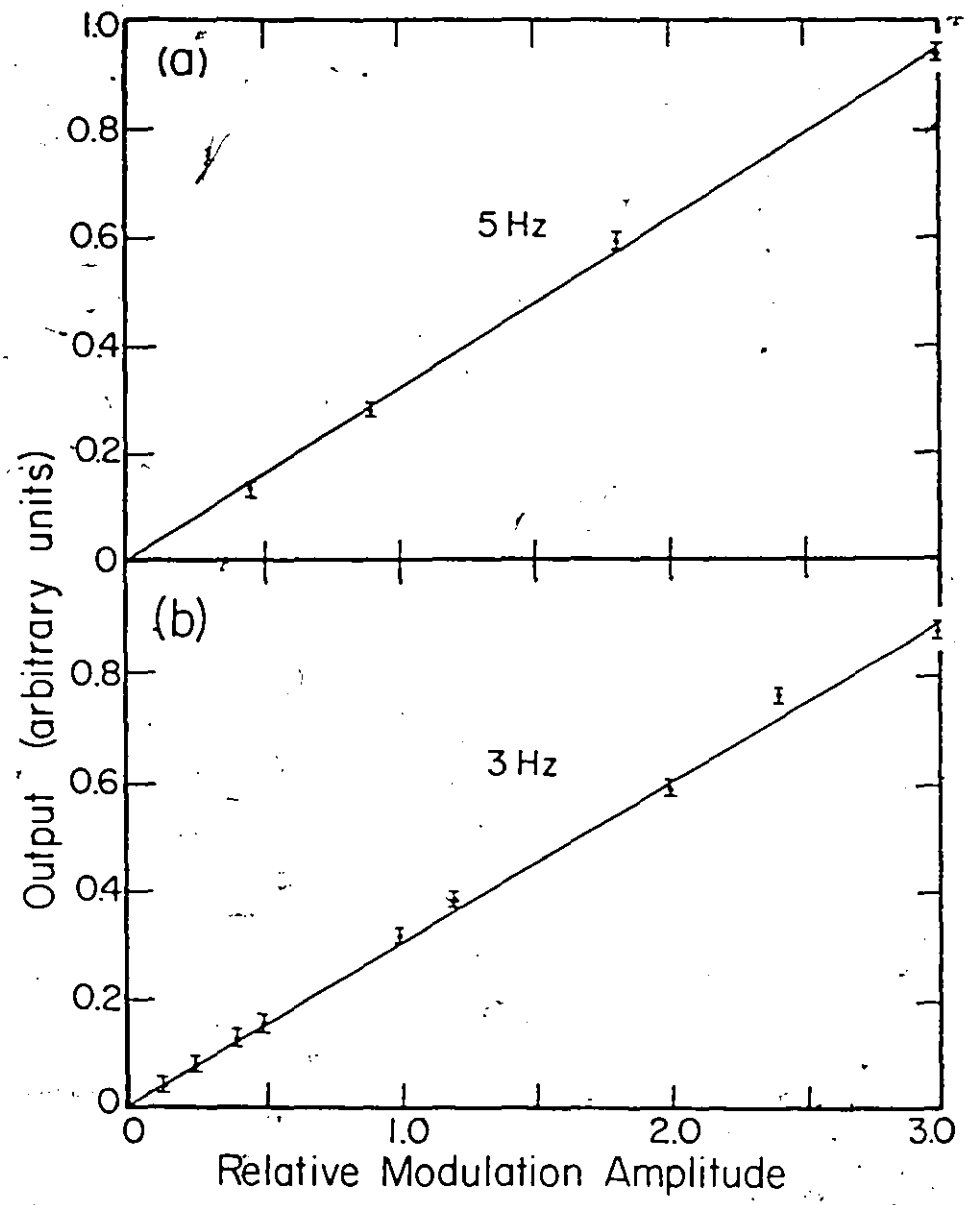

Figure 3-20 The response of the rotating sample magnetometer (a) and the rotating magnet magnetometer (b) to variations in modulation amplitude.

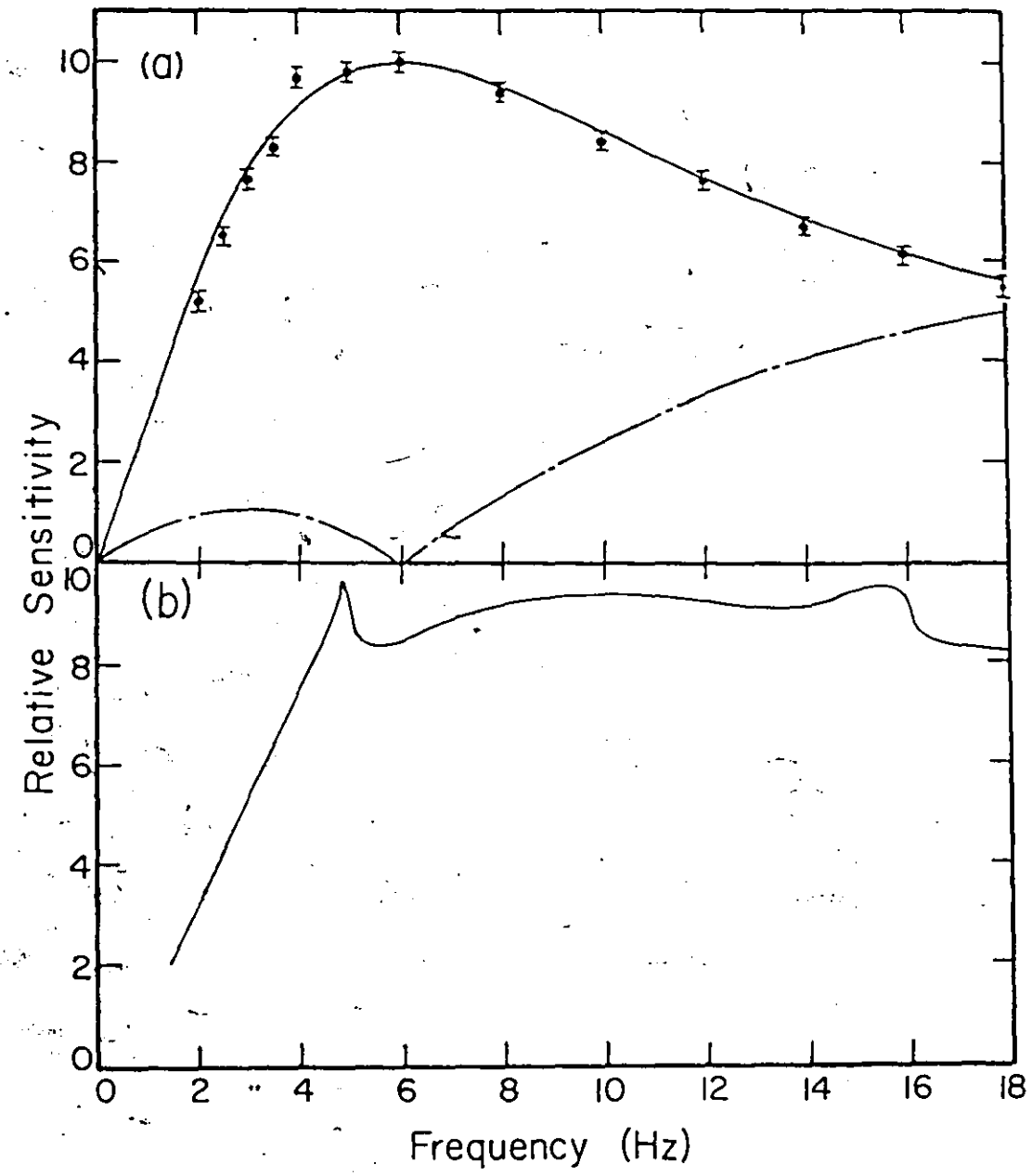

Figure 3-21 a) Frequency response of the rotating sample magnetometer. The solid line is the predicted response to first moments and the chain line the predicted response to second moments.

b) The frequency response of the rotating magnet magnetometer.

varies linearly with frequency. The output falls off due to increased electrical damping in the feedback circuits at higher frequencies. Operation was chosen to lie in the linear region, typically at 3 Hz.

The modulation amplitude was chosen in each experiment to be below saturation and was often varied during the course of the experiment as the magnetic field was changed.

CHAPTER 4

SAMPLE PREPARATION

i) Physical Properties

Let us outline some of the physical properties of potassium that are relevant. It crystalizes at 63°C into a body-centred cubic structure. Potassium has a lattice constant a of 5.327 Å at 20°C (Stetter et al. 1978) which contracts by 1.75% on cooling to 4K. Since there are 1.4×10^{28} electrons/m^3, the free electron fermi radius is $0.620(2\pi/a)$. Thus the fermi surface approaches to within 12% of the Brillouin zone boundary in the direction of closest approach which is the [110]. direction. A typical value for the electrical resistivity is 7.18×10^{-8} Ω m. at 20°C.

Potassium is very soft and will only tolerate stress of less than 100 g/mm^2 before plastically deforming (Hands and Rosenberg 1969). It must thus be handled as carefully as possible to prevent stress from causing plastic flow and recrystallization.

The potassium for these experiments was 99.97% pure source material obtained from Mine Safety Appliances, Callery Pennsylvania or Koch Light Laboratories, England. The spherical single crystals used in these experiments were formed in

one of three ways described in the next section.

ii) Crystal Growth

Some samples were grown in oil. Mineral oil was mixed to give a slight negative buoyancy to solid potassium. The oil was then outgassed by pumping and dried by the addition of small pieces of potassium. The oil was heated to just below the melting point of potassium. In a separate beaker of oil the source potassium was heated to above the melting point. Potassium was drawn up into a glass capillary attached to a syringe and transferred to the prepared oil. Quickly applying smooth even pressure with the syringe forced molten potassium into the oil. While hot, the potassium was neutrally buoyant and surface tension caused the potassium to form a visually perfect sphere with a shiny surface. In most cases a single crystal resulted upon slow cooling of the oil. During handling the surface of the crystal became dulled but by cutting a crystal in half it could be seen that corrosion was confined to a very thin surface layer. The sample could be kept in a glove box with no further degradation for several months.

The sphere while still covered with oil was placed in a Kel-F sample holder as shown in figure 4-1. With the cap removed it was possible to orient the sample with x-rays going through the holes. The cap could then be put on and the sample mounted in the magnetometer without disturbing the orientation.

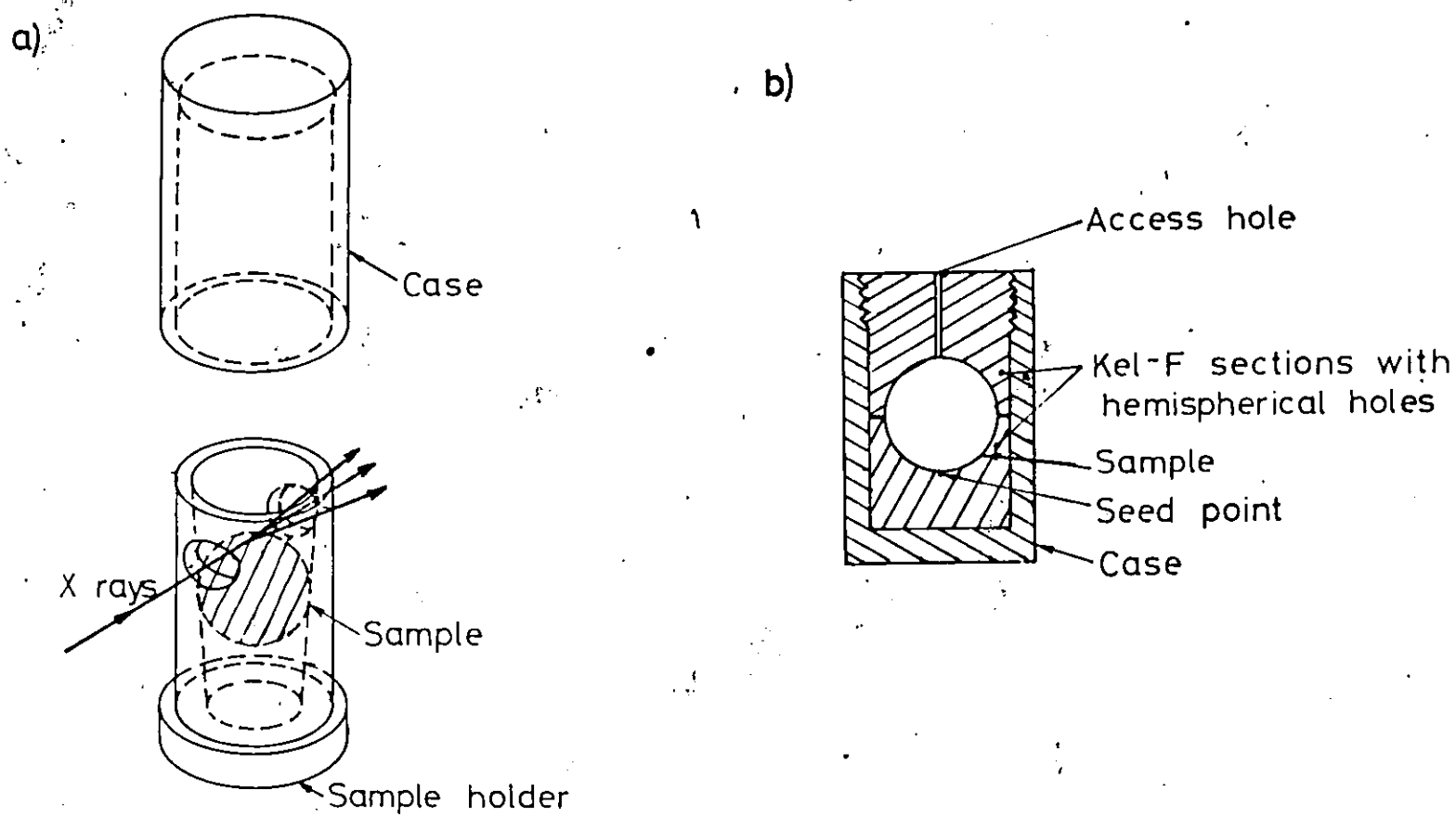

Figure 4-1 a) Sample holders for oil drop samples shown disassembled for x-ray orientation.

b) Sample holder for mold grown samples.

The sample was oriented to ±1° with respect to the cylindrical axis of the sample holder and ±5° in the plane perpendicular to the axis. Samples named KO1 to KO13 were made by this process.

The rest of the samples were made in a mold. The sample holders consisted of two sections with hemispheres of .156" diameter machined to an accuracy of .001" and butted together. In one hemisphere a .020" access hole was drilled while in the other a small seed point was drilled as shown in figure 4-1b. To fill the sample holder a syringe was filled with molten potassium under dry outgassed mineral oil and the oil cleaned off. The growth furnace was quickly assembled as shown in figure 4-2 and evacuated to a pressure of 10^{-5} Torr. The furnace was then heated to 70°C. As the potassium melted gravity caused it to drop into the funnel. The first drop was removed outside the funnel in order to ensure that only clean potassium was used. The molten potassium was pumped for several hours further to ensure trapped gases were removed. Helium gas was then introduced at a pressure of 3/4 atmosphere to force the potassium through the access hole and into the sample holder. All mold sample holders were filled this way.

For samples KM1 to KM3 the crystals were grown by drawing the furnace up at a rate of 1/2" per hour. In a

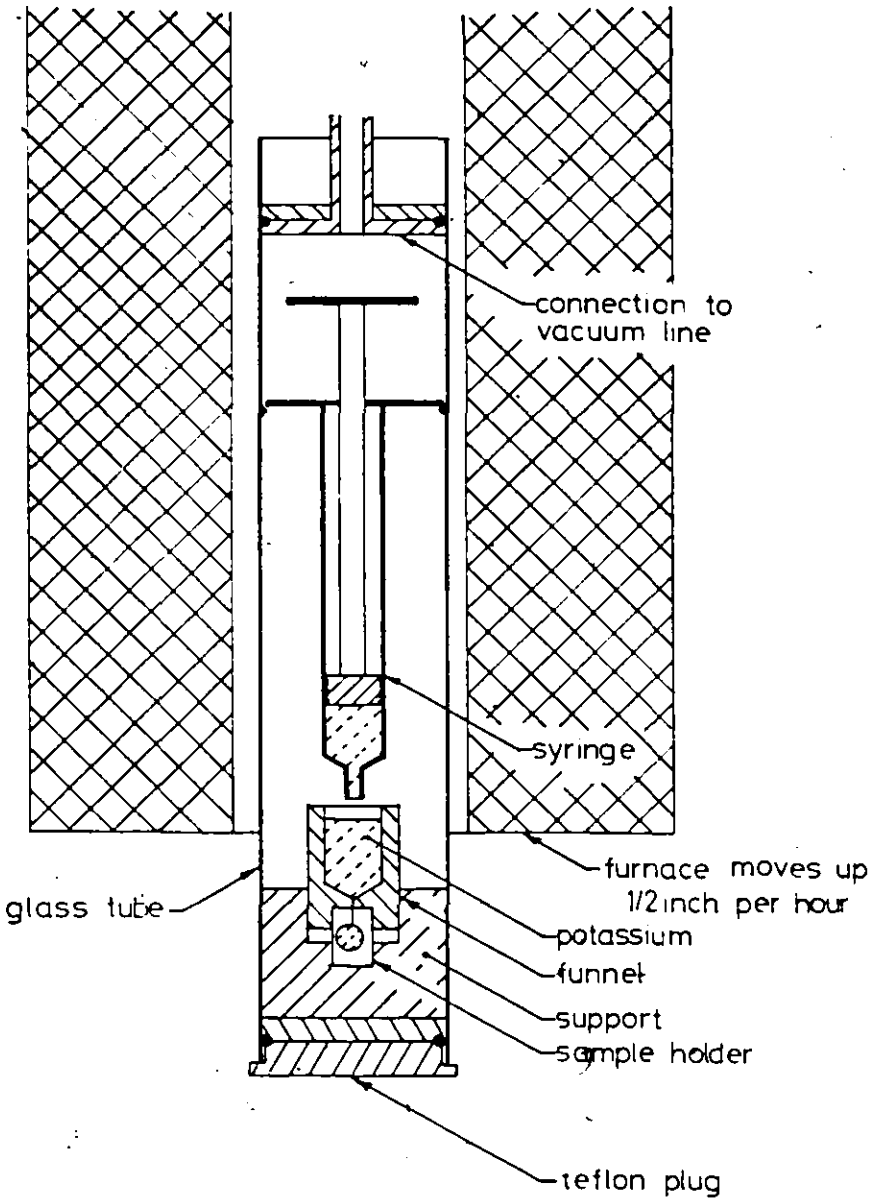

Figure 4-2 Travelling furnace to grow samples in a mold.

Bridgman technique, the crystal seeded in the point and formed a spherical single crystal. The funnel acted as a reservoir to maintain the sample holder filled as the potassium contracted on solidification. For sample KM3 the sections containing the potassium were made of nylon held together with a thin layer of glyptal cement. This holder could be removed from the Kel-F case and x-rayed, giving an accuracy of orientation comparable to that of the oil grown samples.

The rest of the samples were frozen with a temperature gradient, parallel to the axis of an 8.5 T solenoid and to the cylindrical axis of the sample holder. Samples KM4 and KM5 were frozen in a magnetic field of 8.5 T. Samples KM6 to KM12 were prepared under identical conditions except there was zero magnetic field.

The residual resistance ratio of the samples prepared varied between 2000 and 10000 with 6000 being a typical value. The lowest RRR was found for samples which were cooled to 77K within hours of the growth of the sample. If the sample was warmed to room temperature and left for several days to anneal before cooling, a much higher RRR resulted. No significant relation between the RRR and the rate of cooling was found. The samples for which data is given in this work are listed in Table 4-1.

Table 4-1

Properties of potassium samples reported in this work

Sample	Growth Method	Four fold Anisotropy at 2.0 T	Figures				Remarks
KO2†	oil drop	4:1	5-1	5-5	5-8	5-9	x-ray oriented
KM3†	mold 1*	4:1	5-2	5-4	5-8	5-18	x-ray oriented
KM4#	mold 2*	1.2:1	5-3	5-11	5-12 5-16	5-13 5-19	grown at 8.5 T
KM5	mold 2*	6:1	5-7				grown at 8.5 T
KM6#	mold 2*	5:11	5-14				grown at 0 T
KM7	mold 2*	4:1	5-10	5-15			grown at 0 T
KM11	mold 2*	4:1	6-1	6-2			grown at 0 T RRR ≈ 5600
KM12	mold 2*	3:1	5-17				grown at 0 T RRR ≈ 3500 not spherical sample

*mold 1 samples were grown in a travelling furnace
mold 2 samples were frozen in the bore of a superconducting magnet
†data from sample KO2 and KM3 were reported in Coulter and Datars (1980)
#data from samples KM4 and KM6 were reported in Coulter and Datars (1982)

CHAPTER 5

RESULTS

i) Potassium

The induced torque for three different samples is shown in figures 5-1 to 5-3. In each case the sample is rotated through a 180° angle about an axis perpendicular to the magnetic field. The induced torque for sample KO2 grown in oil and mounted without the oil being removed is given in figure 5-1. At 3.5 T the induced torque shows maxima at two magnetic field directions separated by 90°. The ratio of torque at a maximum to torque at a minimum is 4:1. These results are similar to the induced torque observed in magnetic fields between 0.2 and 2.2 T (Holroyd and Datars 1975). This is named four-fold torque since there are four maxima in a 360° rotation. At 5 T there are peaks at a number of sharply defined magnetic field directions in addition to the four-fold torque. This structure becomes more clearly defined at 8.5 T, the largest magnetic field used.

The structure is more evident in the results, for sample KM3 grown in a mold, shown in figure 5-2. Four-fold torque is evident at 3.0 T. However there are 23 peaks in the 180° rotation at 5.5 T. This structure becomes larger and more distinct at 6.8 T.

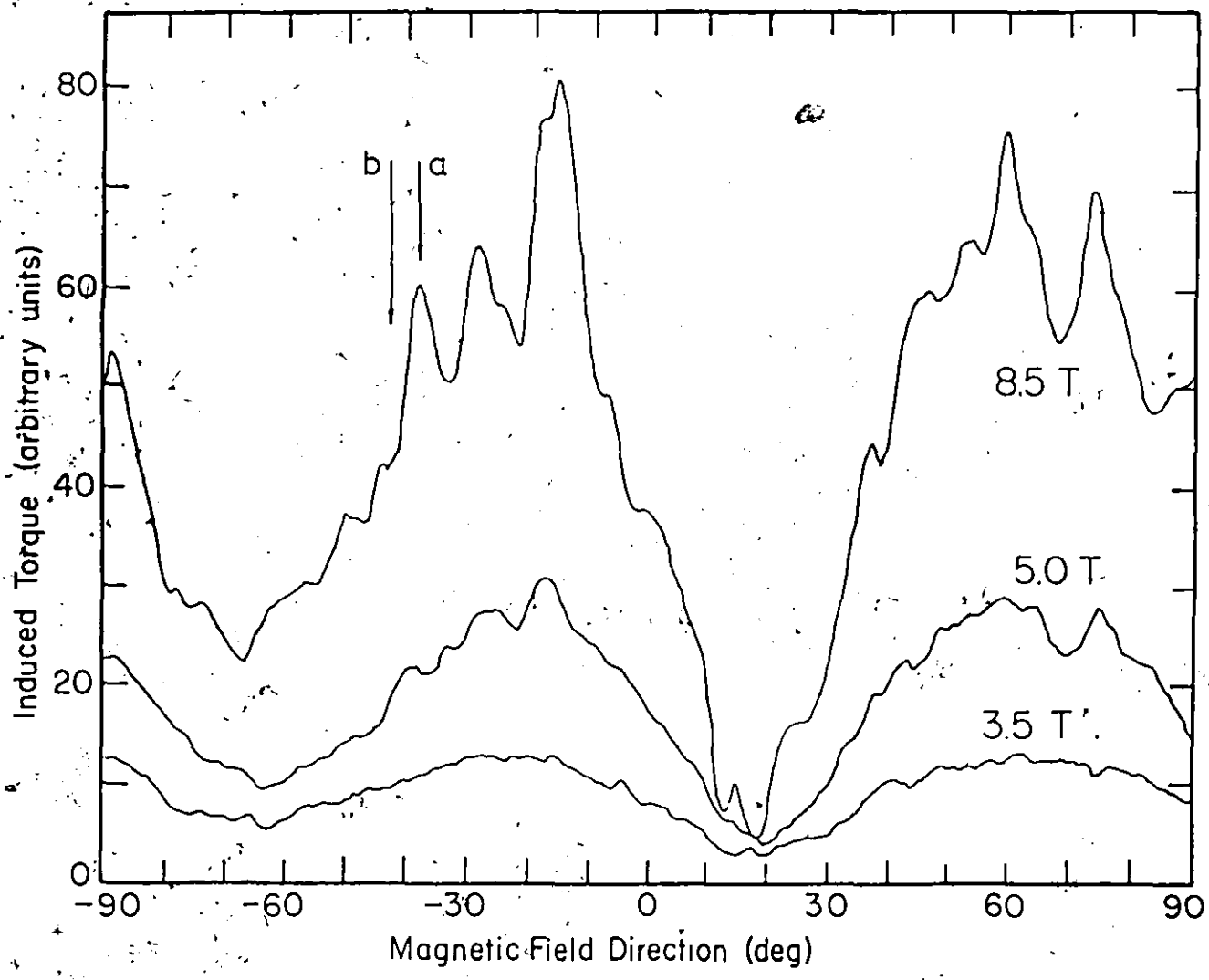

Figure 5-1 The induced torque, as a function of magnetic field direction, on sample KO2 at magnetic fields of 3.5, 5.0 and 8.5 T.

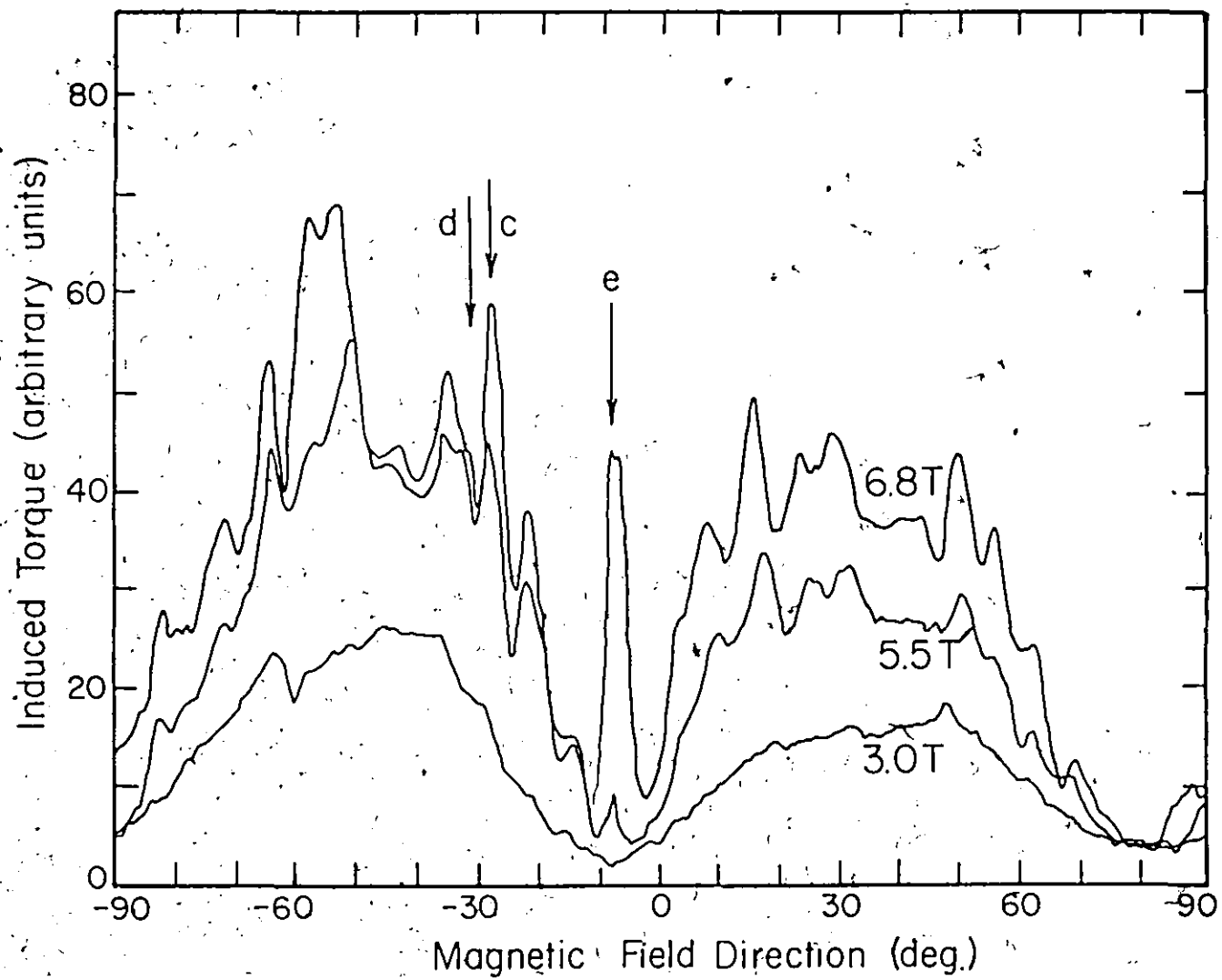

Figure 5-2 The induced torque on sample KM3 as a function of magnetic field direction at magnetic fields of 3.0, 5.5 and 6.8 T.

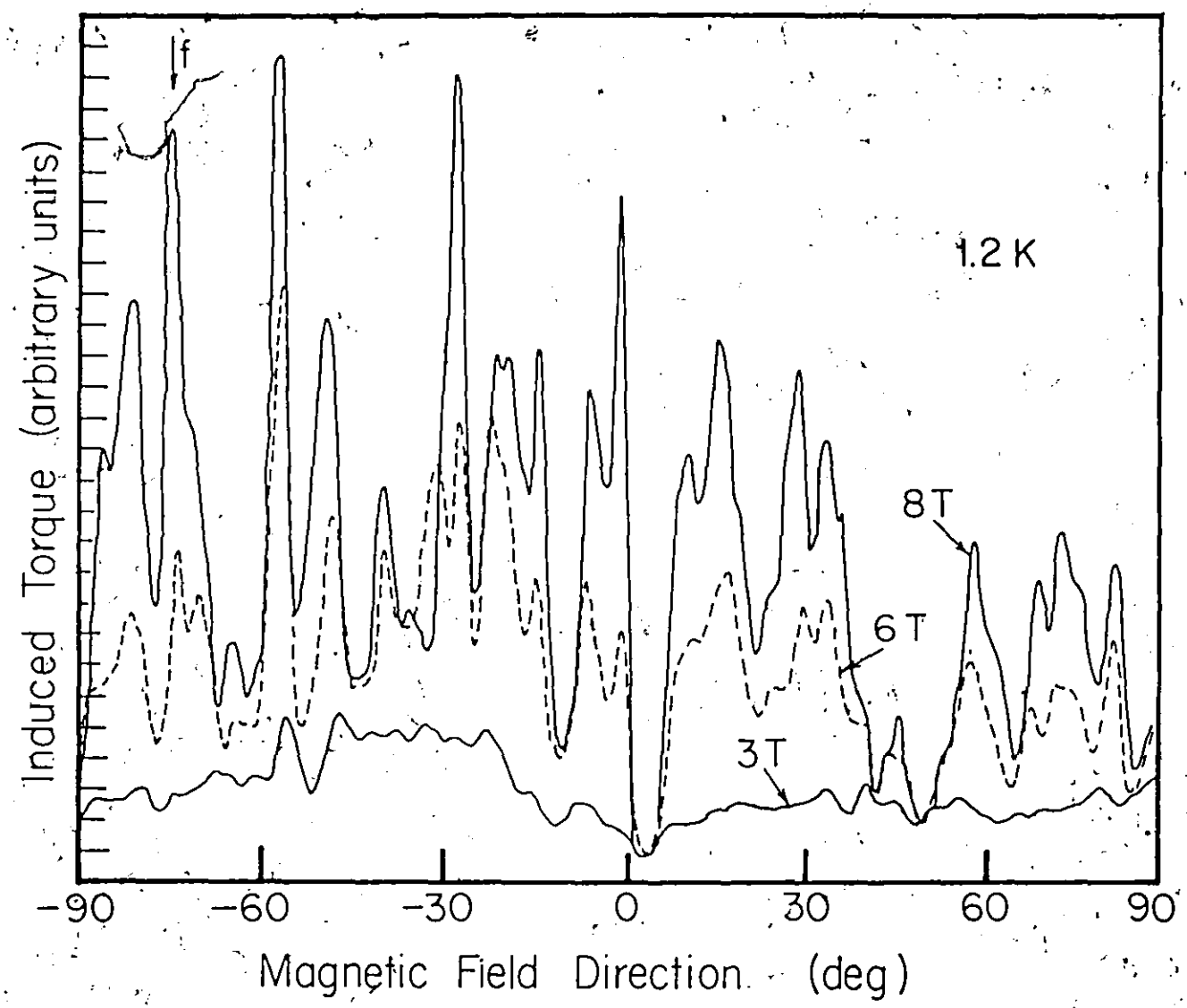

Figure 5-3 The induced torque on sample KM4 as a function of magnetic field direction at magnetic fields of 3.0, 6.0 and 8.0 T. The temperature of the sample was 1.2K.

The results for the mold grown sample KM4 are given in figure 5-3. In this case, the four-fold torque at 3 T is a factor of four smaller than that for samples KO2 and KM3. This allowed the use of increased sensitivity in the detection system and the structure is visible in the induced torque at 3 T. Twenty-six peaks can be identified in the rotation at 8 T. The induced torque varies by a factor of four from the peaks to the minima between them.

Experiments were done on a total of 18 samples. There are a number of features common to the data from all samples. At fields between 2 T and 5 T the induced torque shows structure. At the highest fields used the structure became the dominant feature in the induced torque. The sharp peaks occur in samples which show large four-fold torque and those which do not. The magnitude of the structure increases rapidly with magnetic field when the peaks become evident. There are between 20 and 30 peaks in a 180° rotation. Most peaks occur on what were the maxima of the four-fold torque. Some such as peak e in figure 5-2 do, however, appear in four fold minima.

The magnetic field dependence of the induced torque at the directions indicated by the arrows a to f in figures 5-1 to 5-3 was examined in more detail. The induced torque in magnetic field directions labeled c and d in figure 5-2 is shown in figure 5-4. At low magnetic fields the induced torque in the two directions is the same and is proportional to

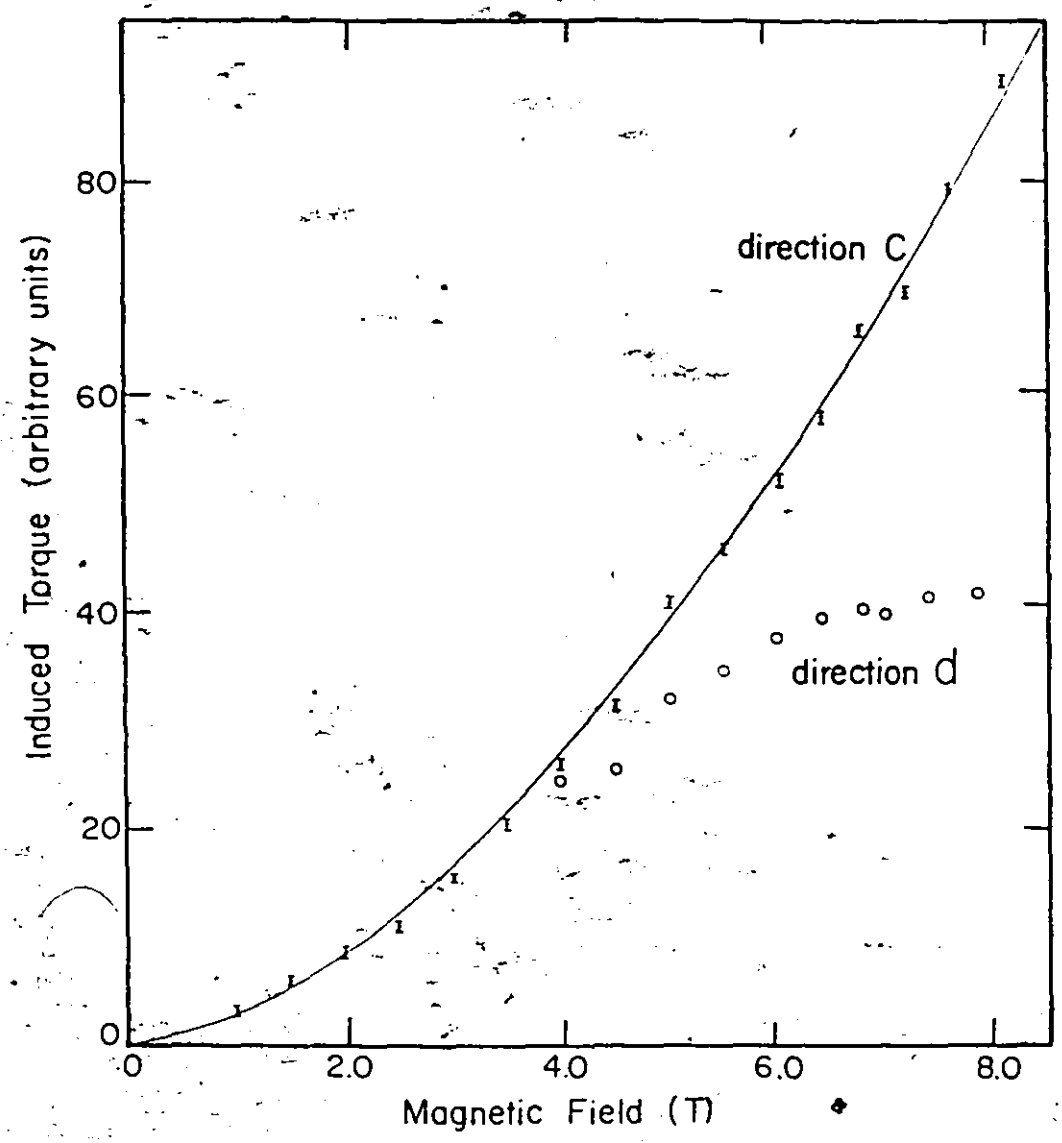

Figure 5-4 The magnetic field dependence of the induced torque in directions labeled c and d in figure 5-2. Direction c(I) is a high field peak and direction d(o) a high field minimum. The solid line is a power law $B^{1.7}$ fit to the amplitude at c.

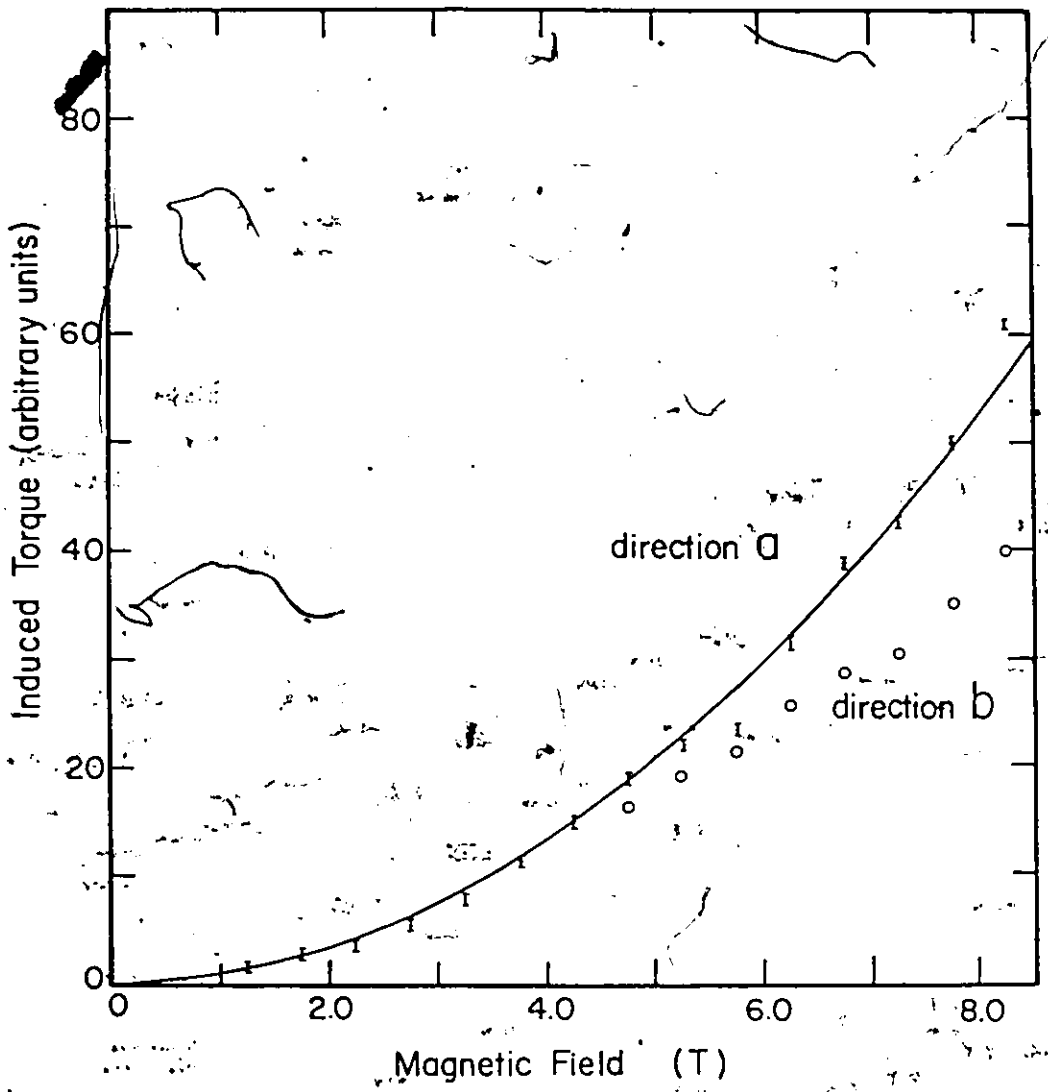

Figure 5-5 The magnetic field dependence of the induced torque in directions labelled a and b in figure 5-1. Direction a(I) is a high field peak and direction b(o) a high field minimum. Where the torque in the two directions is the same only one symbol is drawn. The solid line is a power law $B^{2.0}$ fit to the amplitude at a.

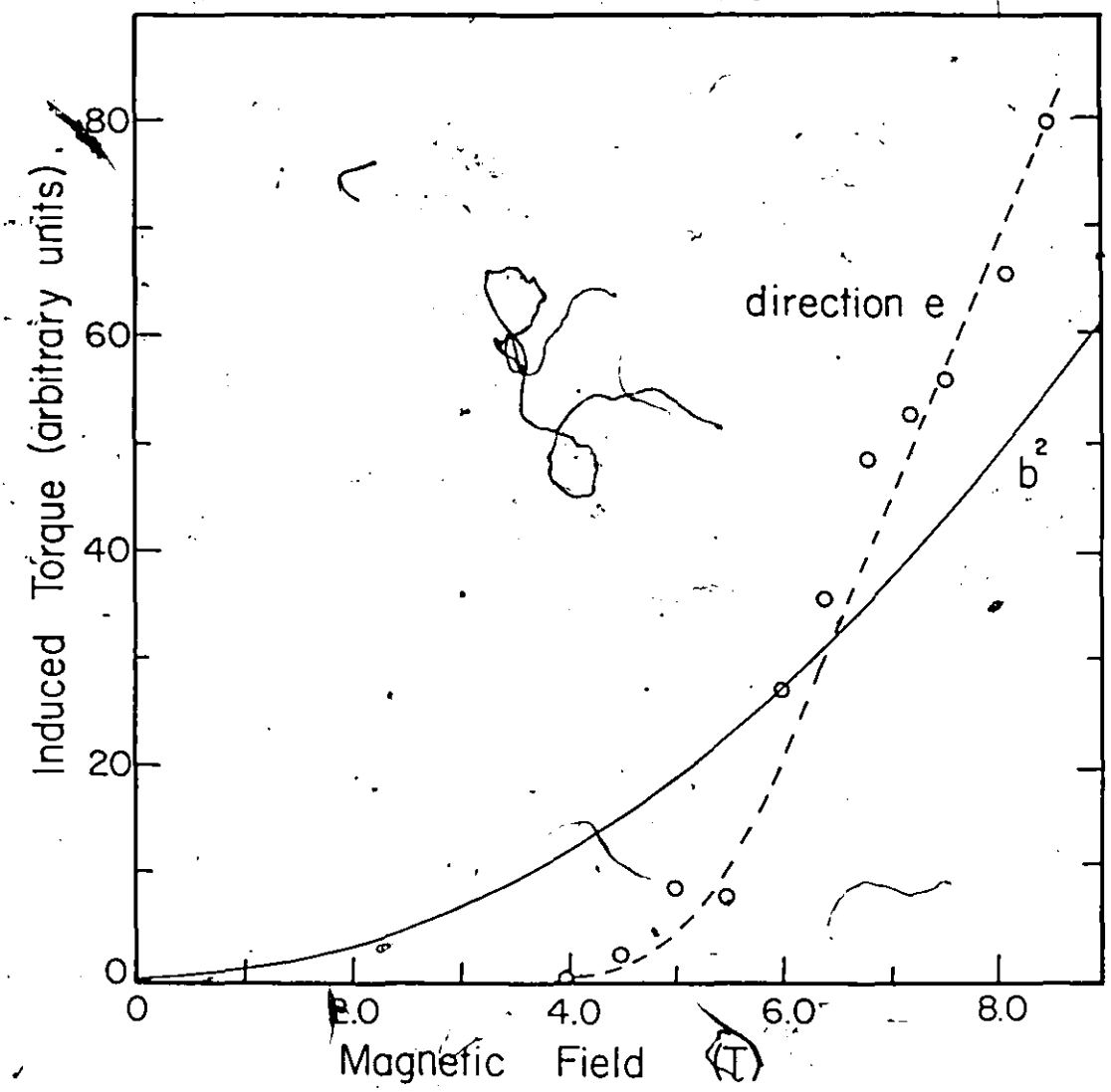

Figure 5-6 The induced torque at peak e(o) which appears at the minimum of the four-fold torque in figure 5-2. Shown for comparison is the best power law B^2 fit to the data. The dashed line is drawn only as an aid to the eye.

$B^{1.7}$. The torque at the high field peak c continues to have a $B^{1.7}$ field dependence up to 8.5 T while the induced torque at high field minimum d saturates above 5 T.

The induced torque in the directions labeled a and b in figure 5-1 is plotted in figure 5-5. In this case the induced torque at high field peak a is proportional to B^2 at magnetic fields from zero to 8.5 T. At the high field minimum b the induced torque which is proportional to B^2 at low field shows a discontinuity at 4.5 T and varies linearly with magnetic field at fields above 5 T. In each case, the magnitude of the induced torque at a structure peak increased smoothly from the four-field torque with no observable discontinuity.

The peaks which do not appear on four-fold maxima have a different field dependence. The induced torque in the direction labeled e in figure 5-2 is plotted in figure 5-6. The peak is not apparent at magnetic fields below 4 T. However at magnetic fields above 4 T the induced torque increases with increasing field much more rapidly than the power law B^2 shown for comparison. The peak labeled f in figure 5-3 is found in a sample which shows little four-fold torque. In contrast, the induced torque at direction f increases smoothly with increasing field. The torque at peak f has a field dependence of $B^{2.9}$ at the temperature chosen.

The torque for all peaks in a 180° rotation was fit to a power law of the form B^{υ}. The exponent υ varied between 1

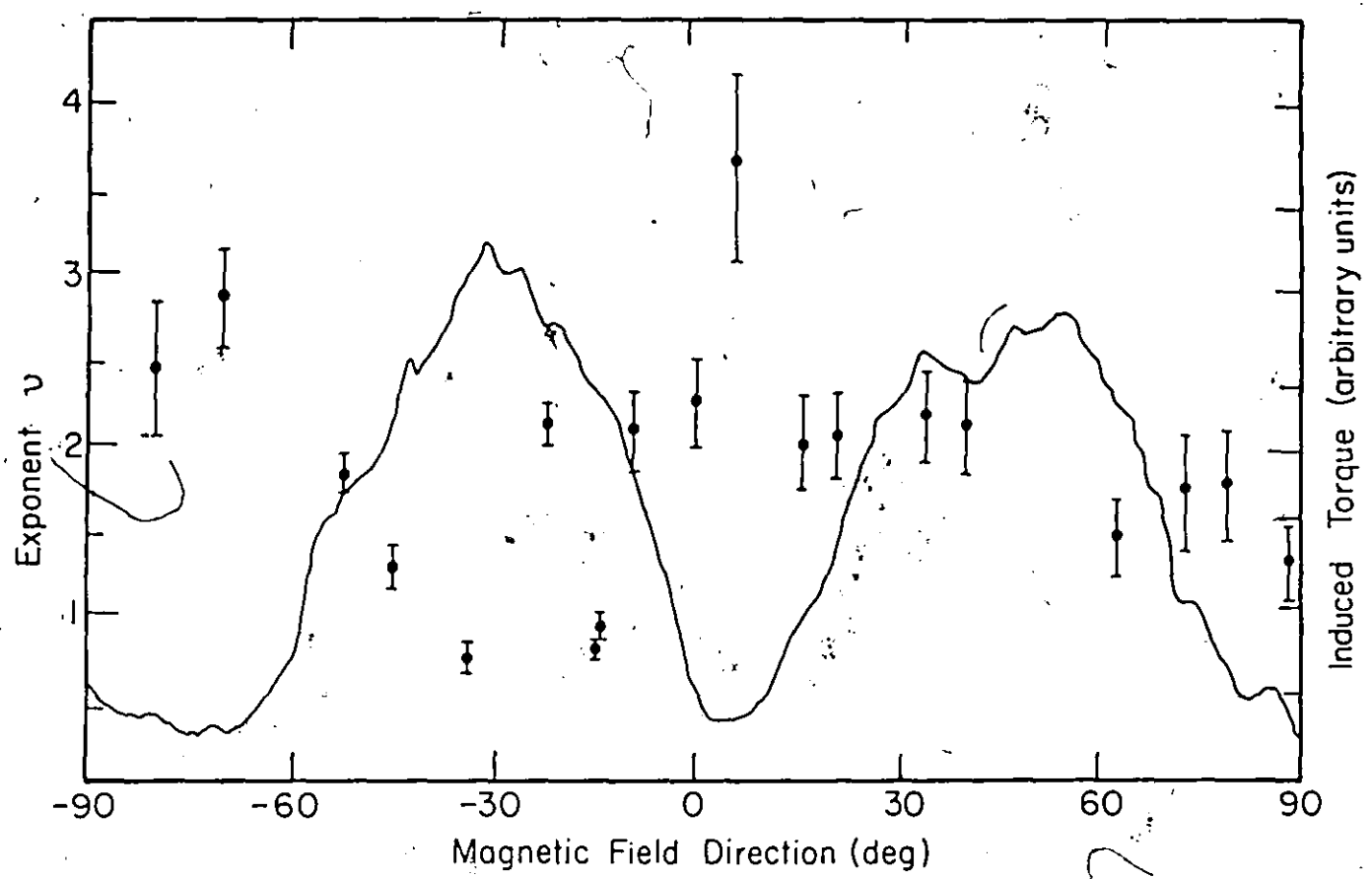

Figure 5-7 The exponent $\upsilon(I)$ in a power law fit of the form aB^{υ} to the induced torque at high field peaks. The induced torque (solid line) for the same sample at 4T is shown.

and 3. The value of υ has been plotted superimposed on the torque for sample KM5 in figure 5-7. Those peaks appearing near four-fold minima increase more rapidly than peaks near maxima. Thus at high field the four fold torque tends to be obscured by a uniform forest of structure peaks. The same result can be seen in figure 5-2. At 6.8 T the structure is a much more dominant feature than the four-fold background.

Sample KO2 was rotated in a series of 13 planes shown as dotted lines in a stereographic projection in figure 5-8. This was accomplished, using the sample rotor shown in figure 3-10, in the magnetic field of a solenoid. Rotation in a plane occurred by turning the rotor through 180°. To change planes the rotor was held in the position shown in figure 3-10 and the sample holder was turned through 10° relative to the rotor.

The magnetic field directions at whic induced torque peaks occur are indicated in figure 5-8. The induced torque peaks can be divided into "families". A "family" consists of one peak from each of a series of successive planes. The magnetic field direction, amplitude and width of peaks varies smoothly between planes in each "family". It was then possible to draw a plane through each "family" of points. Sixteen planes are identified. These planes are shown as solid lines in figure 5-8. In most cases the directions of induced torque peaks lie very close to the great circle of a plane. However, for several planes such as #10 and #15 there are peaks which

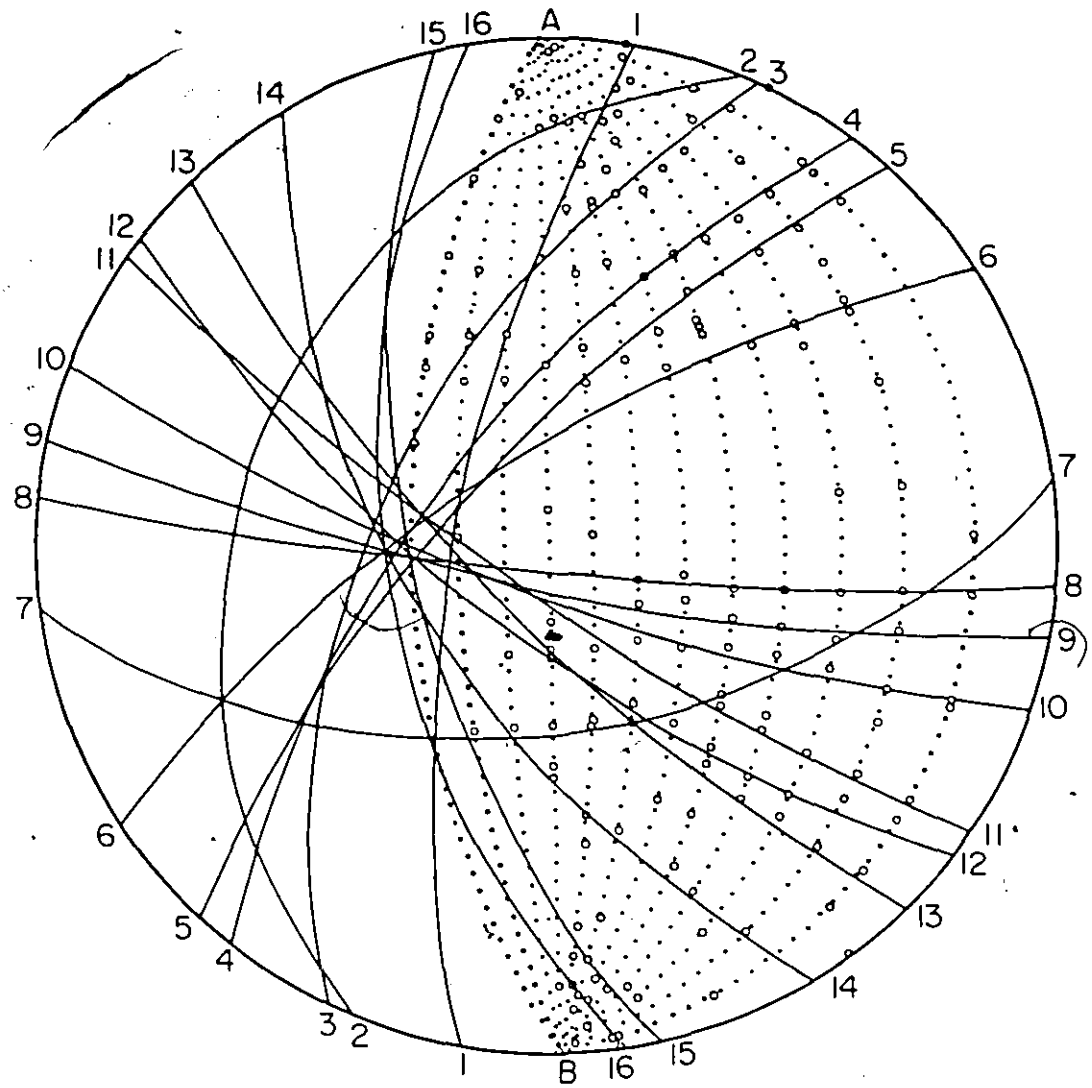

Figure 5-8 Stereographic projection showing the directions of induced torque peaks in sample KO2. The dotted lines are the planes in which the sample was rotated to obtain the induced torque peaks. Solid lines are great circles along which the peaks lie.

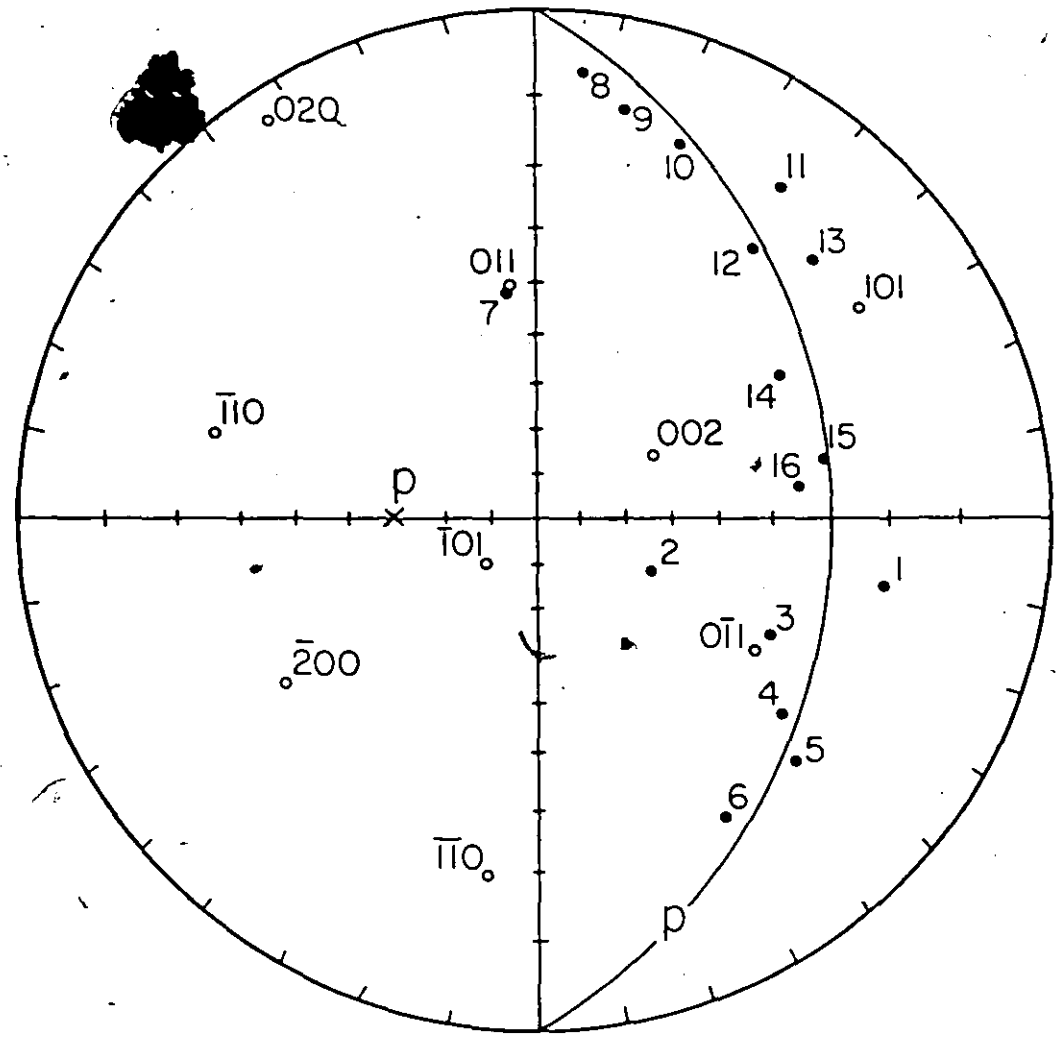

Figure 5-9 Stereographic projection of sample K02 showing the poles (•) of the planes in figure 5-8 and <110> and <200> directions in the crystal. P is the pole of a plane near most of the poles.

do not lie very close to the plane. Several peaks exist as well which do not lie on any plane.

The poles of the 16 planes found in figure 5-8 are plotted on a stereographic projection in figure 5-9. Of the 16 poles 14 lie within 10° of a plane P, shown as a solid line in figure 5-9. Rotation of the sample about the pole of plane P gives rise to the largest four-fold induced torque. It may also be noted that plane P contains the axis of the cylindrical sample holder. The pole of plane P, also shown in figure 5-9, lies in the plane perpendicular to the cylindrical axis of the sample holder.

The crystal was oriented by x-rays and <100> and <110> directions are indicated in figure 5-9. The direction of pole P is within 1° of a <321> direction. For poles 7 and 2 which do not lie near plane P pole, 7 lies 2° from a <110> direction and pole 2 does not lie near a high symmetry direction.

A large number of crystal directions in sample KM7 were examined using a split coil magnet with horizontal field direction, that could be rotated about a vertical axis. The sample holder was fixed in one position in the rotor while the angle between the magnetic field and rotation axis was varied in 10° steps.

The induced torque for three rotations is shown in figure 5-10. In these data it is possible to identify "families" of induced torque peaks as shown by the numbered arrows in

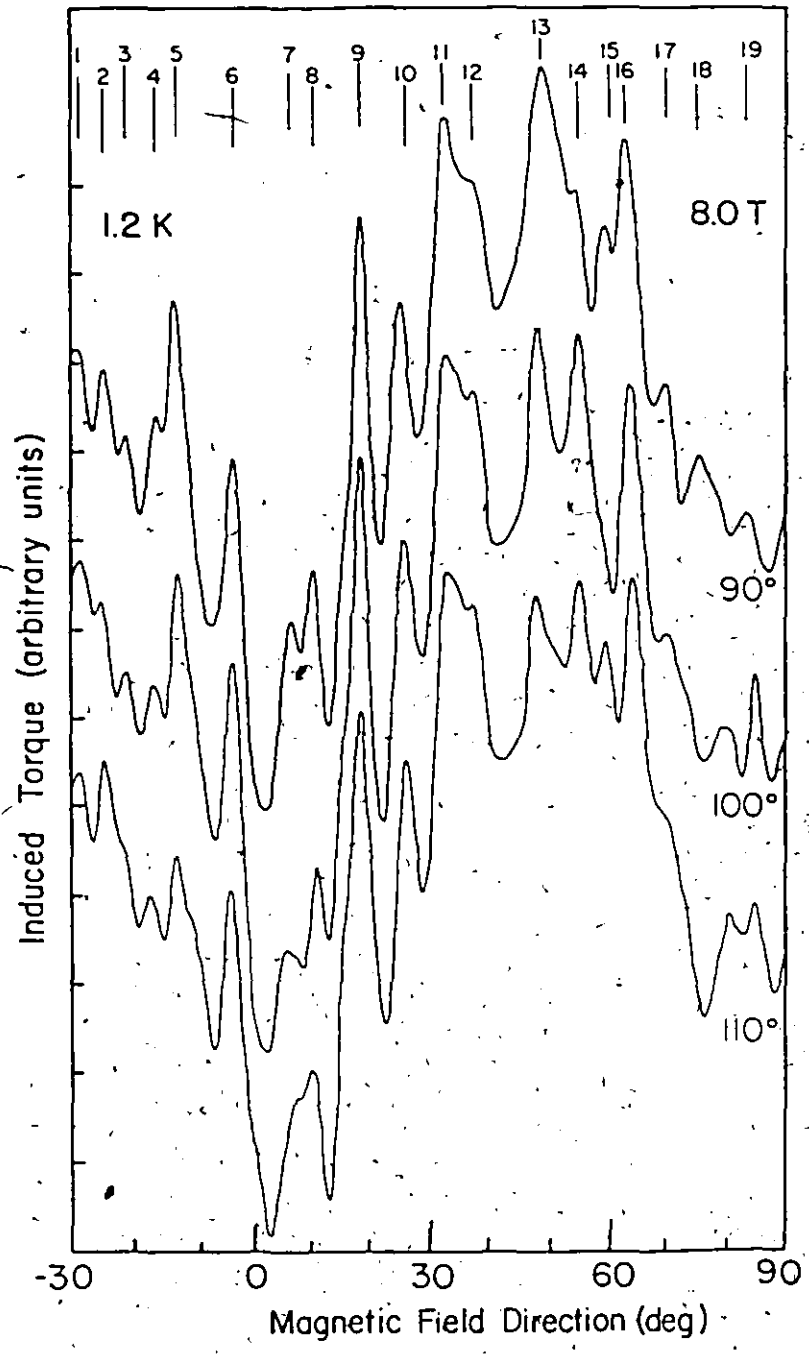

Figure 5-10 The induced torque on sample KM7 as a function of magnetic field direction for rotation about 3 axes at 8.0 T and 1.2 K. The axes are at 90°, 100° and 110° to the magnetic field. The three traces are offset by arbitrary amounts for clarity.

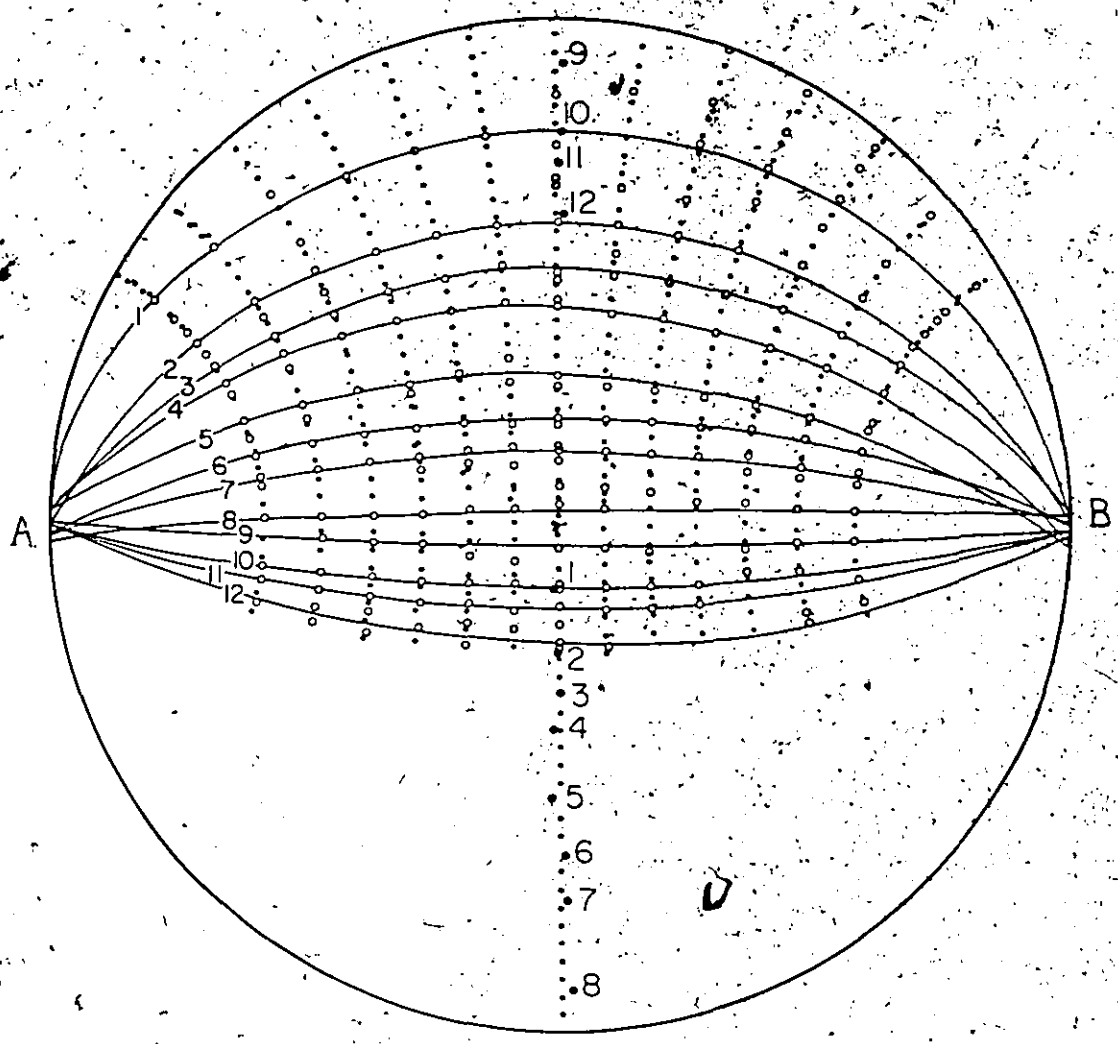

Figure 5-11 The stereographic projection showing the loci of magnetic field directions (dotted lines) and induced torque peaks (o) for a series of rotations about axis AB. The great circles along which induced torque peaks lie (solid lines) and their poles (•) are also shown.

figure 5-10. Most "families" appear at the same angle in each rotation. However peak 4 appears at -15°, -18° and -18° and peak 7 at 5°, 4° and 8° with the angle between magnet and rotation axis 90°, 100° and 110° respectively.

The loci of crystal directions examined in the 13 rotations are shown as dotted lines on a stereographic projection in figure 5-10. The directions at which induced torque peaks appear are also indicated. "Families" of induced torque peaks lie along planes in the crystal. Twelve such planes are shown by solid lines in figure 5-11. The poles of the planes are plotted in the same figure. All poles lie within 2° of a crystal plane that contains the growth axis. The pole of this plane lies along the rotation axis of the sample. The sample was not oriented with x-rays.

An important observation was made when it was discovered that the torque varied significantly when the temperature was changed. It was necessary to stabilize the vapour pressure of the liquid helium in which the sample was immersed to a temperature stability of 0.001 K in order to eliminate temperature variations. The induced torque for sample KM4 as a function of magnetic field direction at a field of 8.0 T and a temperature of 1.25 K is shown in figure 5-12a. There are 22 sharp well-defined peaks with a width of several degrees and there is no four-fold induced torque visible. The induced torque in figure 5-12b taken under identical condition, except for a change in temperature to 1.38 K, is significantly different. The struc-

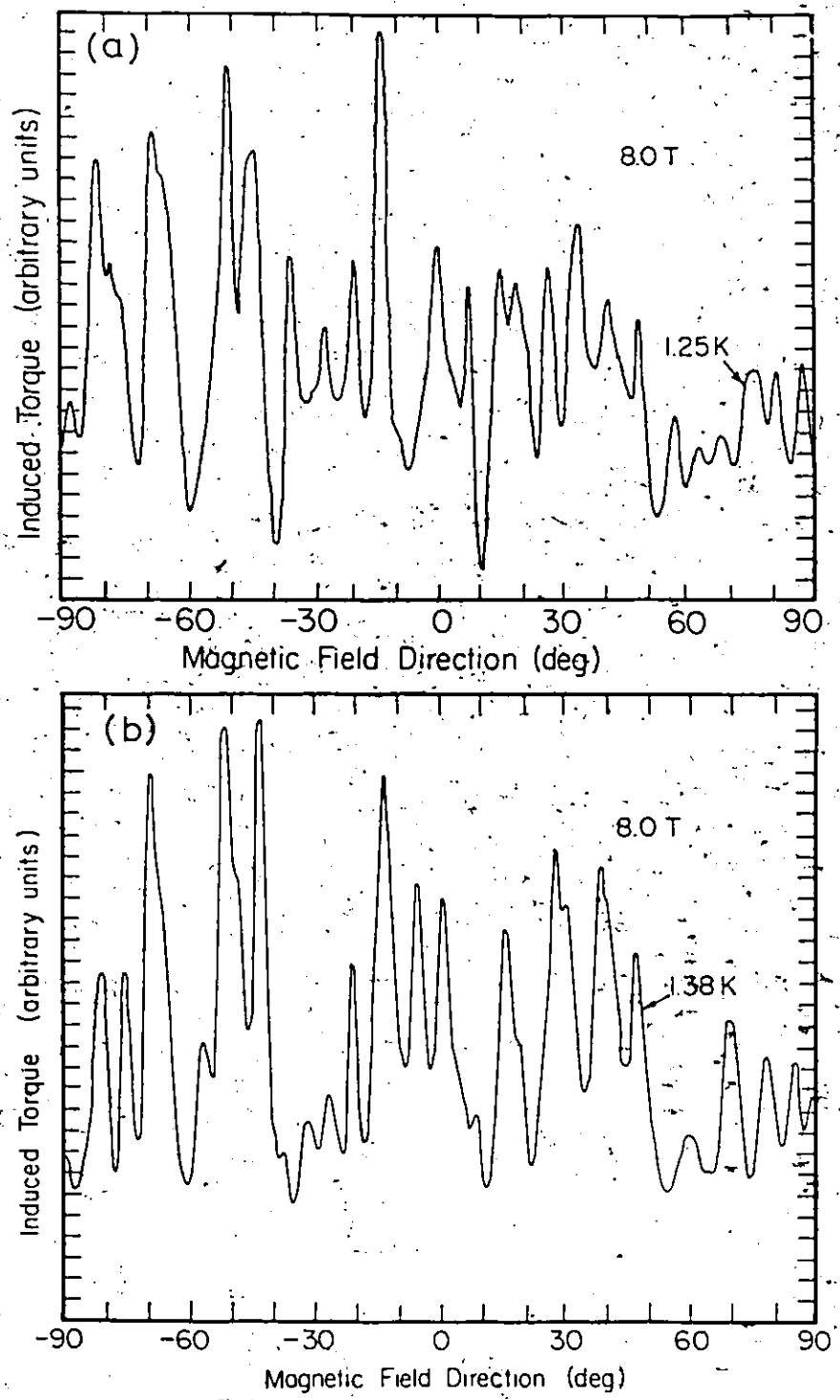

Figure 5-12 Induced torque on sample KM4 as a function of magnetic field direction at 8.0 T for (a) a sample temperature of 1.25K and (b) a sample temperature of 1.38K.

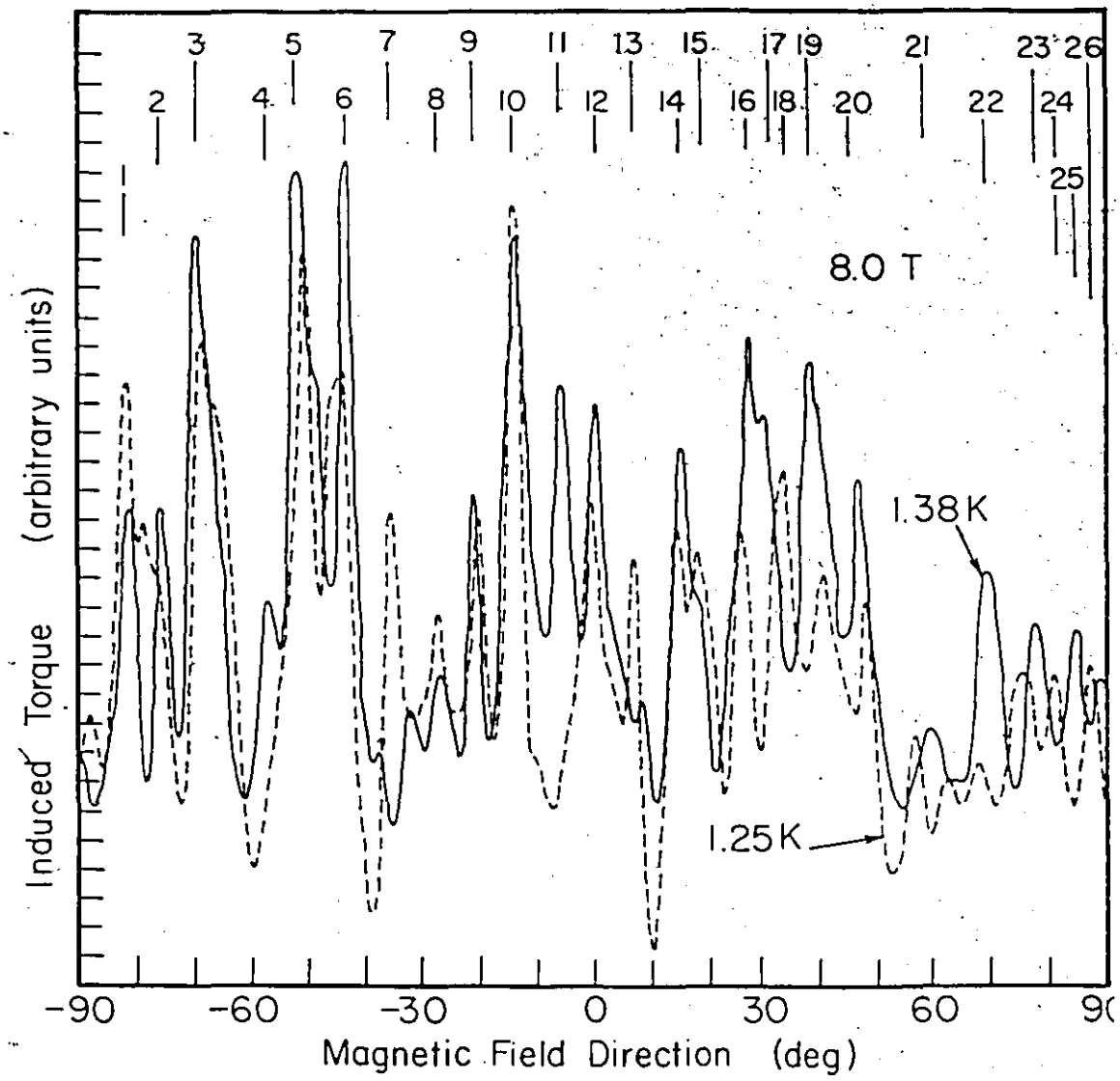

Figure 5-13 Direct comparison of the induced torque traces at 1.25K and 1.38K shown in figure 5-12. All other sample conditions are identical.

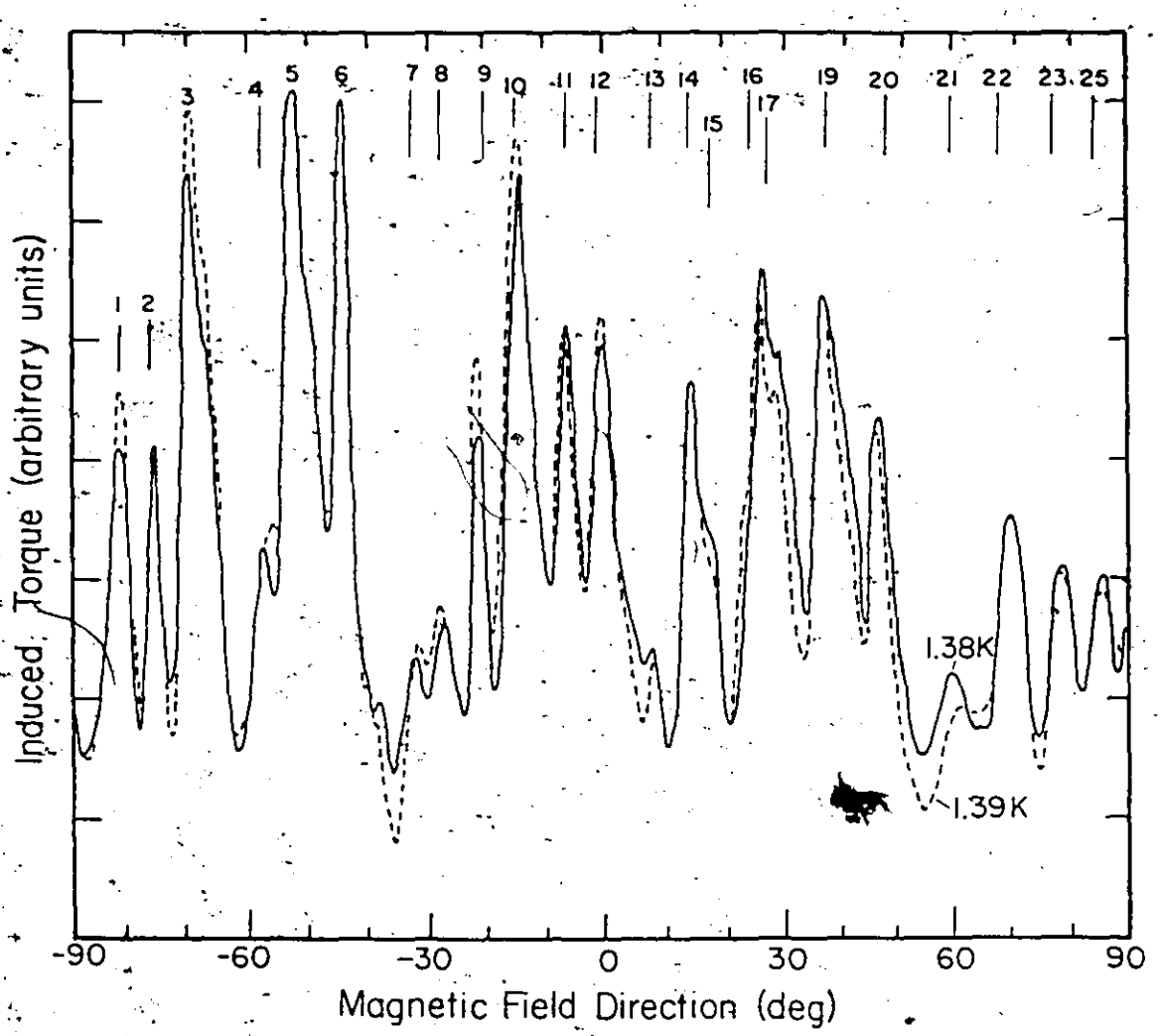

Figure 5-14 Direct comparison of the induced torque on sample KM4 at 1.38K shown in figure 5-12b and the induced torque taken under identical conditions except for a sample temperature of 1.39K. The numbering of peaks is the same as in figure 5-13.

ture is still clear and well-defined but the magnitude and magnetic field direction of some peaks are different.

A direct comparison of the torque at 1.25 and 1.38 K in figure 5-13 shows the changes with temperature. Peaks 6 and 22 increase in amplitude with increasing temperature while peaks 1 and 18 decrease with increasing temperature. Peak 10 is unchanged over the temperature range shown. Peak 7 is evident only at 1.25 K while peak 11 appears only at 1.38 K. The two peaks 14 and 15, distinct at 1.25 K, coalesce to form one peak at the higher temperature. Many other differences can also be identified.

The torque at 1.38 K previously plotted in figure 5-12a, is compared directly to the torque at 1.39 K, in figure 5-14. The peaks are numbered as they were in figure 5-13. For this smaller temperature range the two patterns are the same within the noise level in most directions but small differences are apparent. Peak 4 at 1.38 K is just a shoulder at 1.39 K. The shoulder 13 at 1.38 K is a distinct peak at the higher temperature. Peak 11 moves 1° between the two temperatures. Peaks 16, 17 and 22 increase in amplitude as the temperature is increased while peaks 1, 3 and 9 decrease in amplitude as the temperature increases.

A sample was also held in a fixed orientation while the temperature was varied. Figure 5-15 shows the induced torque at a specific angle for sample KM7 as the temperature

Figure 5-15. The induced torque on sample KM6 as a function of temperature for a sequence of temperature increasing, decreasing and increasing, in a magnetic field of 8.0 T. The traces are offset by arbitrary amounts for clarity.

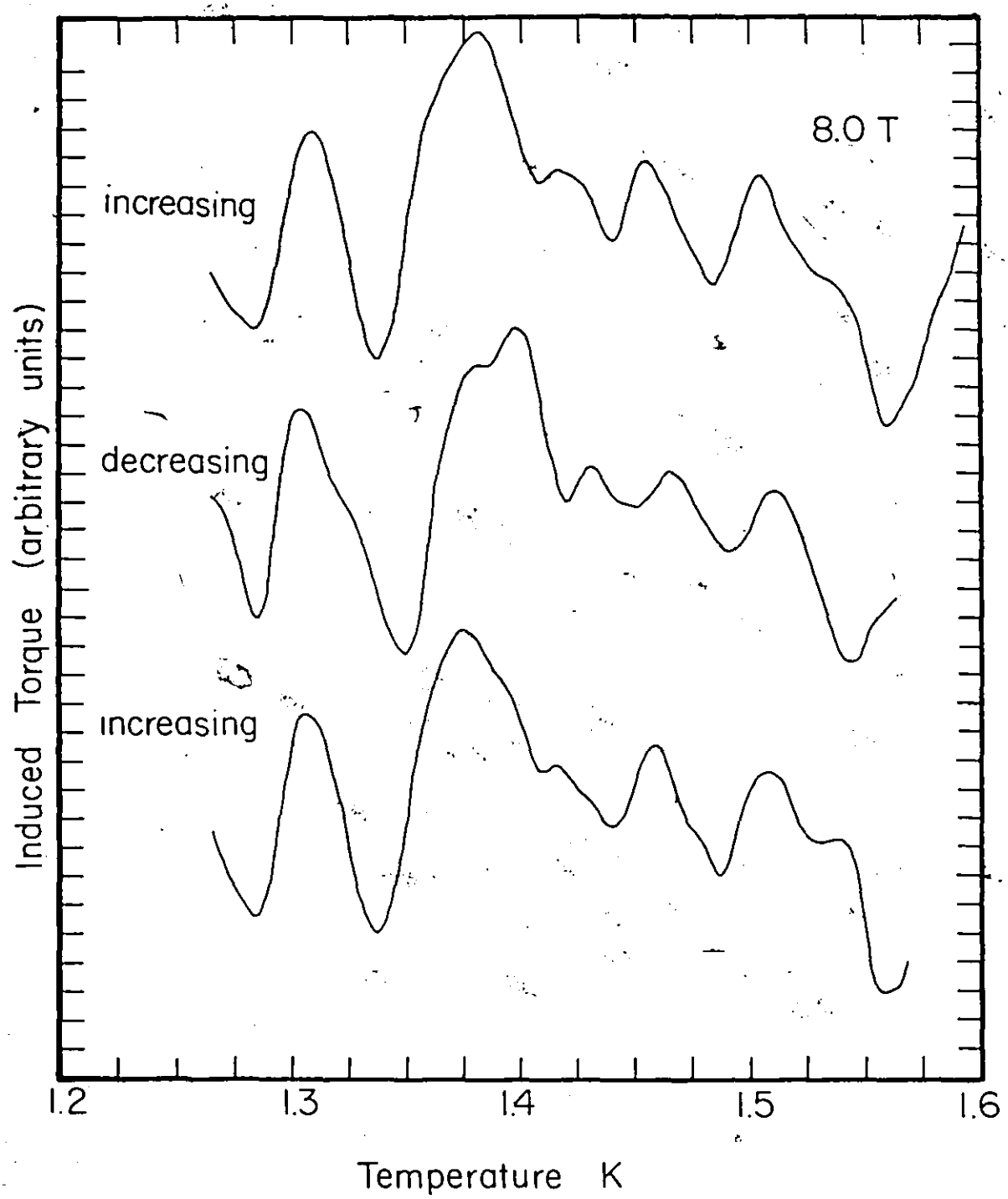
8.0 T
increasing
decreasing
increasing
Induced Torque (arbitrary units)
1.2
1.3
1.4
1.5
1.6
Temperature K

is increased, decreased and increased again. The features of the induced torque are reproduced fully as the temperature is increased. Small differences in the torque for decreasing temperature can be attributed to the time constant of signal filtering, since the rate of cooling varied considerably. Thus the changes of induced torque with temperature were measured directly and are reproducible for increasing and decreasing temperature. The torque for sample KM7 at a fixed angle over the temperature range 1.1 to 2.1 K which was the maximum range possible in these experiments is plotted in figure 5-16. The torque continues to vary non-monotonically with temperature over the entire range.

The torque at a specific magnetic field direction varies by a factor of two as the temperature is varied between 1.2 and 2 K. There are more frequent variations of about 20 percent of the total torque. These smaller variations occur at more closely spaced temperature intervals as the temperature is increased.

Changes in induced torque at fixed magnetic field value and direction are observed at all magnetic fields above 4 T. Below 4 T the induced torque does not depend on temperature.

To summarize, the new features of the induced torque in potassium which must be explained are the following. There are sharp peaks in the induced torque as a function of magnetic

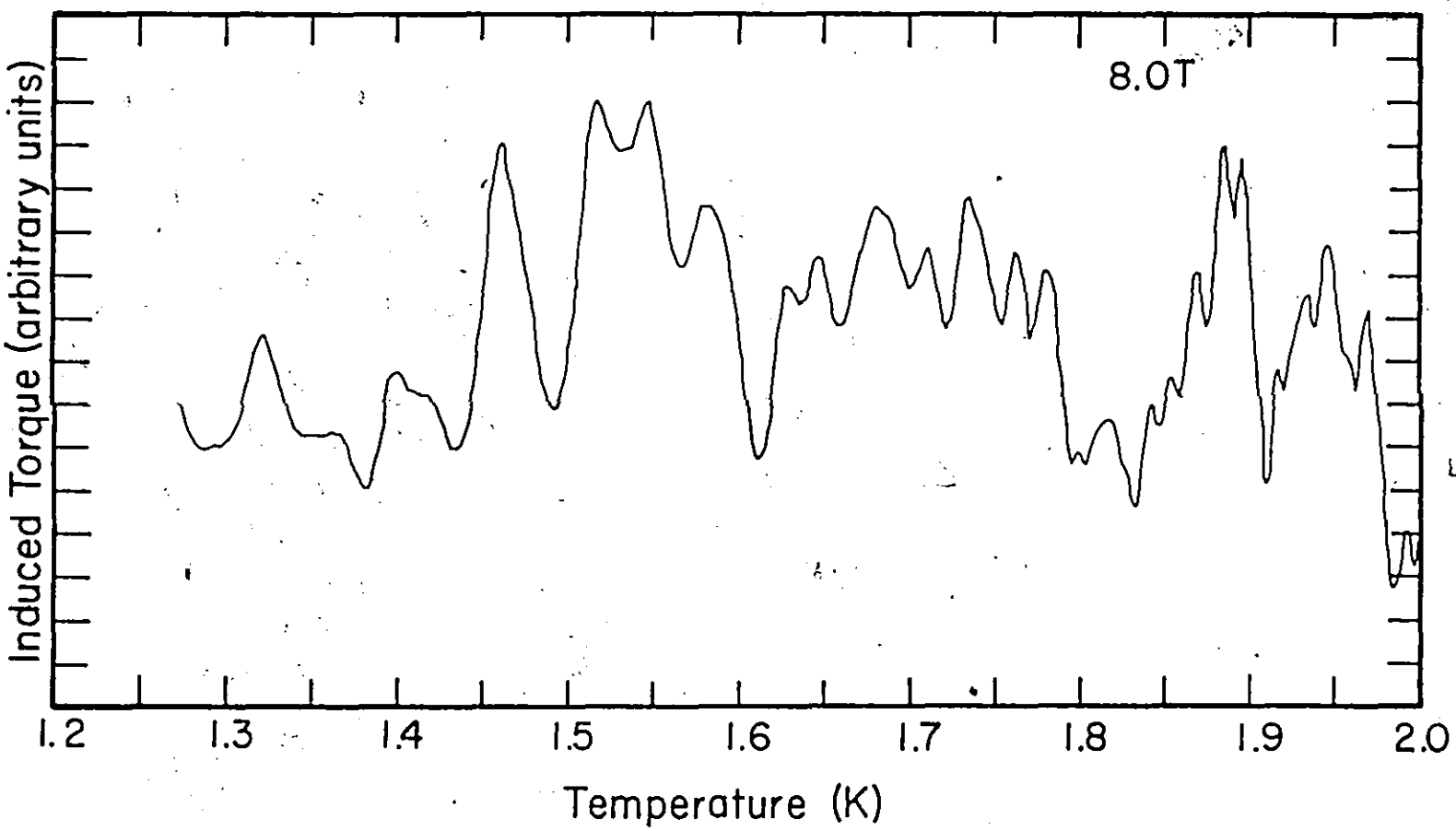

Figure 5-16 The induced torque on sample KM7 as a function of temperature, in a magnetic field of 8.0 T.

field direction at magnetic fields above 4 T . Both the amplitude and angular direction of this structure vary non-monotonically with temperature. The structure peaks are reproducible even after the sample has been warmed to 77 K . The angular position is invariant and the amplitude varies monotonically with magnetic field strength.

Sample KM4 showed very little four-fold torque during the first month of experiments. However it was exposed to air for a short period of time. This caused decomposition at one end of the sample. The resultant sample was named KM5. Subsequent experiments showed four-fold torque at fields above 0.5 T. Induced torque peaks were superimposed on this four-fold torque for fields above 4 T . The four-fold anisotropy at 2.5 T was 4:1, typical of previous results. The torque at 7.5 T and a sample temperature of 1.85 K in figure 5-17 shows structure superimposed on a four fold pattern. The amplitude of the induced torque peaks is similar to that observed before the sample was decomposed. However they appear smaller in comparison to the much larger four-fold background. The number of peaks was not affected by the decomposition at one end of the sample. The amplitude and position of the peaks remained temperature dependent even in the presence of the four-fold background. Thus it appears the properties of the high field induced torque is independent of the presence of four-fold torque.

The four-fold torque can not, however, be attributed only to the partial decomposition since other samples which

Figure 5-17 Induced torque on sample KM4 as a function of magnetic field direction after one end has been exposed to air. The scale of the induced torque is decreased by a factor of four relative to the data taken on the same sample and shown in figures 5-13 and 5-14. The magnetic field was 7.5 T and the temperature 1.85K.

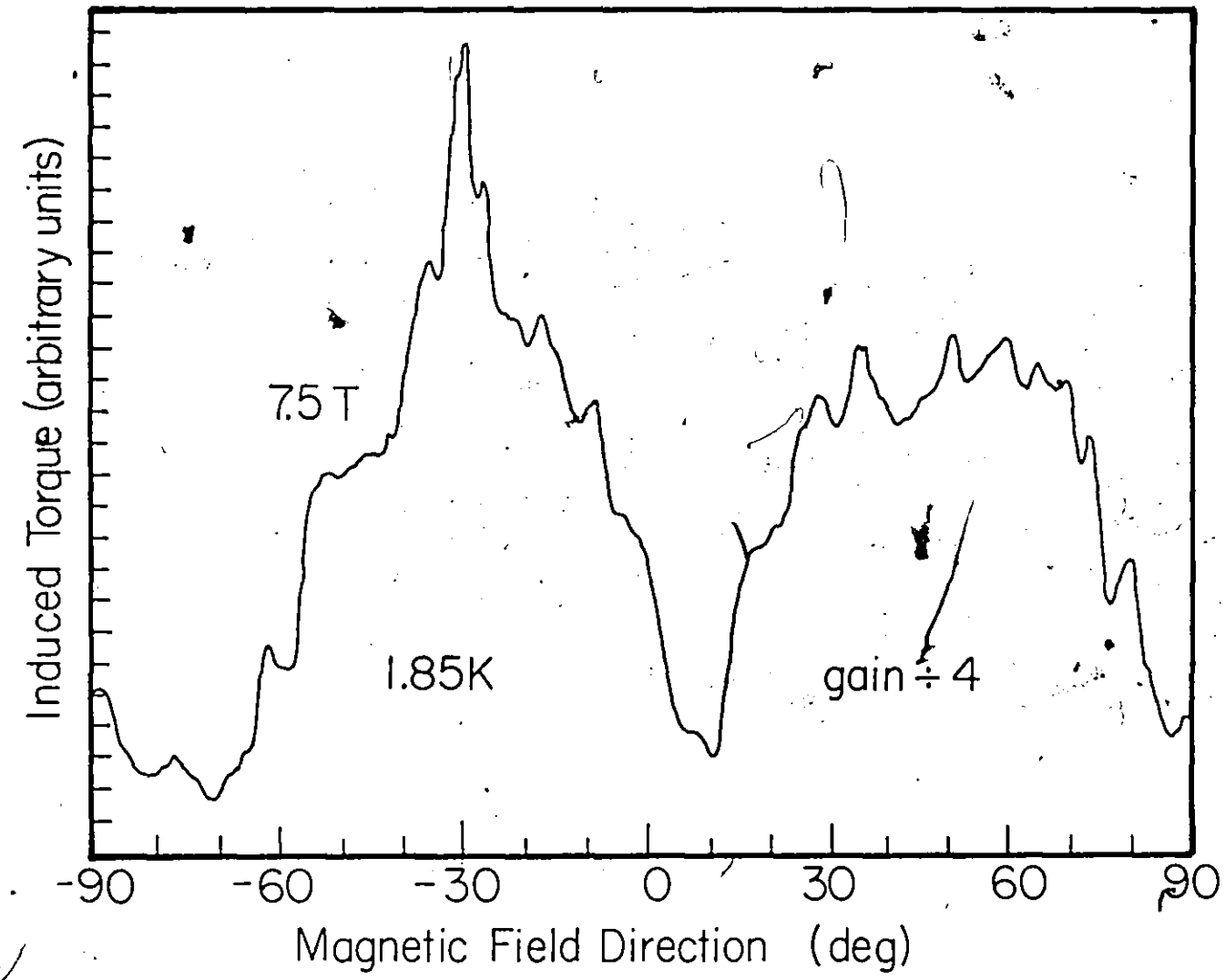
Induced Torque (arbitrary units)
7.5 T
1.85K
gain ÷ 4
-90
-60
-30
0
30
60
90
Magnetic Field Direction (deg)

display four-fold torque are spherical and not decomposed.

Sample KM12 was not a spherical sample. The sample holder only partially filled leaving a hemisphere with an irregular surface. The induced torque showed four fold anisotropy of 3:1 at 2.5 T, typical of previous results. However, the irregular surface is manifested as a series of peaks superimposed on the background four-fold torque as shown in figure 5-18. These peaks are not similar to the structure peaks previously found. These peaks appear at all magnetic fields from 0.2 T to 5.5 T. The amplitude and magnetic field direction of the peaks does not vary with temperature. However, at higher fields there is a temperature dependent structure in addition to these peaks. The properties of this structure are similar to those for the spherical samples.

ii) Magnetometer tests; Potassium

The presence of structure peaks in the induced torque of potassium was completely unexpected for a metal with the Fermi surface found by the dHvA effect. It is thus important to ensure the results are not an artifact of the magnetometer or technique.

First, the torque was shown to be induced. The total torque on the sample was measured as it was rotated through 180° in one direction and back. The total torque in figure 5-19 has several components. The overall slow variation of the torque

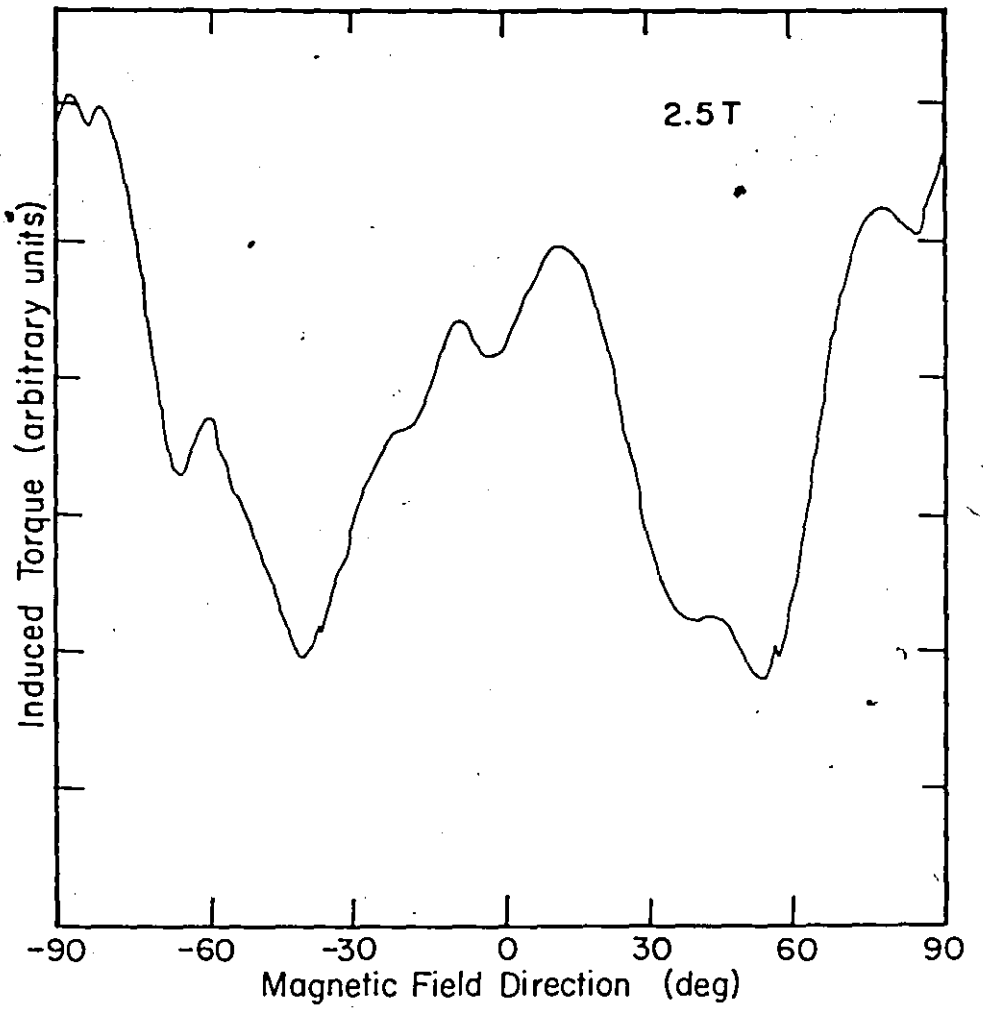

Figure 5-18 Induced torque on sample KM12 as a function of magnetic field direction at a magnetic field of 2.5 T.

in both traces is caused by springs used to position the sample at low field and provide electrical contact. The torque due to induced currents will, however, change sign upon changing the direction of rotation. Frictional torques which always oppose rotation will change sign as well. Thus, the difference between the two curves is the sum of the induced torque and frictional torque. The frictional torque, arising from the rubbing of the stainless steel axles in the jeweled bearings is small and uniform. Its amplitude is assumed independent of rotation speed. The sharp variations with magnetic field direction, shown by arrows in figure 5-19 are due to induced currents because the amplitude of these peaks varies linearly with rotation speed. For sample KM4 the two total torque traces for clockwise and anticlockwise rotation in figure 5-20a were subtracted to give the induced torque in figure 5-20b. This can be compared to the induced torque in figure 5-20c found directly by modulating the sample position. The inaccuracy of the subtraction process leads to large errors but the two patterns correspond except for the feature marked with an arrow. This feature is due to an excess frictional torque over a small angular range. Such a torque could arise for several reasons. If the springs are not accurately positioned they can contact the sides of the support assembly or each other during part of their rotation. Small amounts of impurities could become frozen upon the rotor and contact the support

Figure 5-19 Total torque on sample KM3 as a function of magnetic field direction. Curves are for clockwise and anticlockwise rotation in a magnetic field of 7.5 T and a temperature of 1.1K. Traces were also taken over a restricted angular range with increased gain. Arrows give the magnetic field direction of induced torque peaks.

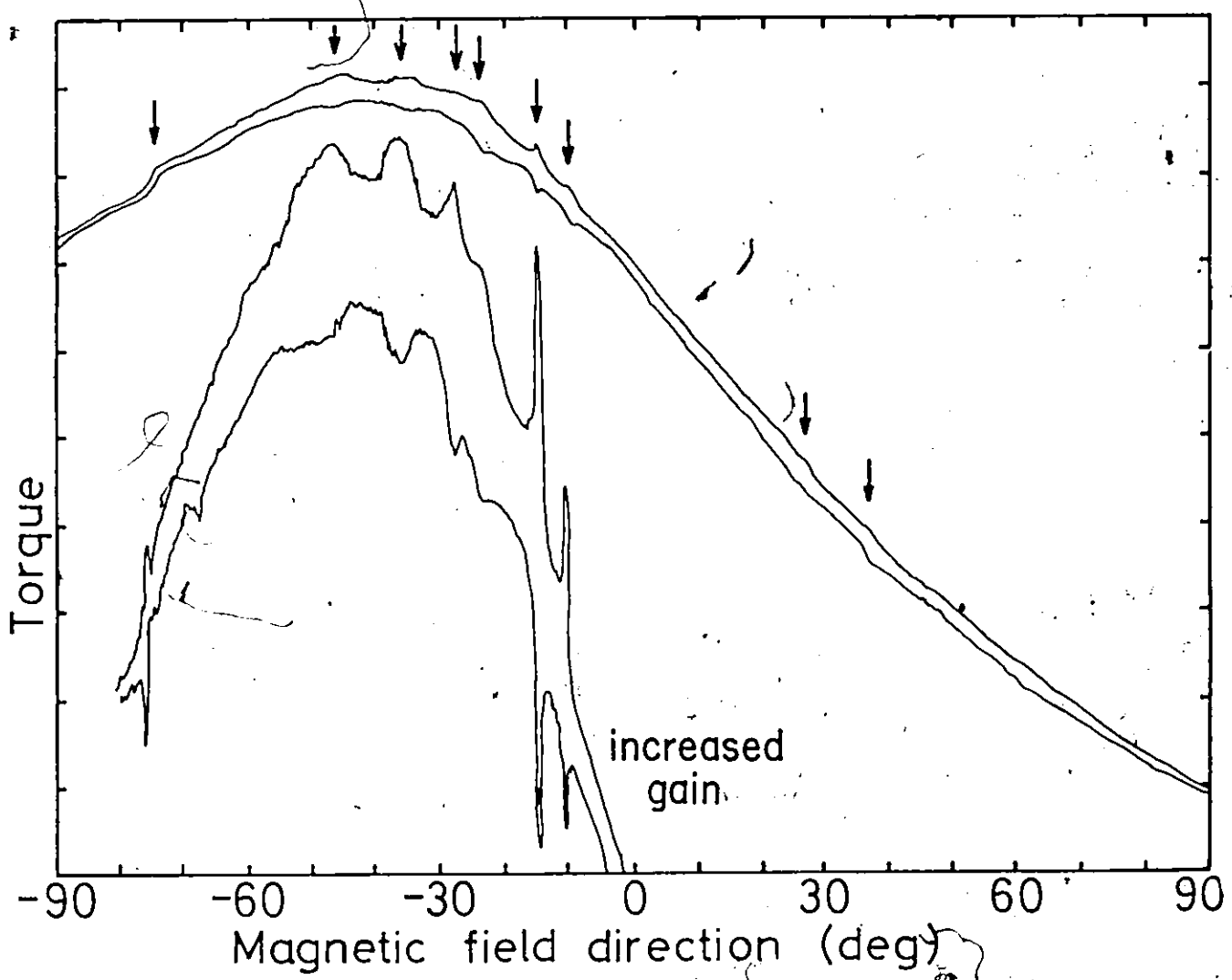
Torque
increased
gain
-90
-60
-30
0
30
60
90
Magnetic field direction (deg)

Figure 5-20 (a) Total torque on sample KM4 as a function of magnetic field direction. Curves are for clockwise and anticlockwise rotation. Induced torque (b) found by subtracting the clockwise from the anticlockwise rotation in Figure 5-20a point by point and (c) using the rotating sample magnetometer.

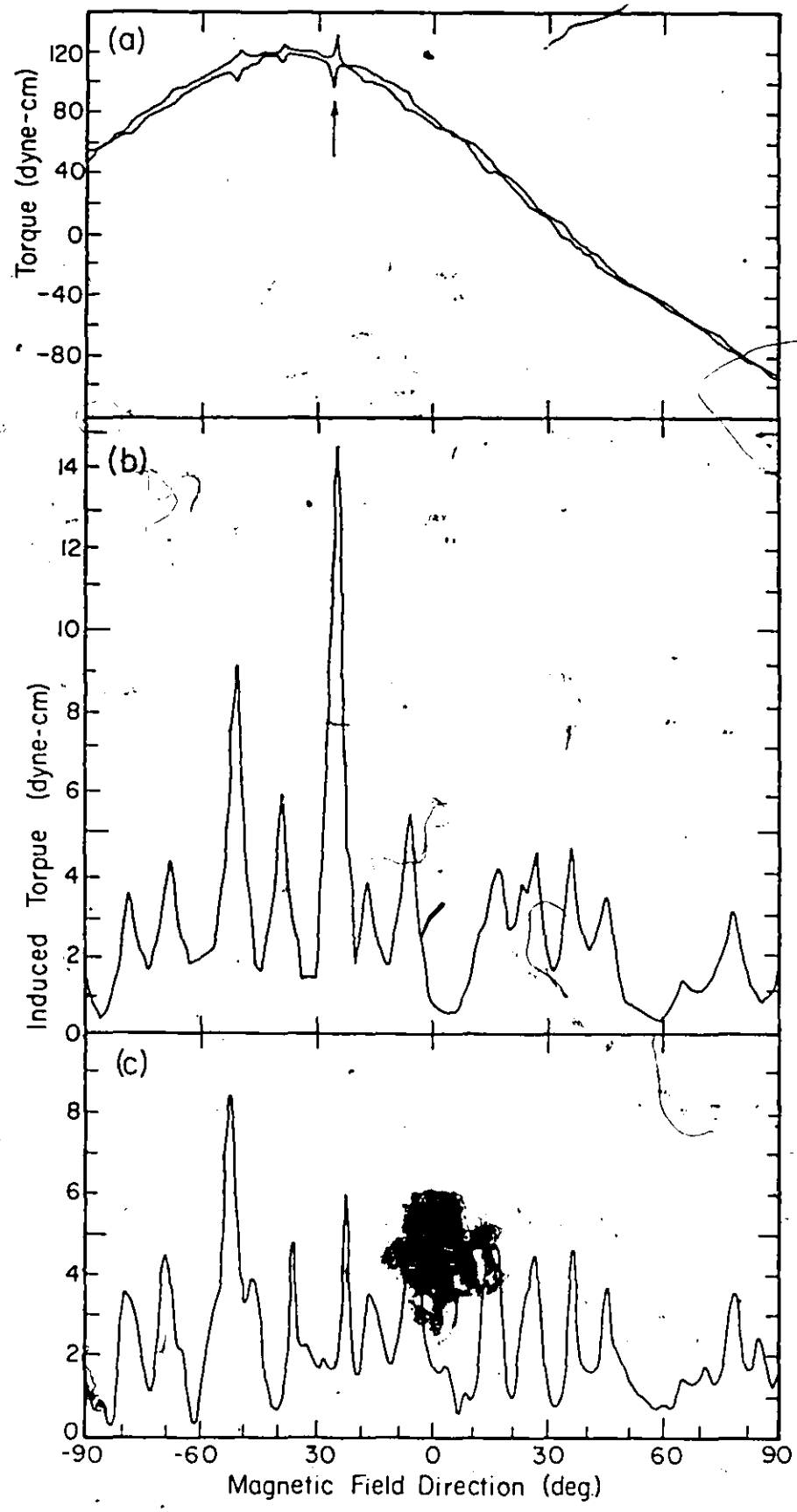
(a)
Torque (dyne-cm)
120
80
40
0
-40
-80
(b)
Induced Torque (dyne-cm)
14
12
10
8
6
4
2
0
(c)
8
6
4
2
0
-90
-60
30
0
30
60
90
Magnetic Field Direction (deg.)

assembly. It is much less significant in figure 5-20c because the modulation technique gives a larger effective rotation speed. This increases the speed dependent induced torque making it now much larger than the speed independent frictional torque.

The above illustrates several useful points. The absolute magnitude of the total torque can be easily measured. This provides a convenient calibration of the torques measured by the more sensitive modulation technique. It also identifies the signature of frictional torques which was then used to eliminate those runs for which measurable frictional torques could be identified.

The rotating magnet magnetometer was used to search for the induced torque structure using a slightly different method. It was possible to obtain the four-fold torque with the axis of modulation perpendicular to the main magnetic field. It was not possible to identify any of the observed peaks to be due to induced torque. This is inconclusive as the structure torque is expected only to be comparable to the noise caused by non uniform rotation of the magnet at 5.5 T, the largest magnetic field available.

iii) Magnetometer Tests, Copper and Indium

The magnetometer system was tested using other materials of known conductivity. The three samples tested were single crystal copper, polycrystalline copper and indium single crystals. The induced torque for a single crystal of copper using the rotating sample and rotating magnet magnetometers is shown in figures 5-21a and 5-21b respectively. The sample is rotated about an axis 10° from a 100 direction to obtain figure 5-21a. This shows the promiment <111> open orbits as well as smaller peaks arising from secondary <110> open orbits. The amplitudes are not equal because the axis of rotation is not exactly a symmetry direction. The amplitudes vary as well because the crystal is not a sphere. The copper crystal was rotated about an axis 2° from a <111> direction to obtain the torque of figure 5-21b. This shows the three-fold symmetry of <111> open orbits with regions of extended orbits between them. The amplitude of the torque at an open orbit induced torque peak could be fit by a power law of the form a B^{υ} with the exponent υ between 1.3 and 2.

The magnetic field dependence of the induced torque in the directions marked a and b in figure 5-21 is shown in figure 5-22. The torque in direction a was fit to a power law with $\upsilon = 1.44$. Peak b also could be fit with a power law with $\upsilon = 1.44$ but larger scale factor. The torque did not increase without limit but began to saturate at 3.5 T. Such saturation was due

Figure 5-21 Induced torque on single crystal copper samples as a function of magnetic field direction (a) using the rotating sample magnetometer and rotating in a (110) plane and (b) using the rotating magnet magnetometer and rotating in a (111) plane.

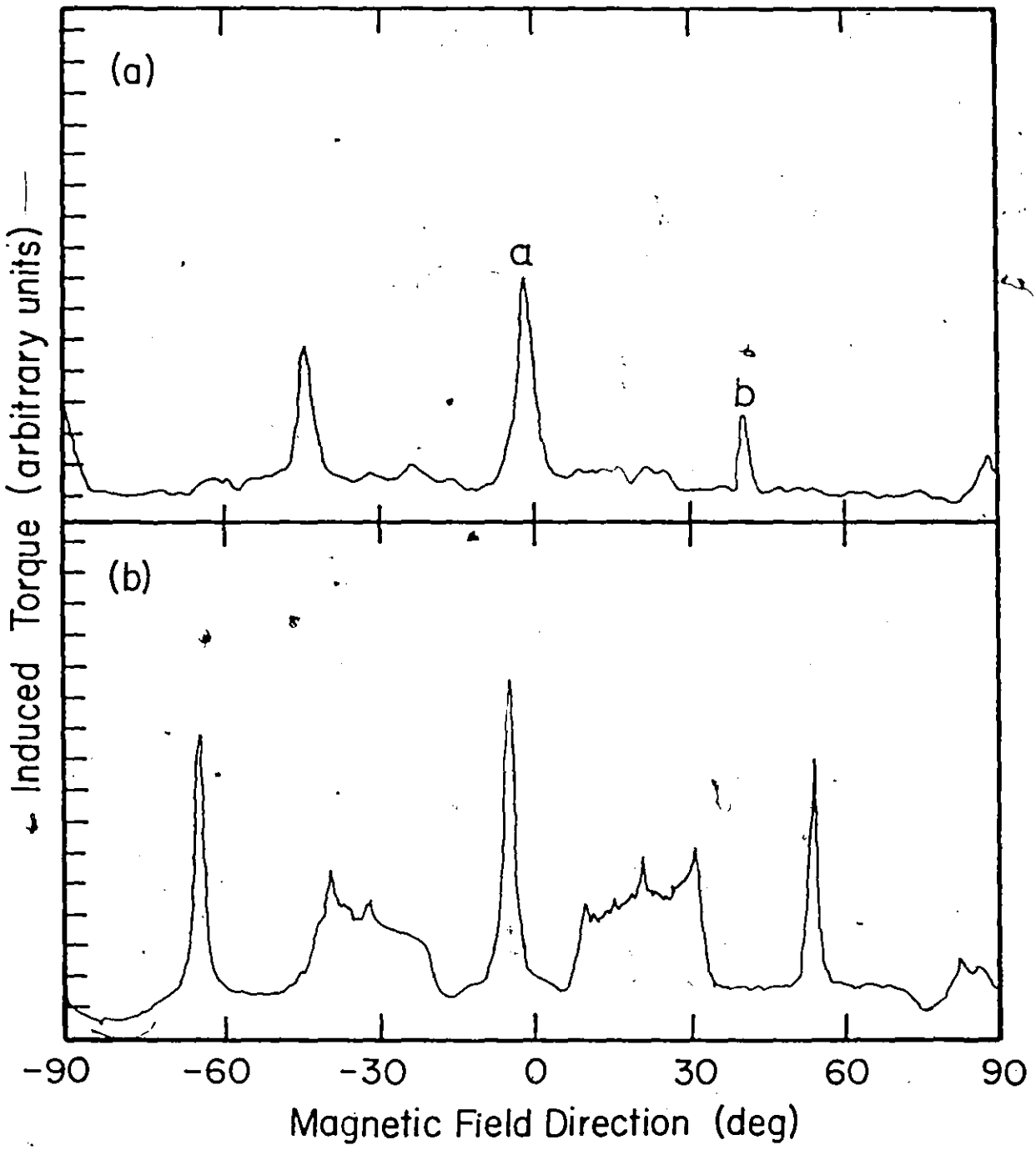
(a)
a
b
(b)
Induced Torque (arbitrary units)
-90
-60
-30
0
30
60
90
Magnetic Field Direction (deg)

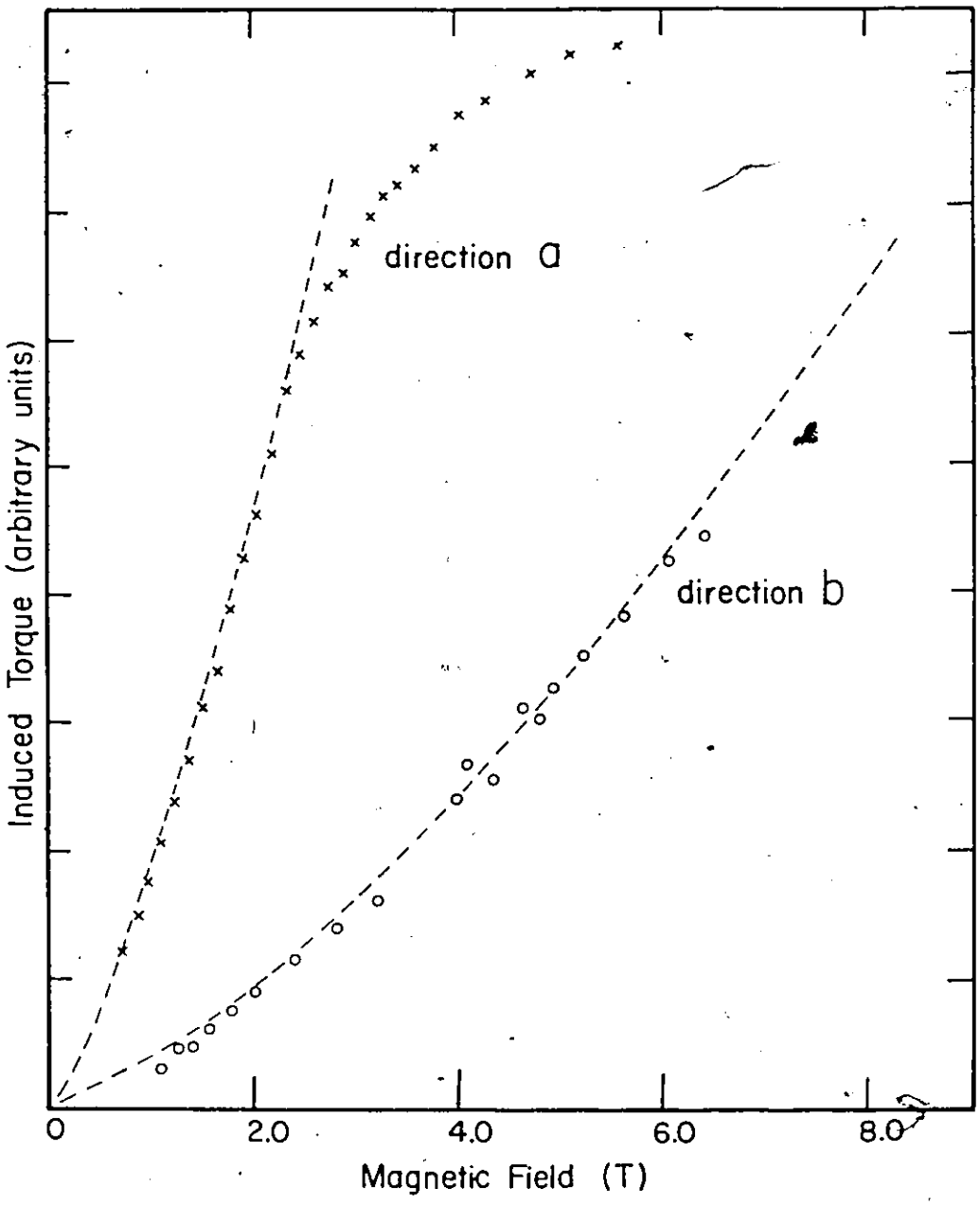

Figure 5-22 The magnetic field dependence of the induced torque at the peaks labeled a and b in Figure 5-21. The dashed lines are proportional to $B^{1.44}$

to overloading the electronics and not due to any property of the copper. It had no effect on the torque in any other direction and could be eliminated by reducing the effective rotation speed as was done to record figure 5-21a.

The polycrystalline copper sample was a 4 mm diameter sphere which consisted of about 10 crystallites. The induced torque at 1.9 T in figure 5-23 did not show any evidence of open orbits. The torque varied smoothly with angle, with an anisotropy of 20%. The torque increased with field at the rate expected for a free electron metal. It responded only as a poor conductor for which $\omega_c\tau$ did not reach 2 until 2.5 T.

The torque was measured in indium as an additional check. Indium is a free-electron metal which does not support any open orbits. The torque was measured using the rotating sample magnetometer in fields up to 5.5 T. The sample shows four-fold torque in figure 5-24. Structure peaks could not be found. The torque does show four peaks in a 360° rotation qualitatively in agreement with the results in potassium. Differences in detail can be noted however. The torque maxima in indium extended over a larger range of magnetic field direction with correspondingly sharper minimum than that found in potassium. The width of the torque minimum becomes narrower with increasing field in indium, unlike that in potassium which does not vary with magnetic field.

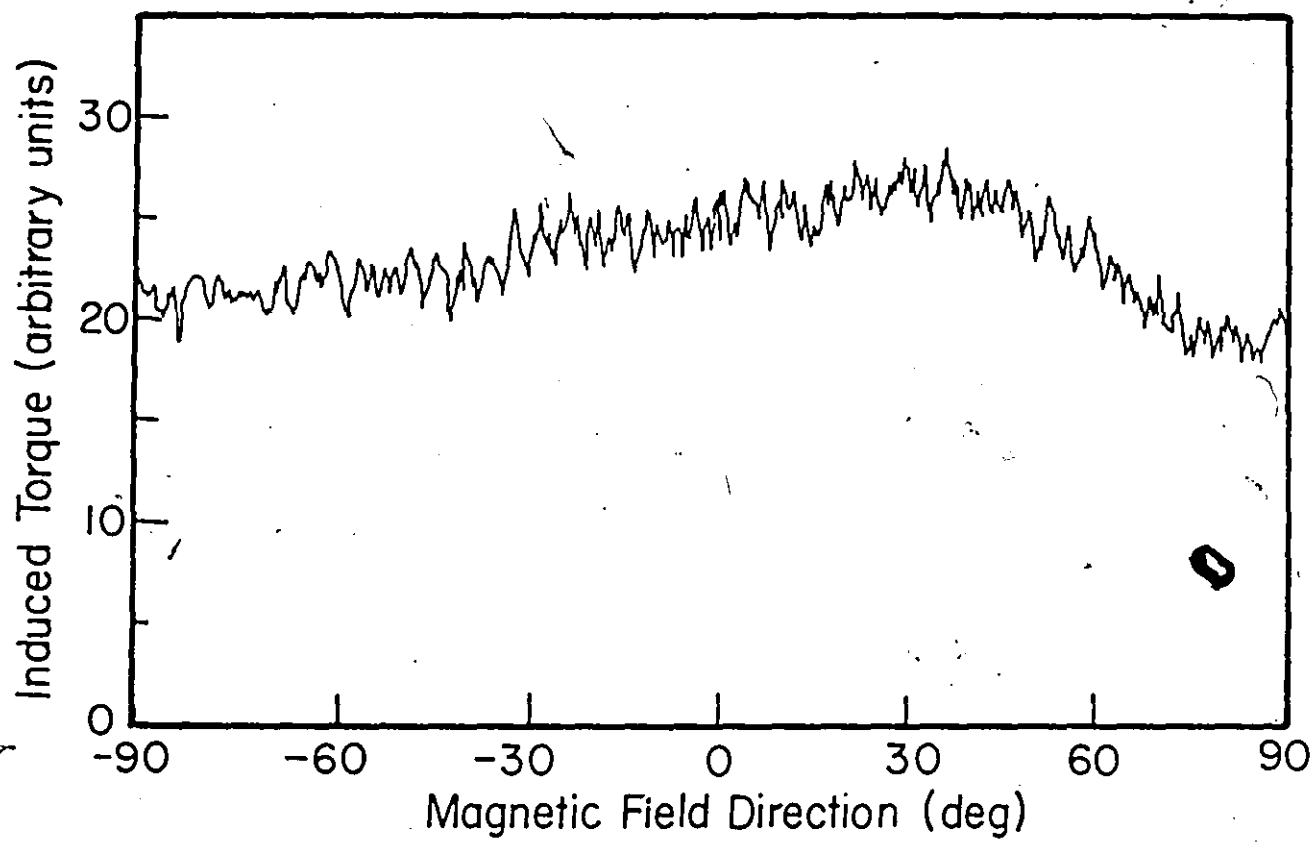

Figure 5-23 Induced torque on a polycrystalline copper sphere as a function of magnetic field direction.

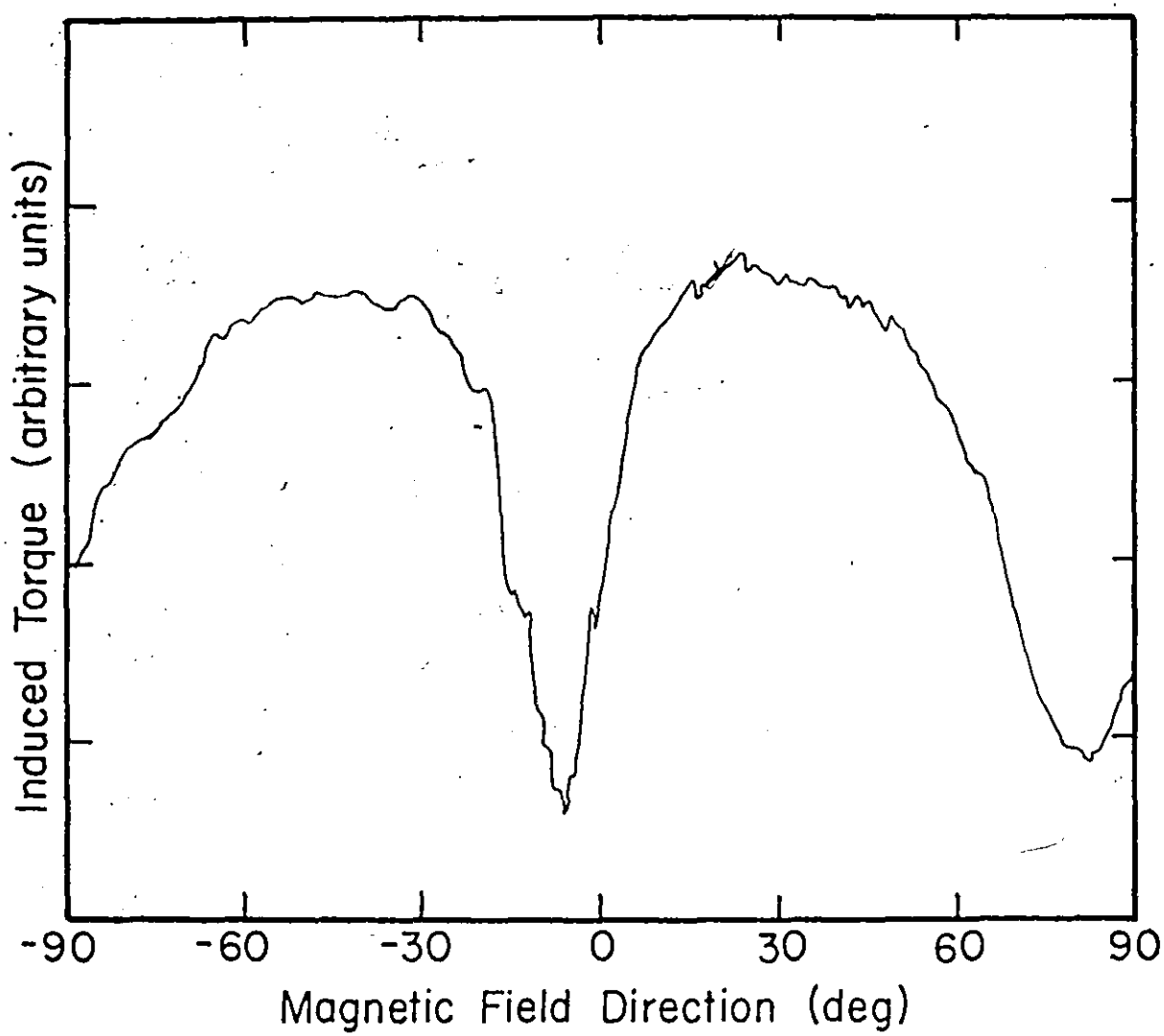

Figure 5-24 Induced torque on a single crystal indium sphere as a function of magnetic field direction.

The indium sphere was shown to be a single crystal by use of the dHvA effect. Since indium has low dHvA frequencies and an anisotropic Fermi surface there is a dHvA torque which was measured using the same magnetometer. The measured torque showed a single crystal contributing to the dHvA signal.

CHAPTER 6

DISCUSSION: LOW FIELD INDUCED TORQUE

i) Four-fold Induced Torque

The four-fold induced torque observed in this work has been found in other experiments measuring the amplitude of the dHvA effect (O'Shea and Springford 1981), longitudinal magnetoresistance (Simpson 1973) and induced torque experiments, (Schaeffer and Marcus 1971, Holroyd and Datars 1975 and Elliott and Datars 1983 (ED)).

The four-fold induced torque was shown to be independent of the induced torque structure in Chapter 5. The four-fold induced torque will be presented and compared to the Lass model of ellipsoidal samples described in Chapter 3 iii) and 3 iv) and the charge density wave model described in Chapter 2.

ED concluded largely on the basis of the amplitude of the induced torque that the Lass model was more successful. Although it will be shown that some of their conclusions are premature, the amplitude and phase of the induced torque does support the Lass model.

Table 6-1

Samples for which Phase Data were Taken

Sample This work	ED	Magnetic field $\omega_c\tau = 2$	$\eta(\mu)$
KOED	1	0.185 T 0.095	-0.132
KM8	2	0.07	0.214
KM11	-	0.055	0.50
KM12	3	0.090	0.5

ii) Amplitude of Low Field Induced Torque

The amplitude of the induced torque on sample KM11, measured using the rotating sample magnetometer, is shown in figure 6-1 at magnetic fields of 0.05, 0.1, 0.2, 0.3 and 1.6 T. At 0.05 T and 0.1 T the induced torque varies sinusoidally with magnetic field direction with two maxima in a 360° rotation and is called two-fold induced torque. The induced torque is two-fold at 0.2 T with the maxima occurring over a smaller range of magnetic field direction than the minima. An additional maximum can be seen in each broad minima at 0.3 T when the induced torque is starting to become four-fold. The four-fold induced torque is the dominant feature at 1.6 T. Superposed on the four-fold induced torque is significant experimental noise which increases with increasing magnetic field.

The induced torque at the two-fold minimum and maximum is plotted as a function of magnetic field in figure 6-2a and the ratio of the two torques in figure 6-2b. The induced torque varies linearly with magnetic field at low field, reaches a maximum at 0.055 T and decreases at higher field. The torque ratio in the limit of zero field is obtained from the slope of the induced torque curves in the linear region. The torque ratio increases monontonically with increasing field.

Both the Lass model and the CDW model predict two-fold induced torque at low fields. The ratio of induced torque at

Figure 6-1 Amplitude of induced torque on sample KM11 at magnetic fields of 0.05, 0.10, 0.20, 0.30 and 1.6 T showing the transition from two-fold to four-fold induced torque. Traces are offset by arbitrary amounts for clarity.

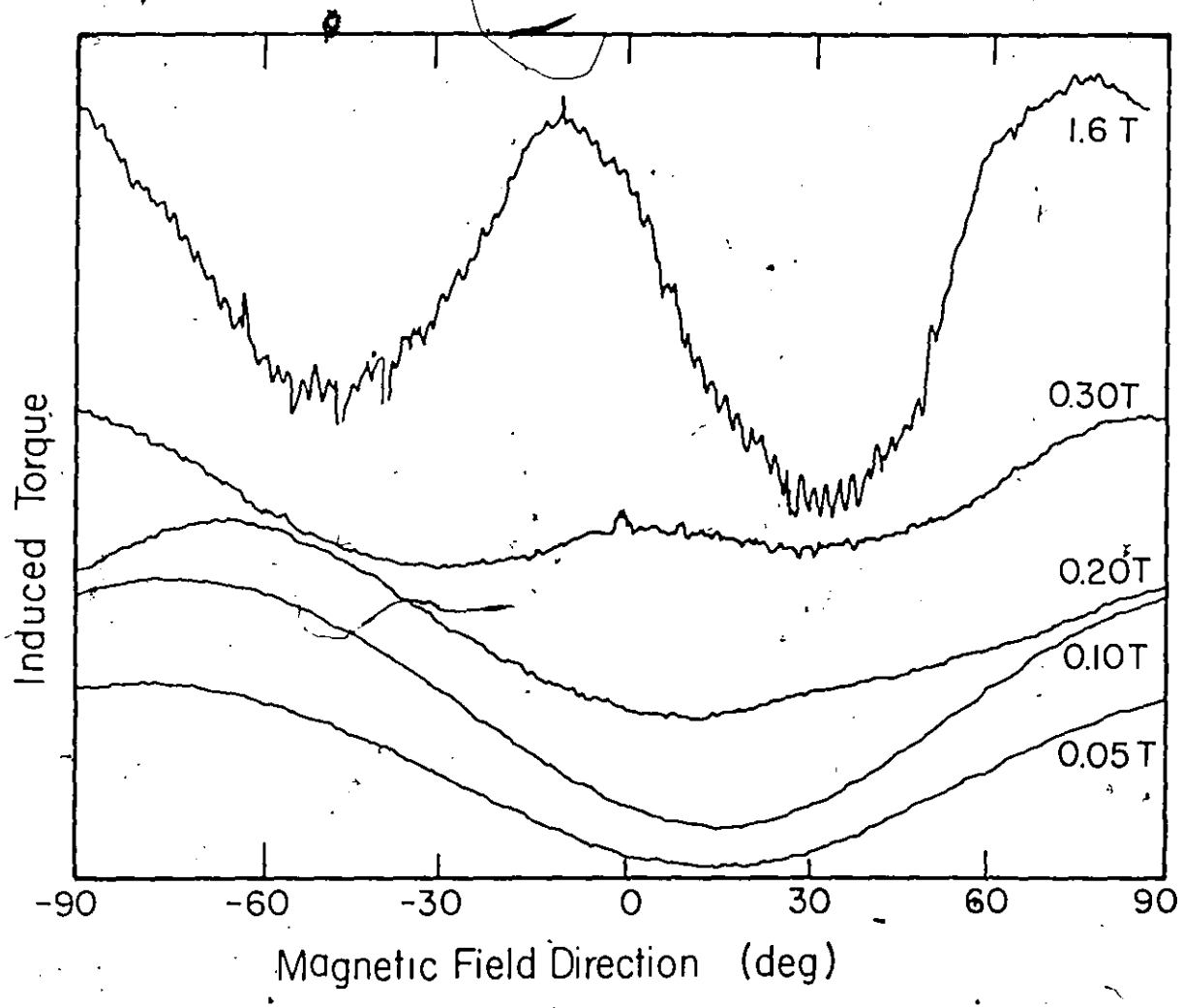
1.6 T
0.30T
0.20T
0.10T
0.05 T
Induced Torque
-90
-60
-30
0
30
60
90
Magnetic Field Direction (deg)

a two-fold maximum to a two-fold minimum is given by ED as

$$F = (1 + \frac{\eta}{2})[1 - \frac{3\eta(\omega_c\tau)^2}{8+2(\omega_c\tau)^2}] \qquad (6\text{-}1)$$

in the Lass model, where η is the anisotropy parameter and

$$F = (1 + \frac{\mu}{2})[1 - \frac{\mu(\omega_c\tau)^2}{8+2(\omega_c\tau)^2}] \qquad (6\text{-}2)$$

in the case of a CDW where μ is the anisotropy of the conductivity tensor.

The value of η or μ was estimated from the zero field limit

$$F = 1 + \frac{\eta}{2} \quad \text{and} \quad F = 1 + \frac{\mu}{2} \qquad (6\text{-}3)$$

of equations (6-1) and (6-2) respectively. Equation (3-5) was used to estimate $\omega_c\tau$ from the peak of the induced torque in figure 6-2a. The values of $\omega_c\tau$ and η or μ for all samples used in this chapter are listed in table 6-1.

The torque ratio predicted by equation (6-1) and (6-2) is shown in figure 6-2b as a dashed line and chain line respectively. The Lass model is qualitatively in agreement with the data while equation (6-2) predicts a monotonic decrease of the data with magnetic field. However, further examination of the CDW model predicts (Overhauser 1983) and some experimental data (Chementi and Marfield 1973, Fletcher 1980) indicates that the Hall coefficient R varies with magnetic field

Figure 6-2 Amplitude (a) of induced torque shown in Figure 6-1 at 2 fold maxima (-75°) and minima (+15°) and their ratio (b). The torque ratio predicted by equation 6.1 (Lass model) dashed line; equation (6-2) (CDW model with constant Hall coefficient), chain line, equation (6-3) (CDW model with angle dependent Hall coefficient), solid line are shown for comparison.

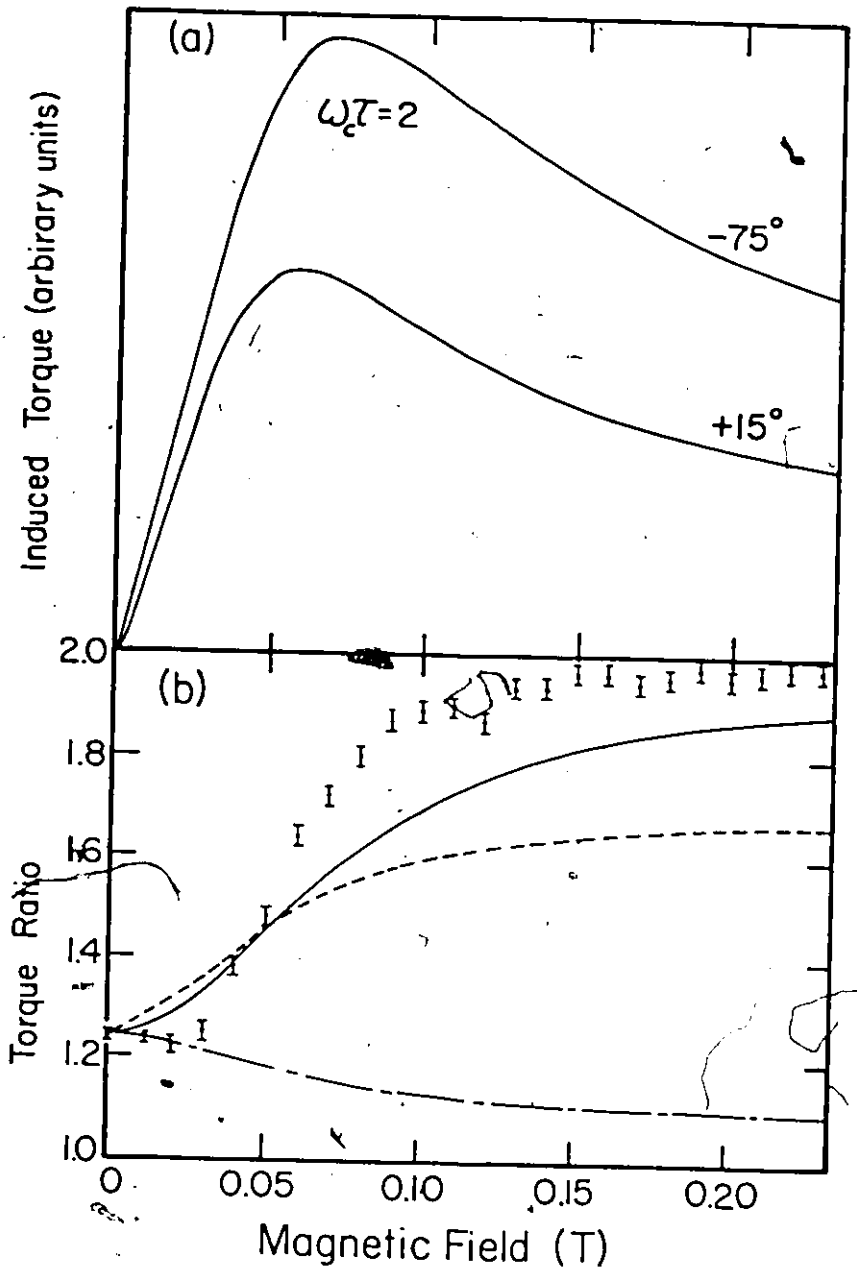
(a)
$\omega_c\tau=2$
-75°
+15°
Induced Torque (arbirary units)
2.0
(b)
1.8
1.6
1.4
1.2
1.0
Torque Ratio
0
0.05
0.10
0.15
0.20
Magnetic Field (T)

direction. The addition of an angle dependent Hall coefficient of the form $1+\mu\cos^2\theta$ changes equation (6-2) to

$$F = [1 + \frac{\mu}{2}] \frac{1+(\omega_c\tau)^2/(4+4\mu)]}{[1+(\omega_c\tau)^2/4+10\mu)]} \quad . \qquad (6\text{-}4)$$

This is a monotonically increasing function of magnetic field shown by a solid line in figure 6-2b.

The torque ratio is thus very sensitive to exact value of the Hall coefficient. Fletcher has shown both theoretically and experimentally that R varies by several percent in magnetic fields up to $\omega_c\tau = 1$. The variation occurs from sample to sample, depending on temperature, purity and magnetic field direction and is sufficient to cause the observed variation in F. Only the zero field limit which depends on the diagonal elements of the resistivity tensor is accurately predicted by this theory. The CDW model predicts open orbits which invalidate the simple theory of equations (6-2) or (6-3). The predictions of the Lass model are valid at high magnetic fields.

iii) Phase of Induced Torque

The phase of the induced torque provides an additional test for the Lass model. The phase shift for sample 1 of ED (KOED) as a function of magnetic field direction is shown in figure 6-3 for a series of magnetic field values. At low values of B the phase of the induced torque is 47° from the a.c. magnetic field. There is small variation of the phase with magne-

Figure 6-3 Phase of induced torque measured for sample KOED in magnetic fields of 0.01T(•), 0.05T(□), 0.10T(+), 0.40T(∇), 1.2T(x) and 1.8T(o). Data have been shifted by 5° as described in the text. The directions of induced torque maxima and minima are shown by dashed lines.

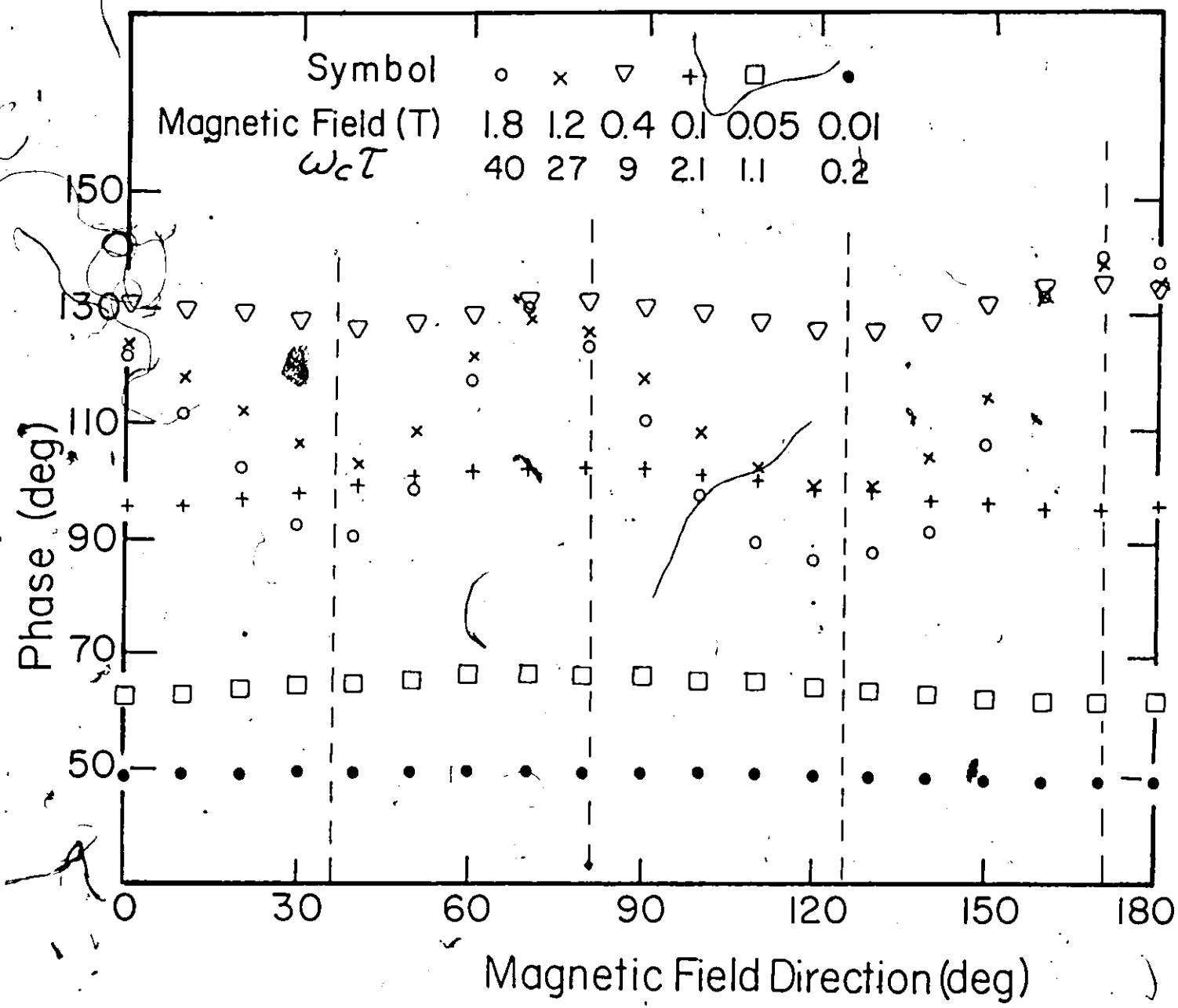
Symbol
Magnetic Field (T) 1.8 1.2 0.4 0.1 0.05 0.01
$\omega_c\tau$ 40 27 9 2.1 1.1 0.2
Phase (deg)
150
130
110
90
70
50
0
30
60
90
120
150
180
Magnetic Field Direction (deg)

Figure 6-4 Phase of induced torque calculated in the Lass model using $\eta = -.132$ estimated from induced torque ratio at zero field. The values of $\omega_c\tau$ were chosen to correspond to those estimated for the data of figure 6-3 from the induced torque amplitude.

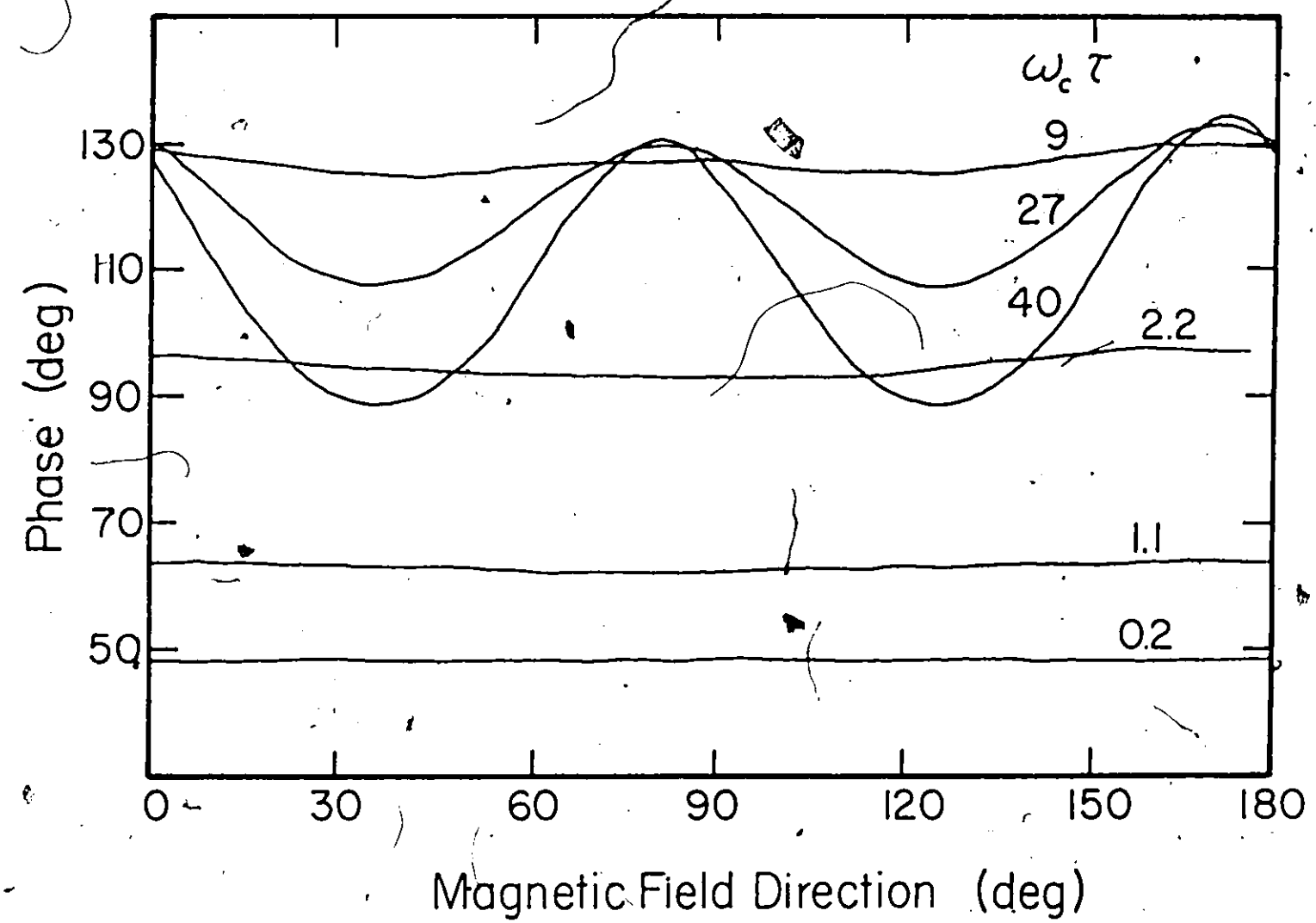
$\omega_c \tau$
9
27
40
2.2
1.1
0.2
130
110
90
70
50
Phase (deg)
0
30
60
90
120
150
180
Magnetic Field Direction (deg)

tic field direction. This variation is two-fold. The phase in all magnetic field directions shifts away from the ac magnetic field as the static magnetic field is increased to 0.2 T. The phase at 0.4 T varies by 5° as the magnetic field direction is changed. The variation with magnetic field direction is four-fold. The phase maxima correspond to minima in the amplitude of the induced torque. The four-fold variation of phase becomes larger as the magnetic field is increased, reaching 45° at 1.8 T. The phase at the phase maxima does not change significantly with magnetic field above 0.2 T.

The phase of the induced torque predicted for an ellipsoidal sample using the values of $\omega_c\tau$ and η previously estimated is shown in figure 6-4. The agreement with the measured data of figure 6-3 is good. The predicted phase is two-fold with small anisotropy at low field, becoming four-fold at high field. If a constant 5° phase shift in the data of figure 6-3 is attributed to the electronics the measured and predicted phases are in quantitative agreement. Small deviations in the measured phase shift from four-fold symmetry can be fitted if the angle ϕ between the axis of the ellipsoid and the rotation plane is treated as a free parameter.

The phase of the induced torque at the four-fold minima (81° and 171°) and at the four-fold maxima (36° and 126°) of sample KOED is plotted in figures 6-5a and 6-5b respectively. The phase at magnetic field direction of 81° and 171° increases from 47° at zero field, passes through 90° at

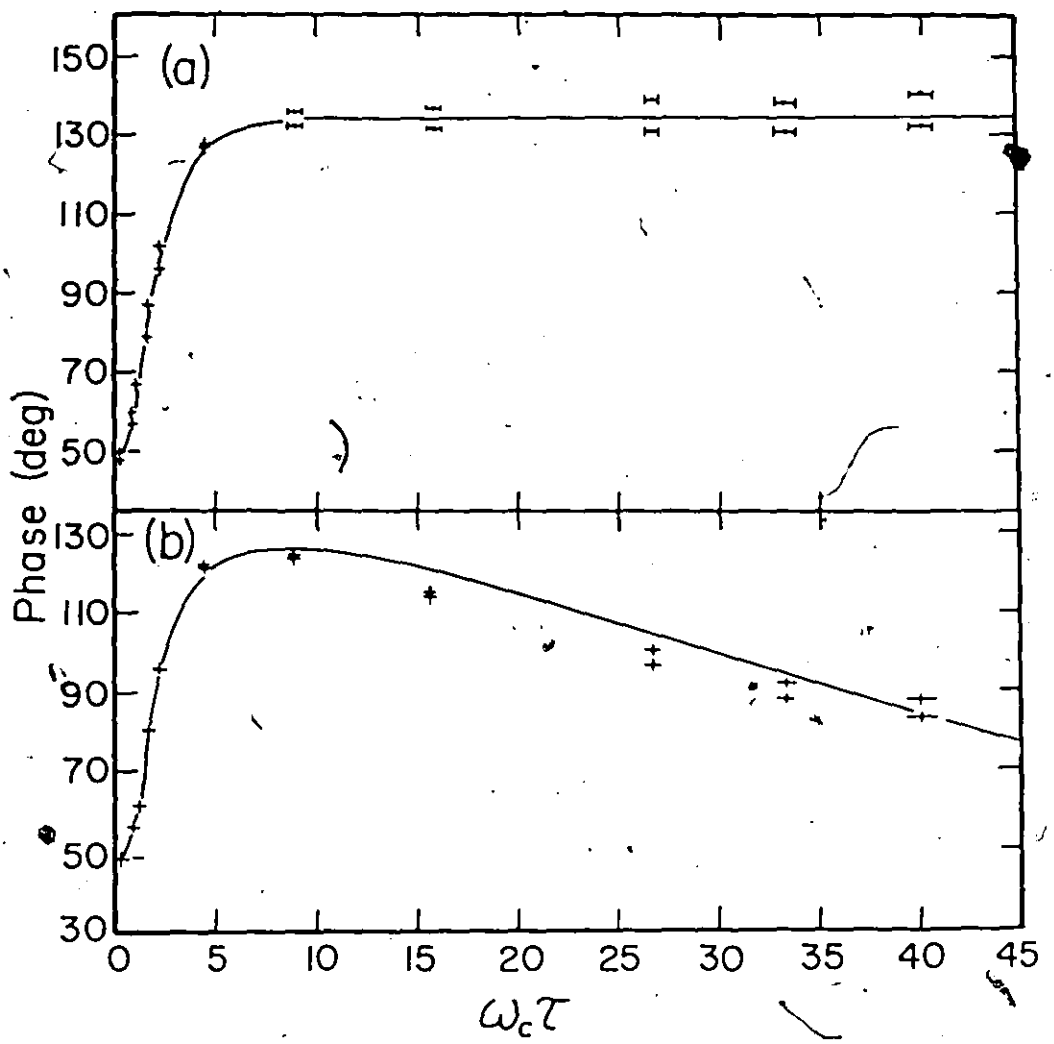

Figure 6-5 Phase of the induced torque at the phase maxima (81° and 171°) (a) and the phase minima (36° and 126°) (b) of sample KOED. The solid line gives the phase predicted by the Lass model.

$\omega_c\tau$ equal to 2 and saturates at 133° at high field. The phase at the amplitude maximum increases from 47° at zero field, passes through a maximum at $\omega_c\tau = 4$ and begins to decrease at high field. There is a large error in the estimate of $\omega_c\tau$ at high field, since $\omega_c\tau$ is estimated at $\omega_c\tau = 2$.

The solid lines in figure 6-5 show the predictions for an elliosoidal sample.

The phase of the induced torque maxima in sample KM9 was measured as a function of frequency. In order to eliminate the effect of phase shifts in the electronics with frequency, the phase difference between 1.6 T and 0.025 T is plotted in figure 6-6. The phase difference increases continuously with increasing frequency. The measured phase shift accurately follows that for the Lass model shown as a solid line.

Exact predictions for the phase shift in the CDW model are not available but it can be descrived qualitatively. If the four-fold torque occurs due to an anisotropic Hall coefficient, the anisotropy of the phase decreases at high field. The presence of open orbits causes the phase to remain at its low field value. In either case there is no peak as a function of magnetic field, unlike the data shown in figure 6-5b.

In conclusion the Lass model with one free parameter explains the two-fold torque, its anisotropy, the four-fold

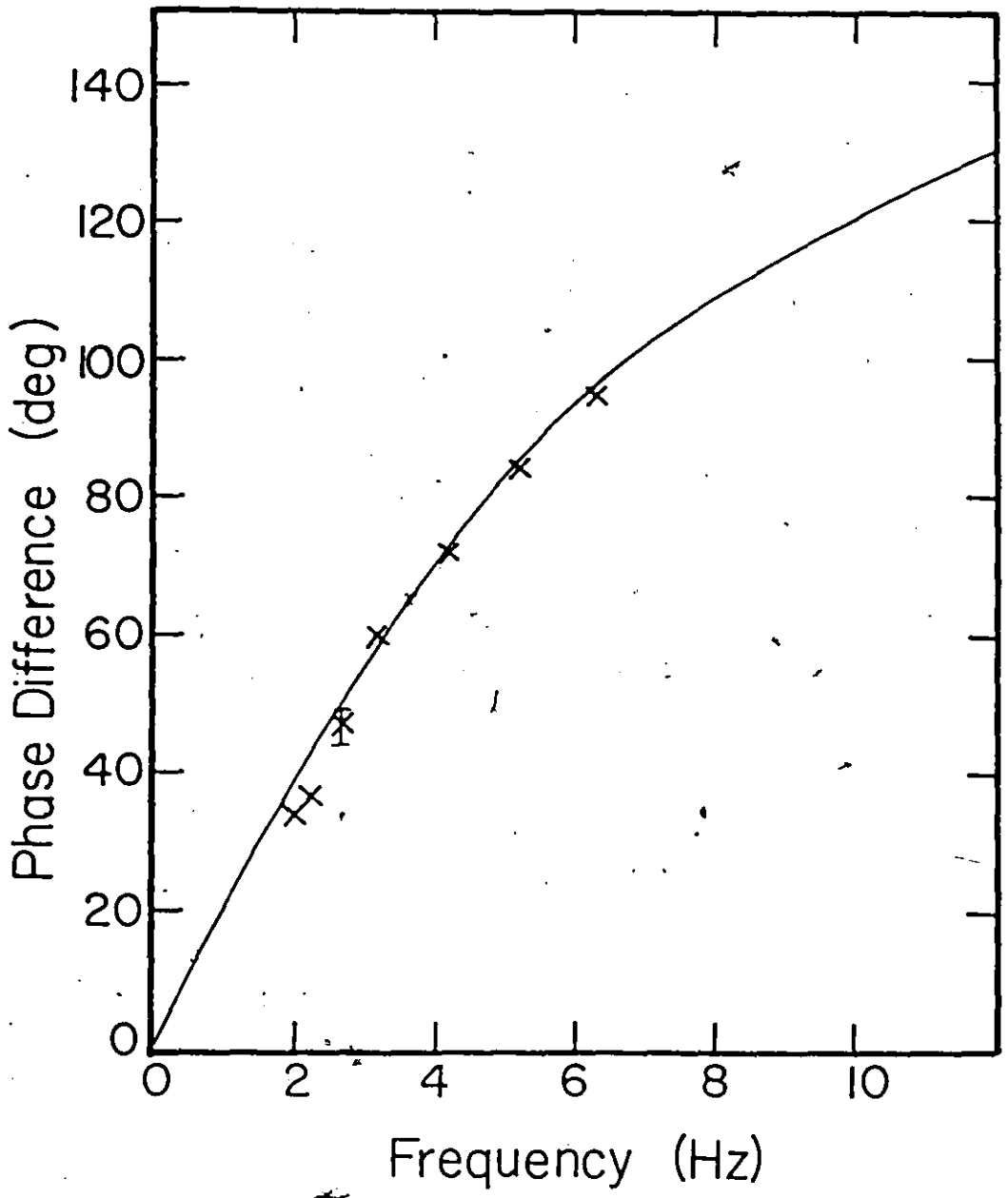

Figure 6-6 Phase difference between 0.025 T and 1.6 T in sample KM9 as a function of frequency. The solid line gives the prediction of the Lass model.

torque and the phase of the torque at all magnetic field values. The CDW model explains the two-fold torque, its anisotropy, and anisotropic torque at high fields. It does not explain the presence of four-fold torque or the phase of the induced torque.

From this variety of evidence it must be concluded that the four-fold induced torque can best be explained by the Lass model. Therefore the sample which is known to be spherical must be electrically non-spherical. This can occur due to a resistivity tensor which varies with sample position as described in Chapter 3 iii).

Delaney and Pippard (1972) found that an aluminum sphere exhibited a low resistivity core and high resistivity shell when dropped several times from a height of two meters. They attributed this to an increased dislocation density at the surface. Since potassium is much softer than aluminum, such a shell could form due to normal handling and cooling procedures.

The known impurity content of the potassium samples used is 200 PPM. If this was assumed to be all sodium the expected residual resistivity would be 150 pΩm (Gugan 1982). This is a factor of 10 greater than the measured residual resistivity. Thus most of the impurities must precipitate out. Both dislocations and impurity precipitation occur along preferred crystallographic directions so they will be anisotropically arrayed in the sample. Altounian et al. (1978) mea-

sured the Dingle temperature to be 0.2K for samples prepared in the same way. Their experimental conditions were such that they were in the skin depth regime. If the Dingle temperature is assumed to result entirely from dislocation scattering estimates by Brown (1978) give a dislocation density of order $7\times10^{11}/m^2$ at the sample surface. The presence of 200 ppm impurities contributes less than 0.1K to the Dingle temperature.

A quantitative development of the ideas of Chapter 3 iii) shows that a metal with resistivity which varies in the xy plane has

$$\frac{\Delta\rho}{\rho_0} = -2\eta \qquad (6\text{-}5)$$

Here $\Delta\rho$ is the resistivity difference between centre and surface and ρ_0 is the average resistivity. This is equivalent to an ellipsoid with anisotropy η. The value of ρ_0 was estimated to be 10×10^{-12} Ωm from a calculation of the residual resistivity ratio. This requires $\Delta\rho$ of order 3×10^{-12} Ωm.

If the difference in dislocation density between surface and centre is assumed to be $5\times10^{11}/m^2$ the contribution to resistivity can be calculated. The dislocation specific resistivity reported by Brown (1982) of 4×10^{-25} Ω/m^3 was used to estimate a resistivity difference between centre and surface of 2.6×10^{-13} Ωcm, a factor of ten too small. However an increased dislocation density near the surface can trap impurities.

The impurity specific resistivity is of order 5.6×10^{-9} Ωm/at % for sodium in potassium (Llewellyn et al 1977).

A difference in impurity content of 10 PPM between centre and surface gives a resistivity difference of 3×10^{-12} Ωm. Thus 20 PPM impurities in the sample at the centre and 30 PPM at the surface, values which are reasonable, are sufficient to cause the sample to appear elliptical.

iv) Phase of High Field Induced Torque

The induced torque amplitude and phase on sample KM9 were measured at 5.5 T with the rotating sample magnetometer, as shown in figures 6-7a and 6-7b, respectively. This shows all the features of the induced torque phase predicted in Chapter 3 iv).

Both the amplitude and phase of the induced torque have a four-fold pattern with structure. The amplitude maxima and minima are symmetric and occur over angular ranges of 45°. There is a large increase in phase near the four-fold amplitude minima at magnetic field directions -13° and 75°. The full width at half maximum of these phase peaks is 25°. This is comparable to the 15° width predicted in the Lass model and is clear evidence of the phase spike behaviour. Broad minima in the four-fold amplitude correspond to narrow maxima in the phase, showing the Lass model is valid to fields of 5.5 T. The phase behaviour of the structure peaks is different. They consist of peaks in the induced torque amplitude which occur at the same magnetic field directions, and

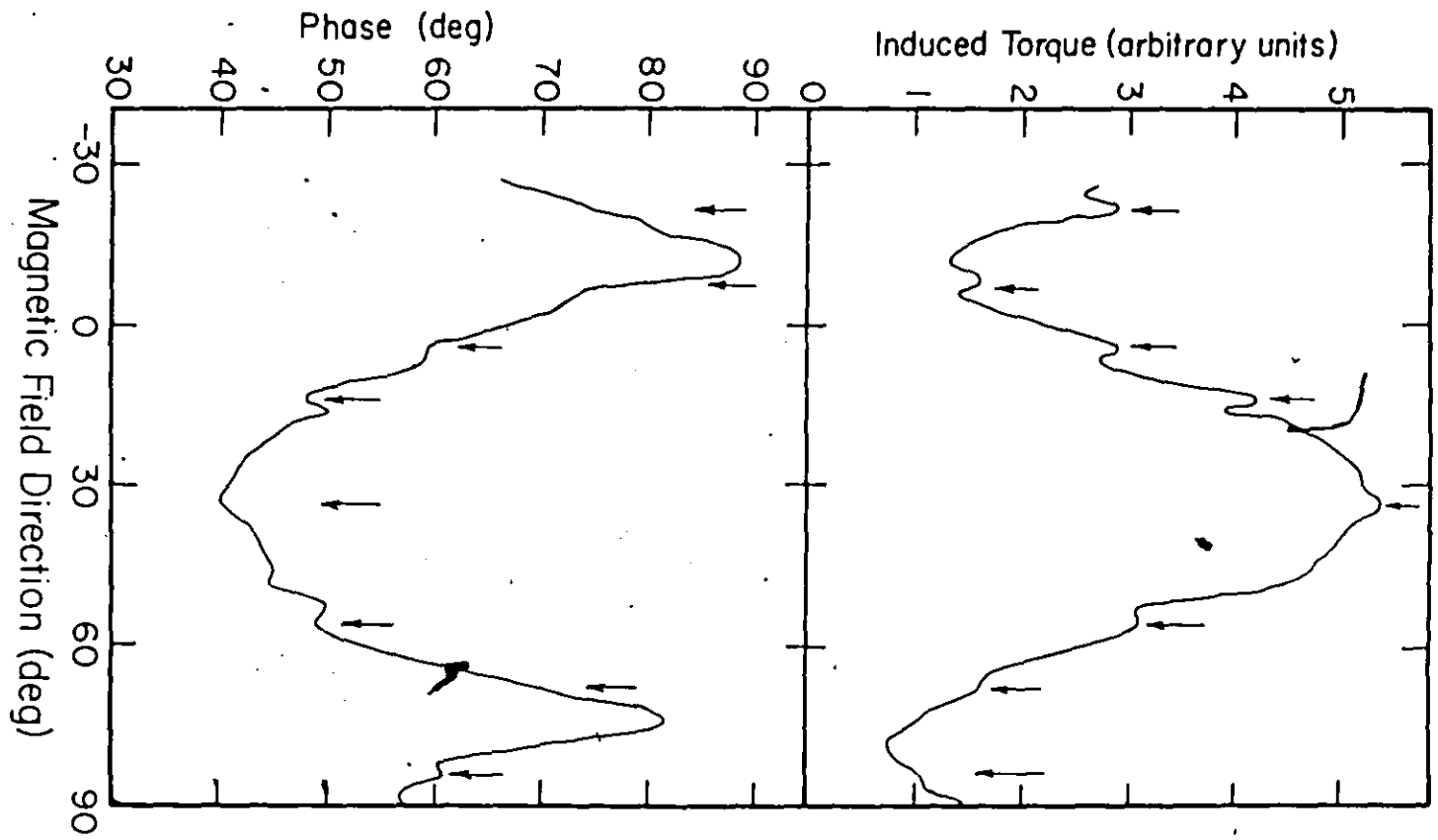

Figure 6-7 The amplitude (a) and phase (b) of the induced torque measured simultaneously on sample KM9. Data were taken at 5.5 T corresponding to $\omega_c\tau = 150$. Arrows give the magnetic field directions of the structure peaks in amplitude. The magnitude of the phase shift is reduced as described in Chapter 3v.

over equal angular ranges as minima in the induced torque phase. This is characteristic of open orbits for which there are narrow maxima in the induced torque amplitude and corresponding narrow minima in the phase.

CHAPTER 7

DISCUSSION: HIGH FIELD INDUCED TORQUE

i) Evidence for Open Orbits

The induced torque from open orbits has three features: there are sharp peaks as a function of magnetic field direction, the amplitude of the induced torque at a peak varies quadratically with magnetic field and the magnetic field directions of induced torque peaks lie along great circles in a stereographic projection.

The induced torque in potassium as shown in figures 5-1 to 5-3 exhibits sharp peaks of width 2° to 3° as a function of magnetic field direction. The magnetic field dependence of the induced torque at peaks as shown in figure 5-7 can be fit by a power law of the form aB^{υ}. The exponent υ is found to vary between 1.5 and 3. It can be seen from figures 5-8 and 5-10 that each "family" of induced torque peaks lies along a great circle as would be expected if each "family" resulted from an open orbit. The phase of the induced torque shown in figure 6-7 shows sharp decreases in the directions of the sharp peaks as is characteristic of open orbits. Thus the induced torque structure in potassium has the character of open orbits in a metal.

The induced torque as a function of magnetic field direction shown in figure 5-3 can be used to provide an estimate

of the open orbit strength for a model Fermi surface consisting of a sphere and a cylinder. Discussion of possible causes for the open orbits will be deferred until later.

Application of equation (3-23) indicates that the torque expected for a free electron metal with conductivity equal to that of potassium corresponds to the minimum of the induced torque pattern shown in figure 5-3. $\omega_c\tau$ was estimated to reach 2 in the magnetic field range between 0.04 and 0.08 T for this sample. Thus $\omega_c\tau$ is between 200 and 400 at 8 T.

The cylinder is assumed to contain a fraction η of the carriers. If both components of the Fermi surface have equal scattering rates the conductivity tensor is

$$\overleftrightarrow{\sigma} = \sigma_0 \begin{vmatrix} \frac{1}{1+(\omega_c\tau)^2} & \frac{-\omega_c\tau}{1+(\omega_c\tau)^2} & 0 \\ \frac{\omega_c\tau}{1+(\omega_c\tau)^2} & \frac{1-\eta}{1+(\omega_c\tau)^2} & 0 \\ 0 & 0 & 1-\eta \end{vmatrix} \tag{7-1}$$

when open orbits are not excited and

$$\overleftrightarrow{\sigma} = \sigma_0 \begin{vmatrix} \frac{1-\eta}{1+(\omega_c\tau)^2} & \frac{-\omega_c\tau}{1+(\omega_c\tau)^2}(1-\eta) & 0 \\ \frac{\omega_c\tau}{1+(\omega_c\tau)^2}(1-\eta) & \frac{1-\eta}{1+(\omega_c\tau)^2} + \eta & 0 \\ 0 & 0 & 1 \end{vmatrix} \tag{7-2}$$

when the open orbits are perpendicular to both the magnetic field and the rotation direction.

Equation (3-30) can be used to find the torque in each case. For the open orbits not active

$$N_y \propto \frac{2-\eta}{(2-\eta)^2+(1-\eta)(\omega_c\tau)^2} \tag{7-3}$$

while for an open orbit direction perpendicular to the magnetic fields the torque is

$$N_y \propto \frac{2+\eta((\omega_c\tau)^2-1)}{(4-2\eta)+(\omega_c\tau)^2(1+\eta)} . \tag{7-4}$$

Table 7-1 gives the required open orbit fractions at several values of $\omega_c\tau$. Of order 0.01% of the carriers are required to produce each peak.

ii) Anisotropic Torque from Closed Orbits

Before expending a great effort examining possible sources of open orbits in potassium it is useful to consider a related question. Can induced torque having the character of open orbits be observed in a metal with only closed orbits? Induced torque peaks would result in potassium if the current loops were tilted through a small angle from the direction predicted for a nearly free electron metal. The problem can be studied in two steps. First the required angle of tilt can be calculated and then the possible causes for such a tilt considered.

The angle ε between the axis of the current loops and the x axis for a free electron metal is given by

Table 7-1

Required open orbit fraction to give torque peaks

$\omega_c\tau$	angle between open orbit and rotation axis	open orbit fraction for peaks 4× background
25	$\pi/2$	96×10^{-4}
50	$\pi/2$	24×10^{-4}
100	$\pi/2$	6.0×10^{-4}
200	$\pi/2$	1.5×10^{-4}
400	$\pi/2$	$.38\times10^{-4}$
400	$\pi/4$	$.75\times10^{-4}$
400	$\pi/6$	1.5×10^{-4}

Table 7-2

Angle by which current loops are tilted out of rotation plane

$\omega_c\tau$	ε for free electron metal	ε to increase torque by 4×	change	ε to increase torque by 8×	change
25	85.43°	80.82°	4.6°	76.96°	8.5°
50	87.71	85.42	2.3	83.51	4.2
100	88.85	87.71	1.15	86.76	2.09
200	89.43	88.83	0.57	88.38	1.05
400	89.71	89.43	0.29	89.19	0.52

$$\tan\varepsilon = \frac{\omega_c \tau}{2} \quad . \tag{7-5}$$

The induced torque is given by

$$N_y \propto \cos^2\varepsilon = \sin^2\lambda \tag{7-6}$$

where $\lambda = 90-\varepsilon$. The angle λ must increase to $\lambda+\delta$ to increase the torque by a factor s. δ is found from equation (7-6) to be

$$\delta = (\sqrt{s}-1)\lambda \quad . \tag{7-7}$$

Thus both λ and δ are proportional to the inverse of $\omega_c\tau$. The change in ε required to increase the induced torque by the factor shown in figure 5-3 is given in Table 7-2.

Thus a change in ε of only a fraction of a degree at large $\omega_c\tau$ gives the observed change in induced torque. By contrast $\omega_c\tau$ must change by a factor of 2 to give a comparable change in torque. A change in ε can occur due to a change in the electric field distribution or a change in the direction of the rotation axis due to a variable compliance of the rotor support.

The electric field in the sample is given by

$$\vec{E} = \overleftrightarrow{\rho}\vec{J} \tag{7-8}$$

where $\overleftrightarrow{\rho}$ is the conductivity tensor. The current density for current loops tilted through an angle ε in cartesian co-ordinates is

$$j_z = k'\sqrt{x^2+y^2} \tag{7-9a}$$

$$j_x = k'Z\cos\varepsilon \tag{7-9b}$$

$$j_y = k'Z\sin\varepsilon \tag{7-9c}$$

where ε is found from equation (3-13) and k' is a constant. For the resistivity tensor of a free electron metal $\rho_{xx} = \rho_{yy} = \rho_{zz} = \rho_0$ and $\rho_{xy} = \rho_{yx} = \rho_0\omega_c\tau$ the electric field is

$$E_{x0} = kZ(\cos\varepsilon - \omega_c\tau\sin\varepsilon) \tag{7-10a}$$

$$E_{y0} = kZ(\sin\varepsilon + \omega_c\tau\cos\varepsilon) \tag{7-10b}$$

$$E_{z0} = k'\sqrt{x^2+y^2} \tag{7-10c}$$

with the constant of proportionality k the same for each term. These electric fields are just those created by the changing magnetic field and the boundary conditions. If the axis of the current loops is at an angle $\varepsilon-\delta$ where δ is small, the electric field is

$$E_x = kZ(\cos\varepsilon - \omega_c\tau\sin\varepsilon) + kZ(\sin\varepsilon - \omega_c\tau\cos\varepsilon)\delta \tag{7-11a}$$

$$E_y = kZ(\sin\varepsilon + \omega_c\tau\cos\varepsilon) - kZ(\cos\varepsilon + \omega_c\tau\sin\varepsilon)\delta \tag{7-11b}$$

and E_0 is unchanged. The first term in each expression is the electric field created by the sample motion in a magnetic field while the second term is the extra field $\delta\vec{E}$ required to cause the tilting. The extra electric field in the limit $\omega_c\tau$ goes

to infinity and λ to zero are

$$\delta E_x = kZ(\sin\varepsilon - \bar{\omega}_c \tau \cos\varepsilon)\delta = 0 \tag{7-12a}$$

$$\delta E_y = kZ(\cos\varepsilon - \omega_c \tau \sin\varepsilon)\delta = kZ \tag{7-12b}$$

where δ is the tilt of the open orbits given by equation (7-7). The extra field required is independent of field and in the x direction. This field can be compared to the fields E_0 given by equation (7-10). In the limit of high field, the electric fields become

$$E_{x0} = -\omega_c \tau kZ. \tag{7-13a}$$

$$E_{y0} = kZ \tag{7-13b}$$

The field in the x direction increases linearly with field. Therefore the constant field required to tilt the current loops through an angle δ becomes a small fraction of the existing electric field which creates the current loops. It is important to note as well that the required field need only exist near the tips in the sample as shown in figure 7-1. Fields in the x direction at Z = 0 would rapidly be cancelled by a surface charge since the sample can not support currents in that direction. The sample in figure 7-1b shows how such a field could arise. The current loops are forced to bend around a pit in the sample. This requires an additional electric field symmetric about the pit. However those currents flowing

Figure 7-1 a) The region of the sample for which electric fields are most effective in tipping the current loops.

b) The distortion of the current flow around a void which can cause the current loops to tilt.

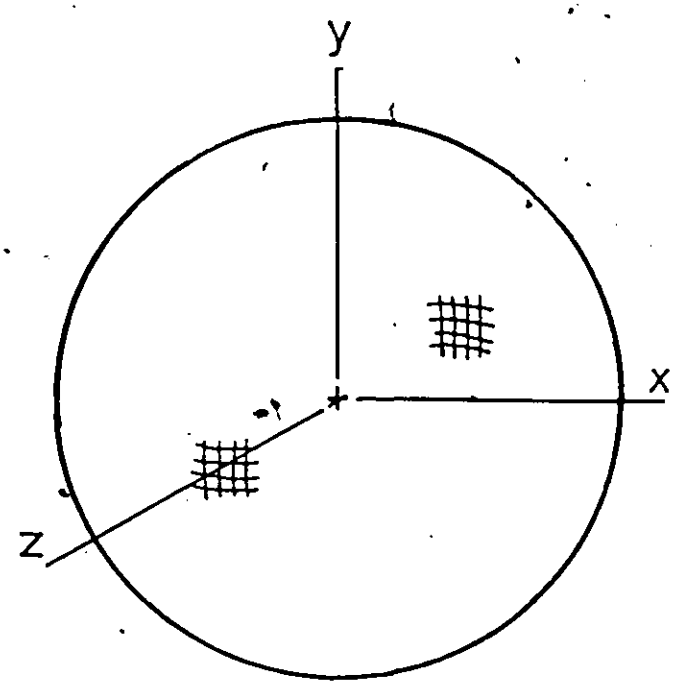
y
x
z

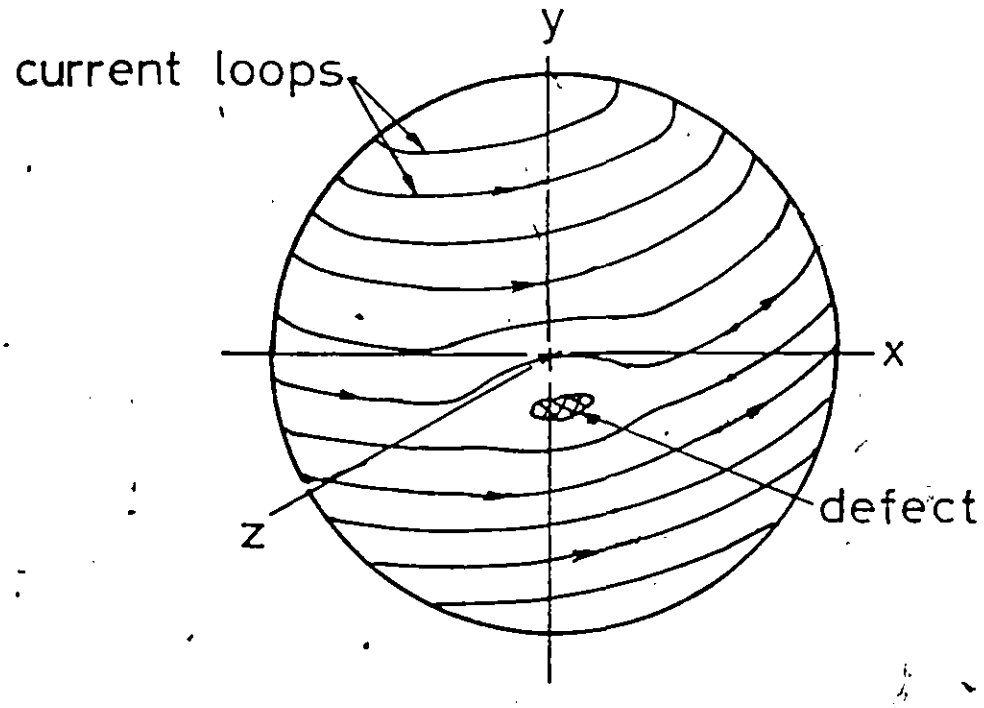
y
current loops
x
z
defect

above the pit have a larger y component and greater effectiveness than those flowing below the pit, leaving a net tilt of the current loops. This, however, gives an effect slowly varying with magnetic field direction. The tilt is zero when the defect is aligned parallel and perpendicular to the field and reaches some maximum values between those positions. The compliance of the rotating sample magnetometer for rotations perpendicular to the bearings is expected to vary by several percent as the rotor turns. This allows the angle between rotation axis and magnetic field and therefore the component of the total torque measured to vary. The variation of torque with angle due to this cause is, however, several percent and does not explain the measured variation by a factor of four.

Changes in compliance can, however, have a dynamical effect by giving an instantaneous rotation about the x-axis. This induces a moment which at high fields almost entirely along the x axis and so produces a torque. All of the torque is about the rotation axis, increasing the sensitivity of the magnetometer to these spurious torques by a factor of $\omega_c \tau$ relative to the sensitivity for desired induced torques.

Although this torque is proportional to rotation speed and so can not be separated directly it has several properties which would identify it. The compliance depends solely on the mechanical properties of the rotor and support bearings which do not vary with temperature, in contrast to the measured

data. The measured spurious torques do not depend on the sample properties. Peaks would be found in the same magnetic field direction for rotation in a series of planes in contrast to the results shown in figure 5-8.

A variable compliance changes the soft helicon resonant frequencies. If these resonances occur near the frequency of operation, typically 5 Hz small changes give rise to large changes in output.

An estimate of the soft helicon frequencies involved can be made using the relation developed by Delaney and Pippard (1972)

$$\chi(\omega) = \frac{C\mu_0}{WB^2} \tag{7.14}$$

where χ is the magnetic susceptibility of the sample, C the compliance of the support, μ_0 the susceptibility of free space, W the sample volume and B the magnetic field. The resonant frequency was found using the Ford and Werner (1973) calculation of $\chi(\omega)$ to be greater than 40 Hz at all magnetic fields used. Small changes in these resonant frequencies have negligible effect on magnetometer properties at 5 Hz and can be ingored. Thus the structure observed in this work can not be attributed to spurious torques caused by a variable compliance.

iii) Magnetic Field Dependence

The induced torque for an open orbit was predicted in Chapter 3 to depend on magnetic field according to a power law with exponent 2 while the data reported in Chapter 5 require an exponent between 1.2 and 3.5. It has been found experimentally in ReO_3 (Razavi and Datars 1979) and copper measured during this work that the induced torque at an open orbit peak is not strictly quadratic but can be fit by a power law with exponent between 1.3 and 2 depending on the angle between open orbit and rotation axis. Some metals such as $Hg_{3-\delta}AsF_6$ which experience magnetic breakdown of their open orbits (Dinser et al 1979) show induced torque peaks which increase faster than quadratically with magnetic field. Since the torque on open orbit carriers increases quadratically and the number of carriers increases exponentially due to magnetic breakdown in this case, the measured torque will vary with field as $B^2 e^{-B_0/B}$. Over a restricted range of magnetic field this can be fit by a power law with exponent greater than 2.

The magnetic field dependence of the induced torque in potassium is fully consistent with the presence of open orbits. It strongly suggests as well that the number of carriers in some open orbit directions is enhanced due to magnetic breakdown.

iv) Temperature Dependence

The induced torque changes from a maximum to a minimum in a specific magnetic field direction for temperature range of less than 0.1K. This corresponds to a change in thermal energy of less than 10^{-5} eV/particle. The total thermal energy in the temperature range 1 to 2K is ten times larger and the magnetic energy in a magnetic field of 4T fifty times bigger than the energy of the fluctuation. The Debye energy by a factor of 10^3 and the Fermi energy, by a factor of 2×10^5 exceeds the fluctuation energy. The energy scale of the temperature fluctuations is therefore at least an order of magnitude smaller than any other energy scale in the problem.

A change over a small temperature range could occur in a phase transition but in order to get the observed temperature variation a series of phase changes is required. While not impossible such a series of phase transformations is highly implausible and has no theoretical basis. It would require a correlated ground state with an energy scale similar to that of superconductivity.

It is not necessary however that open orbits be created or destroyed with increasing temperature in order to account for the observed temperature dependence of induced torque peaks. If the direction of the open orbits changes with temperature, then the magnetic field direction and amplitude of the resulting induced torque peaks also vary with temperature.

The amplitude of the induced torque observed in a specific magnetic field direction as a function of temperature will oscillate as peaks pass in front of the observing direction, like the continuously changing scene observed from the window of a moving train.

v) Sources of Open Orbits

Lass (1978) postulated a partial martensitic transition to a hexagonal close packed structure at low temperature. This would result in a tubular Fermi surface connected along the [0001] direction and thus open orbits. The effective medium theory previously developed for CDW domains is also appropriate. For such a mixture of randomly oriented hcp crystallites embedded in a bcc host the torque pattern would show peaks, due to the open orbits, which appear at a magnetic field determined by the domain size. The open orbits due to such a cause however would not have the observed temperature dependence.

There has been no other evidence presented for a martensitic transformation. Barrett (1956) with X-ray scattering and Werner, Eckert and Shirane (1980) with neutron scattering saw no evidence of a phase transition at low temperature. In addition, the dHvA effect (Altounian, Verge and Datars 1978) showed a Dingle temperature of 0.2K which was not affected by repeated temperature cyclings unlike sodium which does exhibit a martensitic transformation (Barrett 1956). Temperature

cycling in sodium induced the transformation as indicated by an increased Dingle temperature and finally a disappearance of dHvA oscillation (Elliott and Datars 1982). This variety of evidence indicates a martensitic transformation in potassium is highly unlikely and so will not be considered further.

The presence of additional free electrons due to the replacement of potassium ions by impurities of higher valence would, for large enough impurity concentrations, give rise to a Fermi sphere which crossed the Brillouin zone boundary. However for impurities of valence 2 the impurity fraction would have to be 0.3 to change the Fermi wavevector from 0.62 $2\pi/a$ to 0.68 $2\pi/a$ as required to produce open orbits. This is more than 4 orders of magnitude larger than the known part per million level of valence 2 impurities.

The crystal does not have perfect cubic symmetry due to the presence of small strains. A spatial average of the structure factor for the [100] reflection will no longer be zero but rather have a small finite value. The level of strain required to give an energy gap 1% of the known (Overhauser 1968) 0.39 eV gap in the [110] direction, was calculated. The structure factor was calculated for the [100] direction as

$$S \propto \langle 1+(1+\delta)e^{i\vec{k}\cdot\vec{r}_i}\rangle \ . \qquad (7\text{-}15)$$

For the distorted lattice the form factor is $1+\delta$ where δ is the fractional displacement of the lattice from cubic.

The structure factor varies linearly with fractional distortion, a 0.1% distortion of the lattice from cubic in one direction. These values are much larger than any measured lattice distortion which could be seen most clearly as a change from cubic symmetry in the measured dHvA frequency.

The preceding indicates that the cause of the open orbit torque must be either an intrinsic effect or an extrinsic effect associated with macroscopic inhomogeneities.

vi) Charge Density Waves

The charge density wave model gives open orbits as shown in Chapter 2. Indeed, one of the problems in doing a quantitative analysis of the CDW model is an embarassing wealth of open orbits. The strength of energy gaps giving rise to open orbits is of necessity only an order of magnitude estimates.

The large number of open orbits observed (20 to 30 in a 180° rotation) is qualitatively in agreement with the CDW model. The results of Figures 5-8 and 5-9 show 15 and 12 open orbits respectively lie along a great circle in a stereographic projection. Any great circle through the crystal will pass through, at most, 9 of the 24 possible domains. Thus, if more than 9 open orbit directions lie along a great circle, there must be more than one open orbit per domain, regardless of the relative orientation of the open orbits in a domain. This is qualitatively in agreement with the prediction of the CDW model

Figure 7-2 The induced torque calculated with the charge density wave model for rotation in the same plane as Figure 5-2. The value of Π was chosen to fit the data at 8 T. There are five open orbits of equal strength in each of 24 domains. The open orbits chosen are those shown in Figure 2-5.

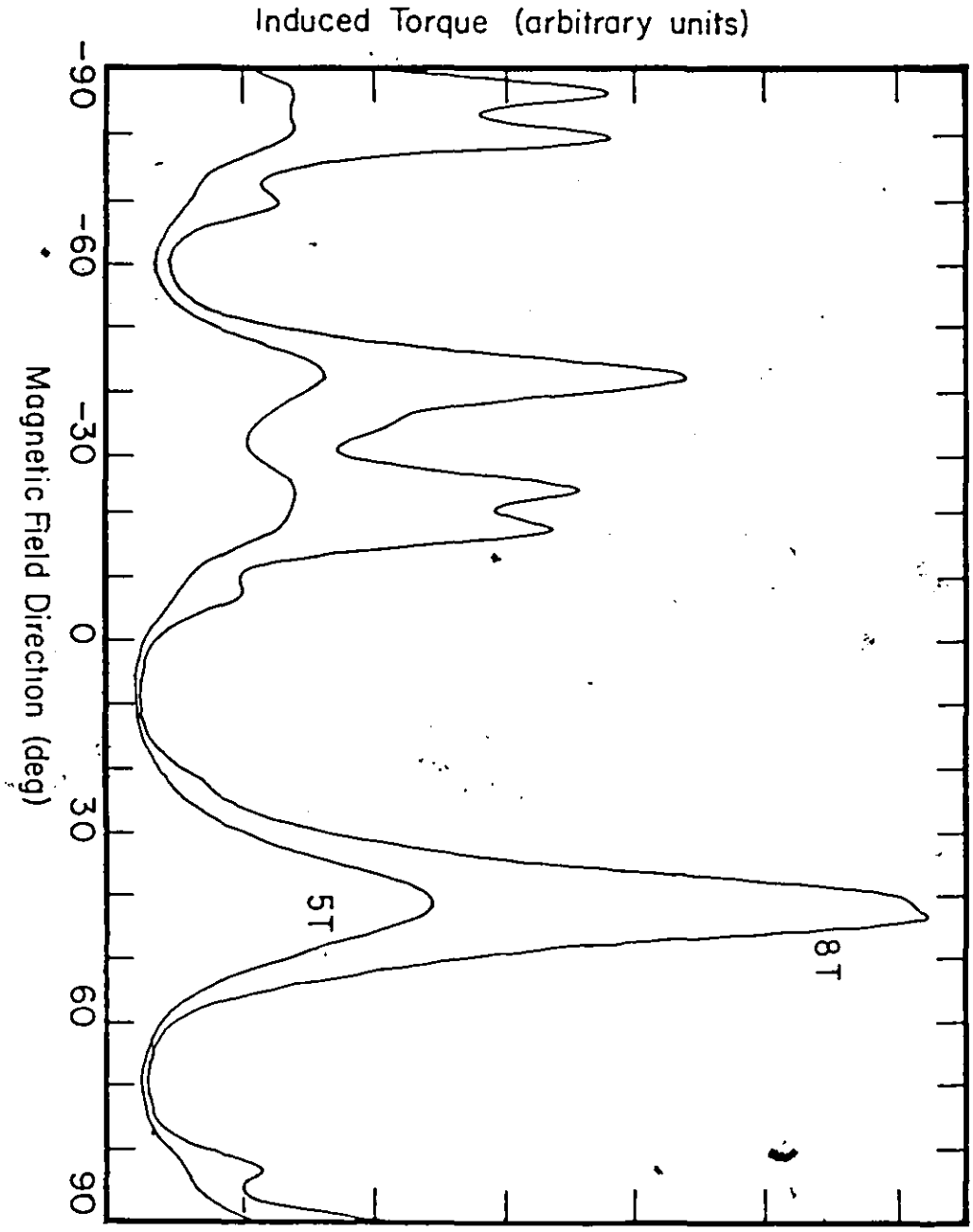
Induced Torque (arbitrary units)
8T
5T
-90
-60
-30
0
30
60
90
Magnetic Field Direction (deg)

that there are 5 open orbits per domain.

The torque pattern predicted from the CDW model as shown in figure 7-2 can be compared directly to the measured induced torque shown in figure 5-3. The conditions for figure 7-2 will be described below.

Detailed quantitative agreement is however much more difficult to attain. The expected open orbit directions calculated using the Q vector direction predicted by Guiliani and Overhauser (1979) are shown on a stereographic projection in figure 7-3. Each group of five open orbit directions per domain predicted in figure 2-5 lies along a great circle through a <110> direction. The open orbit directions lie within 5° of {111} planes with 30 open orbits per plane. This can be compared to the results shown in figures 5-9 and 5-11. The results in figure 5-11 for sample KM7 show all open orbit peaks lie along one great circle. This is consistent with a charge density wave state in a material in which 6 of the 24 possible domains exist. The sample was not X-ray oriented so it was not possible to identify the crystallographic plane along which the open orbit directions lie.

For sample KO2, as shown in figure 5-9, most open orbit directions lie near a lattice plane. In this case, it is a {321} plane. This is not consistent with the charge density wave model. The CDW wavevector must lie near a [110] direction or require a large energy penalty. Changing the

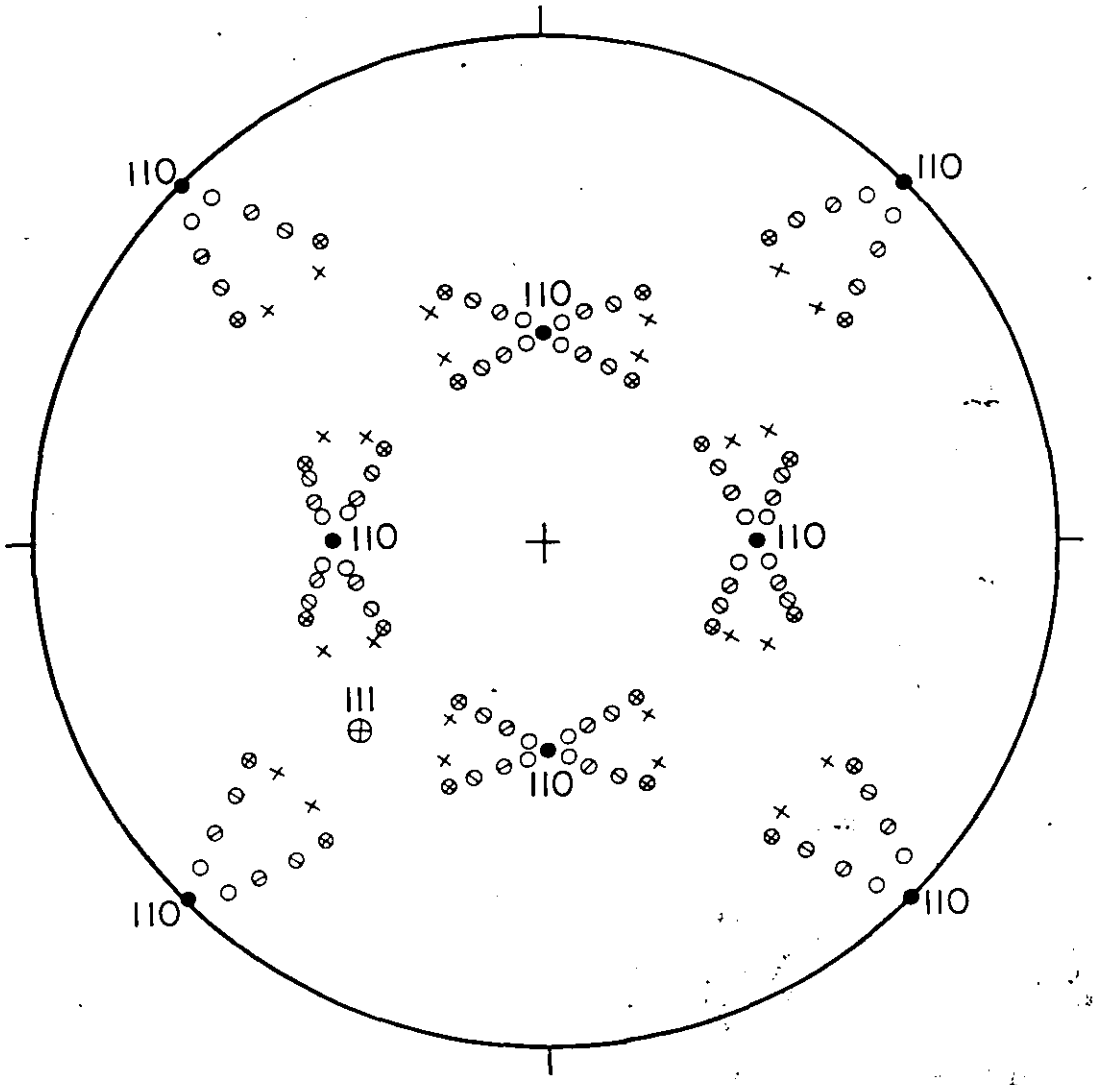

Figure 7-3 Stereographic projection showing the predicted open orbit directions (Table 7-3). The open orbits are $\vec{Q}$(o), $\vec{Q}$-$\vec{Q}'$(⊘), $\vec{Q}$-2$\vec{Q}'$(⊗), $\vec{Q}$-3$\vec{Q}'$(●), $\vec{Q}'$(x).

angle between the plane in which the CDW $\vec{Q}$ vector and [110] direction lie will only increase the scatter of the open orbit directions from {111} planes until open orbits are almost uniformly distributed through space. It is not possible to find any other plane in space along which open orbits would be densely packed. The induced torque due to a CDW ground state was calculated and compared to the measured induced torque in potassium.

In a homogeneous material with an open orbit direction as shown in figure 7-4, the induced torque due to the open orbit gives

$$N = \frac{A}{(\theta-\theta_0)^2+\Pi^2} \tag{7-16}$$

where $A \propto \sin^2\varphi$ and $\Pi \propto 1/\sin\varphi$ for rotation about the y axis.

The effective medium calculation by Huberman and Overhauser (1981) for a multidomain sample does not change the form of equation (7-16) or the value of θ_0. However it makes the value of A smaller and Π larger. The value of A is proportional to magnetic field squared and Π is proportional to inverse field above a minimum field which depends on domain size. The Hall coefficient in the multidomain samples is essentially unchanged from that of the homogeneous sample.

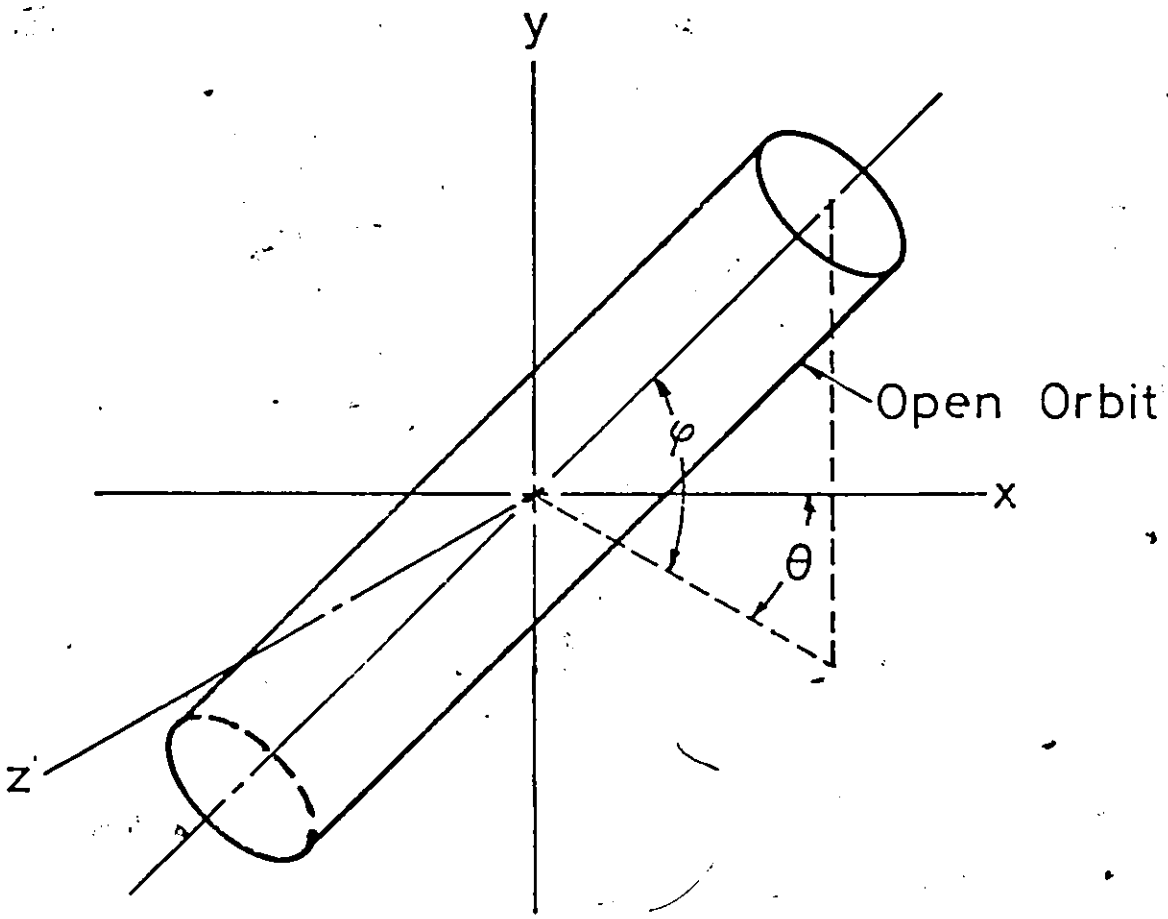

Figure 7-4 Notation for an arbitrarily oriented cylindrical section of Fermi surface.

The induced torque was calculated as a superposition of the torque due to 5 open orbits in each of 24 domains. Each domain was assumed to contribute equally to the induced torque and each open orbit was assumed to have the same number of carriers. A value of the constants A and Π was chosen to match the data at a particular field. Results of this calculation for a specific rotation plane are shown in figure 7-2. There are only 19 peaks resolved in this pattern since many of the 120 possible peaks occur at the same angle or are too small in amplitude to contribute. Induced torque peaks also do not occur in those singular directions for which two open orbit directions are perpendicular to the magnetic field and each other.

Quantitative agreement however is not possible with the CDW model. This is not surprising in view of the strong temperature dependence observed in the data. The CDW model as described does not predict temperature dependent open orbits.

There are however a number of properties of the CDW open orbits which could vary with temperature.

Since the individual peaks are not resolved at the magnetic fields used in these experiments, a change in relative intensity of the open orbits with temperature would cause the magnitude of the torque in a given direction to vary with temperature. The open orbits in the CDW model are listed in table 7-3. The presence of phasons can be expected to enhance some open orbits and break down others. The number of phasons

Table 7-3

Possible open orbits

Path	Direction	Temperature Dependence	T'
··· CC'··· ···AB···B'A'···	$\vec{Q}' = \vec{G}_{110} - \vec{Q}$	almost temperature independent	-7.5
···ABCC'B'A'···	$\vec{Q}$	strong increase	-1
···ABC···C'B'A'···	$\vec{Q}-\vec{Q}'$	strong increase	-1
···BCC'B'···	$\vec{Q}-2\vec{Q}'$	moderate decrease	3
···BC···C'B'···	$\vec{Q}-3\vec{Q}'$	moderate decrease	3

··· indicates a Bragg reflection

will be highly anisotropic since it requires much less energy to change the direction of the $\vec{Q}$ vector than to change its length. A scattering event which scatters an electron over the energy gap instead of allowing it to reach the gap and be Bragg reflected will degrade the strength of the open orbits. An electron which is scattered to a Bragg reflected section of the Fermi surface will act as though it is on an open orbit (Hsu and Falicov 1979). These effects are indicated schematically at the two energy gaps BB' and AA' in figure 7-5.

An increase in the number of phasons will decrease the number of open orbit carriers along BB'. This occurs since there are many more phasons with wave vector parallel to the open orbit. Most will therefore scatter electrons along the closed orbit. The energy gap at AA' occurs at a point and no open orbit carriers are allowed. Thus any phasons which scatter electrons near the gap will enhance the number of open orbit carriers.

There are few phasons with wave vector parallel to either the open or closed orbit path at energy gap CC' and so the hetrodyne gap is expected to be insensitive to the number of phasons. The number of phasons increases with temperature and the phasons are expected to have a Debye temperature of the order 6K (Overhauser 1978). The phason number will thus vary strongly over the temperature range observed experimentally. The change in relative intensity of the open orbits is listed in table 7-3. The change in open orbit strength was incorporated

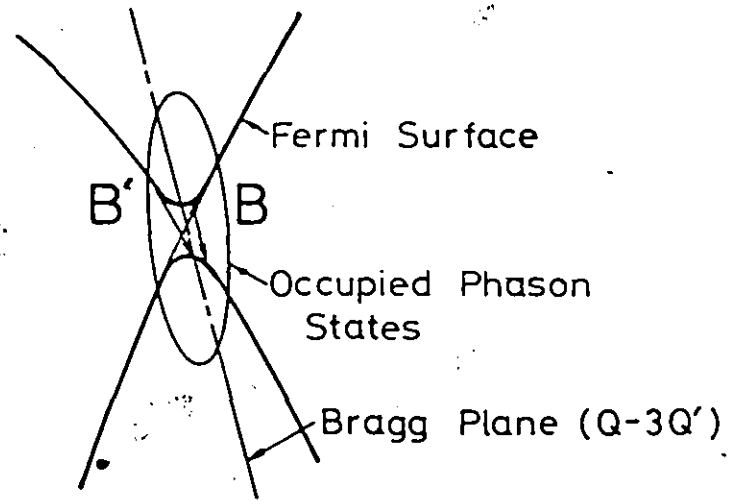

Figure 7-5 a) Electron scattering by phonons (→) to break down open orbits at the phason energy gap B'B.

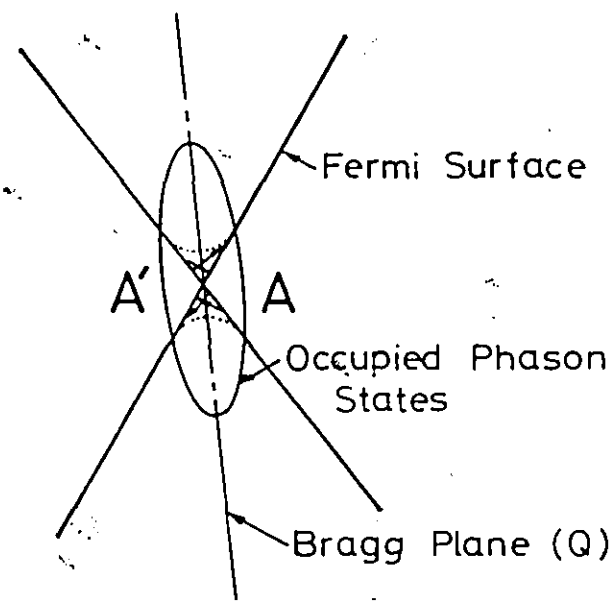

Figure 7-5 b) Electron scattering by phasons (→) to create an open orbit at the main CDW energy gap A'A.

into the program by allowing the number of carriers in each open orbit to vary according to

$$\frac{1}{e^{\frac{T-T_0}{T'}} + 1} \quad . \tag{7-17}$$

This simple relation roughly models a Debye relation. The temperature T_0 at which all open orbits have equal numbers of carriers was chosen to be 3K for all open orbits. The parameter T' for each open orbit was chosen to model the behaviour predicted in table 7-3.

The orientation of the $\vec{Q}$ vector occurs in a weak potential minimum as calculated by Guiliani and Overhauser (1979) and reproduced in figure 2-3. The thermal energy required to change the orientation of the $\vec{Q}$ vector by 1° was calculated to be less than 1K. A temperature dependence of the $\vec{Q}$ vector orientation leads to strong temperature dependence for the directions of some open orbits. The orientation of $\vec{Q}'$ is very sensitive to the orientation of $\vec{Q}$ as shown in figure 7-6. The hetrodyne gaps are tilted through an angle of 45° for a change of 3° in the alignment of $\vec{Q}$. Therefore the hetrodyne gaps are much more temperature sensitive than $\vec{Q}$. The remaining open orbits, formed by combinations of $\vec{Q}$ and $\vec{Q}'$, show intermediate temperature sensitivites. The existence of thermal energies comparable to the energy required to rotate the $\vec{Q}$ vector through a small angle does not imply the orientation of $\vec{Q}$ changes. It leads instead to oscillation of the $\vec{Q}$ vector

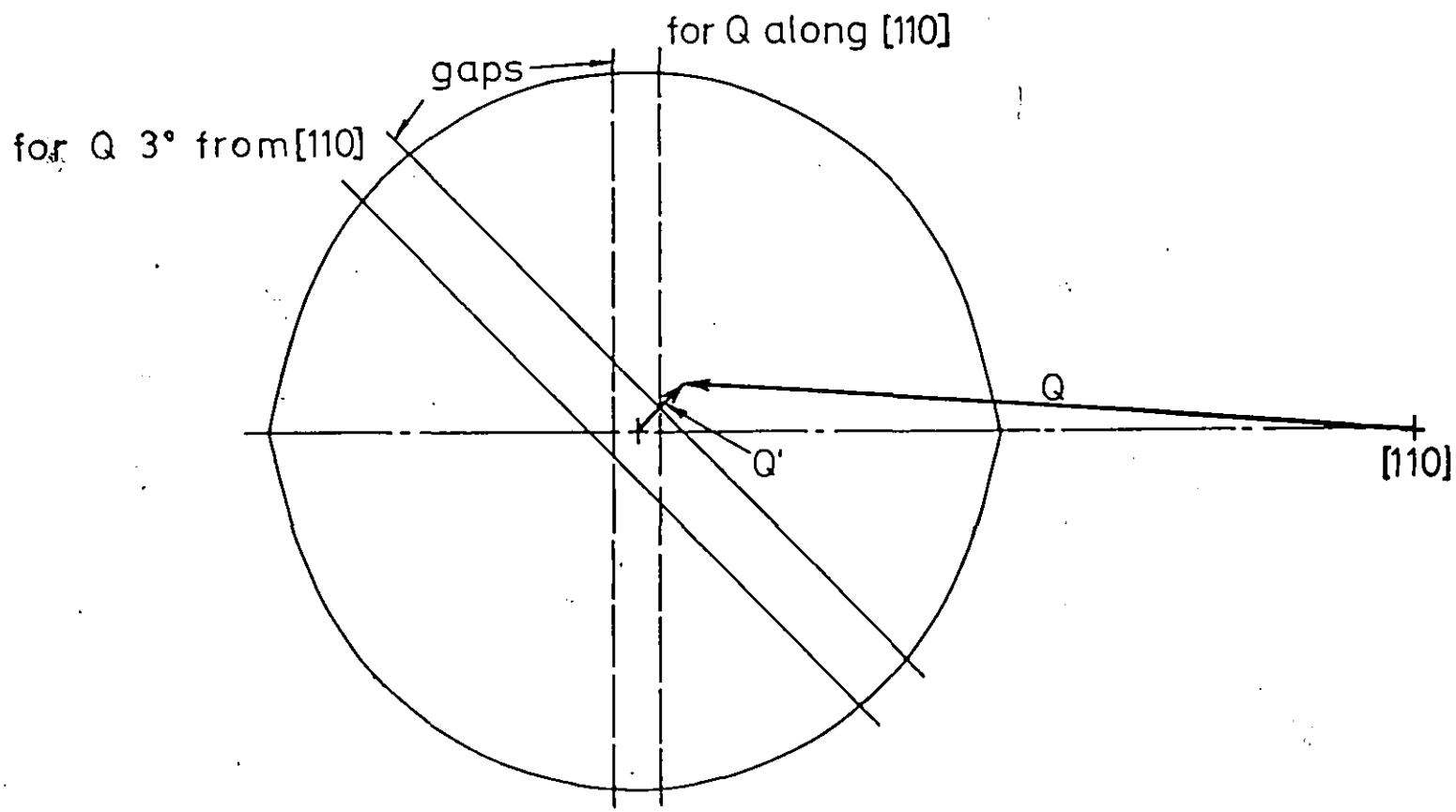

Figure 7-6 The effect of changing the direction of the CDW wavevector on the direction of the hetrodyne energy gap. The $\vec{Q}$ vector is tilted through an angle of 3° to tilt $\vec{Q}'$ through 45°.

about its equilibrium position, the effect already named phasons. Only the asymmetry in the energy minimum would cause the average orientation of the $\vec{Q}$ vector to change, analogous to anharmonic corrections to phonon dispersion curves.

The effect of these temperature dependent corrections on the CDW model was studied. The number of open orbit carriers was allowed to vary as postulated in Table 7-3. The resulting induced torque patterns are shown in figure 7-7a for temperatures of 1.4 and 1.6 K. The direction of the $\vec{Q}$ vectors was allowed to vary at the rate of 1°/K with open orbits of equal amplitude. The results are shown in figure 7-7b. Both the direction and number of open orbit carriers were allowed to vary to get the results shown in figure 7-7c.

The above calculations show that it is possible to get a temperature dependent induced torque within the charge density wave model. However even with the parameters used to obtain figure 7-7c which can be considered an extreme case the calculated temperature dependence of the torque is less than that measured.

At low magnetic fields it is no longer possible to resolve individual peaks and the induced torque is formed of a series of broad peaks. This however is not the same as the four-fold torque as has been suggested (Overhauser 1982) since it differs in several important respects. The measured four-fold torque consists of exactly two peaks in a 180° rotation with minima strictly separated by 90°. This is in

Figure 7-7 Induced torque as a function of magnetic field direction for temperatures separated by 0.2K for (a) the number of open orbit carriers varying according to Table 7-3, (b) the direction of the CDW wavevector varying at $1^{\circ}/K$ and (c) the number of carriers and direction of CDW wavevector by varying simultaneously.

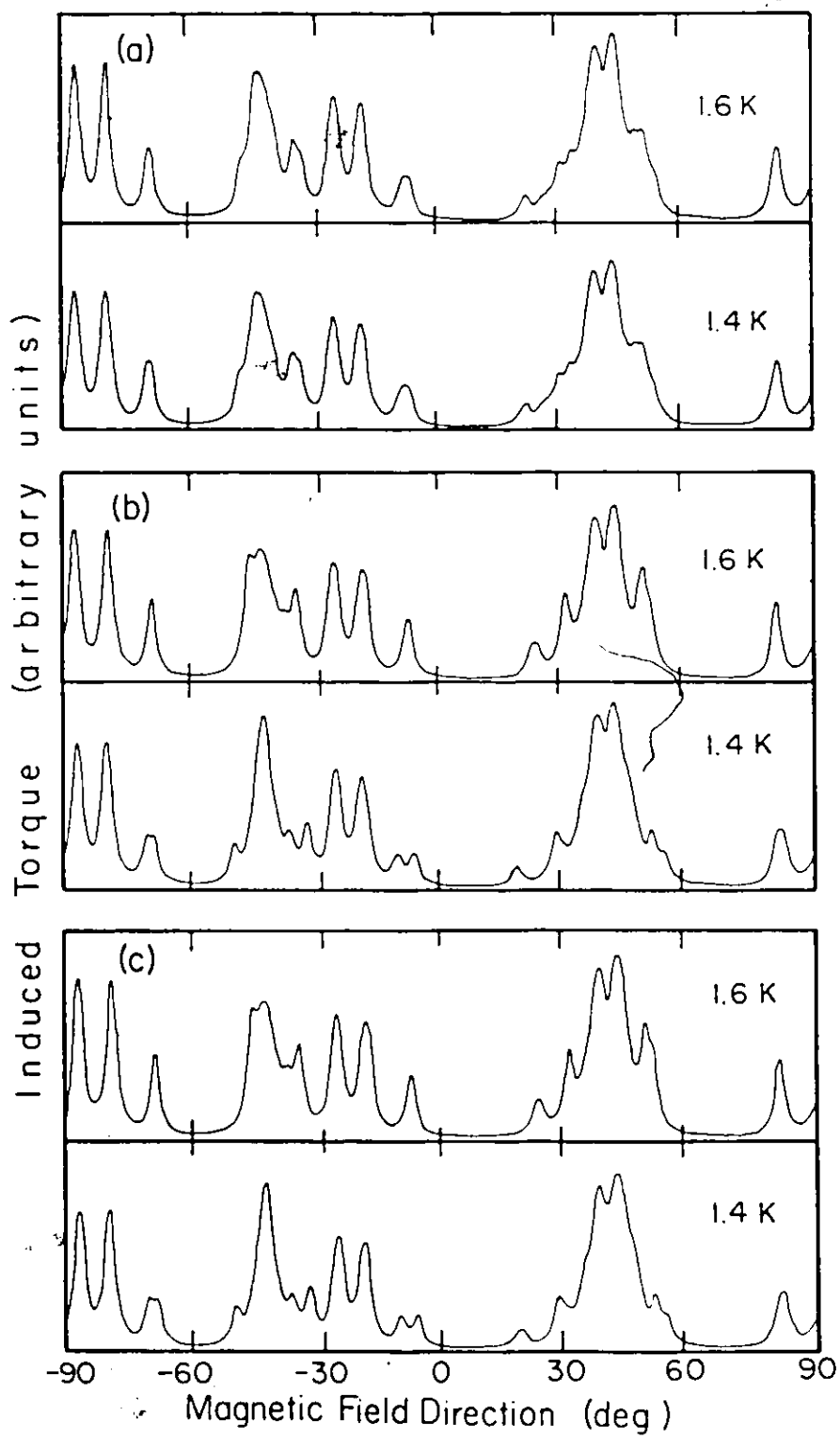
(a)
1.6 K
1.4 K
(b)
1.6 K
1.4 K
(c)
1.6 K
1.4 K
Induced Torque (arbitrary units)
-90
-60
-30
0
30
60
90
Magnetic Field Direction (deg)

contrast to the calculated data which shows two to three peaks in a 180° rotation and 60 to 120° between minima, depending on rotation plane. Therefore the four-fold torque is attributed to a different cause as described in Chapter 6.

vii) Imperfections

The presence of crystal imperfections has long been postulated, without any specific model, as the cause of the anomalies observed in potassium. A synthesis of the various models used to explain defect data was examined and compared to the data measured in this work. These imperfection models must incorporate two features, a magnetoresistance which is also anisotropic with magnetic field direction. The possible types of imperfections can be classed in three broad categories, point defects, extended defects and macroscopic inhomogeneities.

Point defects include vacancies, interstitials and substitutional impurities. They scatter electrons isotropically and independently of temperature. These imperfections were shown by Landaur (1978) not to contribute to the magnetoresistance and so do not feature in the present problem.

Extended defects are formed by dislocations or strings of vacancies. These provide anisotropic scattering centers for electrons. Some success has been achieved by Kaveh, Wiser (1981) and co-workers in explaining the sample dependence

of the electrical resistivity in terms of the contribution of anisotropic scattering at zero magnetic field. the anisotropy of scattering is enhanced at finite magnetic fields. Following a suggestion by Chambers (1968) it can be shown that the presence of dislocations will lead to a linear magnetoresistance. For an electron making a cyclotron orbit around a dislocation a complete orbit in K space results in the electron being displaced in real space by the Burgers vector. This provides an effective open orbit. For a material with a uniform spatial distribution of dislocations the open and closed orbit components are interlaced with no domain boundary between them. The number of electrons making an orbit around a specific dislocation, however, varies as the cyclotron radius or inverse field. Thus the contribution to the resistivity tensor will be strictly linear since each open orbit contributes as magnetic field squared and the number of open orbits decreases as inverse field.

The spacing between dislocations is of order 6×10^{-6} m and the Burger's vector of order 3×10^{-10} m for a sample with dislocation density $10^{11}/m^2$, a result expected to be appropriate in the sample used (Adlhart et al. 1981). For magnetic fields of 0.5 T a cyclotron orbit will intersect an average one dislocation. Thus for fields from 0.5 to 100 T when the cyclotron orbit becomes comparable to the dislocation core size there will be linear magnetoresistance. An isotropic distribution of

dislocations does not, however, give rise to the anisotropic induced torque measured.

Macroscopic inhomogeneities include all defects with linear dimensions greater than a mean free path. Examples include clusters of point defects or extended defects, regions of localized strain, preferentially oriented arrays of dislocations, small angle grain boundaries, macroscopic voids or cracks and surface irregularities. A unique from of macroscopic inhomogeneity is a charge density wave domain. This particular "inhomogeneity", however, has been treated separately in Chapter 7 vi).

An irregular surface gives rise to narrow peaks in the induced torque pattern as shown for sample KM12 in figure 5-18. The irregular surface of KM12 did not, however, give rise to the temperature dependent peaks that appear at magnetic fields above 4T and which must be attributed to another more subtle cause. Macroscopic inhomogeneities have several effects on the magnetoresistance.

The presence of macroscopic voids gives rise to a strictly linear magnetoresistance proportional to the void fraction as shown by Sampsell and Garland (1976).

The magnetoresistance of cylindrical voids is highly anisotropic. The results of Beers et al. (1978) can be summarized as follows. For the current, magnetic field and cylinder axis perpendicular there is the greatest magnetoresistance. About 10% of this magneto-resistance occurs if the current and

magnetic field are parallel and both perpendicular to the cylinder axis. No magnetoresistance occurs if the cylinder axis is parallel to either the magnetic field or current.

The calculated void fraction is, however, several orders of magnitude larger than that measured. The above calculation is, however, expected to be valid even if the defects are comparable in size to the cyclotron radius. The presence of surface scratches and bumps was measured and calculated by Bruls et al. (1981) to provide a significant contribution to the linear magnetoresistance in aluminum in contrast to the measurements in indium by the same group (Beers et al. 1978) which did not show magnetoresistance for surface indentations. The actual irregularity in samples used is difficult to measure and correlate with the measured magnetoresistance.

Internal surfaces can lead to partial (Lass, 1978) or complete (Van Gelder, 1978) trapping of conduction electrons at internal extended defects. These features give rise to a linear magnetoresistance. This theory is given further credence by the calculation of Brown (1982) who shows the resistivity due to dislocations can be calculated in terms of a resonant level near the Fermi surface. In the case of potassium the level is postulated to be within 10^{-4} eV (1K) of the Fermi surface (Gantmakher and Kulesko 1975).

The above implies a very stringent set of criteria for possible defects to cause the measured induced torque. There

must be a preferentially oriented array of dislocations in the sample with the defects clustered largely near the sample surface. This can be justified for several reasons. dHvA experiments on samples prepared in the same way give good signals with Dingle temperature less than .2K. Therefore the average dislocation density must be small. Estimates by Gugan (1982) assuming the Dingle temperature entirely due to dislocation scatter gives $\rho_D < 7\times10^{11}$. The dHvA experiment is strictly a volume effect while the induced torque varies as R^5 so dislocations arrayed primarily at the surface will affect the torque signal much more than the dHvA signal. This is consistent as well with the measurements of O'Shea and Springford (1983). They showed the dHvA signal was isotropic when measured in the entire sample but became anisotropic when the dHvA effect was measured primarily in a surface layer. The four-fold induced torque was discussed in Chapter 6 in terms of a surface shell of higher resistivity.

For specific arrangements of the dislocations induced torque peaks occur. Assume a free electron metal with a single ring of dislocations inclined at an angle to the rotation plane as shown in figures 7-8a. The induced current loops shown as solid lines see a high resistivity region due to the dislocations. By tilting slightly to flow in the direction indicated by dashed lines the current loops flow in a lower resistivity plane parallel to the dislocations and so reduce power dissipation in the sample. The tilt in induced moment causes an

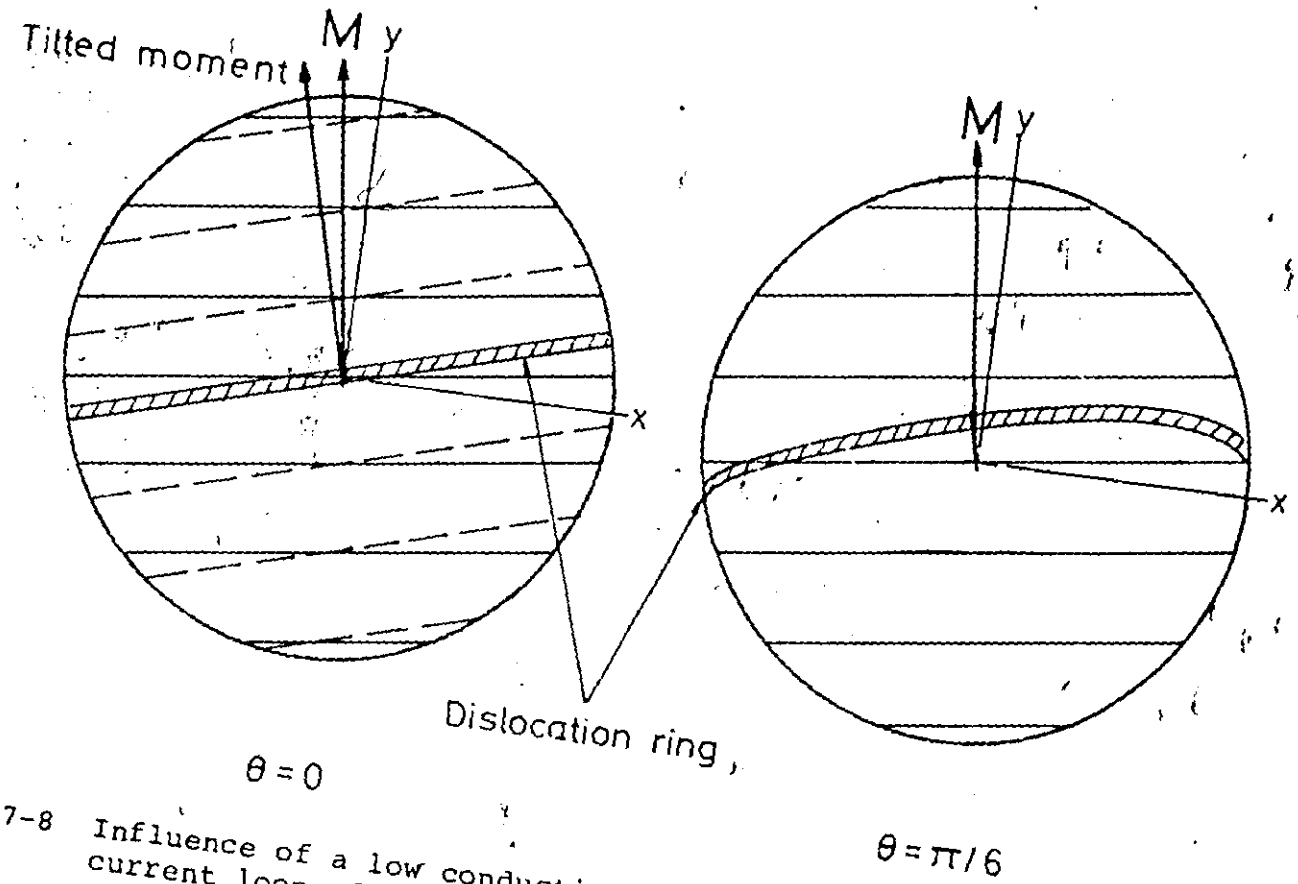

Figure 7-8 Influence of a low conductivity ring caused by imperfections on current loops for the axis of the ring, perpendicular to the magnetic field (a) and rotated through an angle of $\pi/6$ (b). In both cases the magnetic field is normal to the page.

increased torque as described in Chapter 7 ii).

When the sample is rotated as shown in figures 7-8b a small tilt no longer reduces the resistance seen by the current loops significantly, so they do not tilt. Therefore the induced torque is unchanged from the free electron value. The arguments presented above can be extended to the case of several rings of dislocations giving a mechanism for induced torque structure. The non uniform dislocation distribution causes a magnetoresistance which varies with direction in the sample. This gives rise to a slow variation in the induced torque with magnetic field direction in addition to the structure. It also causes the induced torque to increase nonuniformly with magnetic field. The present data is not sufficiently precise to identify such an effect if it occurs.

The question of the temperature dependence of the induced torque is however more speculative. Dislocations will not migrate at the 1 to 2K temperatures of these experiments. The defect recovery process in potassium was shown by Gurney and Gugan (1971) to occur in a series of broad stages centred at 4K, 15K, 40K and 115K. The lowest two stages consisted of interstitial and vacancy migrations, respectively - processes which do not affect the magnetoresistance. The migration of dislocations does not occur until the stage centred at 115K.

If the scattering rate is altered, however, by electrons trapped in states near the Fermi energy a temperature dependent scattering can result. As the temperature is raised

more electrons are excited out of the traps. This increases the scattering as electrons can be then scattered into the weakly bound states. The present model predicts a monotonic change in the torque in a specific direction. It is difficult to see how it could be extended to provide oscillations when the torque is measured in a particular magnetic field direction as a function of temperature.

It can be mentioned in passing that dislocations with trapped electrons provide a mechanism for changing the orientation of a charge density wave with temperature. CDW wavefronts would reduce their energy by aligning along the ribbons of static charge associated with dislocations. As the temperature was raised however, the static charge is reduced and the CDW wave vector could relax back to the direction established by lattice dynamics.

The presence of imperfections in a crystal has been suggested to lead to anisotropic magnetoresistance in a metal. The sharp peaks which appear about 5 T are however still unexplained by these models. In addition, the imperfection models do not explain the measured temperature dependence. More work should be expended on this theory however in light of the success a model of non-uniform conductivity has had in explaining the four-fold induced torque.

CHAPTER 8

CONCLUSIONS

The induced torque has been measured in potassium over the magnetic field range 0.005 to 8.5 T and over the temperature range 1.1 to 2.1 K. The induced torque was shown to be four-fold at magnetic fields above 0.2 T and have structure consisting of sharp peaks at fields above 4 T.

The structure consists of 20 to 30 peaks in a 180° rotation of the sample. These peaks have the character of open orbits in a metal. The structure varies non-monotonically in magnitude and direction as a function of temperature with the induced torque in a specific magnetic field direction varying from a maximum to a minimum in a temperature interval of less than 0.1 K.

The measured amplitude and phase of the four-fold induced torque agrees with the prediction of Lass' model for an ellipsoidal sample. The agreement obtained over a range of magnetic field up to 5.5 T and over a range of measurement frequencies from 2 to 10 Hz with a single adjustable parameter is quite good.

The induced torque structure is independent of the four-fold induced torque. The structure varies with temperature while the four-fold induced torque is temperature independent.

The structure torque does not depend on the shape of the sample while the four-fold induced torque can be increased by making the sample non-spherical. The amplitude of a structure peak is proportional to the same power of the magnetic field as the amplitude of the four-fold induced torque in the same direction.

The high field structure was compared to the predictions of two models, a sample imperfection model and a charge density wave model. Sample imperfections can cause induced torque peaks. However this model does not include a mechanism to cause the observed temperature and magnetic field dependence of the structure. More theoretical calculations on this largely untouched problem are warranted.

The existence of induced torque peaks is explained by the open orbits predicted in the CDW model. The number and magnetic field dependence of the observed induced torque peaks is in agreement with the predictions of the CDW model. A weak temperature dependence of the induced torque structure is expected in the CDW model. However the strong temperature dependence observed is not predicted by the CDW model. The observed magnetic field directions of the induced torque peaks are also not in agreement with the predictions of the CDW model.

The charge density wave model explains the largest number of the observed features of the induced torque in potassium. It is therefore tempting to say a CDW ground state is

established in potassium despite the features of the data still unexplained by the CDW model. However the results of this work can not be considered independently of other experiments such as the dHvA effect and nuclear magnetic resonance which do not support the CDW model.

This work was undertaken to test the charge density wave model in potassium and provides reasonable support for the CDW model. These tests do not fully establish the CDW model however because there are several unexplained features of the induced torque and other experiments which do not require a CDW ground state in potassium. A charge density wave ground state in potassium is therefore possible but not proven.

REFERENCES

Aldhart, W., Stetter, G., Fritsch, G., and Luscher, E. 1981. J. Phys. F, 11, 1347.

Altounian, Z., Verge, C., and Datars, W.R. 1978. J. Phys. F, 8, 75.

Barrett, Charles S. 1956. Acta Cryst., 9, 671.

Basinski, Z.S., Dugdale, J.S., and Howie, A. 1963. Phil. Mag., 8, 1989.

Beers, C.J., van Dongen, J.C.M., van Kempen, H., and Wyder, P., 1978. Phys. Rev. Lett., 40, 1194.

Bishop, Marilyn F., and Overhauser, A.W. 1977. Phys. Rev. Lett., 39, 632.

Bishop, Marilyn F., and Overhauser, A.W. 1978. Phys. Rev. B, 18, 2447.

Bishop, Marilyn F., and Overhauser, A.W. 1981. Phys. Rev. B, 23, 3627.

Boriak, M.L. 1980a. Phys. Rev. Lett., 44, 208.

Boriak, M.L. 1980b. Phys. Rev. B, 22, 6484.

Boriak, M.L., and Overhauser, A.W. 1978a. Phys. Rev. B, 17, 4549.

Boriak, M.L., and Overhauser, A.W. 1978b. Phys. Rev. B, 18, 6454.

Boriak, M.L., and Overhauser, A.W. 1978c. Phys. Rev. Lett., 41, 1066.

Brown, R.A. 1978. J. Phys. F, 8, 1159.

Brown, R.A. 1982. Can. J. Phys., 60, 766.

Bruls, G.J.C.L., Bass, J., van Gelder, A.P., van Kempen, H., and Wyder, P. 1981. Phys. Rev. Lett., 46, 553.

Chambers, R.A. 1968. Simon Fraser University lectures on solid state physics. Vol. 1 Electrons in Metals. Edited by Cochran, J.F., and Haering, R.R., Gordon and Breach, (New York, N.Y.), p. 283.

Chimenti, D.E., and Maxfield, B.W. 1973. Phys. Rev. B, 7, 3501.

Coulter, P.G., and Datars, W.R. 1980. Phys. Rev. Lett., 45, 1021.

Coulter, P.G., and Datars, W.R. 1982. Solid State Comm., 43, 715.

Datars, W.R., and Cook, J.R. 1969. Phys. Rev., 187, 769.

Datars, W.R. 1970. Can. J. Phys., 48, 1806.

Delaney, J.A., and Pippard, A.B. 1971. J. Phys. C, 4, 435.

Delaney, J.A., and Pippard, A.B. 1972. Rep. Prog. Phys., 35, 677.

Dinser, R.J., Datars, W.R., Chartier, D., and Gillespie, R.J. 1979. Solid State Comm., 32, 1041.

Di Salvo, F.J., and Rice, T.M. 1979. Physics Today, 32-4, 32.

Douglas, R.J., and Datars, W.R. 1973. Can. J. Phys., 51, 1770.

Elliott, M., and Datars, W.R. 1982. J. Phys. F, 12, 465.

Elliott, M., and Datars, W.R. 1983. J. Phys. F, 13, 1483.

Fletcher, R. 1977. Phys. Rev. B, 15, 3602.

Fletcher, R. 1980. Phys. Rev. Lett., 45, 287.

Fletcher, R. 1982. Can. J. Phys., 60, 679.

Follstaedt, D. and Schlicter, C.P. 1976. Phys. Rev. B, 13, 1017.

Ford, G.W., and Werner, S.A. 1973. Phys. Rev. B, 8, 3702.

Gantmakher, V.F., and Kulesko, G.I. 1975. Sov. Phys. JETP, 40, 1158.

Giuliani, G.F., and Overhauser, A.W. 1979. Phys. Rev. B, 20, 1328.

Giuliani, G.F., and Overhauser, A.W. 1980a. Phys. Rev. B, 21, 5577.

Giuliani, G.F., and Overhauser, A.W. 1980b. Phys. Rev. B, 22, 3639.

Giuliani, G.F., and Overhauser, A.W. 1980c. Phys. Rev. Lett., 45, 1335.

Giuliani, G.F., and Overhauser, A.W. 1982. Phys. Rev. B, 26, 1660.

Gugan, D. 1971. Proc. Roy. Soc. London A, 325, 223.

Gugan, D. 1982. J. Phys. F, 12, L173.

Gurney, W.S.C., and Gugan, D. 1971. Phil. Mag., 24, 857.

Hands, B.A., and Rosenberg, H.M. 1969. Acta Meta, 17, 455.

Ham, F.S. 1962. Phys. Rev., 128, 2524.

Harms, Peter, 1972. Ph.D. thesis, (Technischen Universität. Clausthal).

Hockett, R.S., and Lazarus, David 1974. Phys. Rev. B, 10, 4100.

Holroyd, F.W., and Datars, W.R. 1975. Can. J. Phys. 53, 2517.

Hsu, W.Y., and Falicov, L.M. 1975. Phys. Stat. Sol. B, 67, 325.

Huberman, M., and Overhauser, A.W. 1981. Phys. Rev. Lett., 47, 682.

Huberman, M., and Overhauser, A.W. 1982. Phys. Rev. B, 25, 2211.

Kapitza , P. 1929. Proc. Roy. Soc. London A, 123, 292.

Kaveh, M., and Wiser, N. 1982. J. Phys. F, 12, 935.

Kubica, P., and Stewart, A.T. 1975. Phys. Rev. Lett., 34, 852.

Landauer, R. 1978. J. Phys. F, 8, L245.

Lass, J.S. 1976. Phys. Rev. B, 13, 2247.

Lass, J.S. 1978. Electrical Transport and Optical Properties of Inhomogeneous Media, Edited by Garland, J.C., and Tanner, D.B., (AIP), P. 183.

Lass, J.S., and Pippard, A.B. 1970. J. Phys. E, 3, 137.

Lee, M.J.G., and Falicov, L.M. 1968. Proc. Roy. Soc. London A, 304, 319.

Lifshitz, I.M., Azbel, M.Ya., and Kaganov, M. I. 1957. Sov. Phys. JETP, 4, 41.

Llewellyn, B., McKPaul, D., Randles, D.L., and Springford, M. 1977. J. Phys. F, 7, 2531.

Mayer, H., and El Naby, M.H. 1963, Z. Physik, 174, 289.

O'Shea, M.J., and Springford, M. 1981. Phys. Rev. Lett., 46, 1303.

O'Shea, M.J., and Springford, M. 1983. J. Phys. F, 13, 357.

Overhauser, A.W. 1960. Phys. Rev. Lett., 4, 462.

Overhauser, A.W. 1962. Phys. Rev. 128, 1437.

Overhauser, A.W. 1964. Phys. Rev. Lett., 13, 190.

Overhauser, A.W. 1968. Phys. Rev., 167, 691.

Overhauser, A.W. 1971a. Phys. Rev. B, 3, 3173.

Overhauser, A.W. 1971b. Phys. Rev. Lett., 27, 938.

Overhauser, A.W. 1974. Phys. Rev. B, 9, 2441.

Overhauser, A.W. 1978. Hyperfine Interactions, 4, 786.

Overhauser, A.W. 1982. Can. J. Phys., 60, 687.

Overhauser, A.W. 1983. Private communication.

Overhauser, A.W., and Butler, N.R. 1976. Phys. Rev. B, 14, 3371.

Overhauser, A.W., and de Graff, A.M. 1968. Phys. Rev., 168, 763.

Overhauser, A.W., and Rodriguez, Sergio. 1966. Phys. Rev. 141, 431.

Penz, P.A. 1968. Phys. Rev. Lett., 20, 725.

Pokorny, Milan. 1982. J. Phys. F, 12, 39.

Pratt, W.P. Jr. 1982. Can. J. Phys., 60, 703.

Razavi, F.S., and Datars, W.R. 1979. Can. J. Phys., 57, 860.

Reifenberger, R., Holroyd, F.W., and Fawcett, E. 1980. J. Low Temp. Phys., 38, 421.

Rowlands, J.A., Duvvury, C., and Woods, S.B. 1978. Phys. Rev. Lett., 40, 1201.

Sampsell, J.B., and Garland, J.C. 1976. Phys. Rev. B, 13, 583.

Sander, L.M., Rose, J.H., and Shore, H.B. 1980. Phys. Rev. B, 21, 2739.

Sawada, Anju, and Satoh, Takeo. 1978. J. Low Temp. Phys., 30, 455.

Schaefer, J.A., and Marcus, J.A. 1971. Phys. Rev. Lett., 27, 935.

Shoenberg, D., and Stiles, P.J. 1964. Proc. Roy. Soc. London A, 281, 62.

Simpson, A.M. 1973. J. Phys. F, 3, 1471.

Springford, M. 1981. International Conference on Electron Transport in Metals, Ottawa, Canada.

Stetter, G., Adlhart, W., Fritsch, G., Steichele, E., and Lüscher, E. 1978. J. Phys. F, 8, 2075.

Taub, H., Schmidt, R.L., Maxfield, B.W., and Bowers, R. 1971. Phys. Rev., B, 4, 1134.

Tausch, Peter J., and Newrock, R.S. 1977. Phys. Rev. B, 16, 5381.

Tausch, P.J., Newrock, R.S., and Mitchel, W. 1979. Phys. Rev., B, 20, 501.

Templeton, I.M. 1982. J. Phys. F, 12, L121.

Vanderkooy, J. 1967. Ph. D. Thesis, (McMaster University, Hamilton), p. 47.

van Gelder, A.P. 1978. Solid State Comm., 28, 481.

van Kempen, H., Ribot, J.H.J.M., and Wyder, P. 1981. J. Phys. F, 11, 597.

Verge, C., Altounian, Z., and Datars, W.R. 1977. J. Phys. E, 10, 16.

Visscher, P.B., and Falicov, L.M. 1970. Phys. Rev. B. 2, 1518.

Walsh, W.M. Jr., Rupp, L.W. Jr., and Schmidt, P.H. 1966. Phys. Rev., 142, 414.

Werner, S.A., Eckert, J., and Shirane, G. 1980. Phys. Rev. B, 21, 581.

Ziman, J.M. 1972. Principles of the Theory of Solids, (Cambridge University Press, Cambridge, U.K.) p. 77.